Forschungszentrum Karlsruhe
Technik und Umwelt

Wissenschaftliche Berichte
FZKA 6031

Large Bundle BWR Test CORA-18: Test Results

S. Hagen, P. Hofmann, V. Noack, L. Sepold, G. Schanz, G. Schumacher

Hauptabteilung Ingenieurtechnik
Institut für Materialforschung
Institut für Neutronenphysik und Reaktortechnik
Projekt Nukleare Sicherheitsforschung

April 1998

Forschungszentrum Karlsruhe
Technik und Umwelt
Wissenschaftliche Berichte

FZKA 6031

Large Bundle BWR Test CORA-18: Test Results

S. Hagen, P. Hofmann, V. Noack, L. Sepold,
G. Schanz, G. Schumacher

Hauptabteilung Ingenieurtechnik
Institut für Materialforschung
Institut für Neutronenphysik und Reaktortechnik
Projekt Nukleare Sicherheitsforschung

Forschungszentrum Karlsruhe GmbH, Karlsruhe
1998

Forschungszentrum Karlsruhe GmbH
Postfach 3640, 76021 Karlsruhe

Mitglied der Hermann von Helmholtz-Gemeinschaft
Deutscher Forschungszentren (HGF)

ISSN 0947-8620

Abstract

Large Bundle BWR Test CORA-18: Test Results

The CORA out-of-pile experiments are part of the international Severe Fuel Damage (SFD) Program. They were performed to provide information on the damage progression of Light Water Reactor (LWR) fuel elements in Loss-of-coolant Accidents in the temperature range 1200°C to 2400°C.

CORA-18 was the large BWR bundle test corresponding to the PWR test CORA-7. It should investigate if there exists an influence of the BWR bundle size on the fuel damage behaviour. Therefore, the standard-type BWR CORA bundle with 18 fuel rod simulators was replaced by a large bundle with two additional surrounding rows of 30 rods (48 rods total).

Power input and steam flow were increased proportionally to the number of fuel rod simulators to give the same initial heat-up rate of about 1 K/s as in the smaller bundles. Emphasis was put on the initial phase of the damage progression. More information on the chemical composition of initial and intermediate interaction products and their relocation behaviour should be obtained. Therefore, power and steam input were terminated after the onset of the temperature escalation.

In general, test CORA-18 showed no difference in the damage behaviour, compared to the smaller bundles. The influence of the temperature escalation was confirmed. The escalation started at the 550 mm elevation (750 mm in CORA-7) and progressed in less than 50 s to the 850 mm elevation. Within about 300 s the elevations 250 mm (downward) and 1050 mm (upward) were reached by the oxidation front. The more symmetric axial temperature profile is possibly connected with the lower steam input of 4 g/s for the BWR case compared to 12 g/s in the PWR bundle CORA-7. Destruction and liquefaction mechanisms, deduced from other CORA tests and supporting separate-effect studies have not only been verified but have also resulted in more clarity. This is due to the choice of the earlier test termination compared to standard CORA tests. With respect to the destruction of the bundle by absorber materials, the interaction of boron carbide with steel was verified as initiating effect, and the strong attack on the Zircaloy channel box walls was demonstrated. Most of the relocated boron carbide is transported as liquefied material containing some undissolved B_4C particles. Boron carbide remained at place up to about 400 mm, held together by oxidised residual melt. After dissolution of the channel box walls, the

liquefaction of the fuel rod cladding has started. Due to the large amount of absorber material relocating from the upper part of the bundle down to 100-200 mm the influence of a possible localised recriticality has to be considered for reflooding a partially damaged core with unborated water.

The preferred axial relocation of melt in the gap between the channel box walls results in less radial distribution of the absorber melt within the bundle. In consequence, in the test bundle CORA-18 less liquefaction of Zircaloy of the cladding was found in comparison to the PWR test CORA-7. 104 g of hydrogen were produced in CORA-18 in comparison to 114 g in test CORA-7. The earlier rise of hydrogen production is in agreement with the earlier temperature escalation at the mid bundle elevation and may be a hint for a contribution of the exothermal B_4C oxidation by steam.

Zusammenfassung

SWR-Versuch CORA-18 mit größerem Bündelquerschnitt: Versuchsergebnisse

Die CORA-Out-of-pile-Experimente wurden im Rahmen des internationalen „Severe Fuel Damage"-Programms durchgeführt. Sie sollten Informationen über Schadensmechanismen an Leichtwasser-Reaktor-Brennelementen bei Kühlmittelverluststörfällen im Temperaturbereich von 1200°C bis 2400°C liefern.

CORA-18 war ein analoger SWR-Versuch zum DWR Versuch CORA-7 mit größerem Bündelquerschnitt. Der Versuch CORA-18 sollte für SWR-Bündel überprüfen, ob die Standardgröße mit 18 Brennstabsimulatoren repräsentativ für die Schadensentwicklung und -fortpflanzung im Brennelement ist. Im Versuch CORA-18 wurde daher das Bündel mit zwei zusätzlichen Reihen von insgesamt 30 Stäben umgeben (insgesamt 48 Brennstabsimulatore). Die Leistungseinspeisung und der Dampffluß wurden proportional zur Stabzahl erhöht, um den gleichen anfänglichen Temperaturanstieg von etwa 1 K/s wie beim Standardbündel zu erreichen.

Beim Versuch CORA-18 sollten insbesondere Informationen über die Zusammensetzung der frühen und zwischenzeitlich flüssigen Reaktionsprodukte und des Verlagerungsverhaltens der Schmelze gewonnen werden. Daher wurde die Leistungseinspeisung und die Dampfzufuhr beendet, sobald der Beginn der Temperatureskalation erreicht war.

Der Versuch CORA-18 zeigte keine signifikanten Unterschiede in der Schadensentwicklung und -fortpflanzung im Vergleich zum kleinen Bündel mit 18 Stäben. Es bestätigte sich die Bedeutung der Temperatureskalation für das Aufheizverhalten des Bündels. Die Eskalation begann in der Höhe von ca. 550 mm (750 mm in CORA-7) und breitete sich in weniger als 50 s bis zu einer Höhe von 850 mm aus. Zum Erreichen der Höhe 250 mm (abwärts) und 1050 mm (aufwärts) wurden danach ca. 300 s benötigt. Die Verschiebung des axialen Temperaturmaximums zur Bündelmitte hin ist durch den geringeren Dampffluß von 4 g/s im SWR-Bündel im Vergleich zu 12 g/s im DWR-Bündel zu erklären.

Das in den anderen CORA-Versuchen und den begleitenden Einzeleffekt-Studien gefundene generelle Materialverhalten konnte nicht nur bestätigt sondern auch besser untersucht werden. Dies wurde aufgrund der frühzeitigeren Versuchsbeendigung möglich. Im Hinblick auf die Schadensentwicklung durch das Absorbermaterial konnte der auslösende Einfluß der Wechselwirkung B_4C/Stahl voll

bestätigt werden. Der größte Teil des Borkarbids wird als unborierter Bestandteil der entstandenen Schmelzen verlagert. Zusätzlich werden B_4C-Partikel in der verlagerten Schmelze beobachtet. Ein mit oxidierter Schmelze gesinterter Rest der Borkarbidstäbe bleibt bis ca. 400 mm Höhe erhalten. Nach der Auflösung der Zircaloy-Kühlkanalwände beginnt der Angriff auf die Hüllrohre der Brennstäbe.

Der relativ große Anteil der aus dem oberen Bereich des Bündels nach unten (100-200 mm) verlagerten Absorberschmelze läßt Überlegungen zur Rekritikalität beim Wiederfluten des Reaktorkerns mit unboriertem Wasser als notwendig erscheinen.

Die bevorzugte axiale Verlagerung der Absorberschmelze innerhalb der Kanalwände hat eine geringere radiale Ausbreitung im Bündel zur Folge. In Übereinstimmung damit wurde im Bündel CORA-18 eine geringere Verflüssigung der Zircaloy-Brennstabhüllen im Vergleich zu derjenigen im Versuch CORA-7 gefunden. Der frühzeitigere Anstieg der Wasserstofferzeugung beim Versuch CORA-18 ist in Übereinstimmung mit der früheren Temperatureskalation und deutet auf einen Beitrag der Oxidation des Borkarbids zur Wasserstofferzeugung hin.

Contents

1. Introduction

The TMI-2 accident has demonstrated that a severe fuel damage transient will not necessarily escalate to an uncontrolled core melt down accident if the design basis accident limits are exceeded. Therefore, comprehensive research programs have been initiated in various countries to investigate the relevant fuel rod bundle damage mechanisms that occur in an uncovered core, after an increase of temperature.

In the Federal Republic of Germany at the Forschungszentrum Karlsruhe (FZK) the Severe Fuel Damage (SFD) Program is now co-ordinated by the Project Nuclear Safety Research (PSF) as successor of Project Nuclear Safety (PNS) and LWR Safety Project Group (PRS). As part of this program, out-of-pile experiments (the CORA-Program) were conducted at the Hauptabteilung Ingenieurtechnik (HIT). These experiments had been designed to provide information on the behaviour of Light Water Reactor (LWR) fuel elements under severe fuel damage (SFD) conditions, up to meltdown. The results of the out-of-pile experiments can be used for the assessment of the SFD computer codes.

Within the frame work of international co-operation the out-of-pile experiments contribute complementary information to the results obtained from the limited number of inpile tests. The investigation of the basic phenomena of the damage process was supported by separate-effect tests.

The most important aspects concerning fuel rod failure and subsequent core degradation are the chemical interactions amongst the fuel element components in competition with the oxidation of the cladding in steam, which causes also the temperature escalation. Melt formation starts around 1200°C by chemical interactions of the Inconel spacer grids and absorber materials (Ag, In, Cd) for PWRs and B_4C/stainless steel for BWRs with the Zircaloy cladding. The dissolution of the UO_2 pellets by liquid Zircaloy starts far below the UO_2 melting point.

Melt relocation, blockage formation and finally fragmentation of fuel elements during reflooding characterise the degraded core and the potential of long-term coolability. Furthermore, the influence of internal pressure of the fuel rods (ballooning and bursting) and external pressure of the system (solid contact between pellets and cladding) on the bundle meltdown behaviour was investigated. Further on, the investigation of the influence of pre-oxidation, initial heat-up rate, steam availability,

water level in the bundle and bundle size were included in the program. The damage behaviour of VVER fuel elements was the subject of the last two CORA-tests.

The tests performed in the CORA-facility are listed in the test matrix (Table 1). The original test matrix focussed on the behaviour of PWR fuel elements. In 1988, discussion showed that in most countries using nuclear energy, information on the behaviour of BWRs in severe accident conditions was needed. In consequence, five planned PWR experiments were replaced by BWR tests in the revised test matrix. Also the original sequence of tests was changed, as one can see from the test numbers.

In this report results of the BWR larger bundle test CORA-18 are being described. CORA-18 should investigate if there is an influence of the bundle size on the fuel damage behaviour for the BWR case. Therefore the standard type BWR CORA bundle with 18 fuel rod simulators was replaced by a bundle with two additionally surrounding rows of 30 rods (48 rods total).

Power input and steam flow were increased proportional to the number of fuel rod simulators to give the same initial heat-up rate of 1 K/s as in the normal bundle. Furtheron the priority of the test was placed on the initial phase of the damage progression. Therefore power and steam input were terminated after the onset of the temperature escalation.

2. Description of the CORA test facility

The CORA out-of-pile facility was designed to investigate the behaviour of LWR fuel elements under severe fuel damage accident conditions. In the experiments the decay heat was simulated by electrical heating. Great emphasis was placed on the fact that the test bundles contained the original materials used in light-water reactor fuel elements so that the different material interactions could be investigated.

Pellets, cladding, grid spacers, absorber rods, and channel box walls were typical of those of the investigated LWRs with respect to their compositions and radial dimensions. In test CORA-18 the following BWR components were used: Original

UO_2 pellets, Zry-4 cladding, Zry spacers, Zry channel box walls and B_4C absorber inside stainless steel tubes surrounded by the stainless steel of the blade.

Figure 1 gives a simplified flow diagram of the facility. The geometrical arrangement of the different CORA components is given in Figure 2. The central part of the facility was the fuel rod bundle. The bundle was enclosed in a Zry shroud with ZrO_2 fibre insulation. A high-temperature radiation shield surrounded the bundle and shroud assembly, leaving an annular space for the movement of the quench cylinder. The bundle was connected to the power supply system at the upper and lower ends.

Below the bundle was the quench unit with a water-filled quench cylinder, which can be moved along the bundle at a controlled speed. The cylinder was guided by three rods, which in addition connected the electric power to the bundle lower end.

The bundle upper end was fixed at the bundle head plate. The plate was connected to the surge condenser by a funnel-shaped tube. The surge condenser was double-walled, leaving access to the bundle end fittings above the bundle head funnel.

The steam was produced in the steam generator, superheated and guided to the lower end of the bundle. The steam not consumed within the bundle was condensed in two parallel condensers and the hydrogen produced was fed into the off-gas system after dilution by air to a low H_2 concentration.

Bundle design:

The bundle and its surroundings are shown in Figures 3 and 4. The bundle horizontal arrangement is given in Figure 5 and the bundle components in Figure 6. Characteristic data of the bundle are presented in Tables 2, 3 and 4. The same components as in the normal tests were used. The bundle of CORA-18 consisted of 28 heated rods, 20 unheated rods, two channel box walls and the absorber blade with 11 rods, representing part of a BWR absorber fuel element arrangement.

The heated fuel rod simulator was sheathed with standard Zry4 cladding tube, containing UO_2 annular pellets with a central heater. The heater consisted of a 1024 mm long tungsten rod (6 mm diameter), the upper electrode (300 mm molybdenum; 689-770 mm copper) and the lower electrodes (300 mm molybdenum; 183-219 mm copper). The electrodes had a diameter of 9 mm. The electrodes were

flame-sprayed with a 0.2 mm thick layer of ZrO_2. Large flexible copper cables provided the connection to the electrical system. The resistance of the flexible cables to the points of voltage measurement for the determination of the power was less than 1 mΩ per rod (recommended value: 0.5 mΩ).

The resistivities R of tungsten, molybdenum and copper are given respectively in the following three equations:

$$R_W = 2.61 \cdot 10^{-2} + 2.63 \cdot 10^{-4} T_W + 2.20 \cdot 10^{-8} T^2_W$$

$$R_{Mo} = 2.29 \cdot 10^{-2} + 5.36 \cdot 10^{-5} T_{mo} + 1.38 \cdot 10^{-7} T^2_{Mo} - 2.22 \cdot 10^{-11} T^3_{Mo}$$

$$R_{Cu} = 7.89 \cdot 10^{-3} + 9.90 \cdot 10^{-5} T_{cu} - 5.49 \cdot 10^{-8} T^2_{Cu} + 3.16 \cdot 10^{-11} T^3_{Cu}$$

with T in [Kelvin] and R in [$\Omega mm^2/m$].

The unheated fuel rod simulators consisted of solid UO_2 pellets and Zry cladding. The unheated rods extended about to the -200 mm elevation, i.e. to about 20 mm above the initial water level of the quench cylinder (-220 mm). Zry-4 spacers were used at three elevations (-33 mm, 578 mm, 1167 mm) to maintain the positions of the rods.

The fuel rod simulators were screwed into the bundle head plate sealing it hermetically. The bundle head plate thus gave the fixed elevation for the axial thermal movement of the rods. The channel box walls were made of 1.2 mm thick Zry-4. The absorber blade contained stainless steel and B_4C and was made of original LWR-components.

To cool the bundle upper end, the heated rods (the copper electrode inside the Zry cladding) and the connectors for the pressure capillaries and the thermocouples of the unheated rods were surrounded by water. The water was cooled by a heat exchanger. Argon was blown against the lower surface of the plate to protect the sealing of the bundle head plate.

At the lower end the heated fuel rod simulators were cooled by the water of the quench cylinder. The initial water level was at the -220 mm elevation. The unheated rods were in contact with the water of the quench cylinder only by the thermocouple

connection cables. The gross volume of water inside the quench cylinder (230 mm ID) was about 70 l.

The bundle was surrounded by a Zry-4 shroud of 1.2 mm thickness. The shroud conducted the steam flow through the bundle. The steam entered at an orientation of 180° into the lower end (0 mm elevation). To minimise the heat losses from the shroud, it was surrounded by a 19 mm (0.75 inch) thick insulating layer of ZrO_2 fibre. On account of the low heat conductivity and heat capacity of the ZrO_2 fibre, the shroud temperature could follow the bundle temperature closely during heatup. The shroud participated in the interaction with steam. The resulting oxidation energy contributed substantially to the bundle heat-up.

The connection between steam inlet at 0 mm elevation and shroud was made by a stainless steel steam distribution tube. This tube extended down into the water of the quench cylinder thus forming a lower closure. The time history of the water level in the quench cylinder in all tests showed that there is no net condensation of steam into the quench cylinder.

At an elevation of 40 mm the steam distribution tube was connected to the shroud. From this elevation the shroud extended in vertical direction for 1195 mm and the insulation for 1070 mm. At six elevations (390-890 mm) windows of 30x30 mm in the shroud and shroud insulation allowed bundle inspection by a video-system (Figure 7).

The annuli between the shroud and the high-temperature shield on one hand and high-temperature shield and pressure containment on the other hand were closed at the upper end by fibre ceramic layers of 38 mm thickness.

High-temperature shield:

To keep the heat losses as low as possible, the bundle was surrounded by an additional high-temperature shield (HTS). The vertical and the horizontal cross-sections of the high temperature shield are given in Figures 3 and 4. The high temperature shield consisted mainly of ceramic fibre plates. The inner layer of plates consisted of ZrO_2, and the outer layer of Al_2O_3. The fibre ceramics were excellent insulators and had a low density which resulted in a low heat capacity. The thermal shock resistance of the fibre ceramics was also extremely good.

The mechanical strength of the high-temperature shield was ensured by external walls of stainless steel (0.9 mm). The fibre ceramic plates were attached to the stainless steel cover by ceramic nails. The inner ZrO_2 layer was 38 mm thick, and the outer Al_2O_3 layer was 76 mm. They were separated by a gap of 23 mm. The distance from the inner insulation surface to the centre of the bundle was 153 mm.

The high-temperature shield was located within the pressure tube. In the pressure tube a large number of flanges allowed access to the bundle. Through these holes and their extensions in the temperature shield, the bundle could be inspected during the test with the help of the videoscope systems.

Heating system:

In test CORA-18 it was necessary to heat 28 rods instead of the normal 12 rods. As the facility only was designed for the use of 24 heated rods, for 4 simulators the copper rods of the electrodes of two adjacent rods were connected by a copper bridge to the connecting cable. Through this lines the current flow was twice as large, as through the single rod cables. The combination of rods can be recognised from the tables on the right side of Figure 17. (A slash between rod numbers.)

The CORA facility allows the rods to be individually connected to three power systems, which could be operated at different voltage, to produce a different power input per rod. In this test the intended power input was the same for all rods. Since the voltages and the currents of the individual rods or "double rod groups" were measured, the power input for each rod could be determined. The power input was controlled by a computer. The time dependent power history was programmed before the test. The power was controlled by measurement of the currents of the groups, and by setting the voltage necessary to obtain the desired power. The distribution of the 32 heated rods to the three power systems can be seen from Figure 17. For the double rods the numbers fo the rods are separated by a slash in the tables on the right side of the pictures for the group of rods connected to the three power systems.

3. Test Conduct

To get comparable results (same starting temperature, same initial temperature increase) we used for the test conduct per rod nearly the same conditions as for the small PWR bundles. The values were chosen according to precalculations at INEL, Idaho Falls and the Technology Centre at Winfrith. The flow of preheated Argon (16 g/s), and the steam input (4 g/s) and the integral power were twice as large, as in the small bundles.

In the CORA experiments the following phases for the test sequence were generally distinguished (Figure 9):

1. 0-3000 s: pre-heating

2. 3000-4150 s: transient

3. > 4150: cooldown.

The pressure in the system was controlled as in all tests to 0.22 MPa. The argon input is separated in two parts. First 16 g/s Argon is preheated and entering at the lower end into the bundle (0 mm elevation). The second amount of 1,4 g/s, not flowing through the bundle, is used for keeping the windows of the videoscopes clean. The second contribution is marked with the label "videoscopes". Both amounts contribute to the dilution of the hydrogen leaving the facility. In test CORA-18 there was not yet an argon flow used for the protection of bundle head plates, as in later performed tests.

The flow of 16 g/s preheated argon through the bundle and a low constant electric power input of about 0.88 kW increase the temperature to a level high enough to avoid condensation of steam (4 g/s) added after 3300 sec.

During the transient phase the initial temperature increase of about 1 K/s was produced by raising the electric power input from 12 to 39 kW (Figure 9). The test was terminated by turning off the electric power at 4150 s (slow cooldown by heat losses). The steam input was stopped at 4100 s.

The boundary conditions during the test are given in detail in (Figures 10 to 24). Figure 10 shows the argon flow within the facility. Figure 11 presents the overpressure of 1,2 bar (2,2 bar absolute) in the system. Figure 12 gives the total electric power input, which was produced by the voltage inputs to the three groups of rods (Figure 13) and the resulting total current (Figure 15). The electric power input is

controlled by measurement of the voltages of the rod groups and the currents of the individual rods (Figure 17). Then the computer sets the voltages to give the power required. The total electric energy input corresponds to the time integral of the power input (Figure 14).

In Figure 16 the time dependence of the resistance of the bundle is given. After about 3900 s the resistance of the bundle is increasing faster. This corresponds to the fact that for getting a linear power increase (Figure 12) the voltage (Figure 13) has to increase faster to compensate the current decrease (Figure 15) after 3900 s. This resistance increase is correlated to the temperature increase caused by the starting of the temperature escalation and reflects the strong temperature dependency of the resistance of the tungsten heater. In Figure 17 the currents of the single rods for the three groups are given. The higher values result from the "double rods". The resistance of the rod groups and the single rods are given in Figure 18 and Figures 19-22. In all graphs the influence of temperature can be seen. The sharp spikes during power shutdown are artificial due to measurement of voltage and current at not exactly the same time.

In Figure 23 the water temperature in the quench cylinder for test CORA-18 at -300 mm is given. At 0 mm elevation (Figure 24) the temperatures measured on the outside of the steam tube (15° and 195°) and 15 mm inside the steam tube (165° and 345°) are shown. For the same side 165°/195° or 345°/15° the temperature measured 15 mm inside the tube is higher than the temperature on steam tube, which has contact to the water of the quench cylinder. But comparing the same type of measurements, the thermocouples on the side of the steam entrance (165°, 195°) give the higher reading.

The temperature of the incoming argon at the steam inlet is measured with two thermocouples (Figure 25). The resulting measurements give practically the same value. The increase of the steam inlet temperature is caused by the heatup of the walls of the connecting tube from superheater to the entrance of the bundle due to the additional heat capacity of the steam.

4. Temperature measurements

The temperatures in the bundle were measured by high-temperature thermocouples of WRe5/WRe26 wires and HfO_2 insulating material. The sheath was made of tantalum and Zircaloy. For the thermocouples used inside the absorber blade only tantalum sheath was used. Six thermocouples (Figure 36) were additionally shielded with a ZrO_2 sheath. The measurements in the high temperature shield were performed with NiCr/Ni-thermocouples sheathed with stainless steel. Also the compensation cables were protected with stainless steel. The positions of the thermocouples in the bundle are given in Table 5 and those in the high temperature shield in Figures 56 and 57.

The temperature measurements of the bundle are presented as function of time in the following way: on one hand, the temperatures of the components (heated rods, unheated rods, channel box walls, absorber blade, etc.) are given in Figures 27 - 42. On the other hand - for comparison reasons - the temperature measurements for different components are grouped by axial elevations (Figures 43 - 53). The temperature of the high temperature shield are given in Figures 58 - 67.

4.1 Temperature in the bundle

Due to the bundle arrangement with a Zircaloy shroud, participating in the exothermic reaction with steam and the low heat conductivity and heat capacity of the fibre insulation, a flat radial temperature profile was obtained. The temperature of the shroud is not lower than that of the components of the bundle. The temperature graphs, measured on identical components at the same elevation are close to each other with a similar shape. The differences in some regions up to about 100 K, may be caused by local differences in the bundle arrangement, relocated material or steam flow. We have therefore defined in Figure 54 best-estimate temperatures of the bundle by using mainly the temperature of the unheated rods.

At the start of the transient the temperature in the bundle was mainly determined by the heating effect of the incoming gas and steam of about 500°C. The result was an axial temperature profile with preference of the lower half of the bundle. With increasing power input and general temperature level the incoming gas and steam

was cooler than the bundle and acted as coolant. The maximum of the temperature moved upwards in axial direction. Due to the smaller amount of steam (4 instead of 12 g/s) this effect was less pronounced in BWR than in PWR tests.

The temperature escalation started at 550 mm and progressed in less than 50 s to 850 mm elevation at about 3900 s. Compared to the PWR large bundle test CORA-7 this happens at a lower elevation (750 mm for CORA-7) and at a earlier time (4200 s for CORA-7). The temperature maximum remains during the whole test at 550 mm elevation. The temperature escalation spreaded down to 250 mm and up to 1050 mm, reaching there about 1400°C compared to 1900°C at 550 mm. In test CORA-7 the axial temperature profile was more developed in the upper half of the bundle. The shift of the maximum temperature to lower elevations in the BWR test CORA-18 may be connected to the smaller amount of steam (4 instead of 12 g/s). In the BWR bundle also the B_4C presents an additional heat source within the bundle, which due to the melt relocation could prefer the middle and lower part of the bundle.

The measured hydrogen production is given in Figure70. The comparison to the escalation region of the temperature graphs of Figure 54 shows the strong correlation between temperature increase and increased hydrogen production.

The comparison of the CORA-18 results to the equivalent CORA-7 data /18/ show that the earlier temperature rise corresponds to the earlier hydrogen increase in CORA-18.

4.2 Temperature measurements at the High Temperature Shield

The results of the temperature measurements in the High Temperature Shield are given in Figures 58 to 69. The temperature on the inner surface of the High Temperature Shield shows the same tendency as in the normal type tests. The maxima at the different elevations are reached some hundred seconds after shutdown of the power input. For CORA-18 the maximum increases from about 150°C at 90 mm to 650°C at 990 mm elevation. This can be compared to CORA-7 with an increase from about 90°C to 850°C. At 590 mm elevation the maximum gets with about 530°C nearly the same temperature as in CORA-7 (570°C), which reflects the influence of the axial maximum of the bundle temperature at 550 mm elevation. Temperatures at equivalent positions for different azimuthal directions are given in

Figures 62 to 66. In general the deviations are less than 50°C. The radial dependency of the temperature at different elevations is given in Figures 67 to 69.

5. Hydrogen generation

The hydrogen produced during the test by the steam/zirconium reaction was measured with mass spectrometer systems installed at two positions, i.e. above the test section, and in the mixing chamber after the gas had passed the condenser (see Figure 1). The gas at the test section outlet could contain a high steam partial pressure and had therefore to be diluted by helium before it entered the analyser through a capillary tube. For this purpose a dilution chamber with flow meters was installed.

A schematic diagram of the probes, gas lines, and gas analysis system is provided in Figure 8. The off-gas mixture which contained hydrogen among other gases is transported to the spectrometer via capillary tubes. It was analysed by quadrupole mass spectrometers of the type Leybold PQ 100. The ion currents representing the concentration of the respective gases were determined. The production rate of a gas component was calculated with the ratio of the partial pressure of the particular gas to that of argon (carrier gas) and multiplied by the argon flow rate through the test bundle. The hydrogen generation rate was evaluated as follows:

$R_m = 2 \bullet p_H F_{Ar} / (22.4 \bullet p_{Ar})$ [g/s]

with

R_m = mass production rate of hydrogen [g/s]

p_H = partial pressure of hydrogen

p_{Ar} = partial pressure of argon

F_{ar} = volumetric argon flow through the mixing chamber [l/s].

The hydrogen production rate and the integrated values are given in Figure 70. The comparison to temperature in the bundle (Figure 54) demonstrates that the

temperature escalation is correlated to the increase in the hydrogen production rate. Both are connected to the exothermic Zry/steam reaction.

6. Post-test appearance of the bundle

The post-test appearance of the bundle is given in Figures 80 to 133. Figures 80 and 81 show the bundle with insulation before and after the test. One can recognise that only minor changes have developed in the arrangement of the insulating material at about 750 mm elevation.

Figures 82 and 83 give the appearance of the shroud after removal of ZrO_2 fibre insulation. In accordance with the axial temperature distribution within the bundle a strong oxidation can be recognised between 250 mm and 950 mm elevation.

In Figures 84 and 85 the post-test appearance of the bundle after partial removal of the shroud is shown. Melt formed during the test had glued the shroud to the bundle so that it was not possible to remove the shroud as a whole. Only some embrittled areas of the shroud could be broken away, without doing damage to the bundle. These areas are shown in Figures 86 to 89 and in detail in Figures 90 to 100.

The damage in the bundle can best be seen from the horizontal and vertical cross sections. To enable the cutting of the cross sections, a Lucite box was set around the bundle for encapsulation with epoxy resin. The lower end of this box was closed by a paraffin layer which was produced by refreezing paraffin floating on the water of the quench cylinder. Rutapox 0273 with the hardener LC (Bakelite GmbH, Iserlohn) was used as epoxy. This epoxy was chosen as its reaction time was slow enough that the shrinkage effect is negligible. The hardening time was one week. The bundle was filled starting from the bottom through the steam inlet. A saw with 2.3 mm thick diamond blade of 500 mm OD (mean diamond grain size 138 μm) was used to cut the bundle at 3200 rpm. The horizontal and vertical cross sections are given in Figures 101 to 110 and in appendix B1 – B 15. In Figures 111 to 134 the damage development is demonstrated in detail with the help of additional enlarged presentations and the results of SEM investigations.

The horizontal cross sections in Figures 101 and 102 and the vertical cross sections in Figures 103 to 110 complement the information gained from the temperature measurements and the inspection of the outer appearance of the bundle. The

maximum of the damage can be seen in the horizontal cross sections at 560 mm and 554 mm elevation.

The comparison of the horizontal cross sections at 1158 mm and 1016 mm demonstrate that the damage is initiated by the interaction of the B_4C/stainless steel absorber melt with Zry of the channel box wall. Separate effect tests have shown that B_4C in contact to stainless steel starts to liquefy quickly in surpassing 1200°C. At 1158 mm the maximum temperature was 1100°C while at 1016 mm a maximum temperature of 1530 °C was reached. One can recognise that the channel box wall close to the absorber blade is completely dissolved, while the channel box wall on the opposite side of the bundle is not attacked at all. On the side of the absorber blade also the attack on the Zry cladding of the fuel rods has started.

At the lower end the cross sections at 97 mm and 112 mm with a maximum temperature of 870°C and 930°C show no destruction of absorber blade and channel box walls. The vertical cross sections of Figure 110 show, that between about 130 mm and 240 mm a blockage has formed between the channel box walls, especially on the open side. Details are discussed in the next section. Between 254 mm and 1016 mm the absorber blade and the channel box walls are destroyed. At 269 mm and 413 mm remnants of most of the B_4C rods can be recognised.

7. Microstructural observations

7.1 Procedure

According to the sectioning schedule given in Fig. 102a the bundle had been prepared by horizontal and vertical cuts at informative positions. For a detailed microstructural investigation the selected planes were treated by the metallographic procedures of grinding and polishing. The samples were examined microscopically and detailed enough to allow the choice of representative positions for the photo documentation. On this basis the observations were interpreted and will be treated in the following. The figures have been composed either as an overview on the respective section or as illustration of special items. The bundle is described in upward direction.

7.2 Vertical section CORA-18-c-L, elevation 114-254 mm

At this elevation the bundle is characterised by melt accumulation especially within the absorber channel, resulting from absorber destruction at higher elevations. At an originally rather low temperature range and supported by heat transported by the melt, the interactions remain incomplete and thus observable (Fig.111-114):

The blockage was initiated by individual flaws of melt with some closed porosity, their solidification and sintering into a flat pool, whereas additional melt preferentially solidified at the side of the absorber blade (Fig.111).Remaining fragments of the absorber rods with B_4C particles can be seen in Fig. 112 ,in close contact with accumulated melt of complex microstructure. In comparison with separate effect investigations of steel/boron carbide interaction this microstructure can be interpreted to result from the process, which went on at higher elevations and generated this type of melt. Fig. 113 shows an example of embedded boron carbide particles, with undefined elevation origin, however with only slight dissolution progress. This illustrates that B_4C can be partly transported in unreacted form as well.

Fig. 114 is presented to illustrate, that the melt pool is not uniform in composition and properties, as indicated here for the microstructure and the oxidation behaviour at free surfaces. Layered scale systems of porous outer layer and incompletely converted inner layer or internal oxidation along grain boundaries are observed at different positions. This is typical for multicomponent materials and the often resulting reduced protection of the scale. The oxidation of relocated melt is thus identified as relevant aspect. However, missing information on oxidation kinetics and expected anomalies would complicate any intention to simulate this behaviour.

7.3 Cross section CORA-18-03 (top), elevation 269 mm

Slightly above the previously described vertical section this cross section is characterised by essentially intact or partly damaged fuel rods, damaged absorber blade, melts accumulated between fuel rods, along the shroud and within the channel box, and relocated fragment rubble (Fig.115). The higher magnifications of the macrographs of Fig. 116 allow to realise the presence of partly embedded but still undissolved fuel rod cladding, fractured but intact fuel pellets, residues of the absorber blade in free standing condition and despite severe destruction of absorber

tube cladding and blade by reactive melting, as well as the remaining of often thin and bare scale structures. The metallic, ceramic or composite rubble particles are not further interpreted.

Unrelocated bundle components and reaction products are described according to Fig. 117 in their oxidation status. Fuel rod cladding external oxidation and internal interaction with the pellet, which have proceeded at about 1800 °C, are observable in prototypical morphology. The same holds for the shroud, for which the big difference between the external and the internal scale thickness is mentioned. In addition the oxidation status of the absorber blade and of metallic melt is illustrated.

7.4 Cross section CORA-18-04 (top), elevation 413 mm

Proceeding towards higher bundle elevation, the aspect of fuel pellet dissolution by molten cladding is one dominant degradation mechanism (Fig. 118). In competition with the cladding oxidation this results in the loss of cladding integrity by formation of axially oriented cracks through the scale, the axial splitting of the cladding (flowering phenomenon), and the formation of melt bridges between adjacent rods. Downward relocation of the (Zr,U,O)-type of melt has occurred as well, leaving behind bare pellet surfaces and oxidised cladding segments (Fig. 119). Absorber channel and shroud walls are heavily bent, partly melted and partly thickened by accumulated melt (Fig. 118, 120). Again the internal shroud oxidation is more advanced than the external oxidation, for which a pronounced limitation of steam supply should have moderated the reaction (Fig.120).

7.5 Vertical section CORA-18-e-L, elevation 415-545 mm

The vertical section directly above and through the absorber channel gives detailed information on the mechanisms of absorber blade degradation (Fig. 121-124). In the overview macrograph of Fig. 121 the faint structures shining through the transparent epoxy have to be distinguished from those at the cut. The latter are lumps of different melts, residual B_4C, and rubble. A typical absorber melt, composed of undissolved B_4C, precipitated C, and porous matrix is shown. Two other morphologies of this melt type are depicted in Fig.122. In direct vicinity the distribution and morphology of the other melt type, containing less absorber material and more steel components, is documented in Fig. 123. This melt also contains considerable porosity, and the

several phases are of rounded or acicular form. Accumulated rubble consists essentially of pellet and fuel cladding fragments, often with adherent melt (Fig.124).

7.6 Cross section CORA-18-05 (top), elevation 560 mm

This cross section at the elevation of the spacer grid demonstrates severe damage of bundle components, the shroud, and especially of the absorber components, but still the overall fuel rod geometry is mostly intact (Fig.125). Fig.126 and 127 demonstrate the severe oxidation status of different components and products: Melt lumps distributed in the fuel rod region have been converted essentially to ceramic materials with embedded residual metallic phase (Fig.126) or may have preserved a metallic core (Fig.127). Fuel rod cladding and spacer parts are completely oxidised. An unidentified Zircaloy structure, possibly relocated from above shows typical aspects of partial scale spalling during mechanical deformation under oxidation (Fig.127).

The status of the absorber blade region indicates ongoing reaction between absorber melt and still remaining B_4C particles, ongoing melt movement identified by unoxidized free surface, and free access for relocated pellets, which are found collected in oblique orientations after falling from above (Fig.128).

7.7 Cross section CORA-18-06 (top), elevation 717 mm

At this elevation there are no residues at all from the absorber related part of the bundle, whereas most of the fuel rods have remained at least in fragmentary form (Fig.129). The figures 130 and 131 refer to details of the status of severe oxidation, melting, and materials interaction. The cladding, heavily bent, fractured, melted, and interacted with the fuel, is found mostly in oxidic form (Fig.130). Interaction melt and void formation between pellet and cladding scale can be distinguished from externally adherent melt, which attacks and dissolves the scale and comes into contact with the pellet. It is again mentioned that this melt itself is exposed to steam, so that the fuel dissolution together with the steam exposure finally terminates the reactivity and the presence of metallic residues (Fig.131).

7.8 Cross section CORA-18-07 (top), elevation 874 mm

This finally examined elevation gave no new or unique information. In the overview of Fig.132 the presence of reacted absorber blade residues and on the opposite bundle side of a part of the absorber channel is clearly visible. Fig.133 combines morphological details of the primarily formed boron rich melt, the secondary more diluted absorber melt, its interaction with the fuel and its steam oxidation. Fig.134 identifies confined or recently released metallic melt residues at this mostly oxidised level.

8. Summary and discussion of major results

CORA-18 was the correspondent large BWR bundle test to the PWR test CORA-7. It should prove also for BWR bundles that there is no influence of the bundle size on the fuel damage behaviour . Therefore the standard type BWR CORA bundle with 18 fuel rod simulators was replaced by the large bundle with two additional surrounding rows of 30 rods (48 rods total).

Power input and steam flow were increased proportional to the number of fuel rod simulators to give the same initial heat-up rate of 1 K/s as in the normal bundle. Furtheron the priority of the test was placed on the initial phase of the damage progression. More information on the chemical composition of initial and intermediate interaction products and their relocation behaviour should be obtained. Therefore power and steam input were terminated after the onset of the temperature escalation.

In general, test CORA-18 showed no difference in the damage behaviour compared to the smaller bundles. The escalation started in the region 550 to 850 mm elevation and progressed in about 300 s downwards to 250 mm and upwards to 1050 mm elevation.

The strong contribution of the exothermic heating is shown by the fact, that the temperature still increased after the electric power input to the bundle had stopped. At 250 mm and 1250 mm the maximum of the temperature was only reached about 300 s after initiation of the power shutdown. Limiting processes for the exothermic reaction are the decrease of metallic Zircaloy or steam and the increase of the protective oxide layer thickness.

The more symmetric axial temperature profile, compared to CORA-7, was possibly caused by the lower steam input of 4 g/s for the CORA-18 bundle compared to 12 g/s in the PWR bundle CORA-7.

The post-test bundle appearance and the cross section examinations show, that the damage progression developed in accordance to the axial temperature distribution. Oxidation and interaction with absorber materials are competitive reactions for the Zircaloy of the cladding. Undisturbed oxidation can preferentially be seen in the upper and lower parts of the bundle. Attack from the absorber material can be recognised from about 300 mm to 700 mm elevation.

With respect to destruction by absorber material the interaction of boron carbide with steel is verified as initiating effect and the strong attack on the channel box walls is demonstrated. Most of the relocated boron carbide is transported as component of melts, some as embeded particles or by free falling. Residual boron carbide remains at place, held by oxidised residual melt or thin blade scale residues.

After dissolution of the channel box walls, the liquefaction of the fuel rod cladding was started. The liquefied cladding attacks the pellets by dissolution far below the melting point of the Zircaloy.

Due to the geometrical arrangement (free space between channel box walls) the vertical melt relocation has a high probability compared to the horizontal spreading within the bundle. In consequence a large amount of absorber material relocated from the upper part of the bundle down to 100-200 mm elevation. The influences of this separation between fuel and absorber have to be considered, for instance, the possible recriticality, if reflooding with unborated water should take place after absorber and before fuel relocation in an ongoing accident.

In connection to the relocation behaviour CORA-18 has proved the results gained in the smaller size tests. The melt formed by interaction in the upper part of the bundle has formed a blockage due to the axial temperature profile in the lower part. The axial cross sections show that the blockage was formed stepwise. Material was oxidised and then new melt relocated on top of the oxide layer.

Melt relocation and axial temperature distribution are always strongly connected, i.e. the melt relocation is determined by the axial temperature distribution, but the axial temperature distribution itself is influenced by the heat transported with the relocating

melt and the heat released by the continued or even accelerating oxidation reaction of the melt during its relocation and at its final position.

9. References

1. J.M. Broughton; P. Kuan, D.A. Petti; "A Scenario of the Three Mile Island Unit 2 Accident", *Nuclear Technology*, Vol. 87, 34-53 (1989).
2. S. Hagen, K. Hain: "Out-of-pile Bundle Experiments on Severe Fuel Damage (CORA-Program)", *KfK* 3677 (1986).
3. S. Hagen, P. Hofmann, G. Schanz, L. Sepold; "Interactions in Zircaloy/UO_2 Fuel Rod Bundles with Inconel Spacers at Temperatures above 1200°C (CORA-2 and CORA-3)", *KfK* 4378 (1990).
4. S. Hagen, P. Hofmann, V. Noack, G. Schanz, G. Schumacher, L. Sepold; "Results of SFD Experiment CORA-13 (OECD International Standard Problem 31)" *KfK* 5054 (1993).
5. M. Firnhaber, K. Trambauer, S. Hagen, P. Hofmann, G. Schanz, L. Sepold:ISP-31, "CORA-13 Experiment on Severe Fuel Damage" GRS-106, *KfK* 5287, NEA/CSNI/R (93) 17 (1993).
6. S. Hagen, P. Hofmann, V. Noack, G. Schanz, G. Schumacher, L. Sepold; "BWR Slow Heat-up Test CORA-31: Test Results", *KfK* 5383 (1994)
7. S. Hagen, P. Hofmann, V. Noack, G. Schanz, G. Schumacher, L. Sepold; "Dry Core BWR Test CORA-33: Test Results", *KfK* 5261 (1994).
8. S. Hagen, P. Hofmann, V. Noack, G. Schanz, G. Schumacher, L. Sepold; "Behaviour of a VVER Fuel Element Tested under Severe Accident Conditions in the CORA Facility (Test Results of Experiment CORA-W1)" *KfK* 5212 (1994).
9. S. Hagen, P. Hofmann, V. Noack, G. Schanz, G. Schumacher, L. Sepold; "Behaviour of a VVER-1000 Fuel Element with Boron Carbide/Steel Absorber Tested under Severe Fuel Damage Conditions in the CORA Facility (Results of Experiment CORA-W2)", *KfK* 5363 (1994).
10. J. Burbach; "Results of SEM/EDX Microrange Analyses of the PWR Fuel Element Meltdown Experiment CORA-13", *KfK* 5162 (1993).

11. J. Burbach; "Results of SEM/EDX Microrange Analyses of the BWR Fuel Element Meltdown Experiment CORA-16", *KfK* 5282 (1994).

12. S. Hagen, P. Hofmann, V. Noack, L. Sepold, G. Schanz, G. Schumacher;" Comparison of the Quench Experiments CORA-12, CORA-13, CORA-17", *FZKA* 5679, (1996).

13. S. Hagen, P. Hofmann, V. Noack, L. Sepold, G. Schanz, G. Schumacher; "Impact of absorber rod material on bundle degradation seen in CORA experiments", *FZKA* 5680 (1996).

14. S. Hagen, P. Hofmann, V. Noack, L. Sepold, G. Schanz, G. Schumacher; "Pre-oxidised BWR Test CORA-28: Test Results"; FZKA 5571 (1997)

15. S. Hagen, P. Hofmann, V. Noack, L. Sepold, G. Schanz, G. Schumacher; "Pre-oxidised PWR Test CORA-29: Test Results"; FZKA 5928 (1997)

16. S. Hagen, P. Hofmann, V. Noack, L. Sepold, G. Schanz, G. Schumacher; "Slow Heatup PWR Test CORA-30: Test Results" FZKA 5929 (1997)

17. S: Hagen, P. Hofmann, V. Noack, L. Sepold, G. Schanz, G. Schumacher; "Cold Lower End Test CORA-10: Test Results" FZKA 5572 (1997)

18. S: Hagen, P. Hofmann, V. Noack, L. Sepold, G. Schanz, G. Schumacher; "Large Bundle PWR Test CORA-7: Test Results" FZKA 6030 (1998)

10. Acknowledgements

At the Forschungszentrum Karlsruhe a variety of support needed for preparation, conduct, and evaluation of the experiment is hereby gratefully acknowledged.
The facility was designed by K. Hain and his team. The special bundle set up was designed by Mr. H. Junker. The test rods were assembled by Mr. E. Mackert, the test bundles by Messrs. H. Gießmann and R. Röder. The authors would like to thank Messrs. H. Benz, C. Grehl and H.J. Röhling for test preparations and conduct.
Mr. K. P. Wallenfels was responsible for arrangement of camera and video systems and for the preparation of temperature measurements. Messrs. R. Huber and H. Malauschek prepared and conducted the on-line measurements of the off-gas composition.

The post-test investigations by the optical microscope were performed by Mr. Metzger and the SEM investigations by Mr. Burbach.

Finally we would like to express our gratitude to Mrs. U. Ivanitsch for the careful typing of this report.

List of tables

Tab. 1: CORA Test Matrix

Test No.	Max. Cladding Tempera-tures	Absorber Material	Other Test Conditions	Date of Test
2	≈ 2000°C	-	UO_2 refer., inconel spacer	Aug. 6, 1987
3	≈ 2400°C	-	UO_2 refer., high temperature	Dec. 3, 1987
5	≈ 2000°C	Ag, In, Cd	PWR-absorber	Febr. 26, 1988
12	≈ 2000°C	Ag, In, Cd	quenching	June 9, 1988
16	≈ 2000°C	B_4C	BWR-absorber	Nov. 24, 1988
15	≈ 2000°C	Ag, In, Cd	rods with internal pressure	March 2, 1989
17	≈ 2000°C	B_4C	quenching	June 29, 1989
9	≈ 2000°C	Ag, In, Cd	10 bar system pressure	Nov. 9, 1989
7	< 2000°C	Ag, In ,Cd	57-rod bundle, slow cooling	Febr. 22, 1990
18	< 2000°C	B_4C	59-rod bundle, slow cooling	June 21, 1990
13	≈ 2200°C	Ag, In, Cd	OECD/ISP; quench initiation at higher temperature	Nov. 15, 1990
29*	≈ 2000°C	Ag, In, Cd	pre-oxidized,	April 11, 1991
31*	≈ 2000°C	B_4C	slow initial heat-up (≈ 0.3 K/s)	July 25, 1991
30*	≈ 2000°C	Ag, In, Cd	slow initial heat-up (≈ 0.2 K/s)	Oct. 30, 1991
28*	≈ 2000°C	B_4C	pre-oxidized	Febr. 25, 1992
10	≈ 2000°C	Ag, In, Cd	cold lower end 2 g/s steam flow rate	July 16, 1992
33	≈ 2000°C	B_4C	dry core conditions, no extra steam input	Oct. 1, 1992
W1	≈ 2000°C	-	WWER-test	Febr. 18, 1993
W2	≈ 2000°C	B_4C	WWER-test with absorber	April 21, 1993

Initial heat-up rate: ≈ 1,0 K/s; Steam flow rate, PWR: 6 g/s, BWR: 2 g/s; quench rate (from the bottom) ≈ 1 cm/s

Tab. 2: Design characteristics of bundle CORA-18

Bundle type:			BWR
Bundle size:			59 rods
Number of heated rods:			28
Number of unheated rods:			20
Pitch:			14.3 mm
Rod outside diameter:			10.75 mm
Cladding material:			Zircaloy-4
Cladding thickness:			0.725 mm
Rod length	- heated rods:		1840 mm
	(elevation		-369 to 1471 mm)
	- unheated rods:		1672 mm
	(elevation		-201 to 1471 mm)
Heated length:			1000 mm
Heater material:			Tungsten (W)
Heater diameter:			6 mm
Fuel pellets	- heated rods:		UO_2 annular pellets
	- unheated rods:		UO_2 full pellets
Pellet stack	- heated rods:		0 to 1000 mm
	- unheated rods:		-200 to 1300 mm
U-235 enrichment			0.2 %
Pellet outer diameter (nominal)			9.1 mm
Grid spacer	- material:		Zircaloy-4
	- length:		42 mm
	- location	lower	- 33 mm
		center	+ 578 mm
		top	+ 1167 mm
Shroud	- material		Zircaloy-4
	- wall thickness		1.2 mm
	- outside dimensions		138 x 135 mm
	- elevation		40 mm - 1235 mm
	- insulation material		ZrO_2 fiber
	- insulation thickness		20 mm
Absorber rod	- number of rods		11
	- material		B_4C powder
	- cladding		Stainless steel
	- cladding OD		5.77 mm
	- cladding ID		4.57 mm
	- length inside		1578 mm
	outside		1600 mm
Absorber blade			
	- material		Stainless steel
	- dimensions inside		66 x 6 mm
	- wall thickness		1 mm

Note: Elevations are referred to the bottom of the heated zone (0 mm = EL 5121). The values for the grid spacers refer to the top end.

Table 3: Total specific mass data of bundle CORA-18

Specific mass [kg/m]	
Tungsten heater elements	15.28
UO_2	24.31
Zircaloy in rods	7.20
Absorber, B_4C	0.311
Absorber rods , Stainless steel	0.852
Absorber blade, Stainless steel	1.293
Grid spacer	0.304
Zircaloy of channel box wall *	2.42
Zircaloy of shroud	4.29
Total zircaloy	13.91

* two walls inside the bundle

Table 4: Areas of bundle CORA-18

Cross section areas [m^2]	
Tungsten	$7.92\ 10^{-4}$
UO_2	$2.34\ 10^{-3}$
Zircaloy cladding	$1.096\ 10^{-3}$
Absorber, B_4C	$1.828\ 10^{-4}$
Absorber rods , Stainless steel	$1.08\ 10^{-4}$
Absorber blade, Stainless steel	$1.637\ 10^{-4}$
Zircaloy of channel box wall *	$3.68\ 10^{-4}$
Zircaloy of shroud	$6.53\ 10^{-4}$

* two walls inside the bundle

Tab. 5: Positions of thermocouples

Positions of thermocouples in unheated rods (CORA-18)			
Slot number	Elevation [mm]	Rod number	Type of TC
153	1450	4	NiCrNi
154	1450	0.4	NiCrNi
155	1250	0.2	NiCrNi
156	1250	6.8	NiCrNi
157	1250	8.4	NiCrNi
158	1250	0.8	NiCrNi
159	1250	0.6	NiCrNi
160	1250	4.8	NiCrNi
101	1150	2.4	WRe *
102	950	4.6	WRe *
103	750	8.6	WRe *
104	750	6.4	WRe *
105	750	4.2	WRe*
106	750	2	WRe *
107	750	6.2	WRe *
108	750	8	WRe *
109	750	2.6	WRe *
201	550	4.6	WRe *
202	350	2.4	WRe *
203	150	0.2	WRe *
231	50	8.6	NiCrNi
232	50	6.4	NiCrNi
233	50	4.2	NiCrNi
234	50	2	NiCrNi
204	50	6.8	NiCrNi
235	50	8.4	NiCrNi
236	50	4	NiCrNi
237	50	0.8	NiCrNi
238	50	0.4	NiCrNi

Positions of thermocouples at heated rods (CORA-18)			
Slot number	Elevation [mm]	Rod number	Type of TC
197	1468	T3	NiCrNi
110	950	1.3	WRe *
111	950	5.7	WRe *
112	750	3.1	WRe *
113	691	7.5	WRe *
205	550	1.3	WRe*
206	550	5.7	WRe *
207	350	3.1	WRe *
208	350	7.5	WRe *
209	150	3.5	WRe *
210	150	R7	WRe *

Positions of thermocouples located inside the absorber blade (CORA-18)			
Slot number	Elevation [mm]	Orientation of TE	Type of TC
114	1350	300°	WRe **
115	1150	300°	WRe**
116	950	300°	WRe **
117	750	300°	WRe **
211	550	300°	WRe **
212	450	300°	WRe**
213	350	300°	WRe **
214	250	300°	WRe **
215	150	300°	WRe **
216	50	300°	WRe **

Positions of thermocouples located outside the absorber blade (CORA-18)			
Slot number	Elevation [mm]	Orientation of TE	Type of TC
131	1150	300°	NiCrNi
134	1150	120°	NiCrNi
135	1050	120°	NiCrNi
132	950	300°	NiCrNi
136	950	120°	NiCrNi
137	850	120°	NiCrNi
133	750	300°	NiCrNi
138	750	120°	NiCrNi
139	650	120°	NiCrNi
239	550	300°	NiCrNi
244	550	120°	NiCrNi
245	450	120°	NiCrNi
241	350	300°	NiCrNi
246	350	120°	NiCrNi
247	250	120°	NiCrNi
242	150	300°	NiCrNi
248	150	120°	NiCrNi
243	50	300°	NiCrNi
249	50	120°	NiCrNi
250	-50	120°	NiCrNi

*) WRe wires,duplex sheath (Ta/Zr)

**) WRe wires,Ta sheath

Tab. 5: (continued)

Positions of thermocouples near by the bundle head (CORA-18) *			
Slot number	Elevation [mm]	Orientation of TE	Type of TC
152	1937	180°	NiCrNi
148	1740	180°	NiCrNi
151	1734	180°	NiCrNi
150	1531	180°	NiCrNi
149	1511	180°	NiCrNi
198	1491	345°	NiCrNi
196	1450	90°	NiCrNi
195	1120	180°	NiCrNi

Positions of thermocouples at the channel box wall (CORA-18)			
Slot number	Elevation [mm]	Orientation of TE	Type of TC
124	1150	300°	WRe*
125	1150	120°	WRe *
126	950	300°	WRe *
127	950	120°	WRe *
128	750	300°	WRe*
129	750	120°	WRe*
217	550	300°	WRe *
218	550	120°	WRe *
219	350	300°	WRe *
220	350	120°	WRe*
221	150	300°	WRe *
222	150	120°	WRe *
223	50	300°	WRe *
224	50	120°	WRe*

Positions of thermocouples at the shroud (CORA-18).			
Slot number	Elevation [mm]	Orientation of TE	Type of TC
130	950	75°	WRe*
141	950	255°	WRe*
142	765	75°	WRe*
143	780	255°	WRe*
225	550	75°	WRe*
226	350	75°	WRe*
227	350	255°	WRe*
228	150	255°	WRe*
199	50	75°	NiCrNi

Positions of thermocouples at the shroud insulation (CORA-18)			
Slot number	Elevation [mm]	Orientation of TE	Type of TC
251	950	75°	NiCrNi
252	750	75°	NiCrNi
253	550	75°	NiCrNi
254	350	75°	NiCrNi
255	150	75°	NiCrNi
256	50	75°	NiCrNi

Positions of thermocouples between bundle and shroud (CORA-18)			
Slot number	Elevation [mm]	Orientation of TE	Type of TC
146	1350	165°	NiCrNi
147	1350	345°	NiCrNi
144	1250	165°	NiCrNi
145	1250	345°	NiCrNi

Positions of thermocouples btw. bundle and shroud in ceramic tube (CORA-18)			
Slot number	Elevation [mm]	Orientation of TE	Type of TC
118	965	345°	WRe*
122	920	120°	WRe*
119	840	165°	WRe*
121	820	75°	WRe*
120	710	255°	WRe*
123	710	120°	WRe*

Positions of thermocouples for gas temp. and at steam distribution tube (CORA-18)			
Slot number	Elevation [mm]	Orientation of TE	Type of TC
257	0	315°	NiCrNi
258	0	135°	NiCrNi
259	0	180°	NiCrNi
260	0	180°	NiCrNi
193	0	15°	NiCrNi
194	0	195°	NiCrNi

*) WRe wires,duplex sheath (Ta/Zr)

**) WRe wires,Ta sheath

Tab. 6: List of cross sections for test bundle CORA-18

Sample	Sample length	Axial position bottom	top	Remarks
18-a	ca. 40 mm	ca.-100 mm	-45 mm	
Cut	2 mm			Lower grid spacer
18-b	140 mm	-43 mm	97 mm	
Cut	2 mm			
18-02	13 mm	99 mm	112 mm	Cross section
Cut	2 mm			
18-c	140 mm	114 mm	254 mm	Two add. longit. cuts (18-c-L)
Cut	2 mm			
18-03	13 mm	256 mm	269 mm	Cross section
Cut	2 mm			
18-d1	63 mm	271 mm	334 mm	Additional longitudinal cut
Cut	2 mm			
18-d2-L	47 mm	336 mm	383 mm	18-d2-R top 398 mm
Cut	2 mm			
18-01	13 mm	385 mm	398 mm	18-d2-L shortened by 18-01
Cut	2 mm			
18-04	13 mm	400 mm	413 mm	Cross section, lower window
Cut	2 mm			
18-e1	64 mm	415 mm	479 mm	18-e with 2 longit. cuts (18-e-L)
Cut	2 mm			
18-e2	64 mm	481 mm	545 mm	18-e-L not horizontally divided
Cut	2 mm			
18-05	13 mm	547 mm	560 mm	Cross section, central spacer
Cut	2 mm			
18-f	140 mm	562 mm	702 mm	
Cut	2 mm			

Tab. 6: (continued)

18-06	13 mm	704 mm	717 mm	Cross section
Cut	2 mm			
18-g	140 mm	719 mm	859 mm	
Cut	2 mm			
18-07	13 mm	861 mm	874 mm	Cross section
Cut	2 mm			
18-h	140 mm	876 mm	1016 mm	
Cut	2 mm			Above heated zone
18-i	140 mm	1018 mm	1158 mm	
Cut	2 mm			Upper grid spacer
18-j	xx mm	1160 mm	xxxx mm	Upper remnant

Table 7: Distribution of void volumes in unheaed and heated rods

Void volume of one unheated rod

	elevation [mm]	volume [cm^3]	relative volume [cm^3/cm]
dishing of uranium pelletts; gap between pellet stack and cladding	-201 to 1315	4.083	0.027
void volume above pellet stack	1315 to 1439	8.378	0.678
	1439 to 1456	0.711	0.419
	1456 to 1522	3.658	0.55
	1522 to 1531	0.387	0.43
	1531 to 1762	6.531	0.283
	1762 to 1764	0.084	0.419
system for pressure measurement		15.120	
total void volume		38.952	

Void volume of one heated rod

	elevation [mm]	volume [cm^3]	relative volume [cm^3/cm]
void volume below pellet stack	-369 to -334	0.826	0.236
	-334 to 0	1.391	0.0417
gap between pellet stack and cladding and between pellet stack and heater	0 to 1024	2.311	0.023
void above pellet stack	1024 to 1875	3.545	0.0417
	1875 to 1911	0.852	0.24
system of pressure measurement		10.860	
total void volume		19.785	

List of figures

25 : Temperatures at steam inlet

26 : Thermocouple locations within the bundle (CORA-18)

27 : Temperatures of heated rods

28 : Temperatures of unheated rods, 1250 mm elevation

29 : Temperatures of unheated rods, 750 mm elevation

30 Temperatures of unheated rods, 50 mm elevation

31 Temperatures of unheated rods (TCs in central position)

32 : Temperatures on the channel box wall

33 : Temperatures on the absorberblade, 120° orientation

34 : Temperatures on the absorberblade, 300° orientation

35 : Temperatures in the absorber blade

36 : Temperatures measured with ceramic protected TCs

37 : not used

38 : Temperatures of the outer side of the shroud

39 : Temperatures on shroud insulation

40 : Gas temperatures above the heated zone

41 : Gas temperatures between shroud and HTS

42 : Gas temperatures measured in the bundle head blade

43 : Temperatures at elevations given (1350, 1250 mm)

44 : Temperatures at elevations given (1150-1050 mm)

45 : Temperatures at elevations given (950 mm)

46 : Temperatures at elevations given (850 - 820 mm))

47 : Temperatures at elevations given (750 - 710 mm)

48 : Temperatures at elevations given (550 mm)

49 : Temperatures at elevations given (450 mm)

50 : Temperatures at elevations given (350 mm)

51 : Temperatures at elevations given (250, 150 mm)

52 : Temperatures at elevations given (50 mm)

53 : Temperatures at elevations given (0, -50 mm)

54 : Best-estimate bundle temperatures at different elevations

54a : Vertical profiles of the best-estimate temperatures (CORA-18)

54b : Iso-temperature plots of unheated rods in the transient phase compared to electrical and chemical power input (CORA-18)

54c : Iso-temperature plots of unheated rods for heatup and cooldown compared to electrical and chemical power input (CORA-18)

55 : not used

56 : Locations of thermocouples in the high temperature shield

57 : Position of thermocouples in high temperature shield

58 : Temperatures of HTS, Inner surface at 153 mm radius

59 : Temperatures of HTS, Temperatures in HT shield at 192 mm radius

60 : Temperatures of HTS, Temperatures in HT shield at 255 mm radius

61 : Temperatures of HTS, outer surface at 293 mm radius

62 : Temperatures of HTS, Comparison on inner surface at 153 mm radius

63 : Temperatures of HTS, Comparison on inner surface at 153 mm radius, 990 mm and 890 mm elevation

64 : Temperatures of HTS, Comparison on inner surface at 153 mm radius, 390 mm and 90 mm elevation

65 : Temperatures of HTS, Comparison on inner surface at 192 mm radius, 950 mm and 750 mm elevation

66 : Temperatures of HTS, Comparison on inner surface at 192 mm radius, 550 mm and 150 mm elevation

67 : Temperatures of HTS, Radial dependence at about 950 mm elevation

68 : Temperatures of HTS, Radial dependence at about 550 mm elevation

69 : Temperatures of HTS, Radial dependence at about 100 mm elevation

70 : Measured hydrogen production (uncorrected values); production rate (top) and integral values (bottom)

71 : not used

72 : not used

73 : Internal pressure of fuel rod simulators

74 : Measurement of failure time by pressure loss determination

75 : not used

76 : Melt movement as seen by the video system

77 : not used

78 : not used

79 : not used

80 : Bundle with insulation before test

81 : Posttest appearance of the bundle with shroud and insulation

82 : Posttest appearance of the shroud after removal of the insulation

83 : Posttest appearance of the shroud after removal of the insulation

84 : Posttest appearance of the bundle after partial removal of the shroud

85 : Posttest appearance of the bundle after partial removal of the shroud

86 : Posttest partial view at 30° and 210° orientation

87 : Posttest partial view at 75° and 255° orientation

88 : Posttest partial view at 120° and 300° orientation

89 : Posttest partial view at 165° and 345° orientation

90 : Posttest partial view at 300° orientation, 650 - 900 mm elevation

91 : Posttest partial view at 300° orientation, 400 - 650 mm elevation

92 : Posttest partial view at 300° orientation, -150 - 100 mm elevation

93 : Posttest partial view at 285° orientation, 650 - 900 mm elevation

94 : Posttest partial view at 285° orientation, 350 - 650 mm elevation

95 : Posttest partial view at 135° orientation, 650 - 900 mm elevation

96 : Posttest partial view at 135° orientation, 350 - 600 mm elevation

97 : Posttest partial view at 135° orientation, -200 - 100 mm elevation

98 : Posttest partial view at 30° orientation, 650 - 900 mm elevation

99 : Posttest partial view at 30° orientation, 400 - 650 mm elevation

100 : Posttest partial view at 30° orientation, -50 - 100 mm elevation

101 : horizontal cross sections; 1158 - 560 mm elevation

102 : horizontal cross sections; 554 - 97 mm elevation

102a : Bundle sectioning

103 : Vertical cross section; in absorber region, 415 - 545 mm

104 : Vertical cross section; in simulator region, 415 - 545 mm

105 : Vertical cross section; in absorber region, 271 - 398 mm

106 : Vertical cross section; in absorber region, 114 - 254 mm

107 : Vertical cross section; in simulator region, 114 - 254 mm

108 : Two sides of vertical cross section; in absorber region, 415 - 545 mm elevation

109 : Two sides of vertical cross section; in absorber region, 271 - 398 mm elevation

110 : Two sides of vertical cross section; in absorber region, 114 - 254 mm elevation

111 : Vertical section CORA-18-c-L, elevation 114-254 mm, overview and detail of melt within absorber channel

112 : Vertical section CORA-18-c-L, elevation 114-254 mm, absorber blade remnants, embedded by melt

113 : Vertical section CORA-18-c-L, elevation 114-254 mm, B_4C particles, embedded by melt, start of dissolution

114 : Vertical section CORA-18-c-L, elevation 114-254 mm, melt microstructure, oxidation

115 : Cross section CORA-18-03 (top), elevation 269 mm, overview

116 : Cross section CORA-18-03 (top), elevation 269 mm, macrographs of absorber blade, melt and fragments

117 : Cross section CORA-18-03 (top), elevation 269 mm, oxidation status of bundle components and products

118 : Cross section CORA-18-04 (top), elevation 413 mm, overview, detectable fuel pellet dissolution

119 : Cross section CORA-18-04 (top), elevation 413 mm, cladding oxidation

120 : Cross section CORA-18-04 (top), elevation 413 mm, components oxidation

121 : Cross section CORA-18-e-L, elevation 415-545 mm, overview on absorber channel; typical absorber melt

122 : Cross section CORA-18-e-L, elevation 415-545 mm, morphologies of absorber melt

123 : Cross section CORA-18-e-L, elevation 415-545 mm, morphologies of melt within absorber channel

124 : Cross section CORA-18-e-L, elevation 415-545 mm, rubble fragments after relocation within absorber channel

125 : Cross section CORA-18-05 (top), elevation 560 mm, overview

126 : Cross section CORA-18-05 (top), elevation 560 mm, details of fuel rod region

127 : Cross section CORA-18-05 (top), elevation 560 mm, morphologies of oxide scales

Appendix A:

A12 : Temperatures on the absorber blade, 300° orientation

A13 : Temperatures in the absorber blade

A14 : Temperatures measured with ceramic protected TCs

A15 : not used

A16 : Temperatures of the outer side of the shroud

A17 : Temperatures on shroud insulation

A18 : Gas temperature above the heated zone

A19 : Gas temperature measured between shroud and HTS

A20 : Gas temperature measured in the bundle head plate

Appendix B:

B1 : Horizontal cross section at 1158 mm elevation

B2 : Horizontal cross section at 1016 mm elevation

B3 : Horizontal cross section at 874 mm elevation

B4 : Horizontal cross section at 859 mm elevation

B5 : Horizontal cross section at 717 mm elevation

B6 : Horizontal cross section at 702 mm elevation

B7 : Horizontal cross section at 560 mm elevation

B8 : Horizontal cross section at 545 mm elevation

B9 : Horizontal cross section at 413 mm elevation

B10 : Horizontal cross section at 398 mm elevation

B11 : Horizontal cross section at 334 mm elevation

B12 : Horizontal cross section at 269 mm elevation

B13 : Horizontal cross section at 254 mm elevation

B14 : Horizontal cross section at 112 mm elevation

B15 : Horizontal cross section at 97 mm elevation

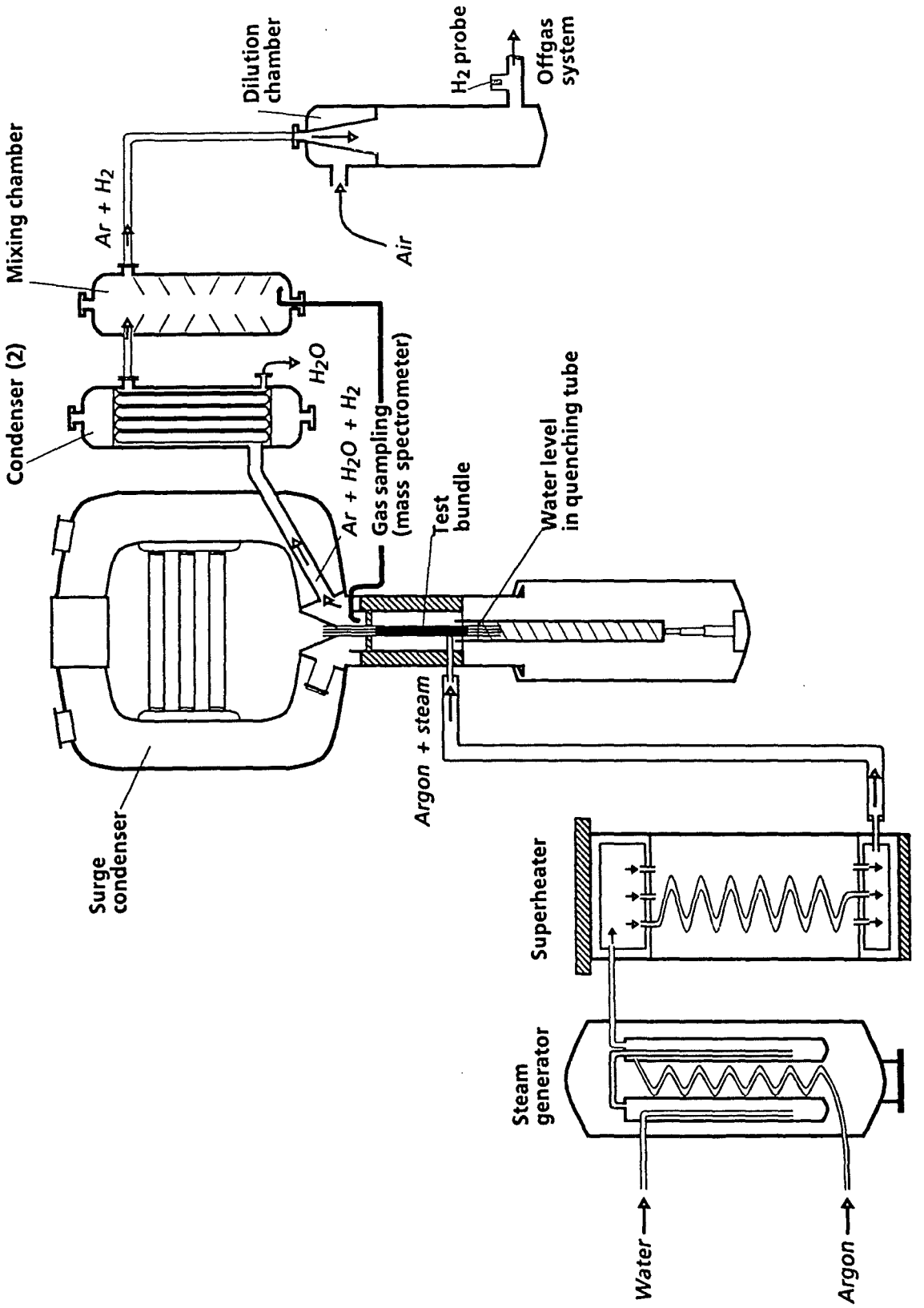

Fig. 1: SFD Test Facility (simplified flow diagram)

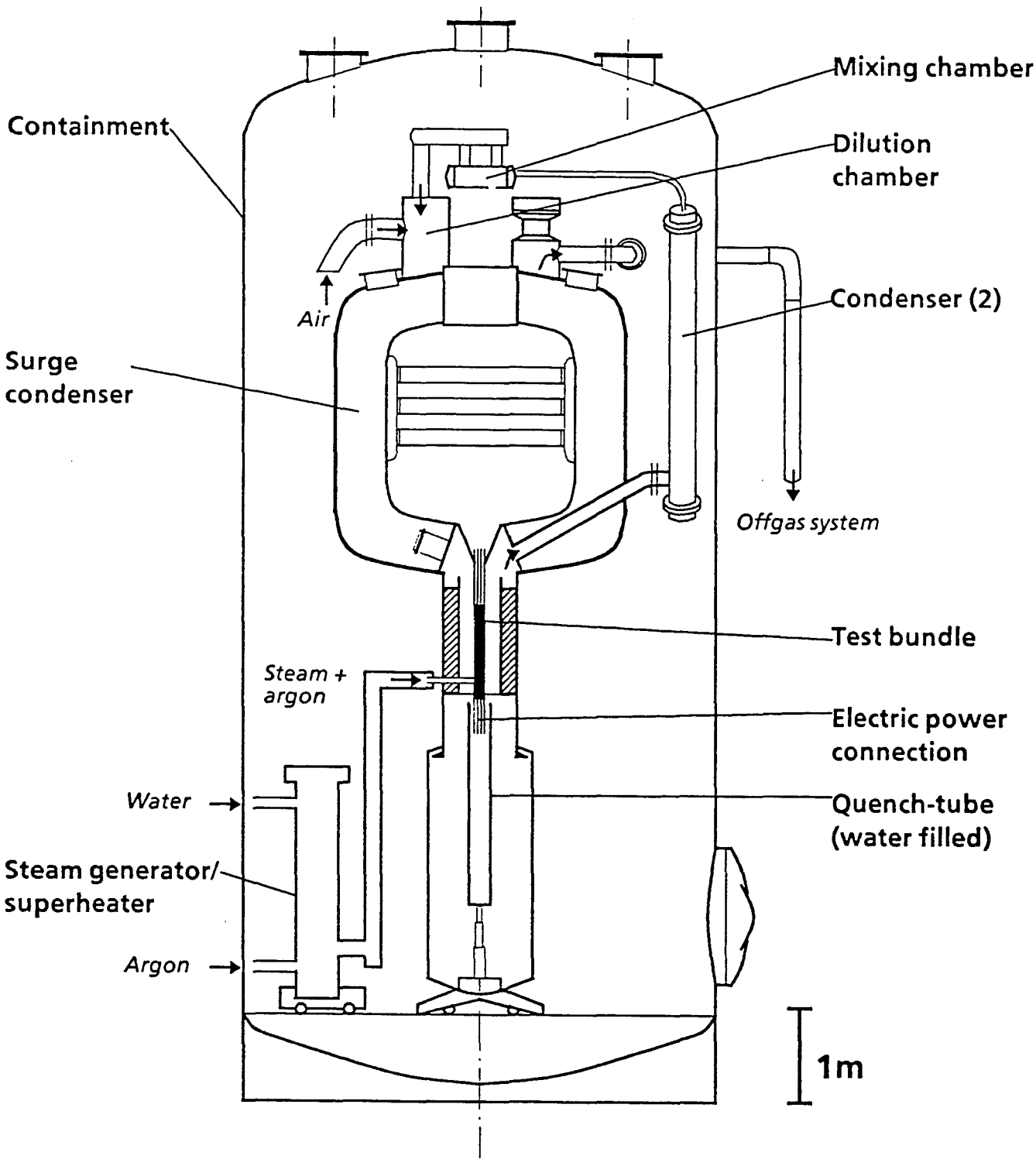

Fig. 2: SFD Test Facility CORA (Main Components)

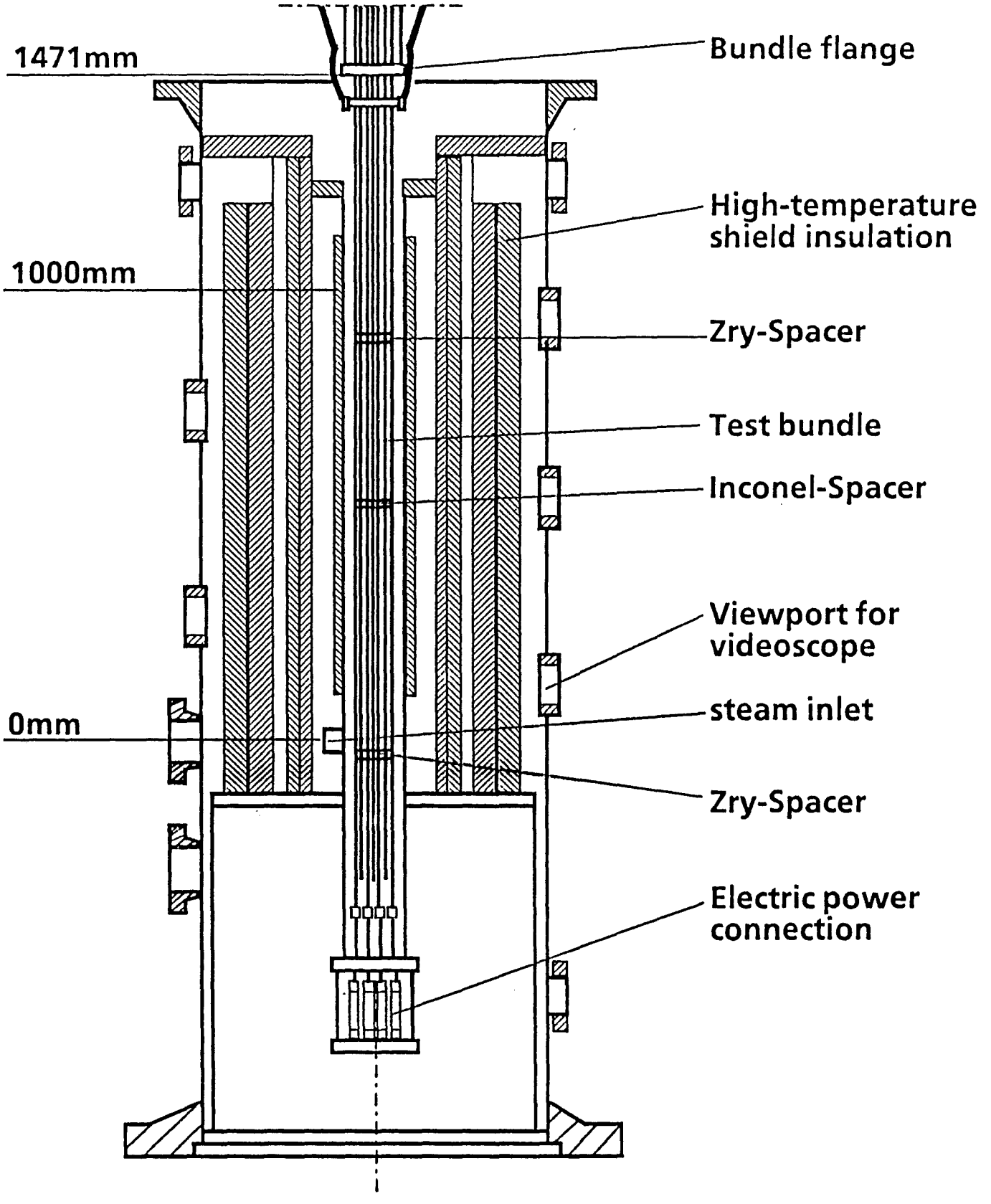

Fig. 3: CORA bundle arrangement

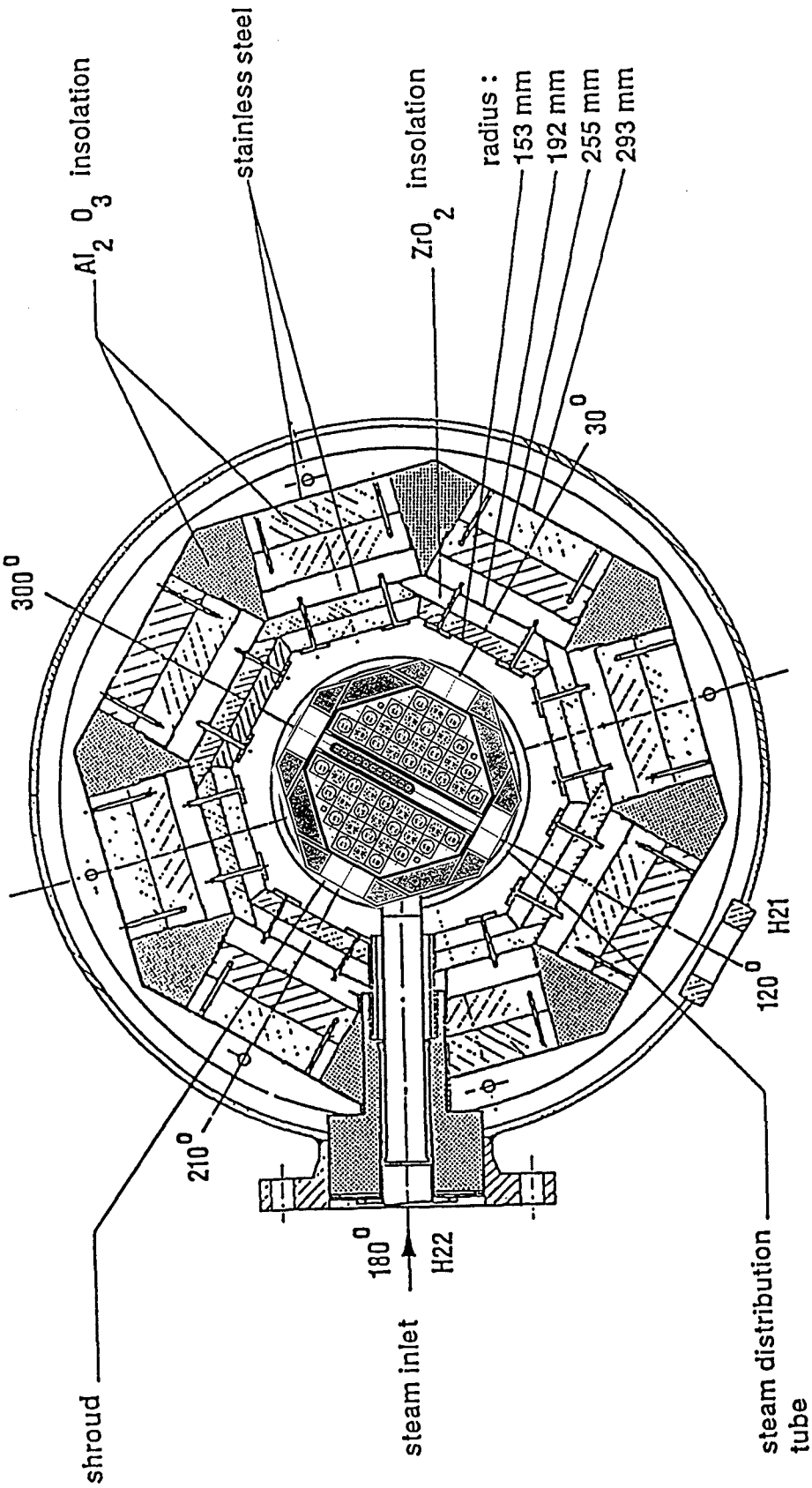

Fig. 4: CORA-18; Horizontal cross section of the high temperature shield

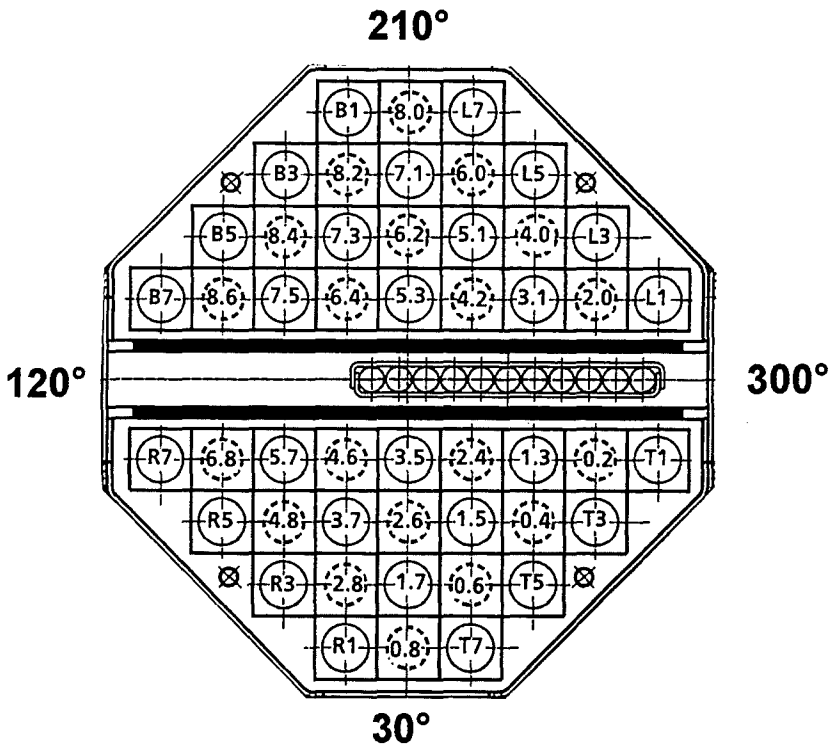

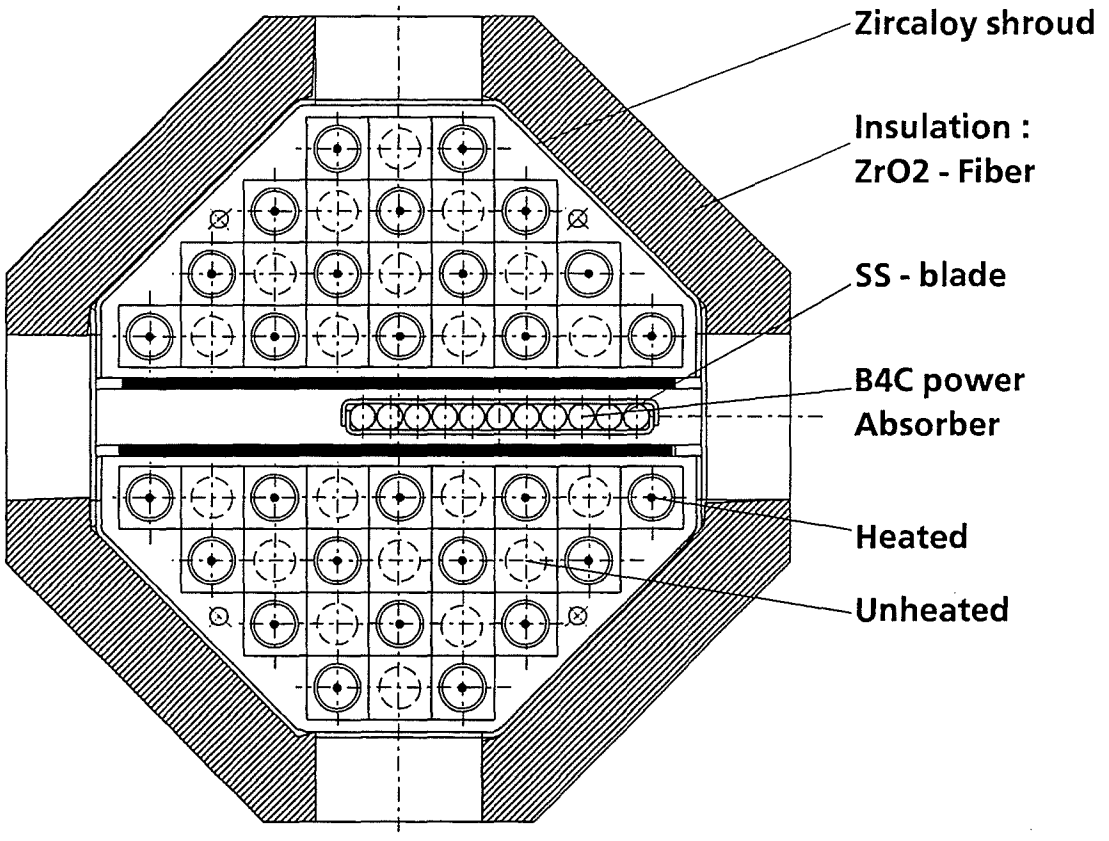

Fig. 5: CORA-18; Rod arrangement and test rod designation

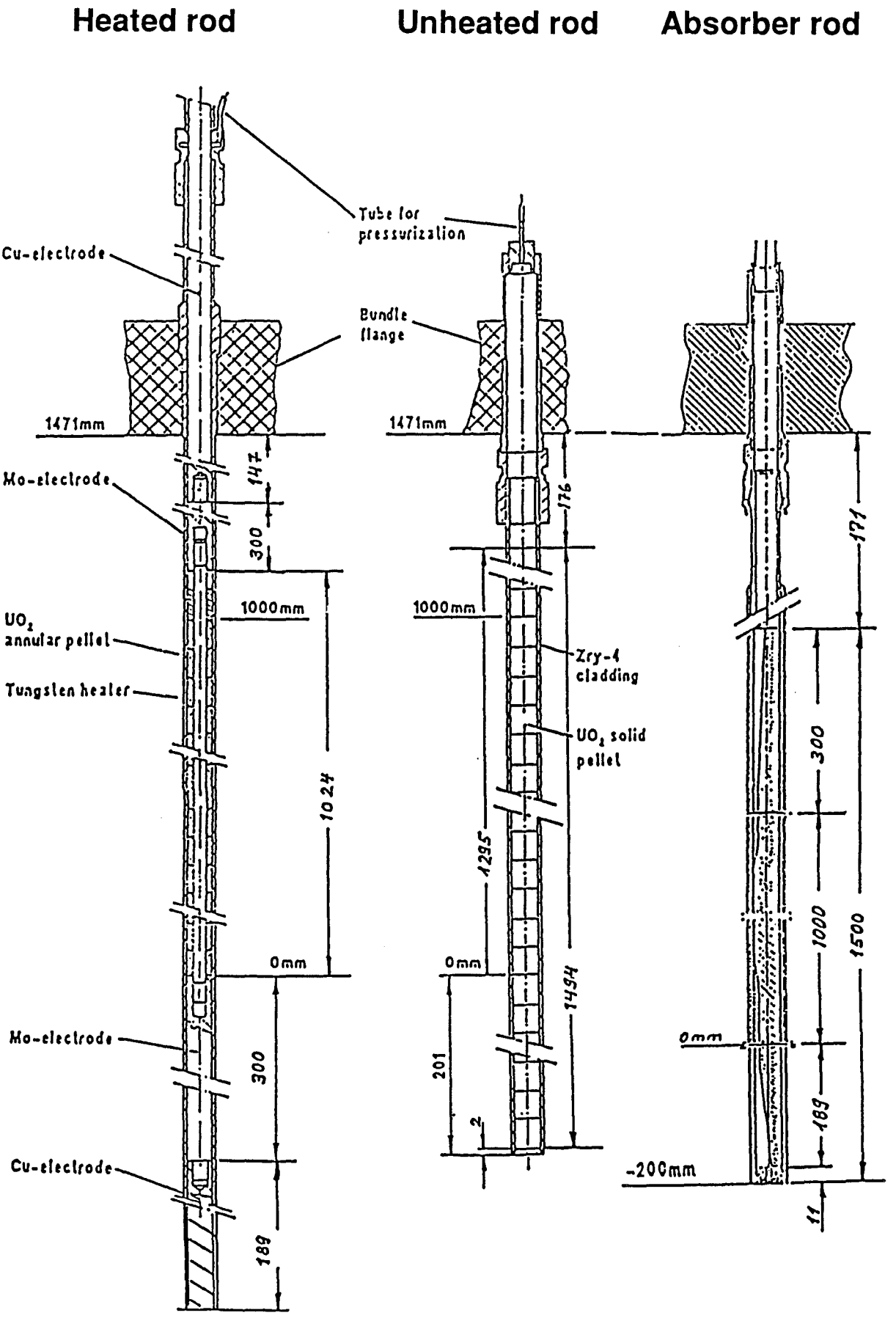

Fig. 6: Rod types used in the CORA experiments

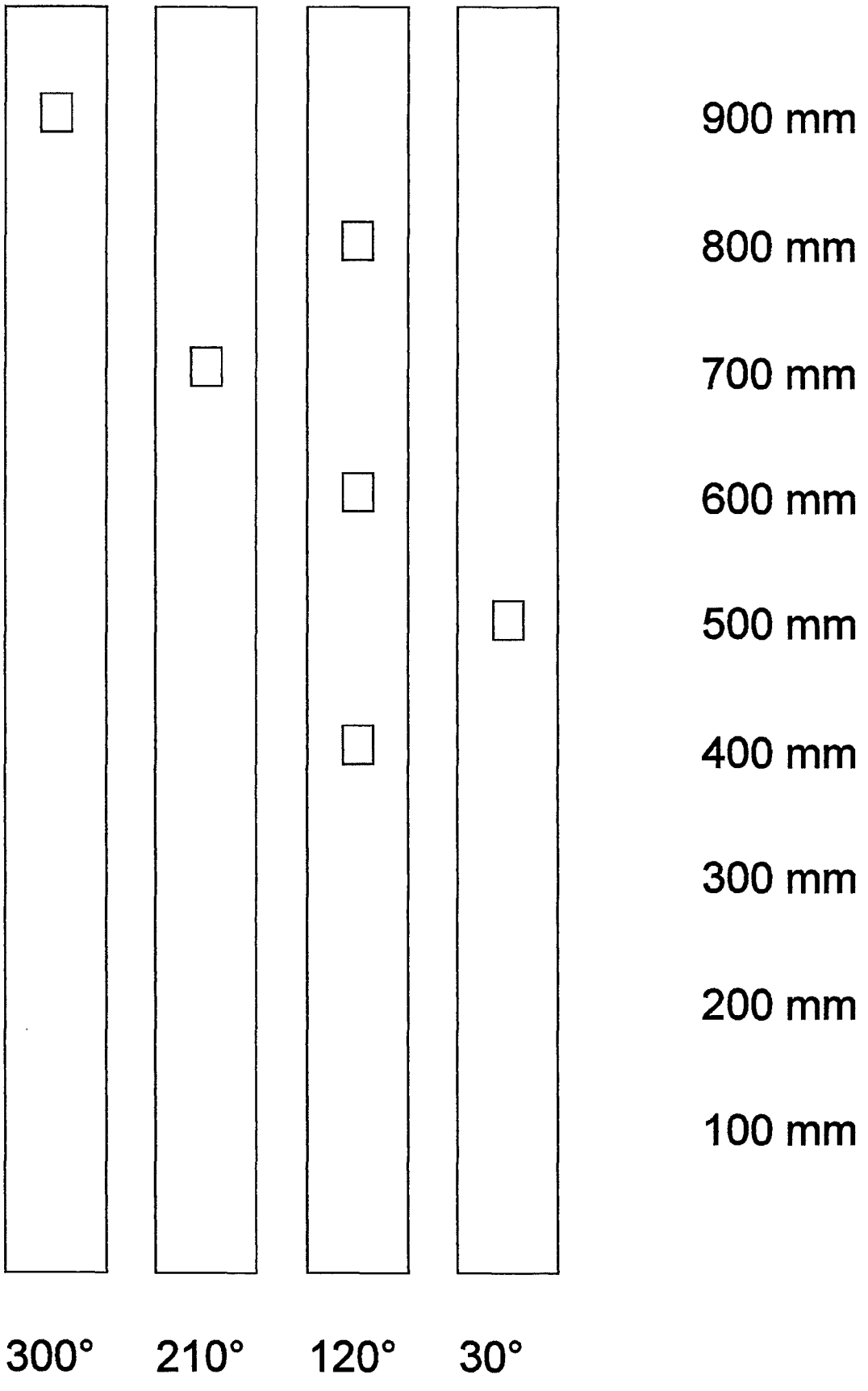

Fig. 7: CORA-18; Positions of windows in the shroud

(a)

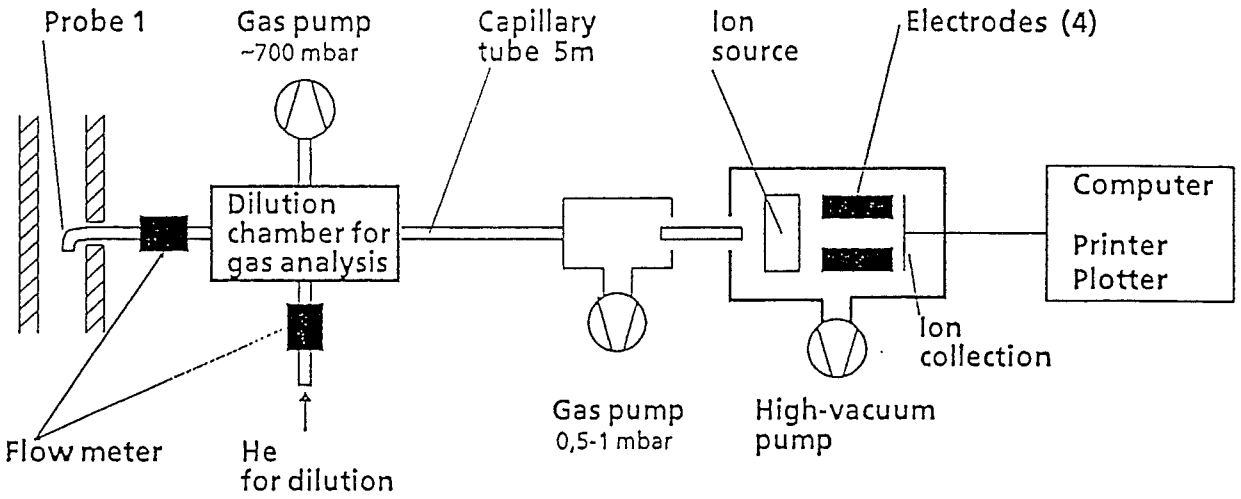

(b)

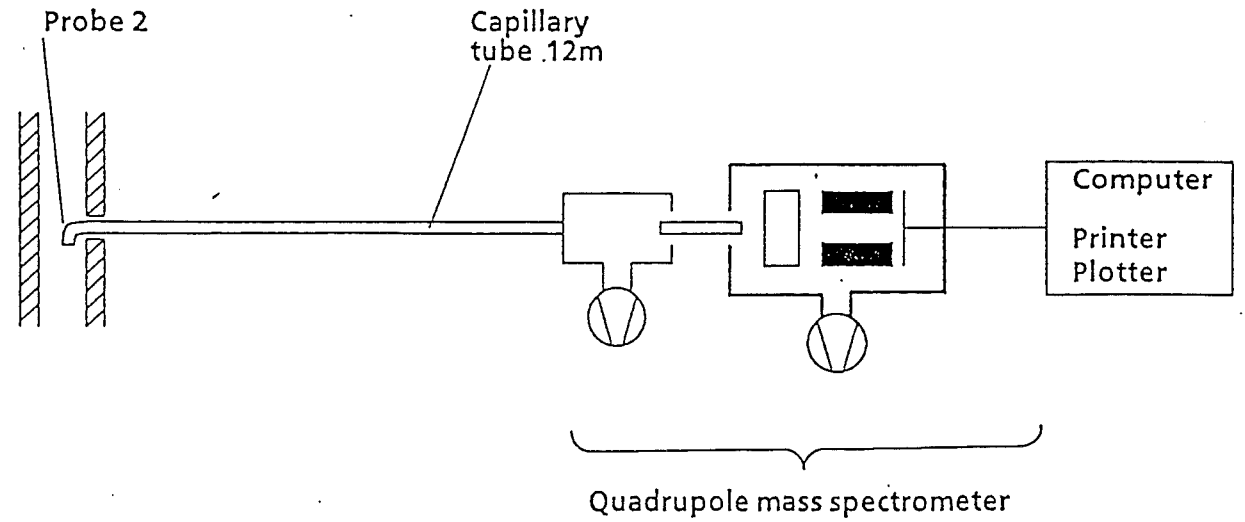

Location (a) : Outlet of test section

Location (b) : Mixing chamber

Fig. 8: Facility of hydrogen measurement

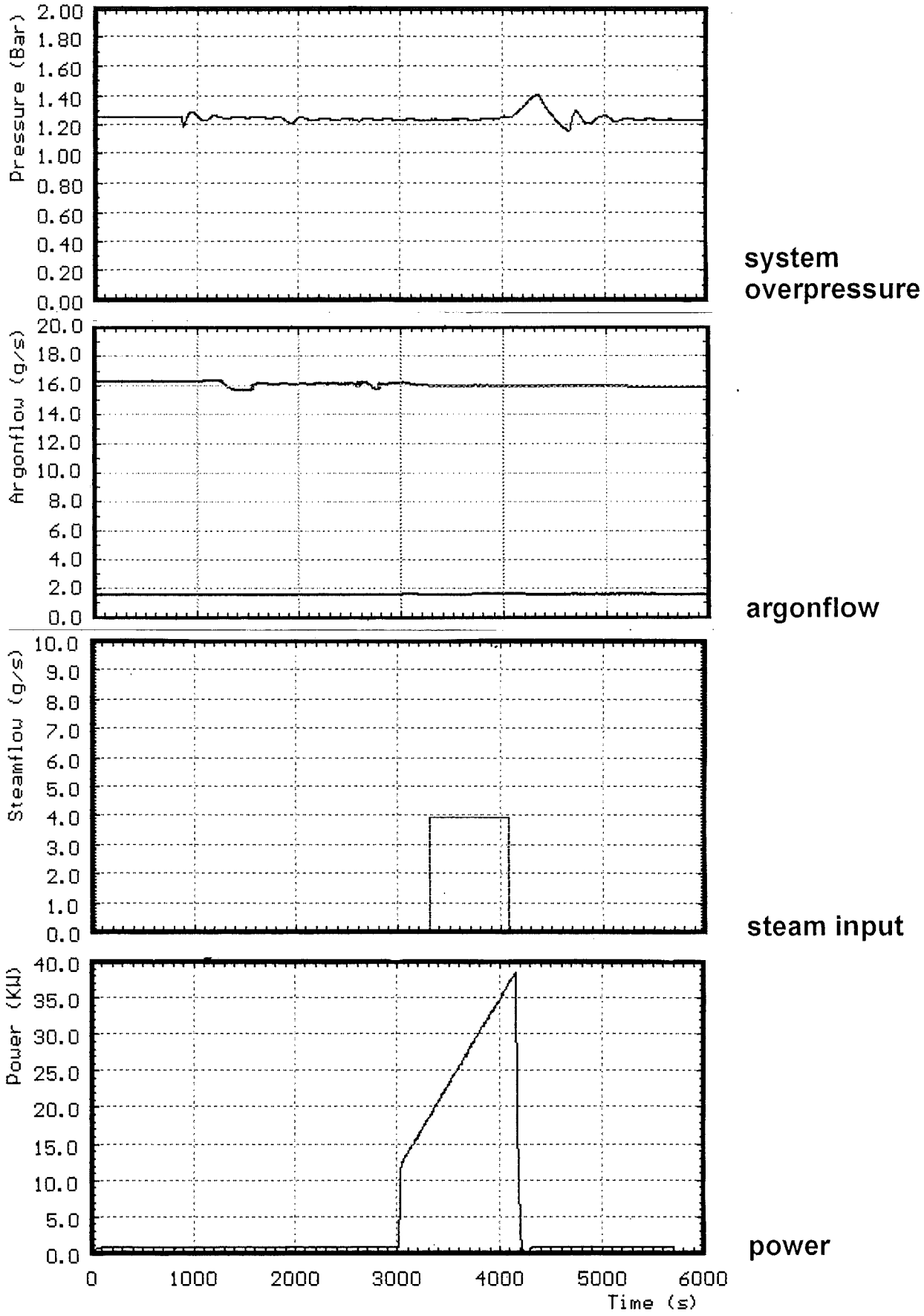

Fig. 9: CORA-18; System pressure, argon flow, steam input and power

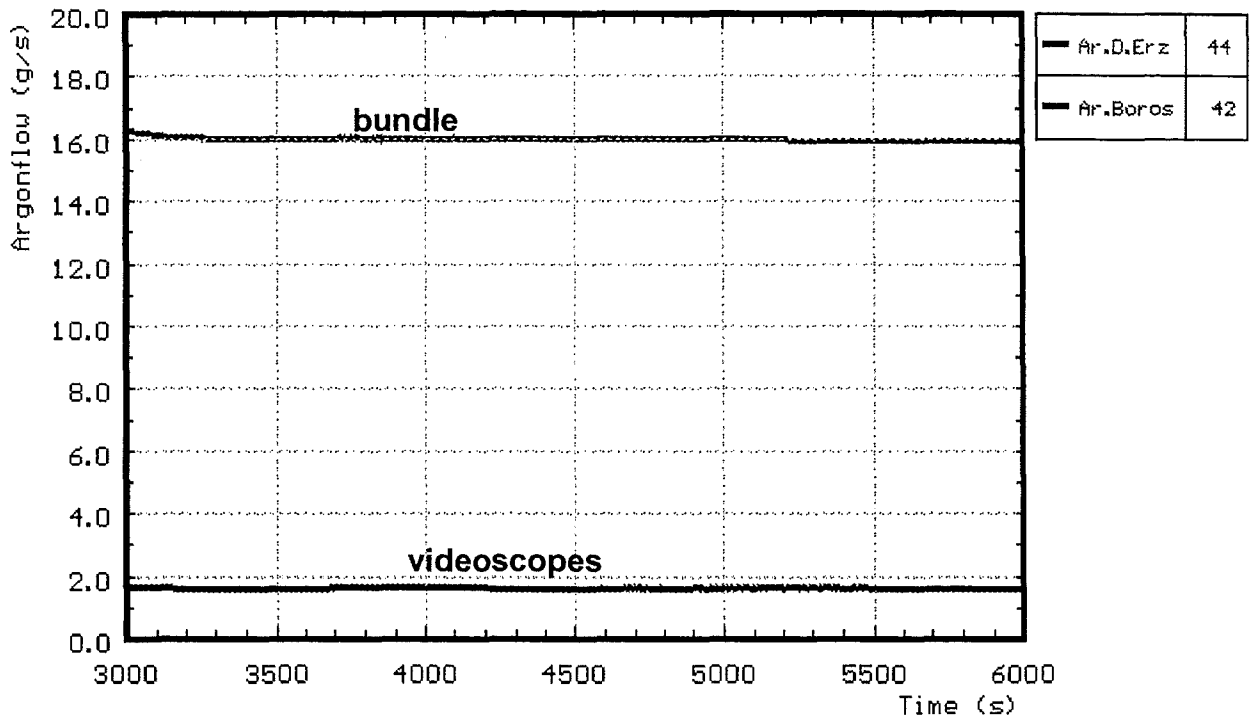

Fig. 10: CORA-18; Argon flow through bundle and videoscopes

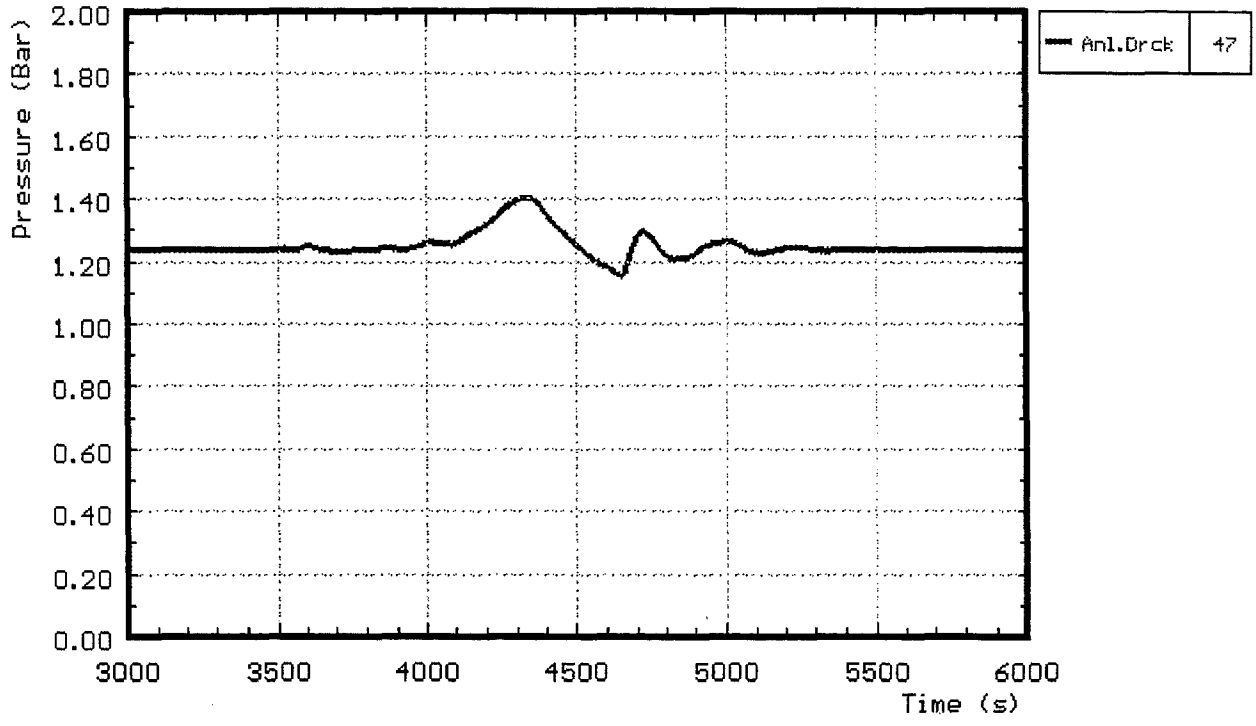

Fig. 11: CORA-18; System pressure (gauge)

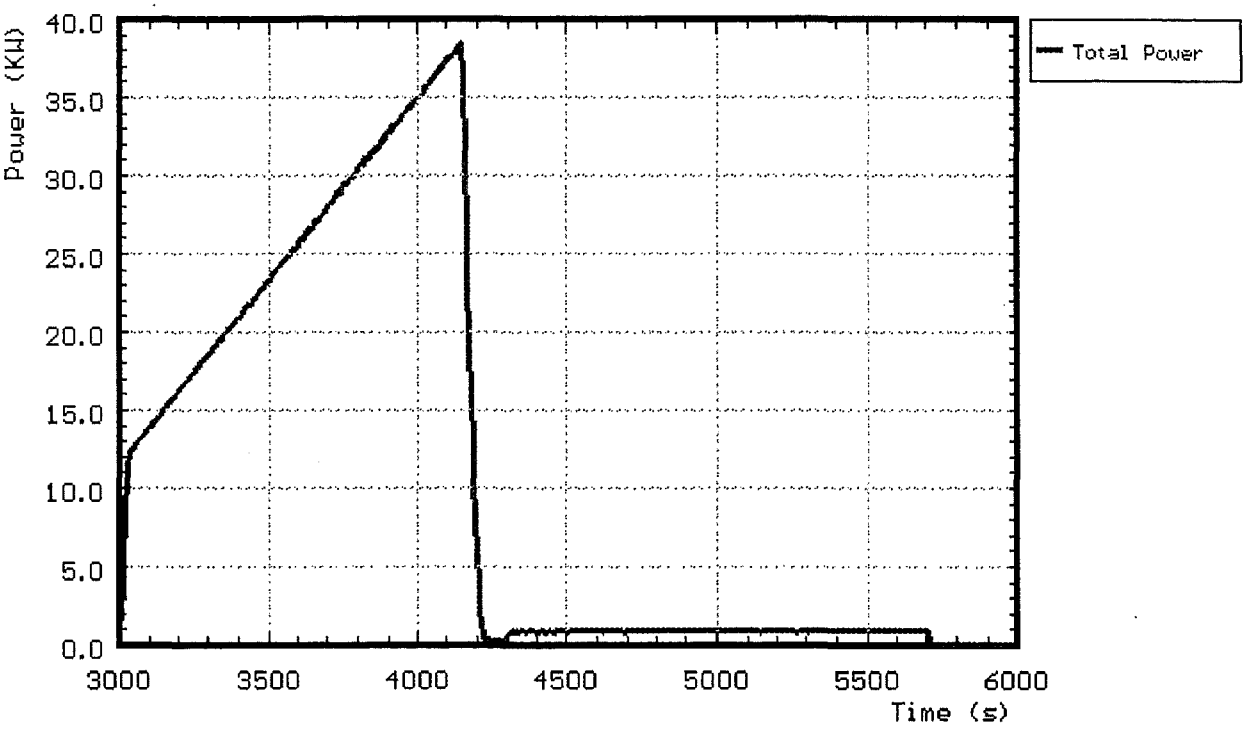

Fig. 12: CORA-18; Total electric power input

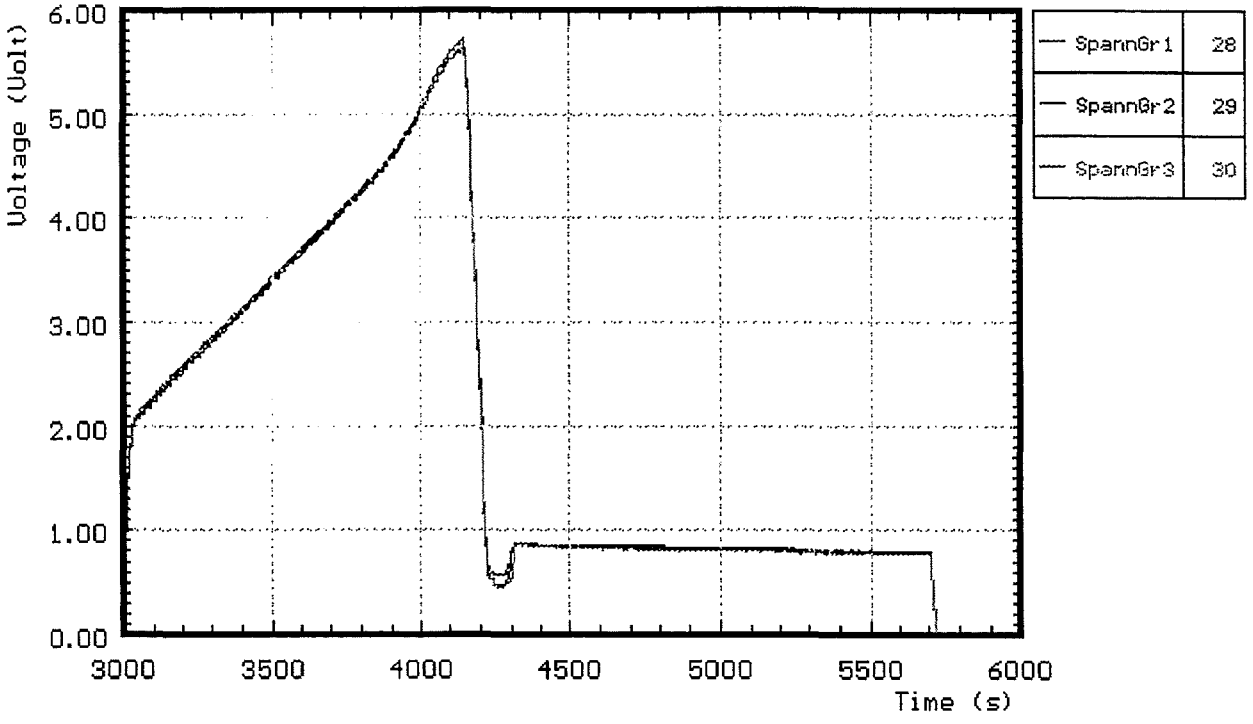

Fig. 13: CORA-18; Voltage input for the 3 rod groups

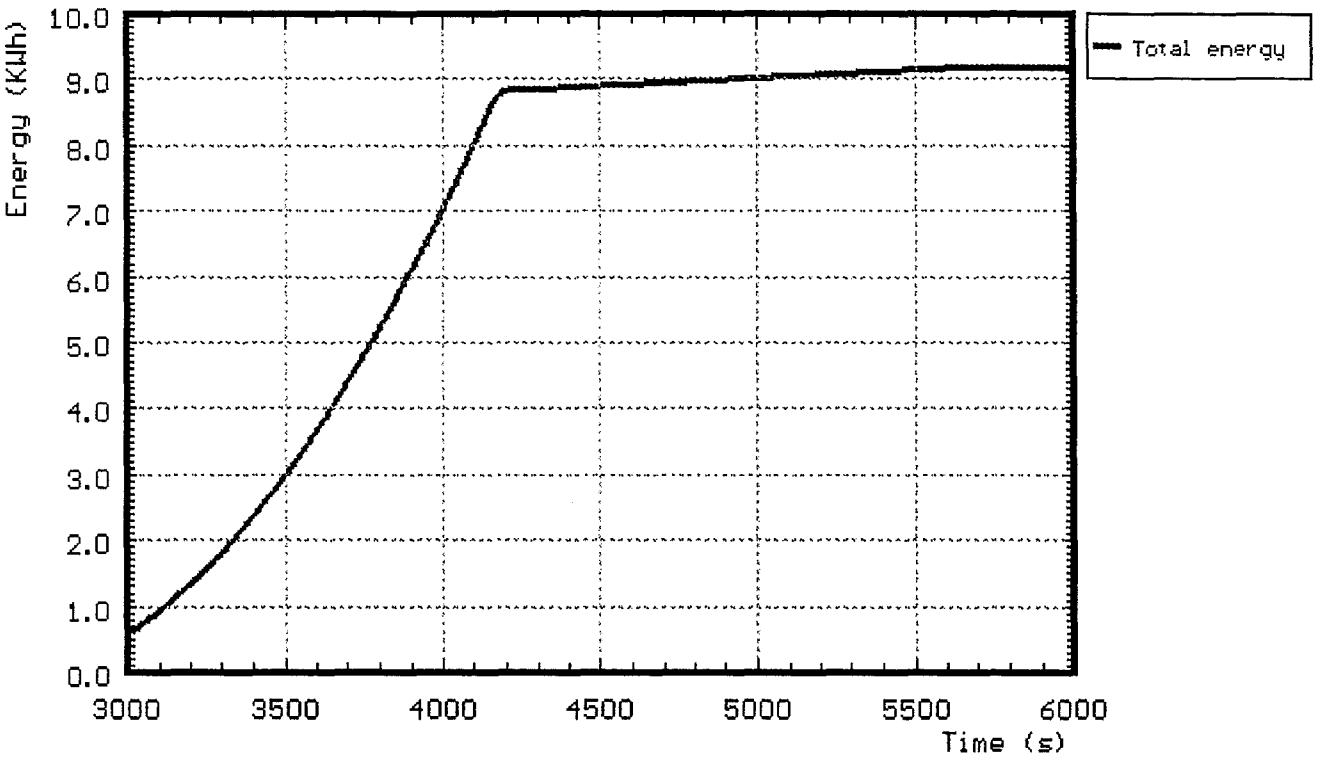

Fig. 14: CORA-18; Total electric energy input

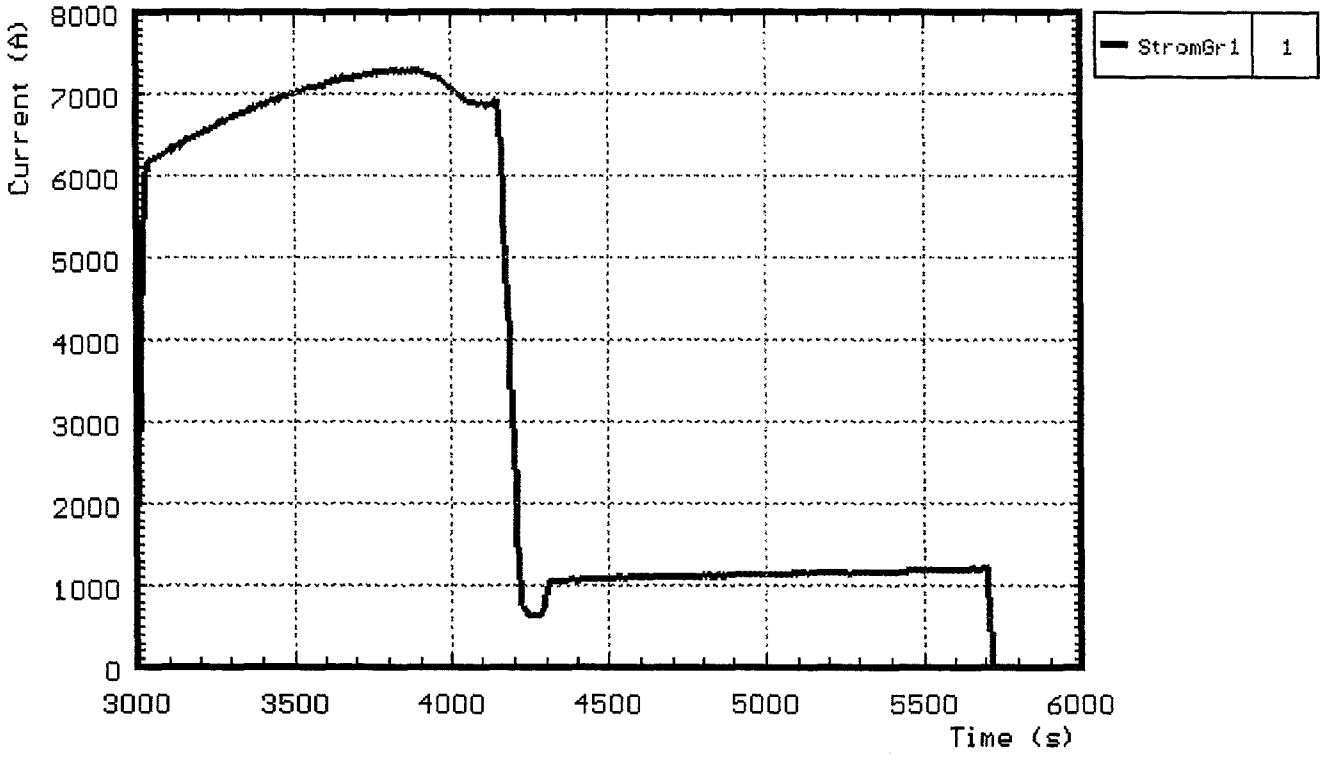

Fig. 15: CORA-18; Total current

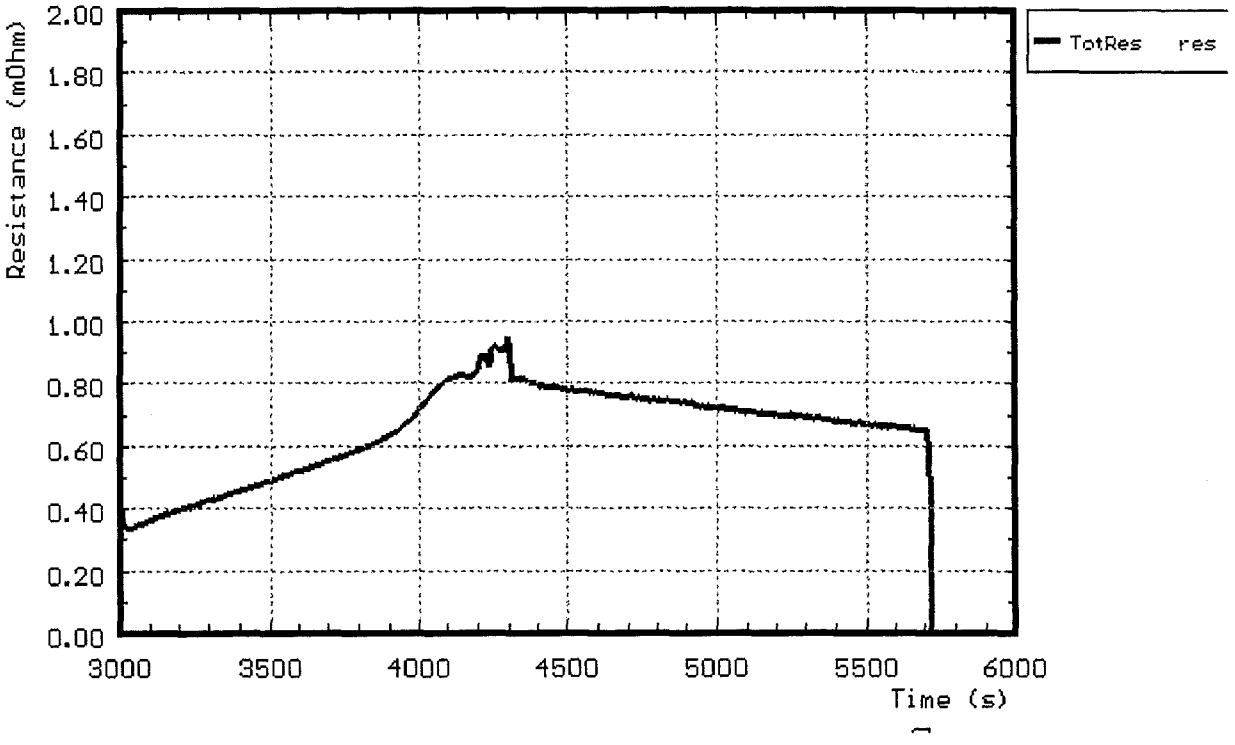

Fig. 16 : CORA-18; Resistance of bundle (Voltage group 1 / total current)

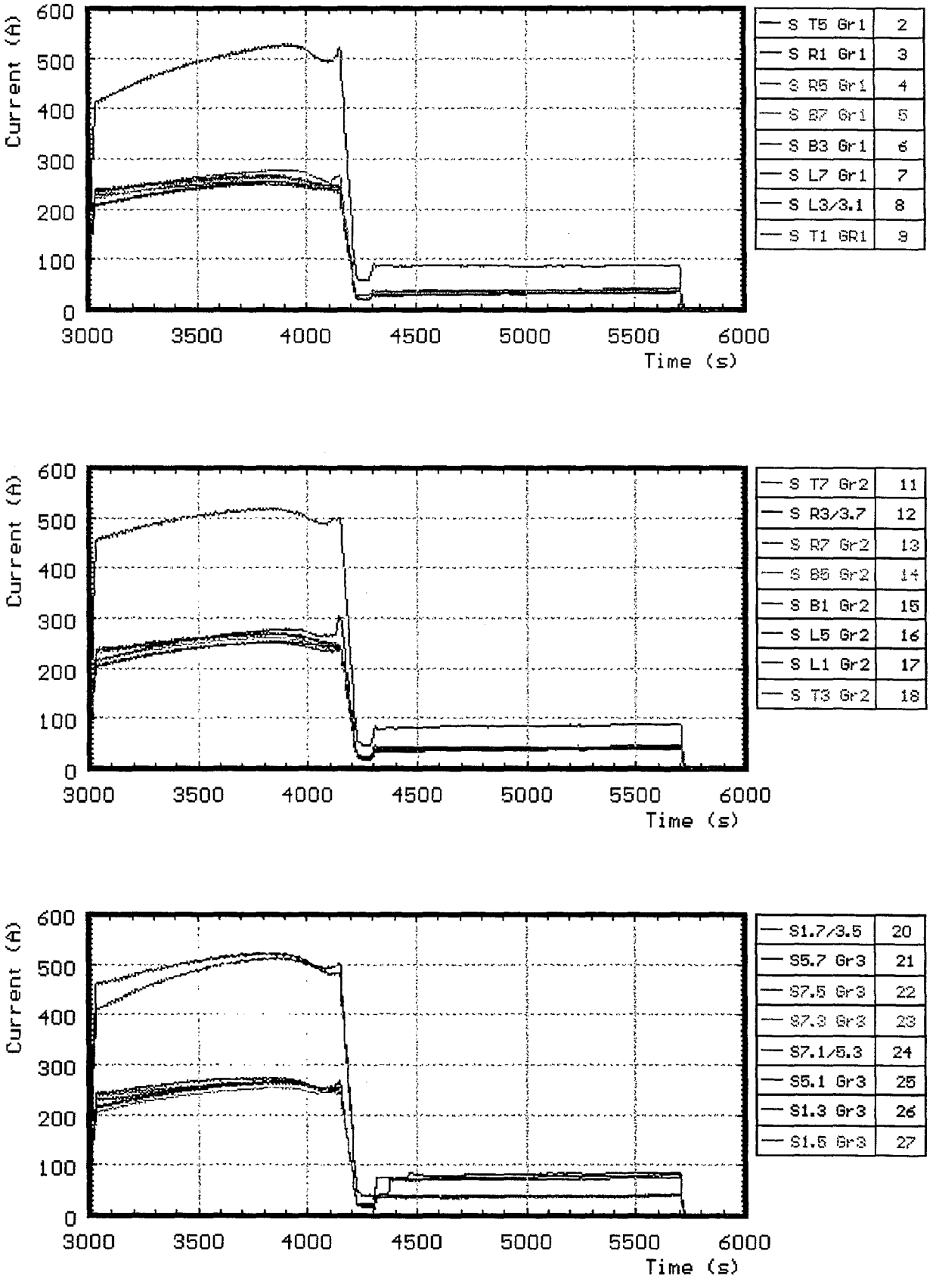

Fig. 17 : CORA-18; Variation of currents within the rod groups

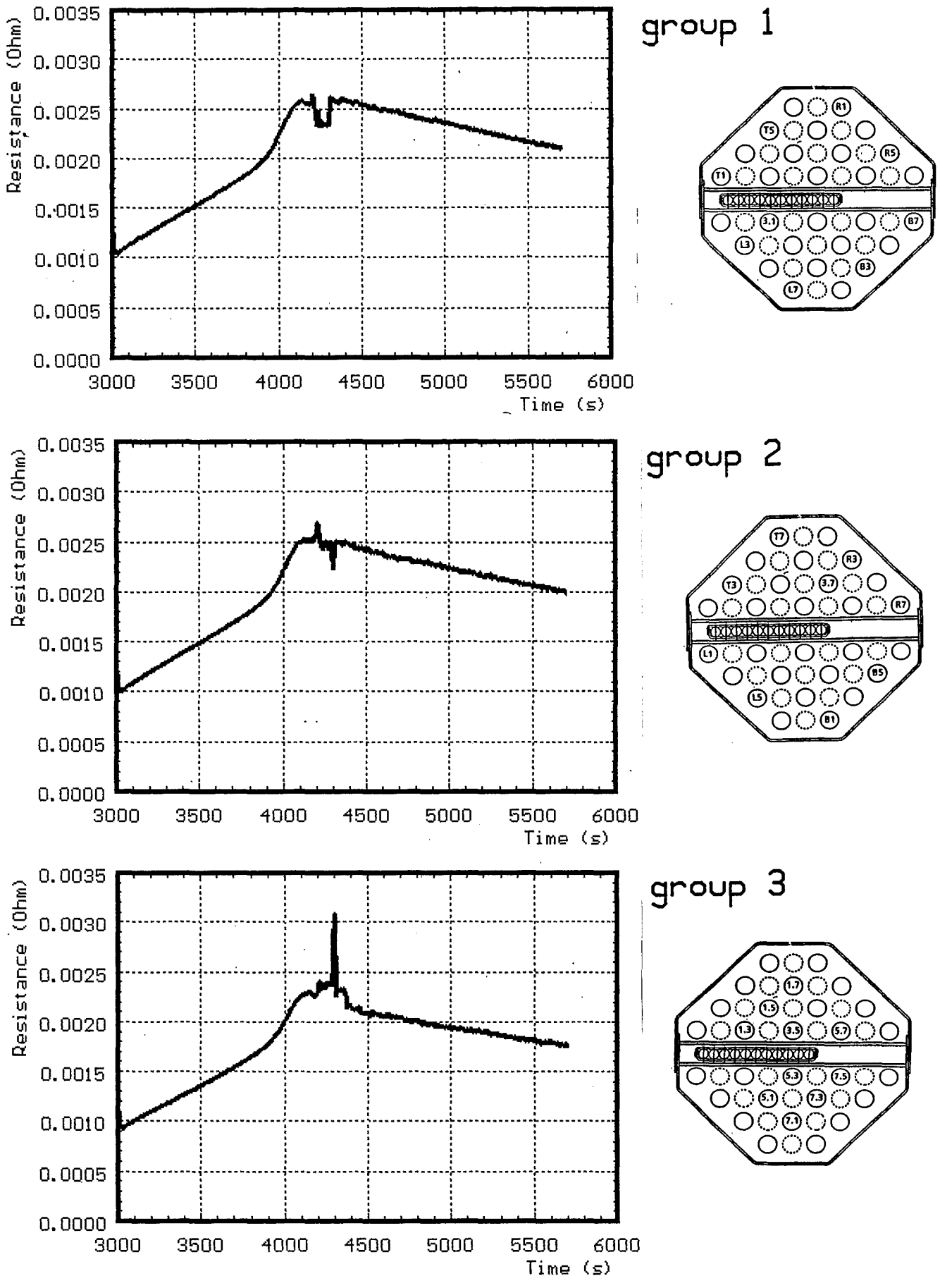

Fig. 18: CORA-18; Resistance of the rod groups

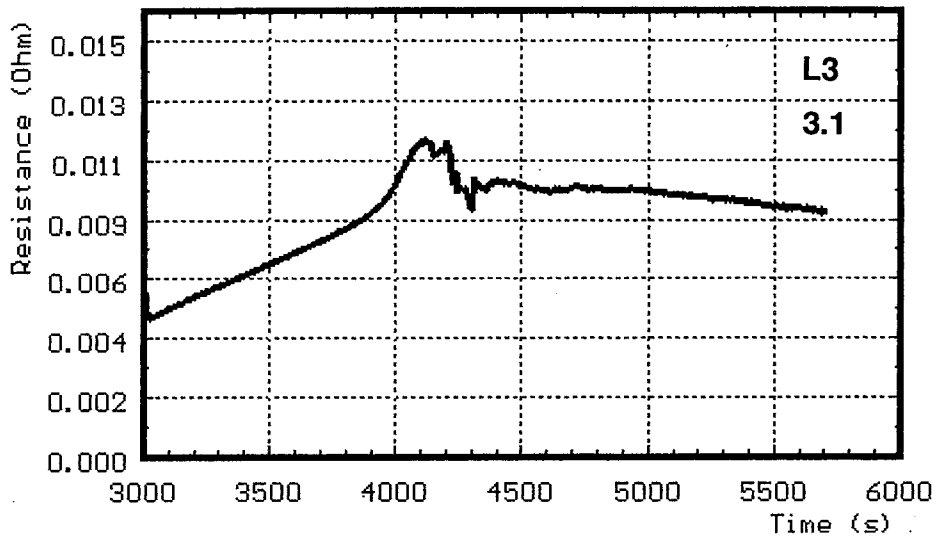

group 1

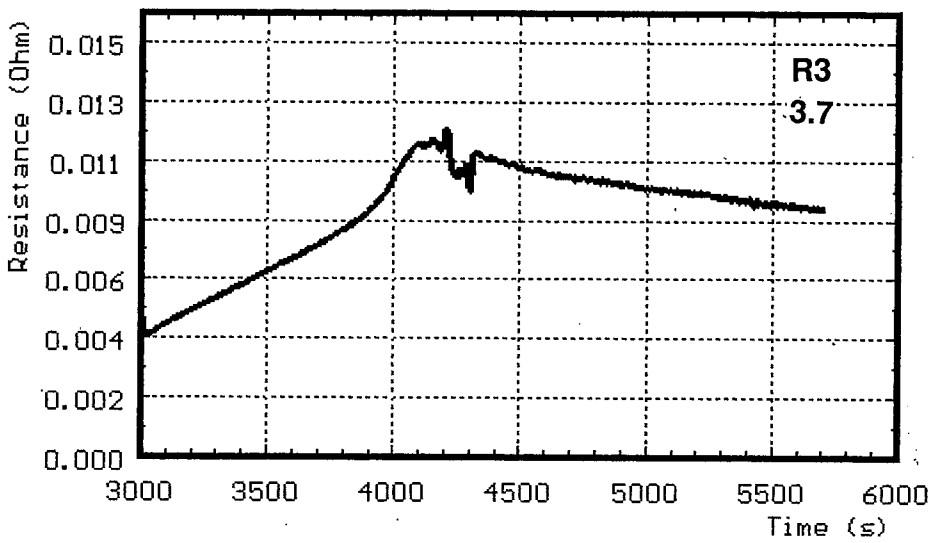

group 2

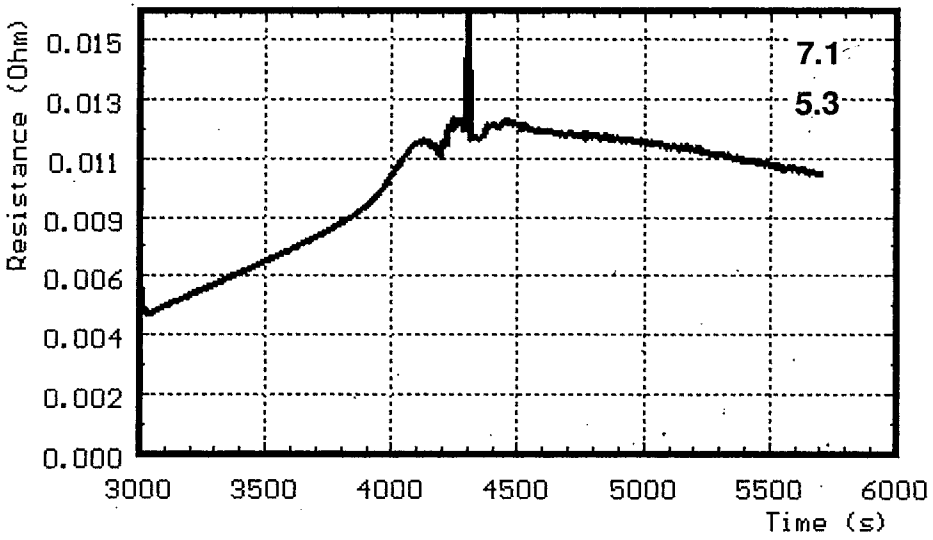

group 3

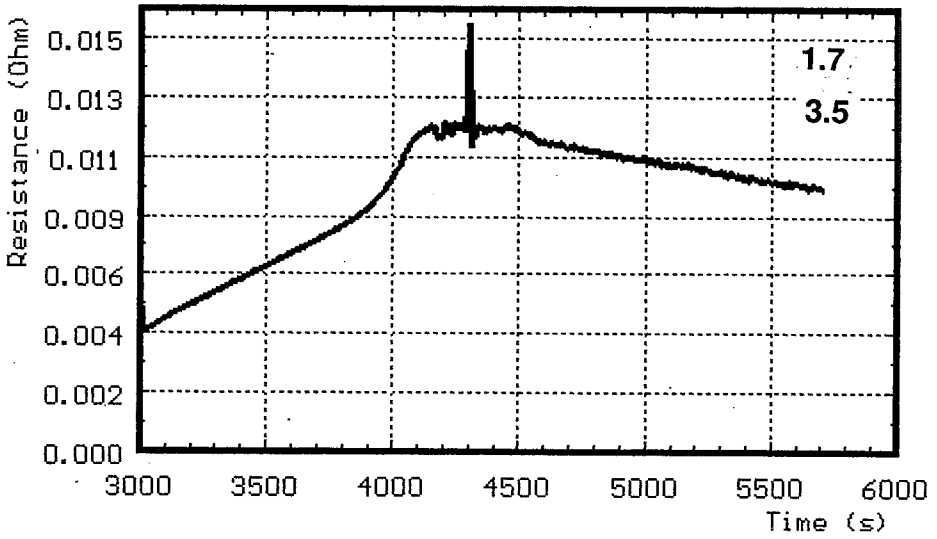

group 3

Fig. 19: CORA-18; Sum of resistance in two connected rods

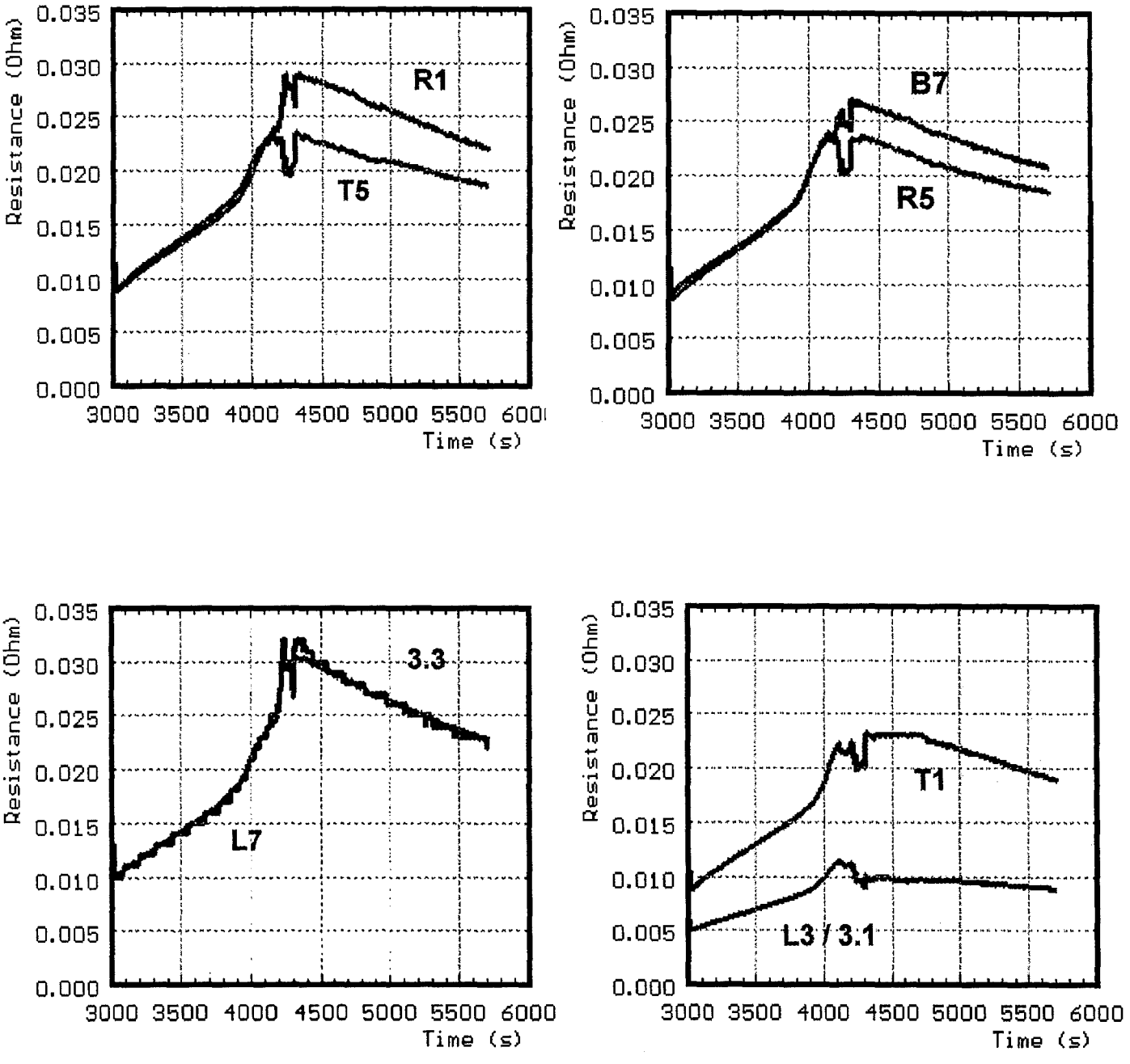

Fig. 20: CORA-18; Resistance of single rods groups 1

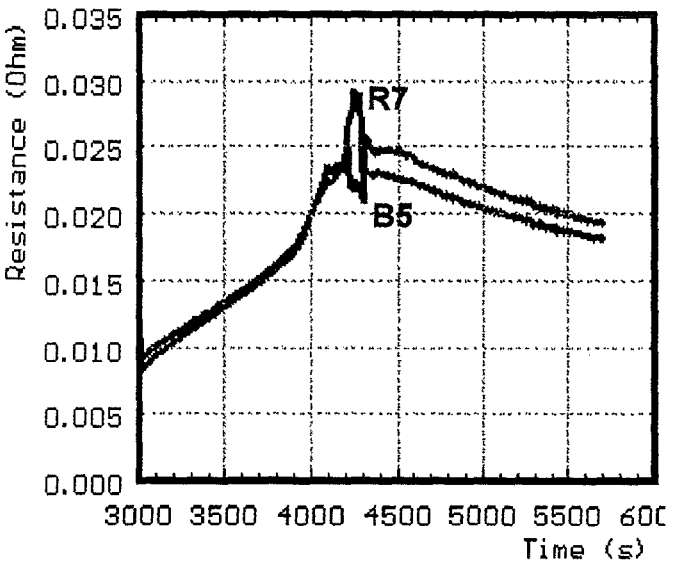

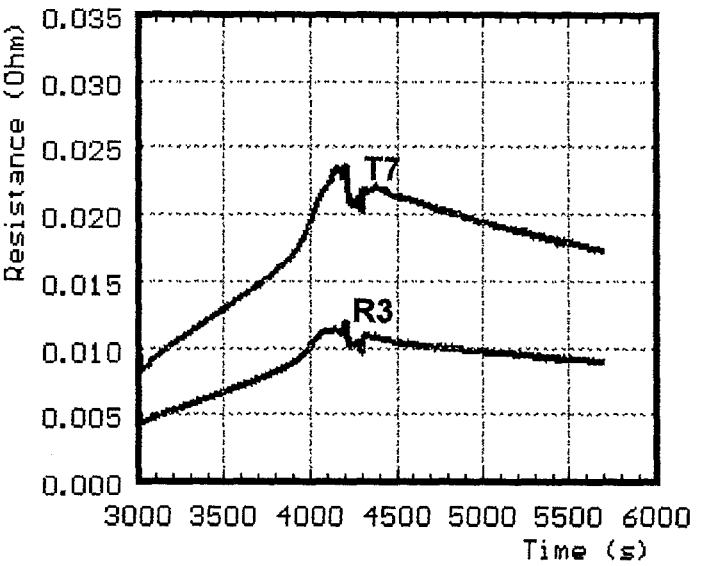

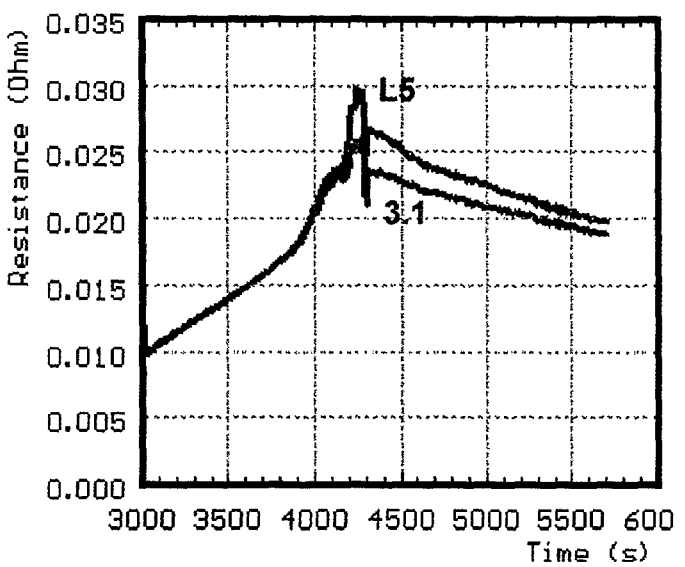

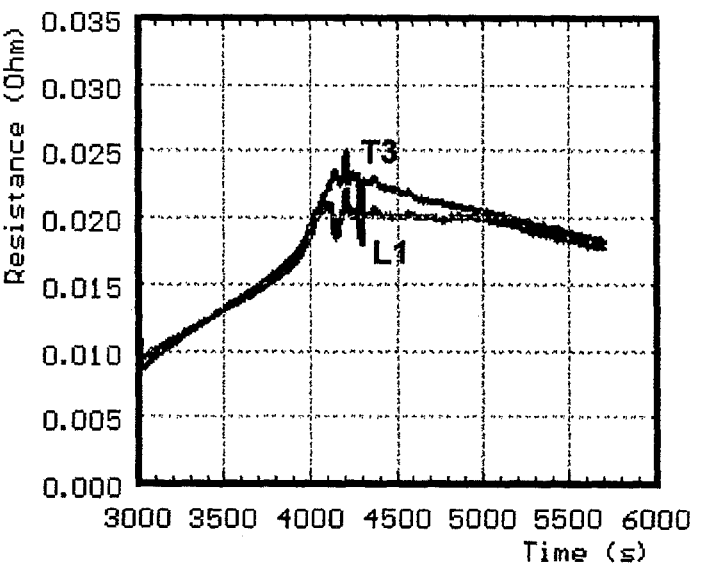

Fig.21 : CORA-18; Resistance of single rods groups 2

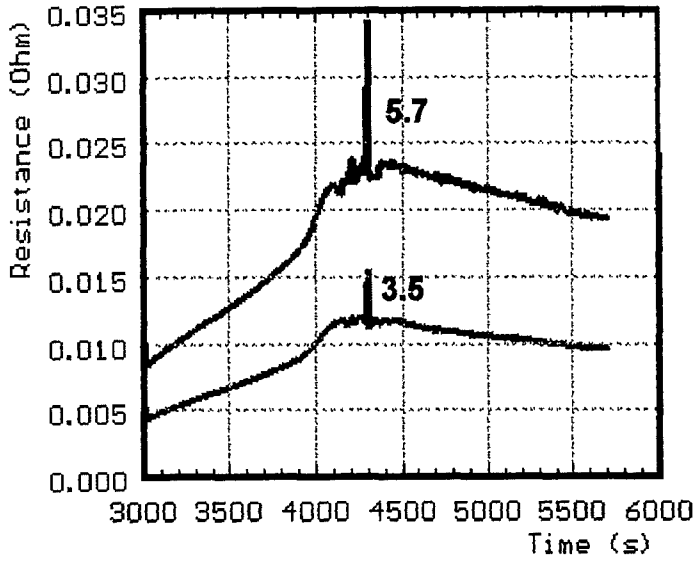

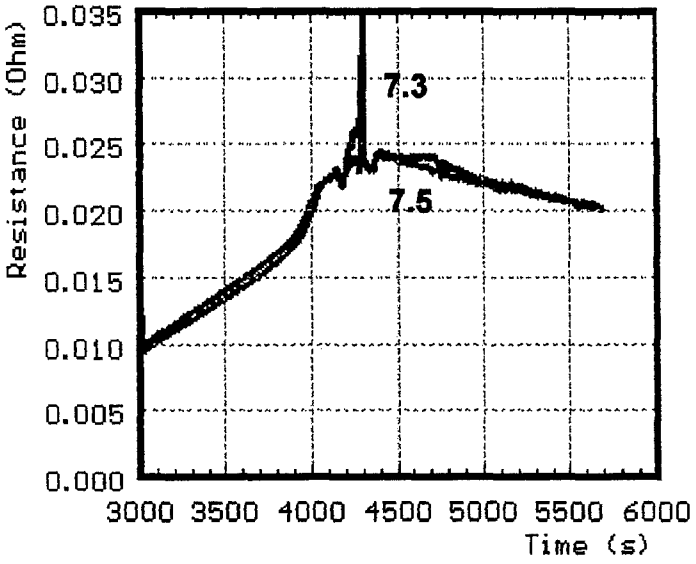

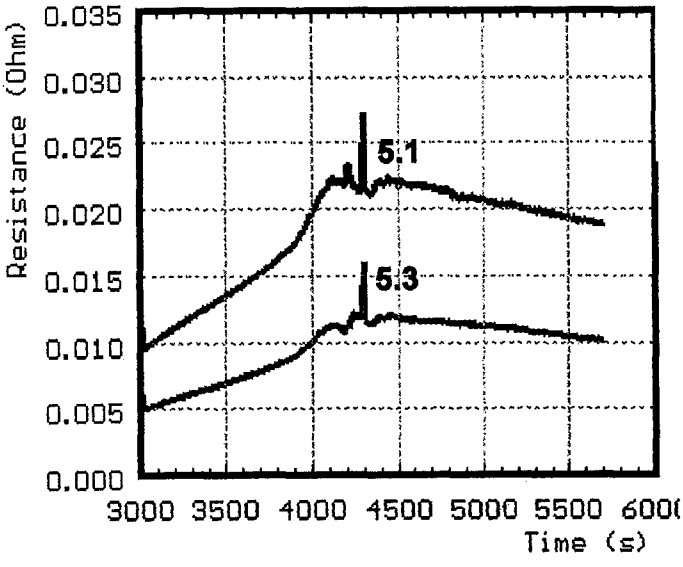

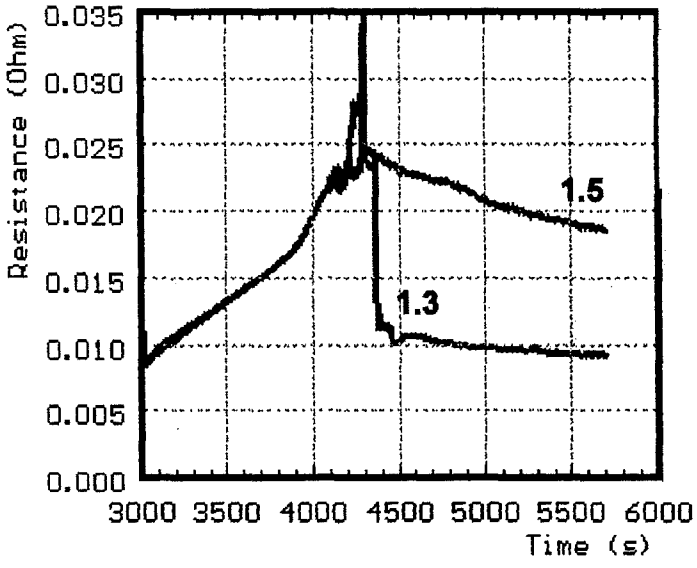

Fig.22 : CORA-18; Resistance of single rods groups 3

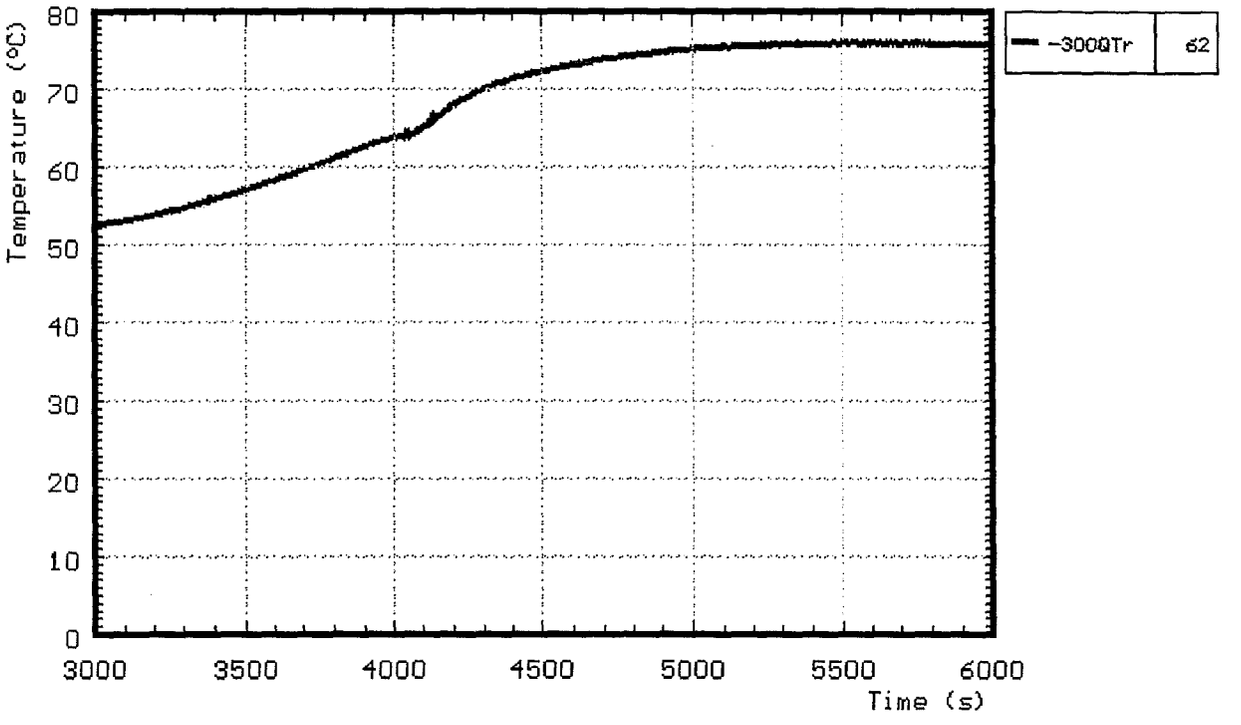

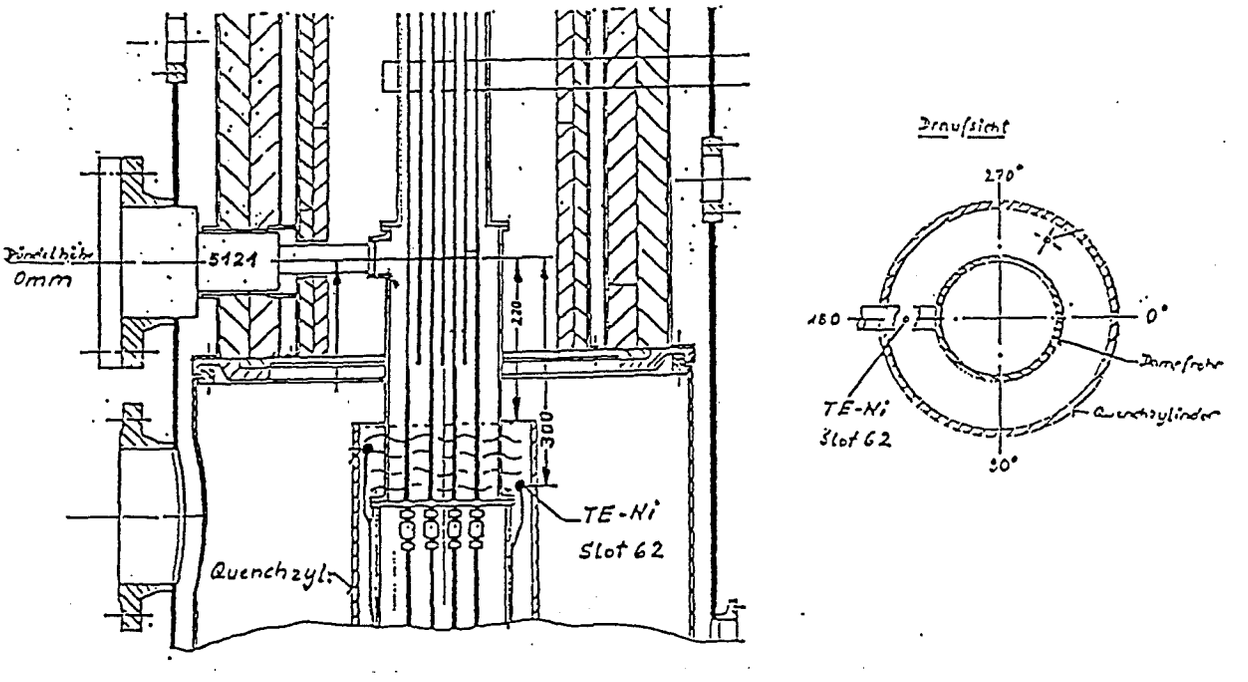

Fig. 23: CORA-18; Water temperature in the quench cylinder

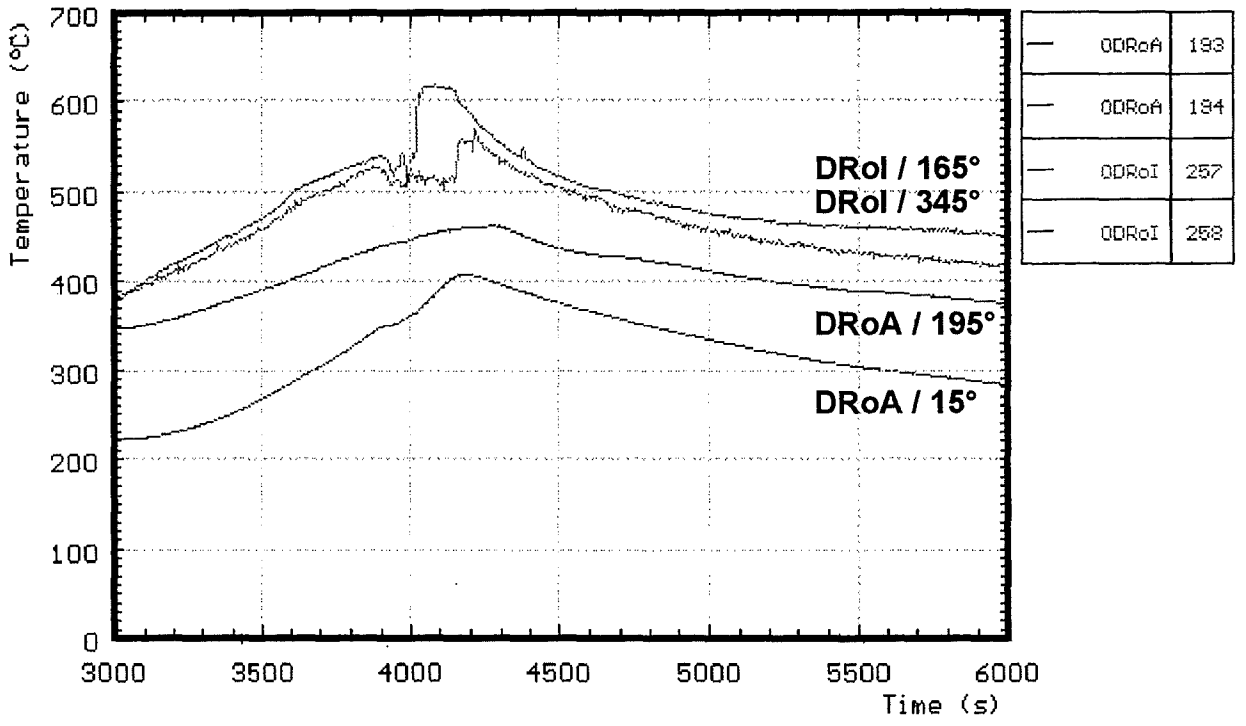

DRoA: steam tube, outer side
DRoI: steam tube, inner side

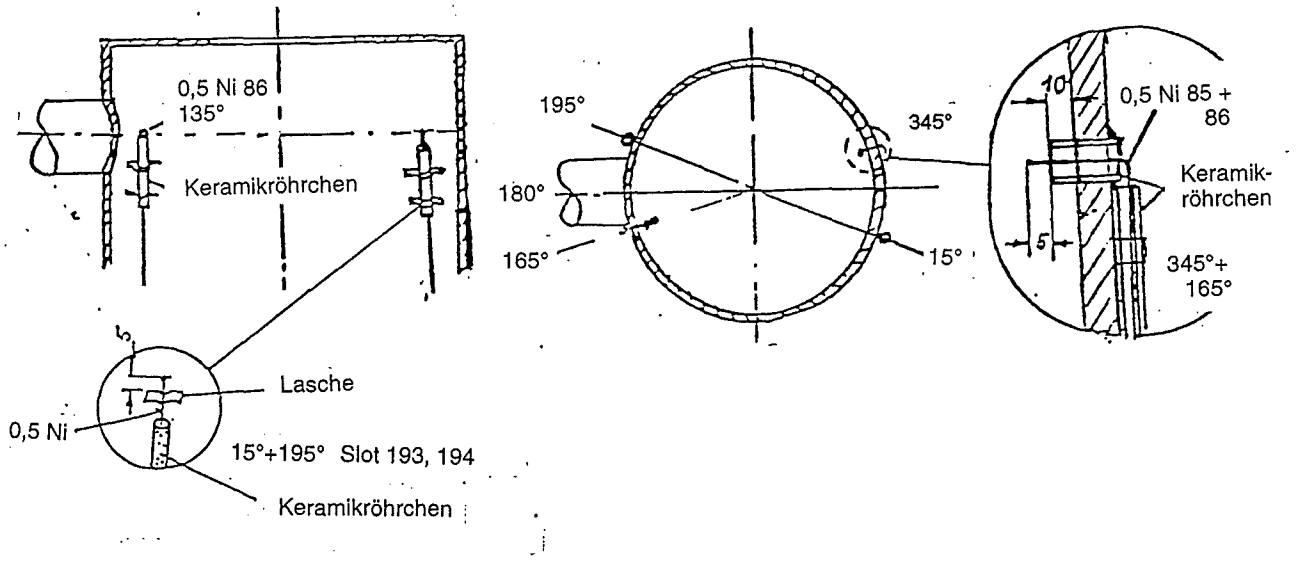

Fig. 24: CORA-18; Temperature in and on steam tube at 0 mm elevation

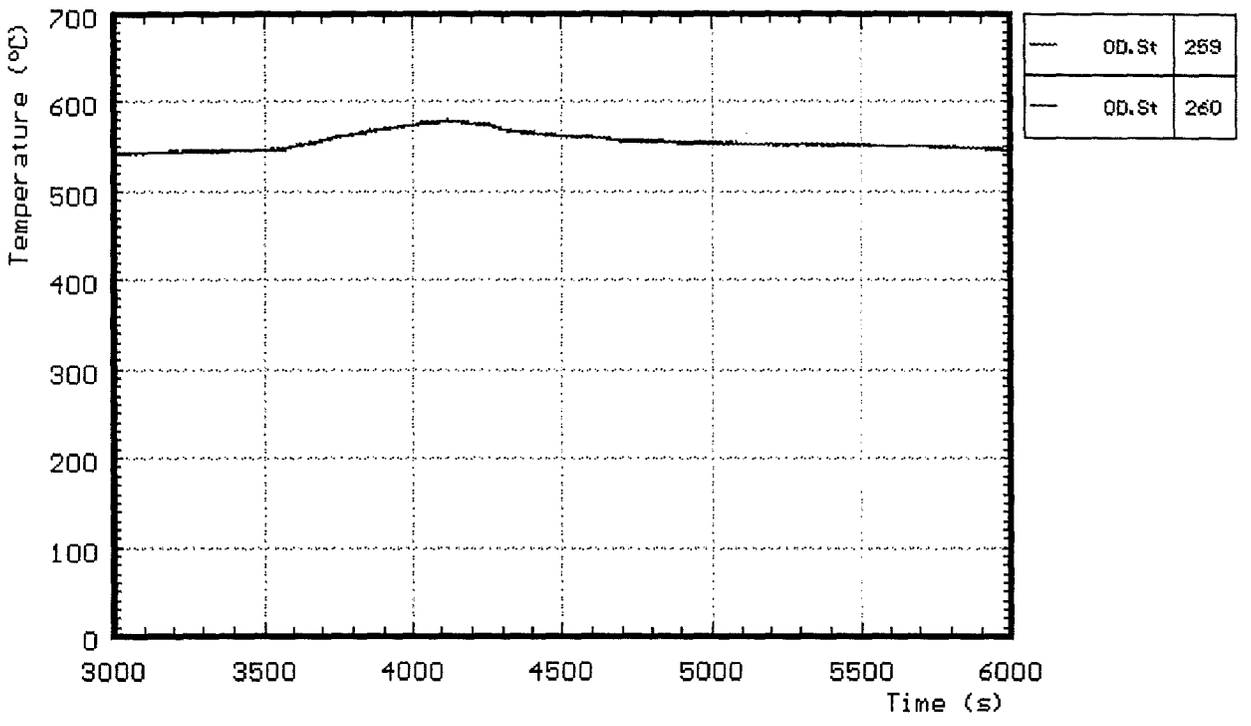

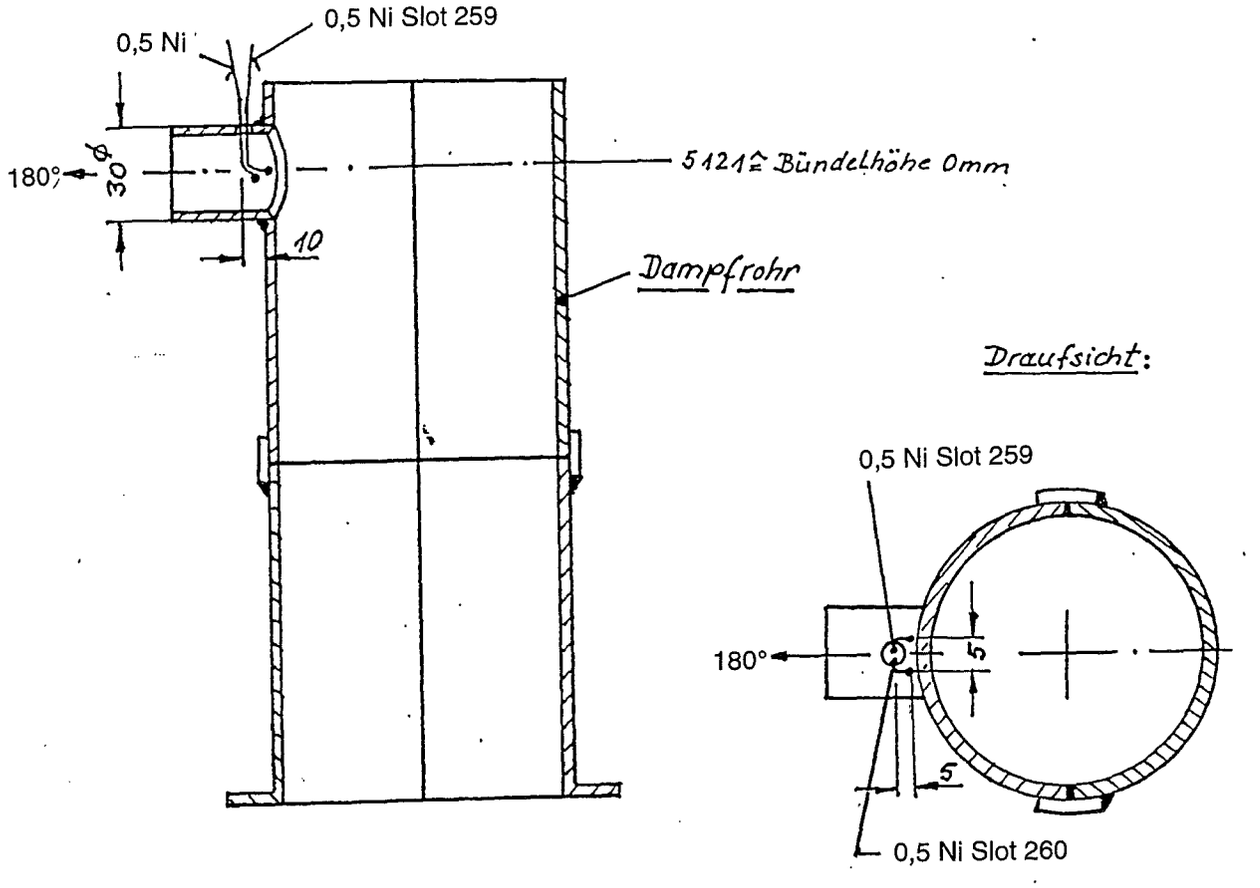

Fig. 25: CORA-18; Temperatures at steam inlet

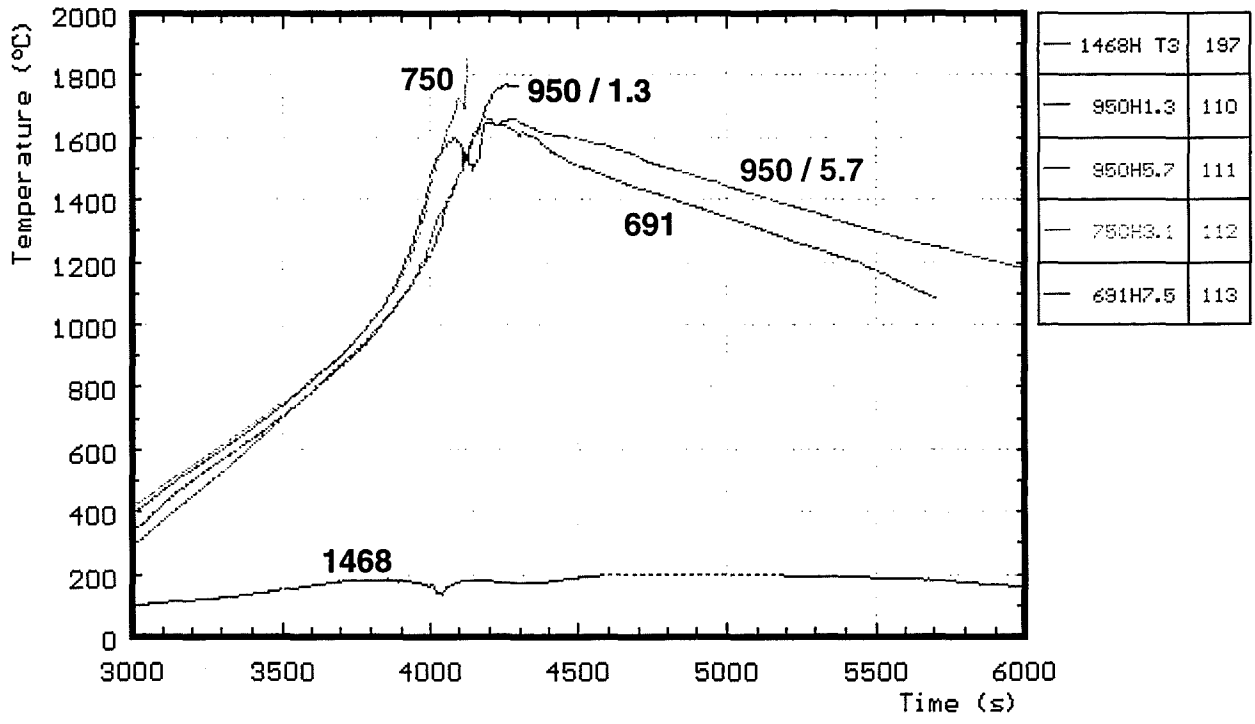

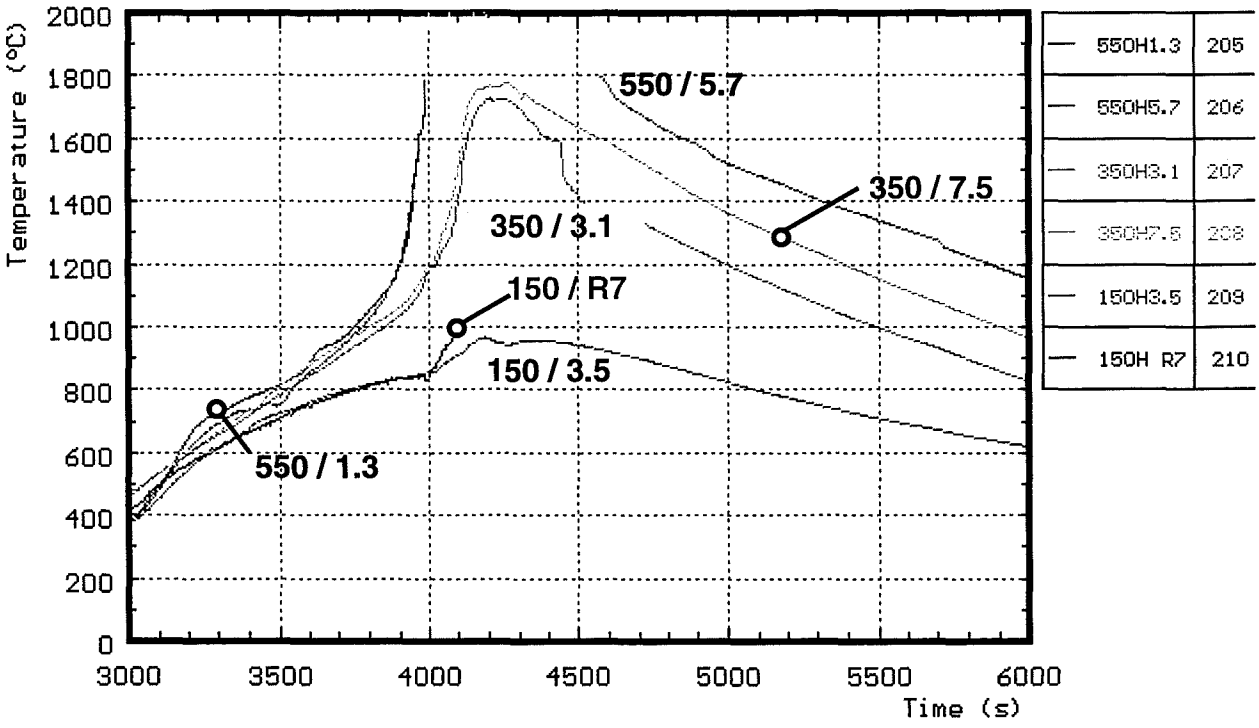

Fig 27: CORA-18; Temperatures of heated rods

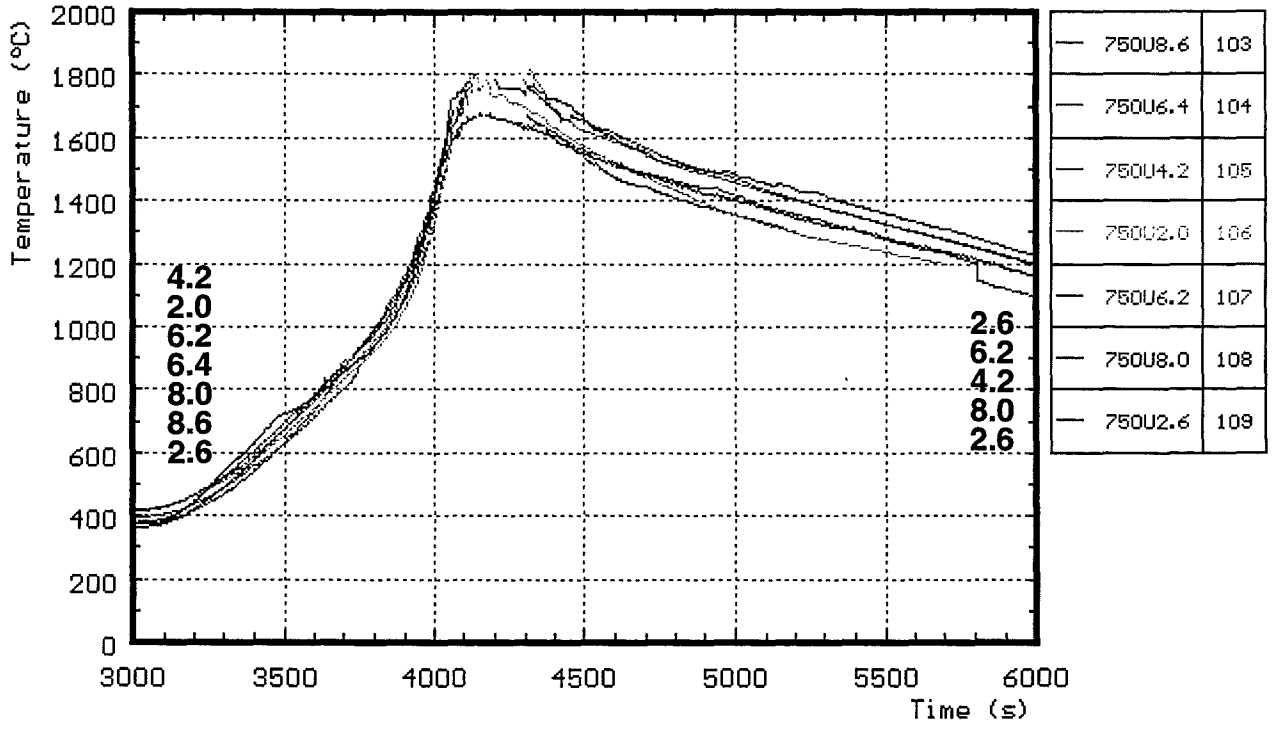

Fig. 28: CORA-18; Temperatures of unheated rods, 750 mm elevation

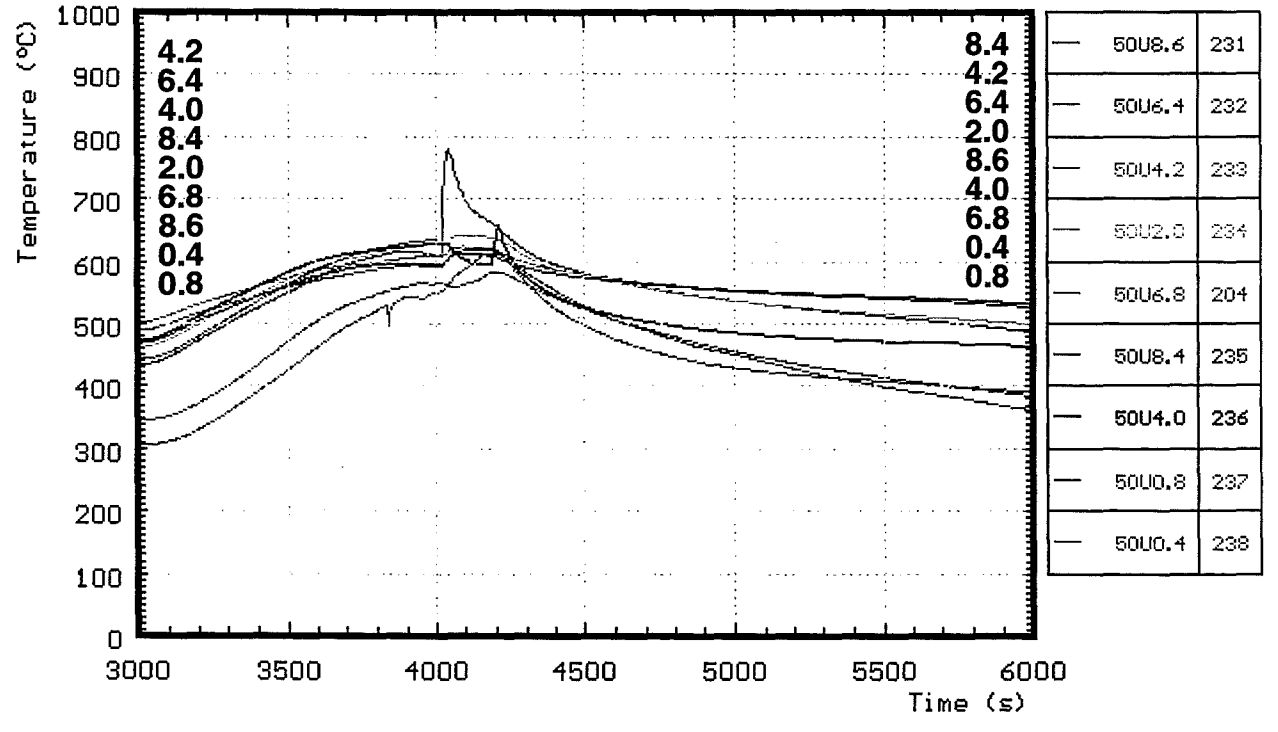

Fig. 29: CORA-18; Temperatures of unheated rods, 50 mm elevation

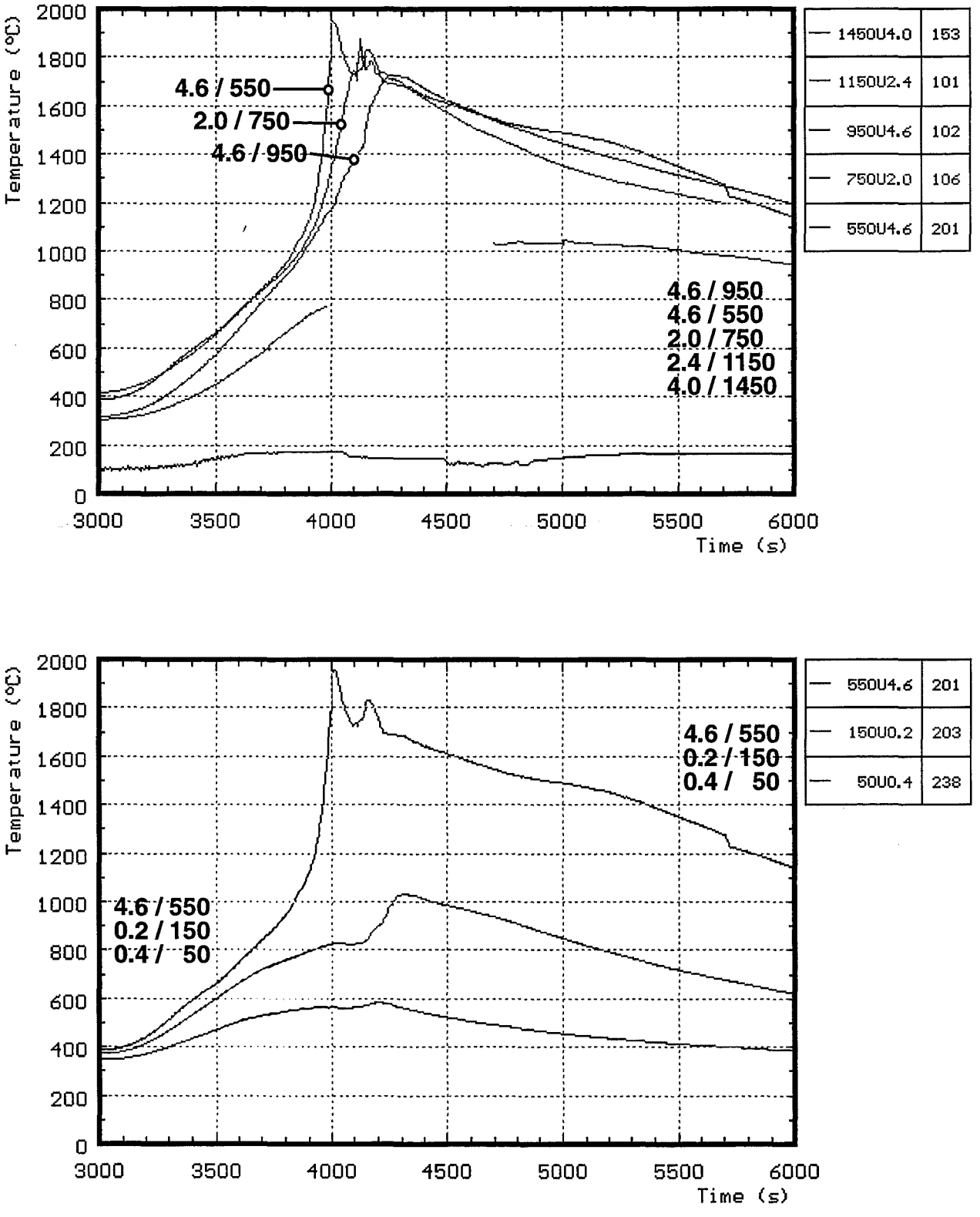

Fig. 30: CORA-18; Temperatures of unheated rods (TCs in central position)

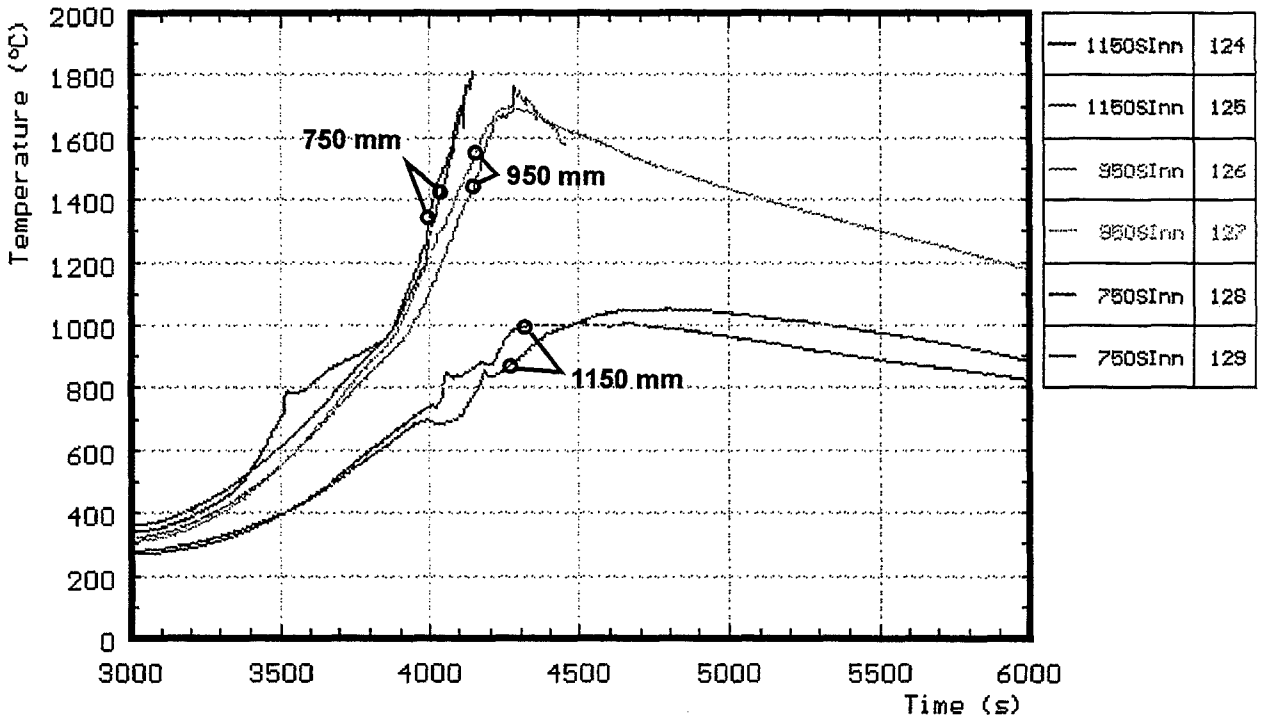

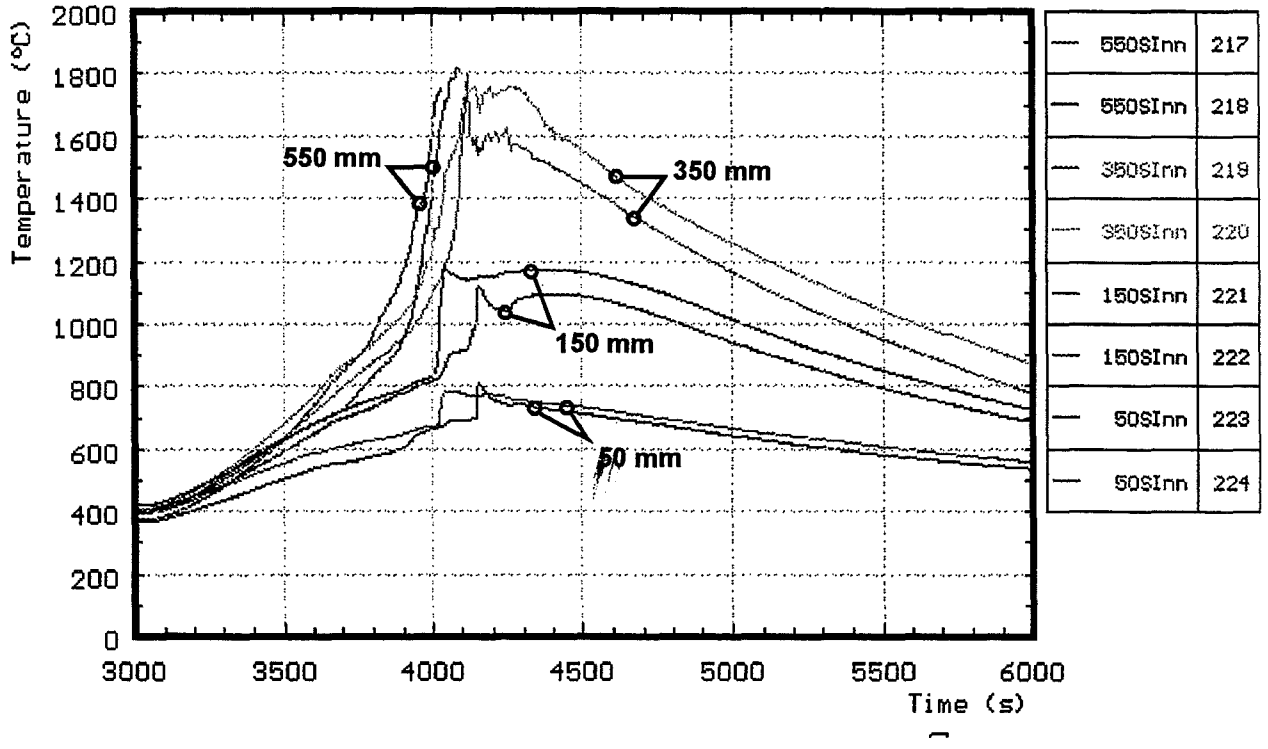

Fig 32: CORA-18; Temperatures on the channel box wall

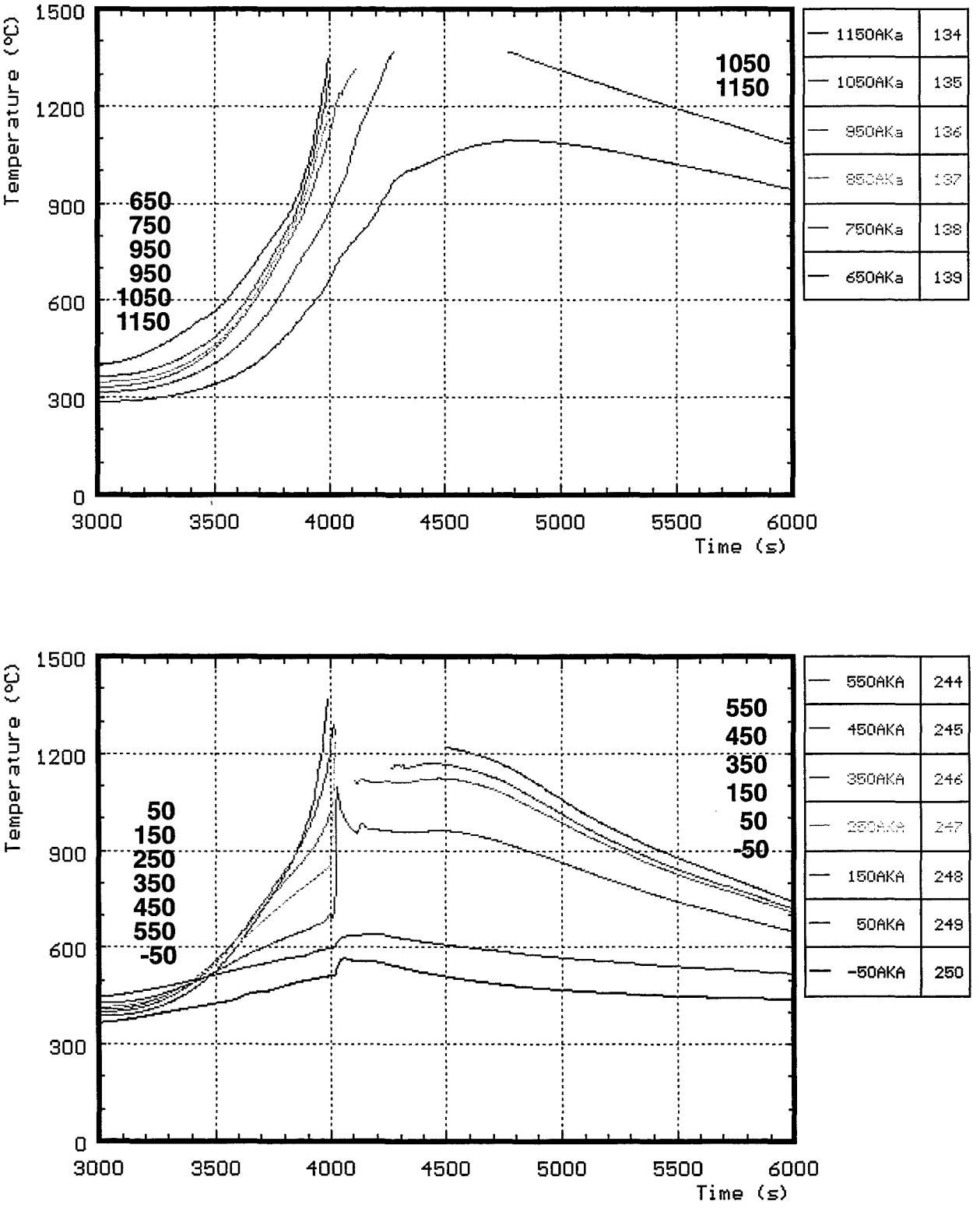

Fig. 33: CORA-18: Temperatures on the absorber blade, 120° orientation

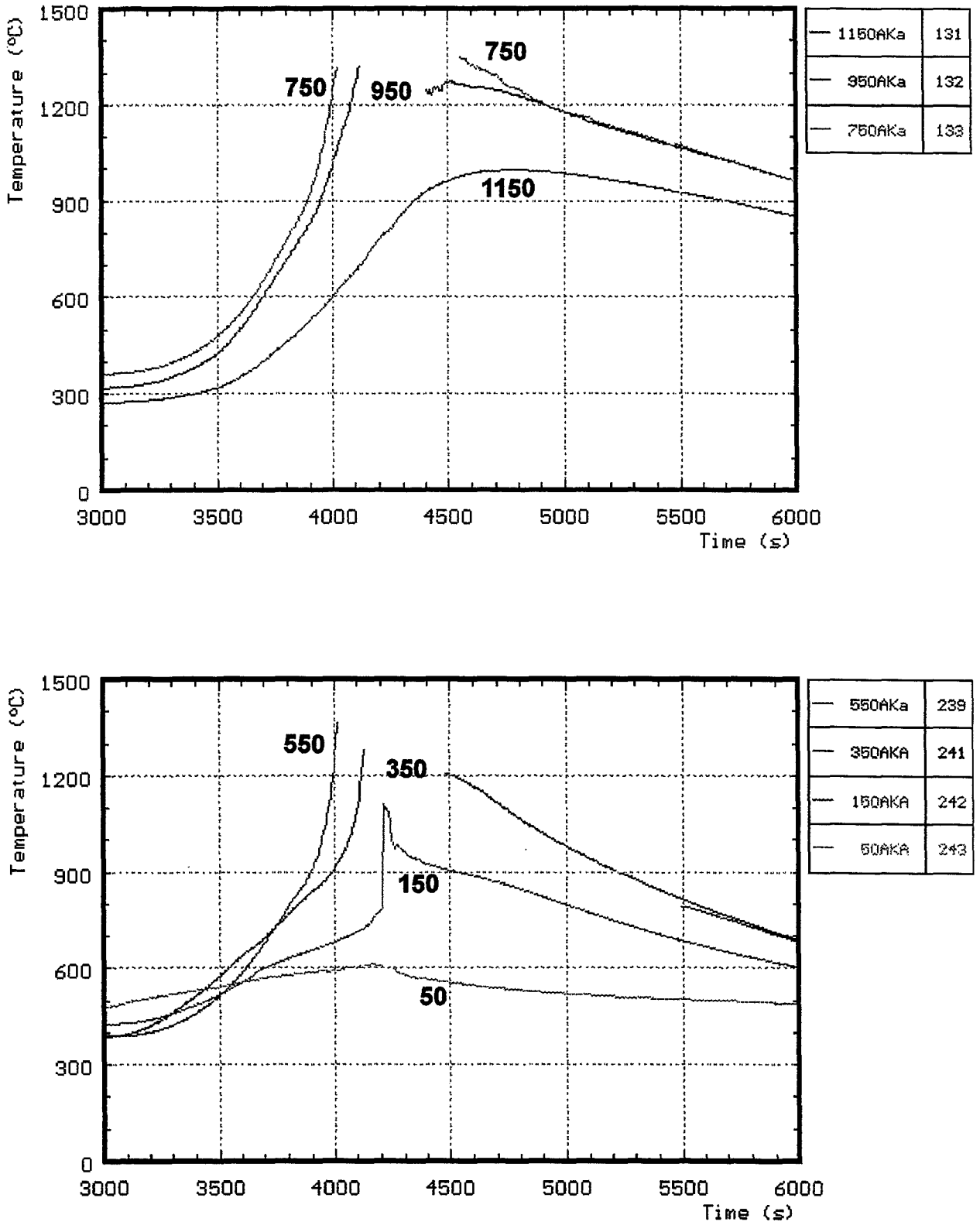

Fig. 34: CORA-18: Temperatures on the absorber blade, 300° orientation

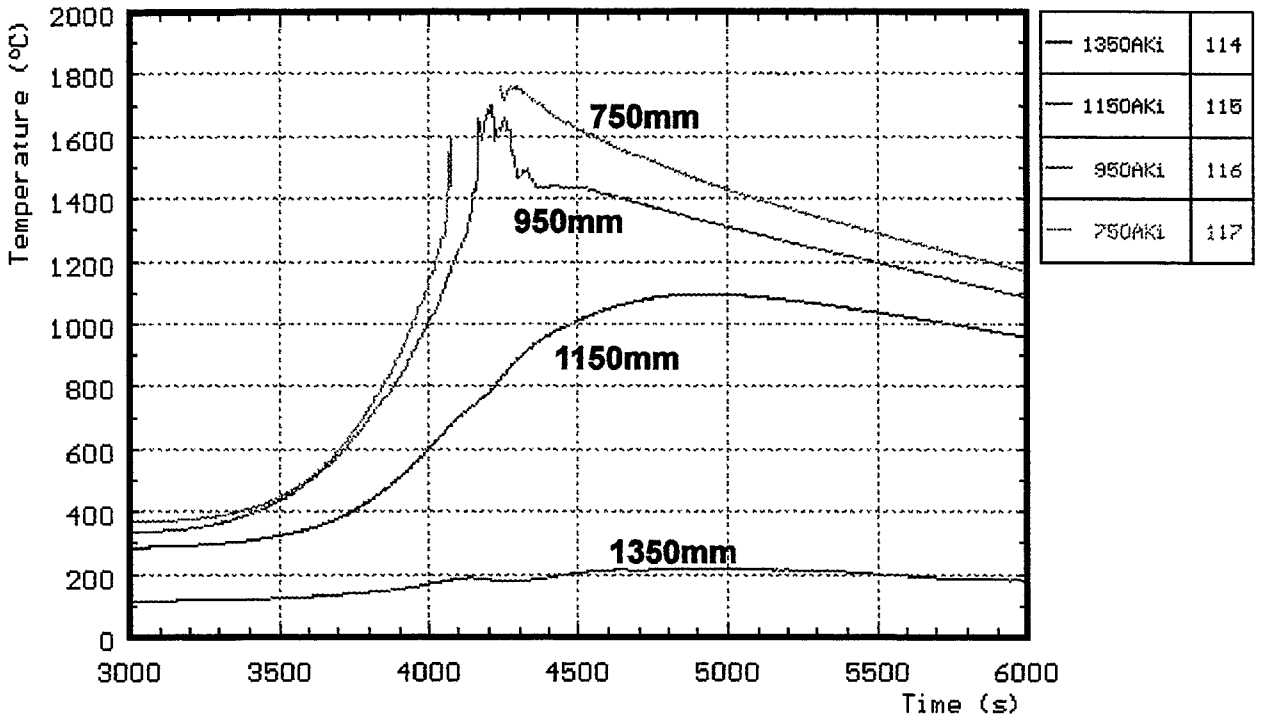

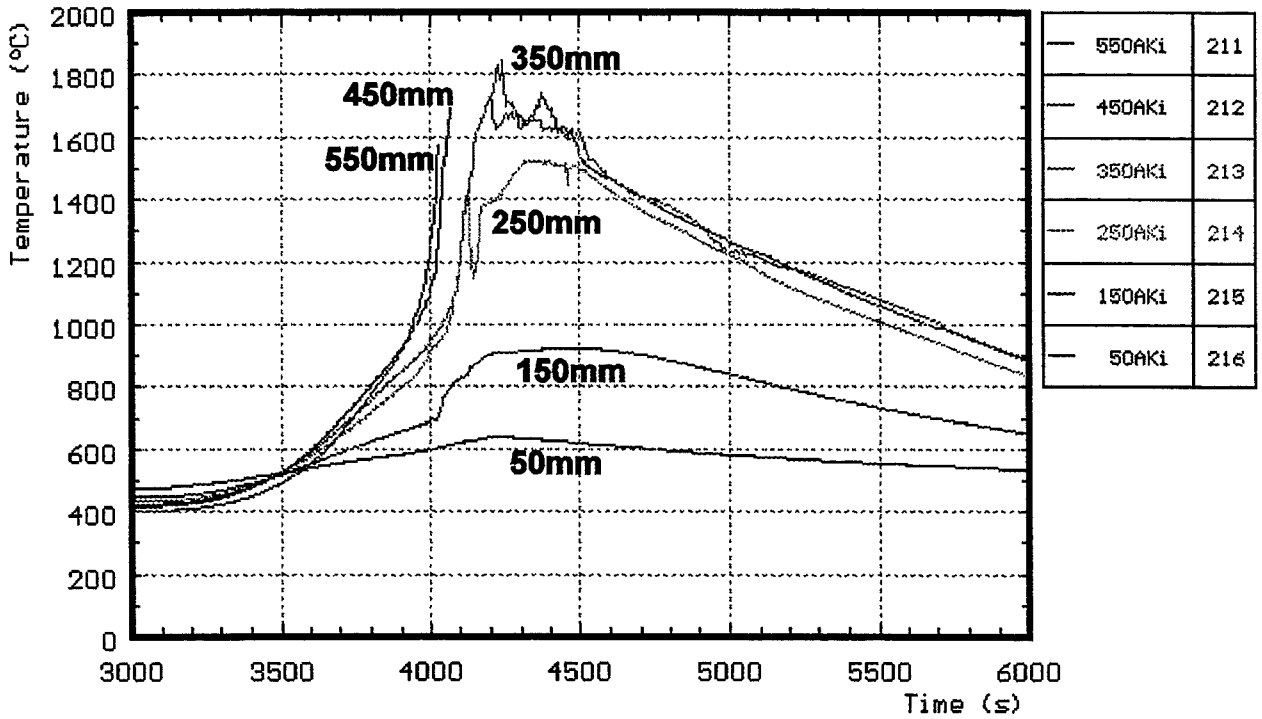

Fig. 35: CORA-18; Temperatures in the absorber blade

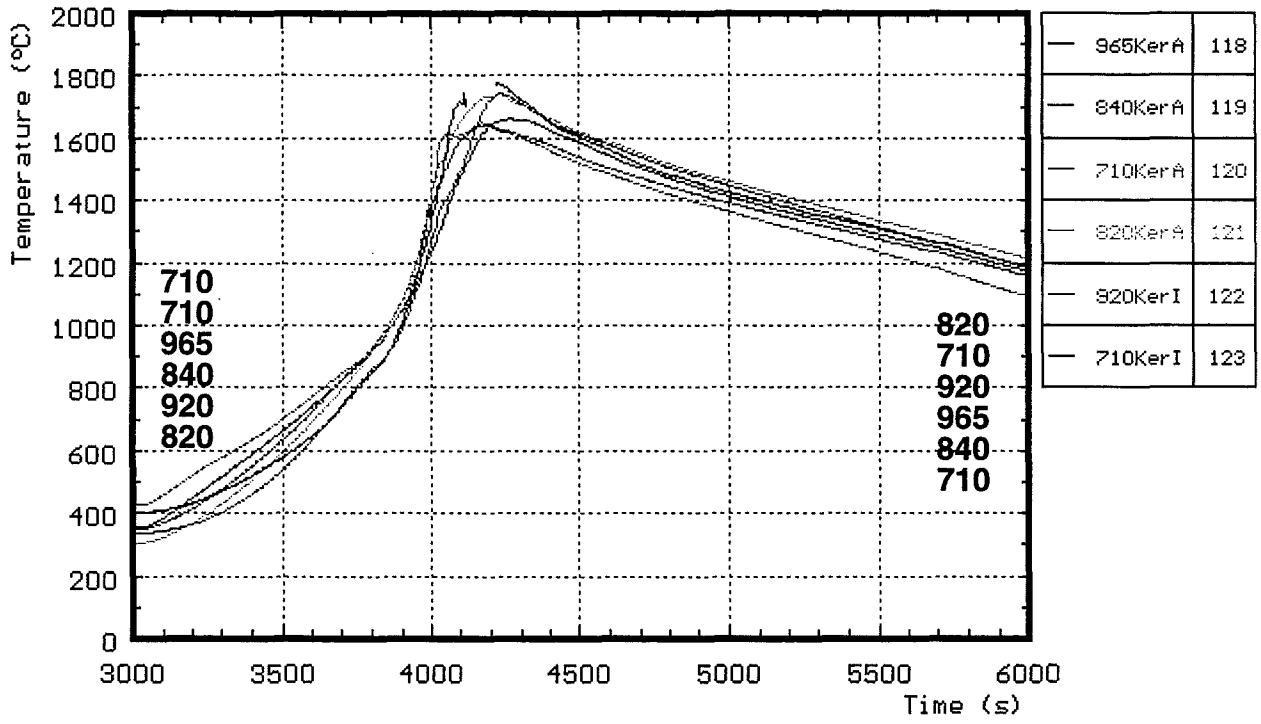

Fig. 36: CORA-18: Temperatures measured with ceramic protected TCs

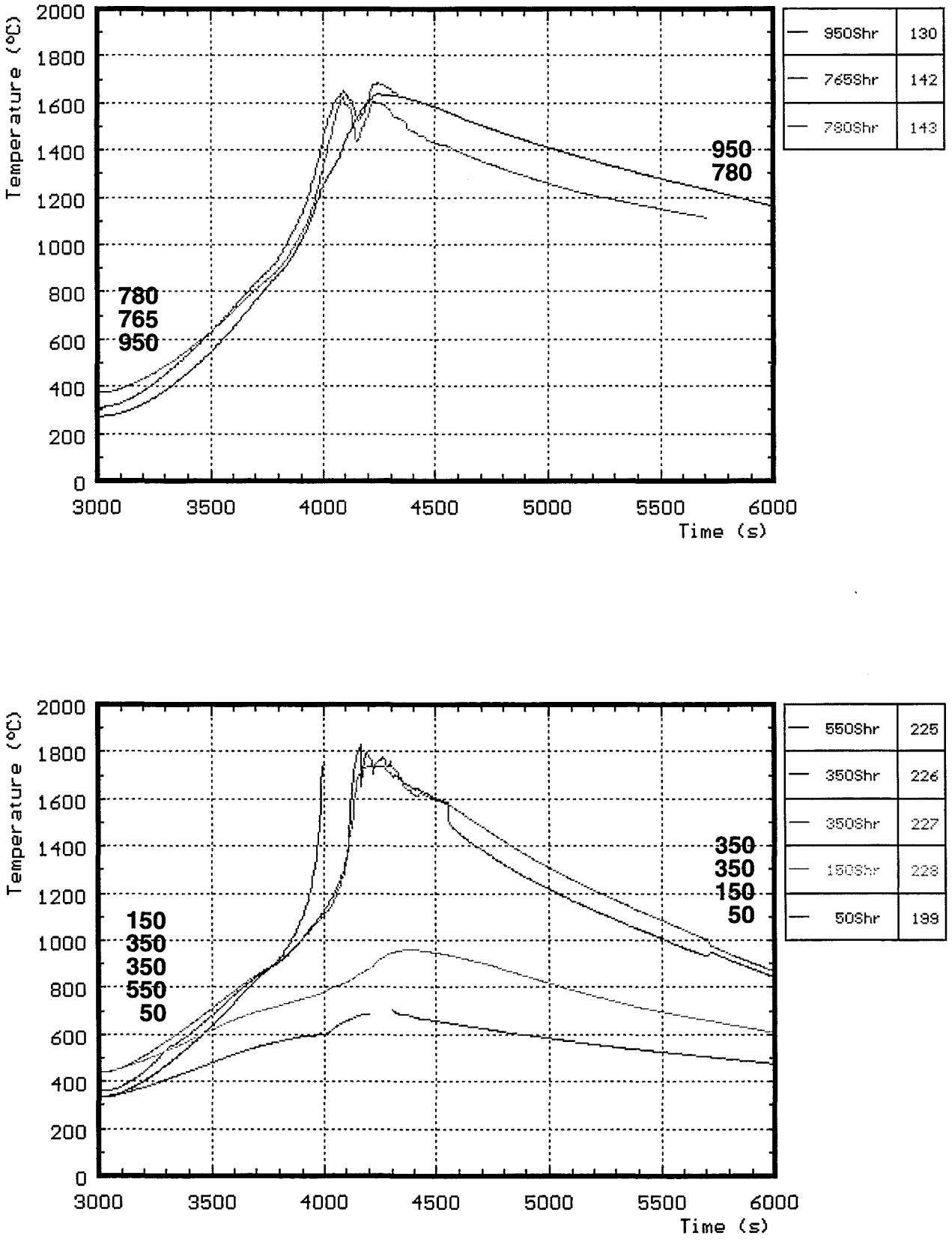

Fig 38: CORA-18; Temperatures of the outer side of the shroud

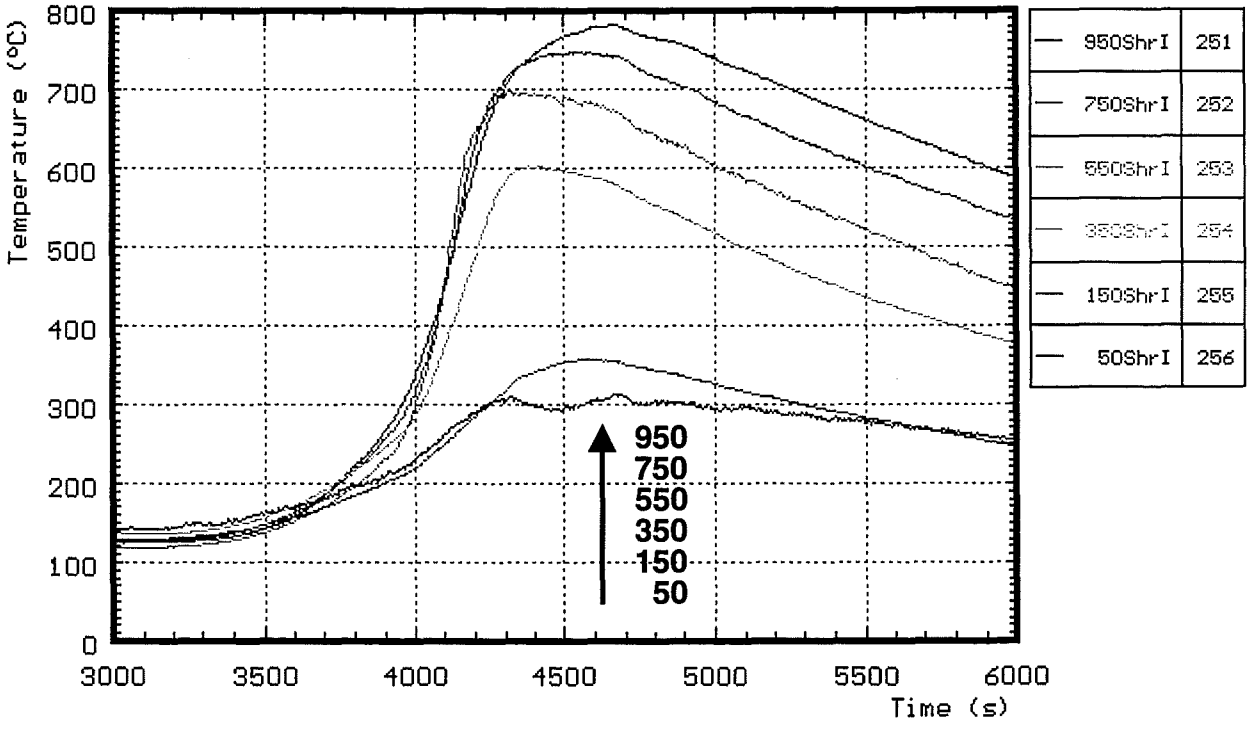

Fig. 39: CORA-18; Temperatures on shroud insulation

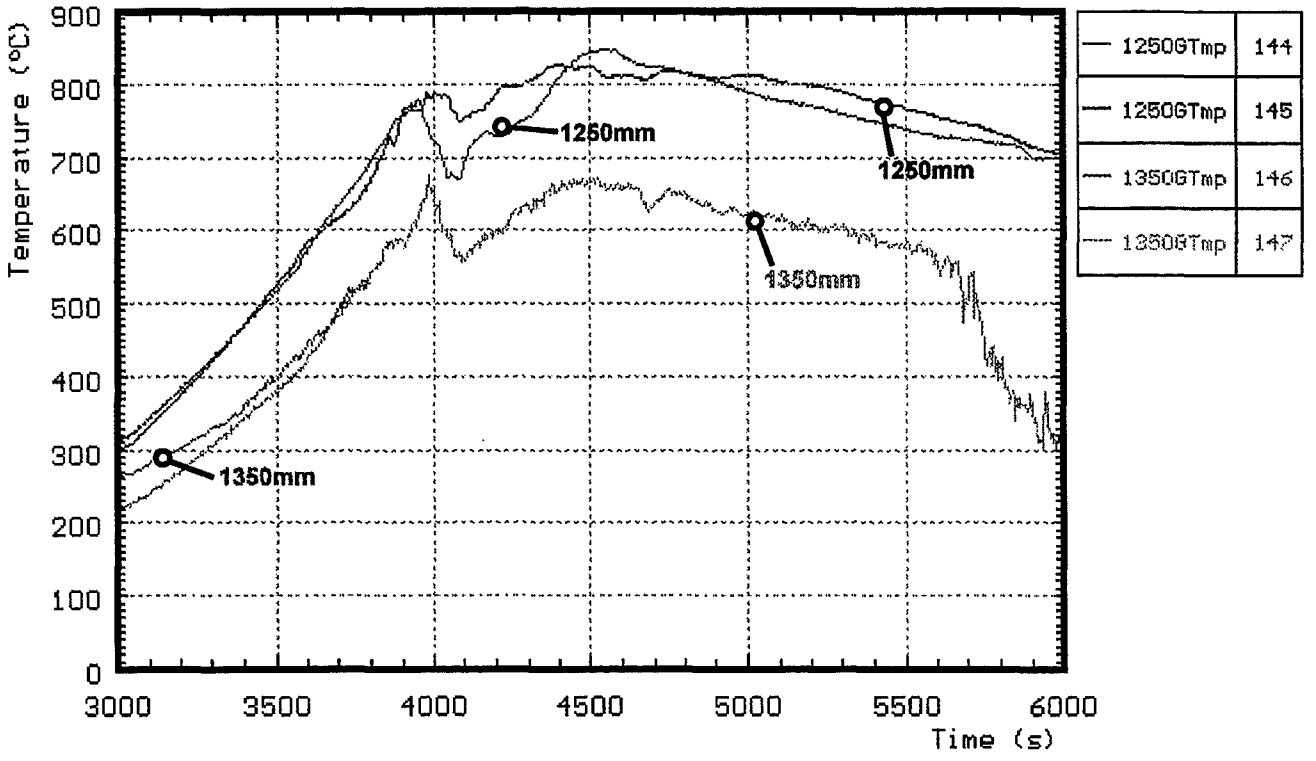

Fig.40: CORA-18; Gas temperatures above the heated zone

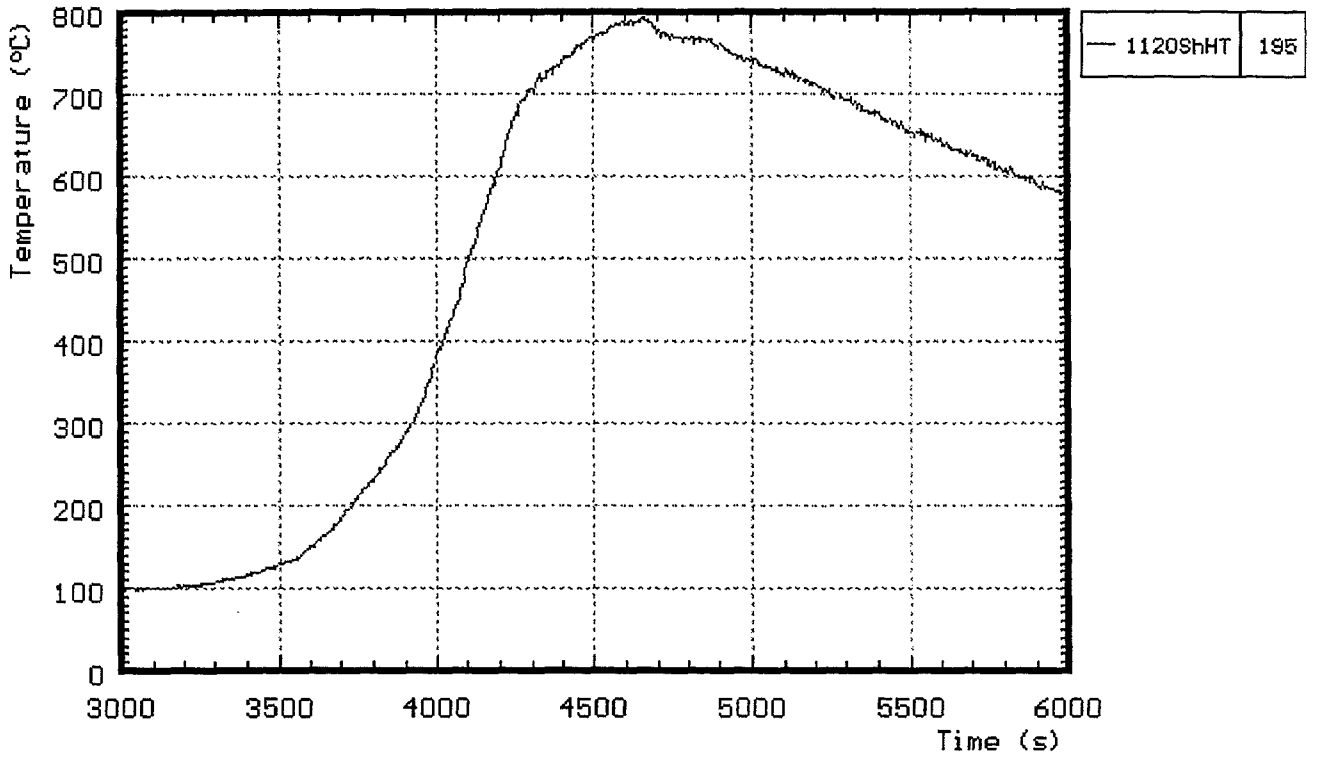

Fig.41: CORA-18; Gas temperatures between shrould and HTS

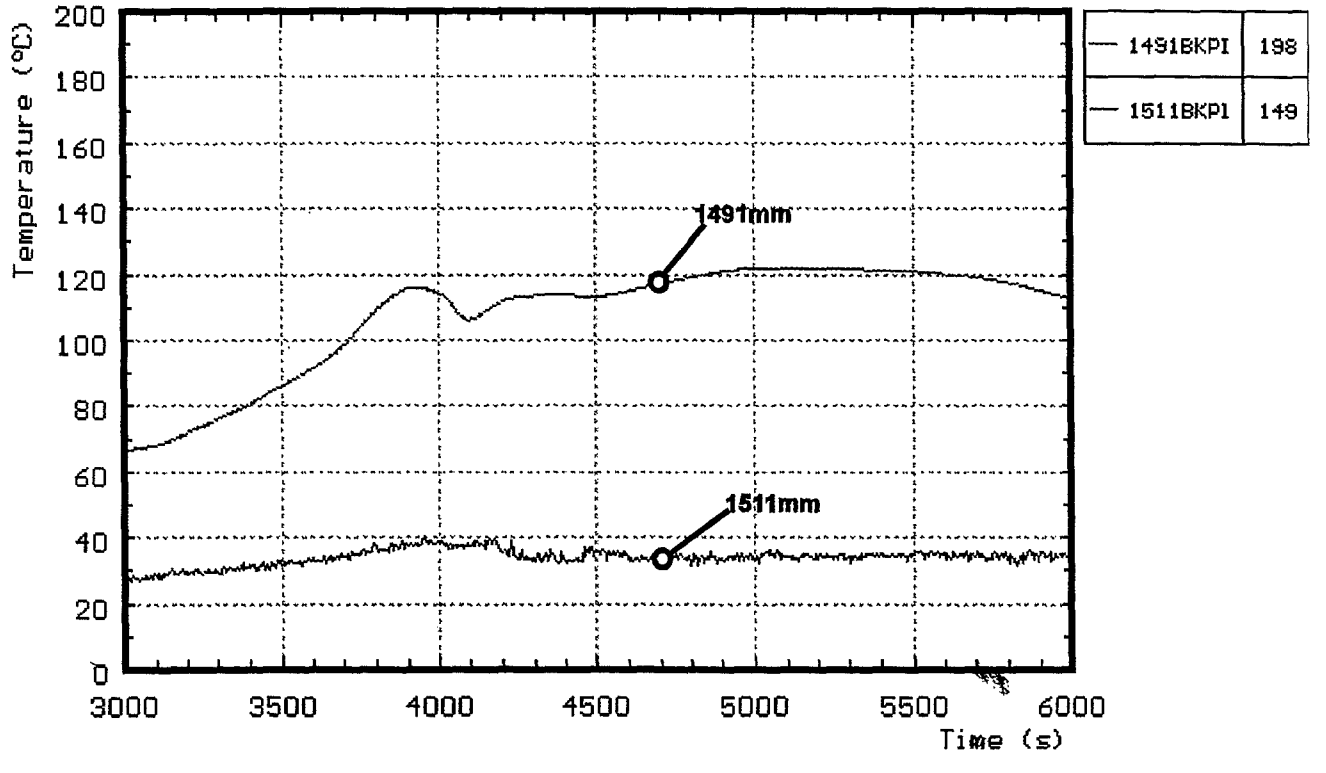

Fig.42: CORA-18; Gas temperature measured in the bundle head plate

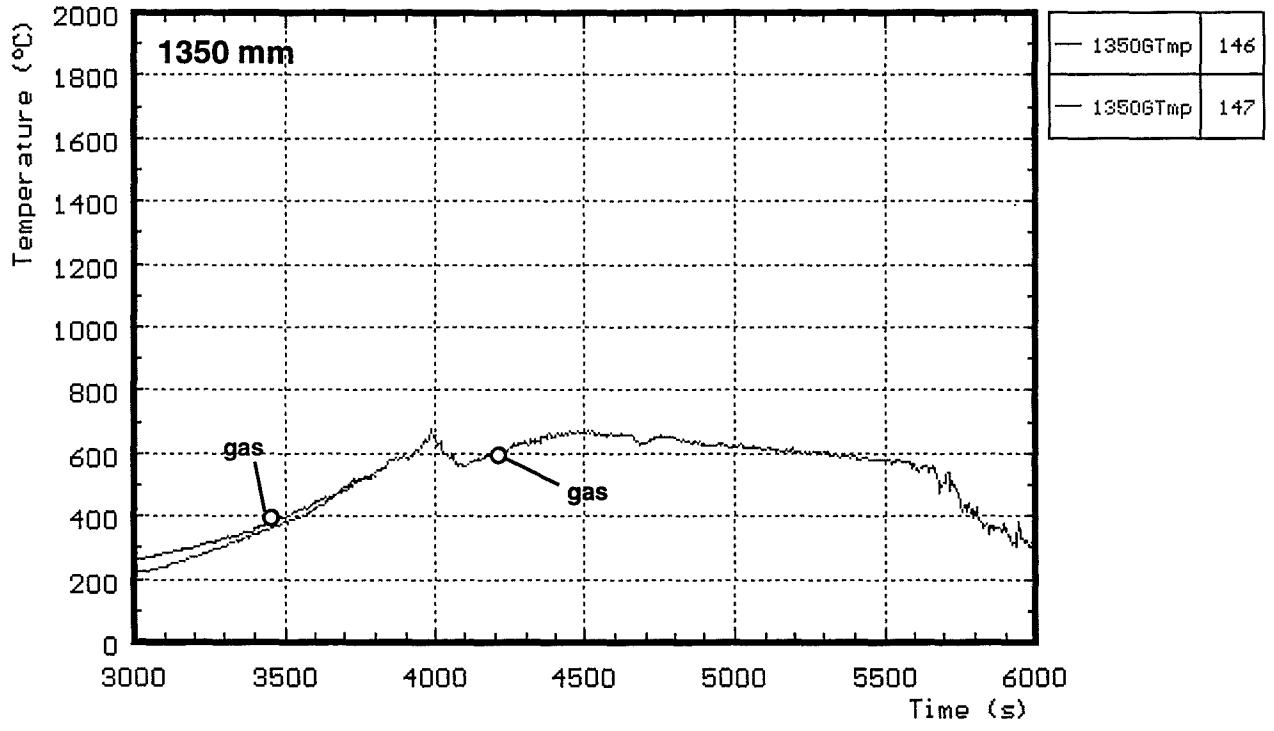

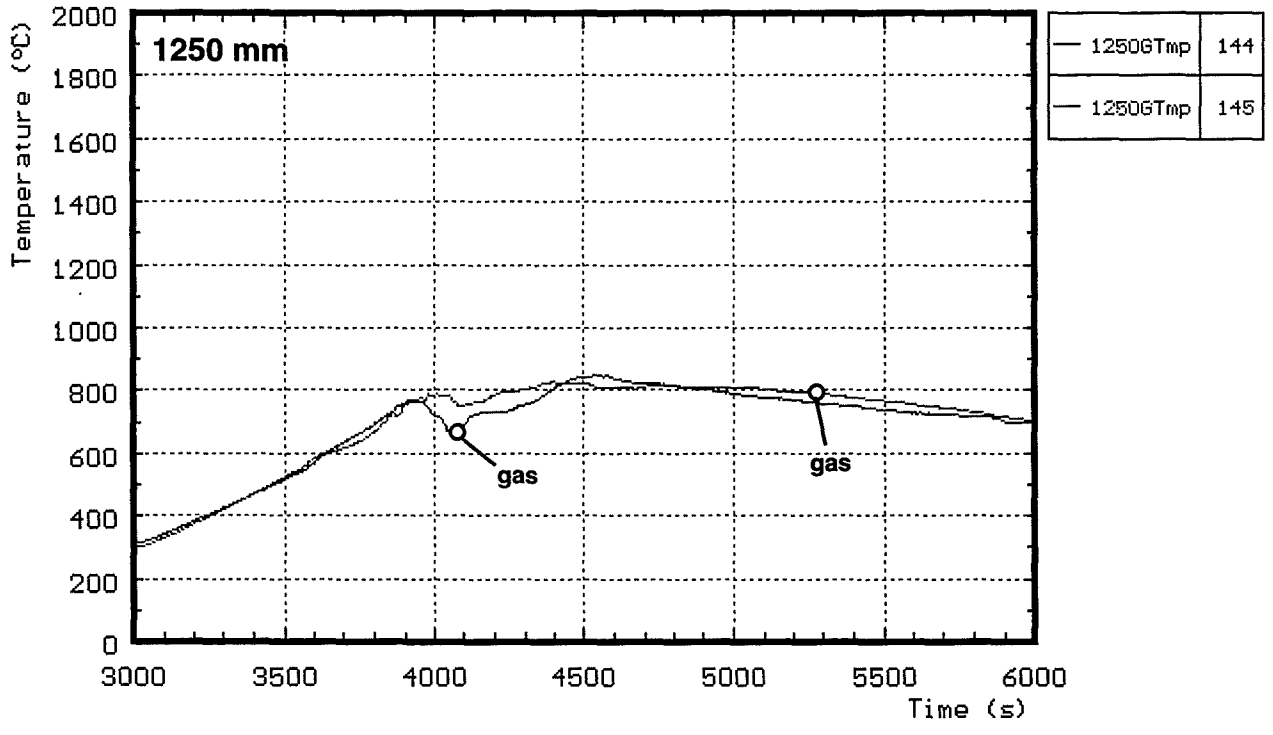

abs: in absorberblade **gas: Gas temperature**

Fig.43: CORA-18; Temperatures at elevations given (1350, 1250mm)

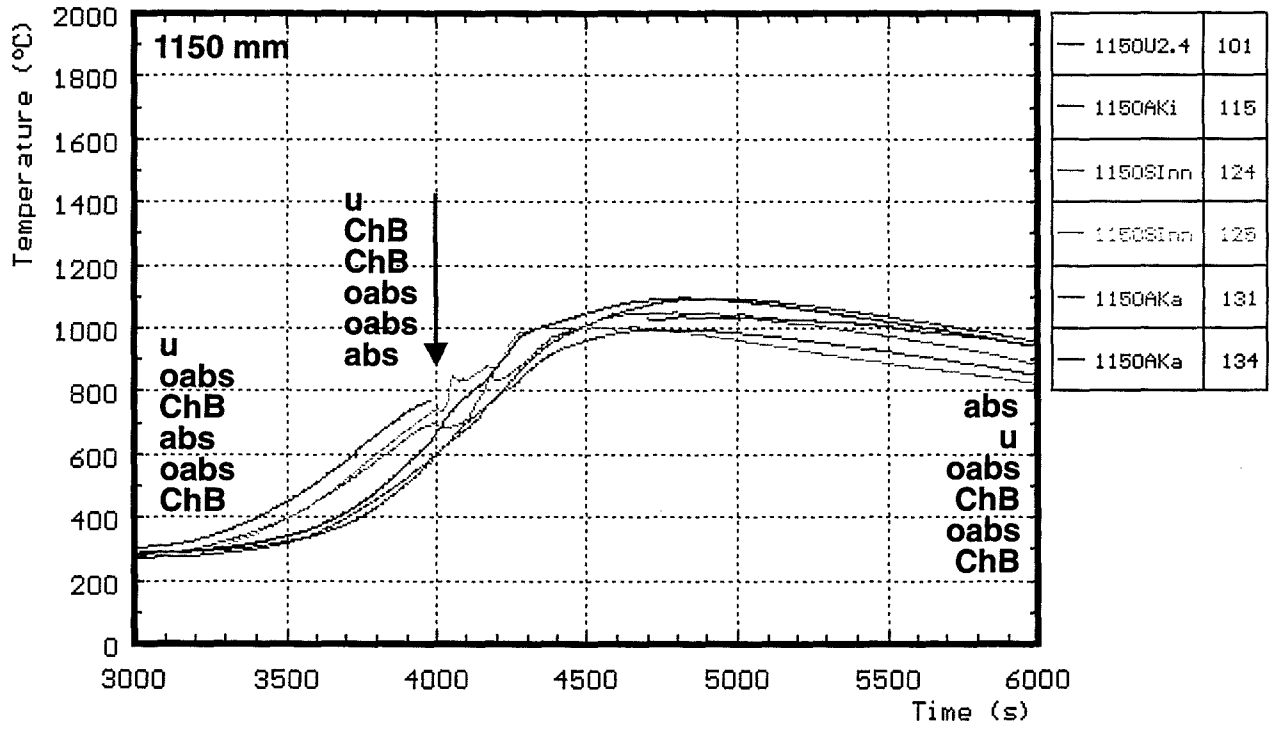

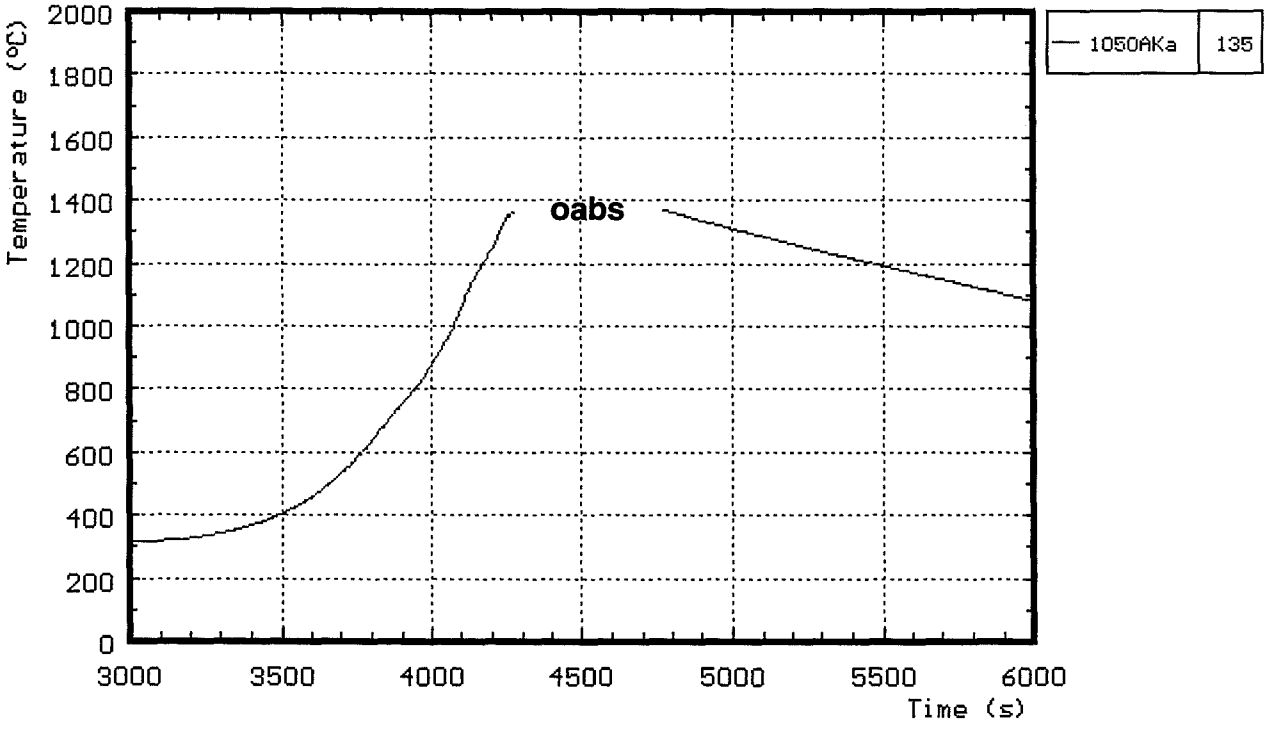

h: heated rods abs: in absorberblade

ChB: Channel box wall oabs: on absorberblade

Fig.44: CORA-18; Temperatures at elevations given (1150, 1050 mm)

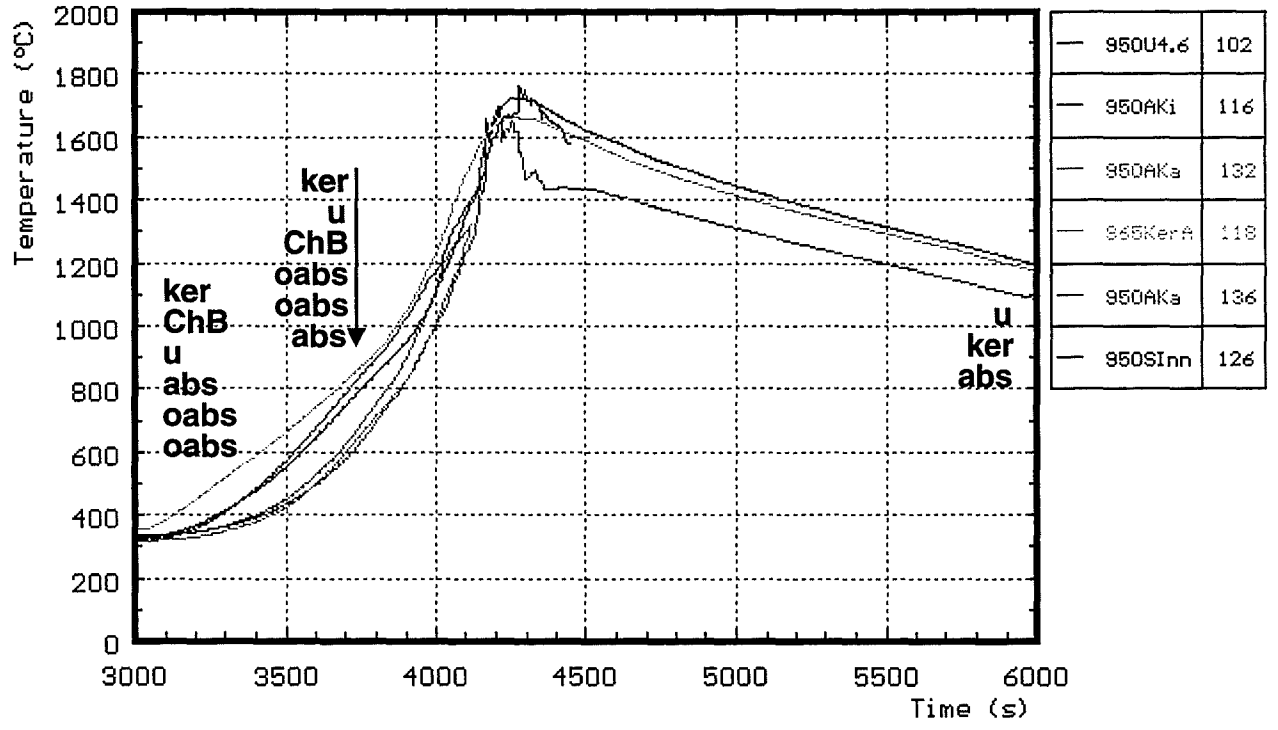

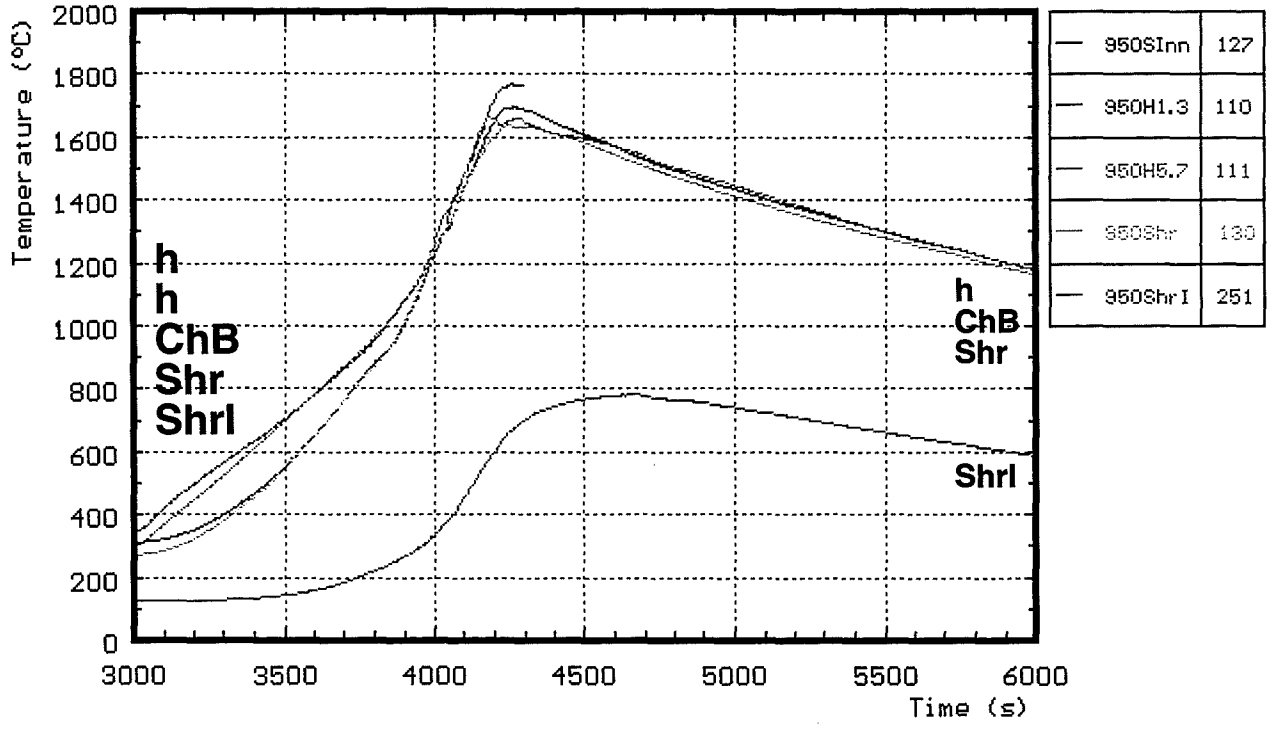

h: heated rods
u: unheated rods
ker: ceramic protected termocouples
ChB: Channel box wall
abs: in absorberblade
oabs: on absorberblade
shr: on shrould
shri: shrould ins

Fig. 45: CORA-18; Temperatures at elevations given (950 mm)

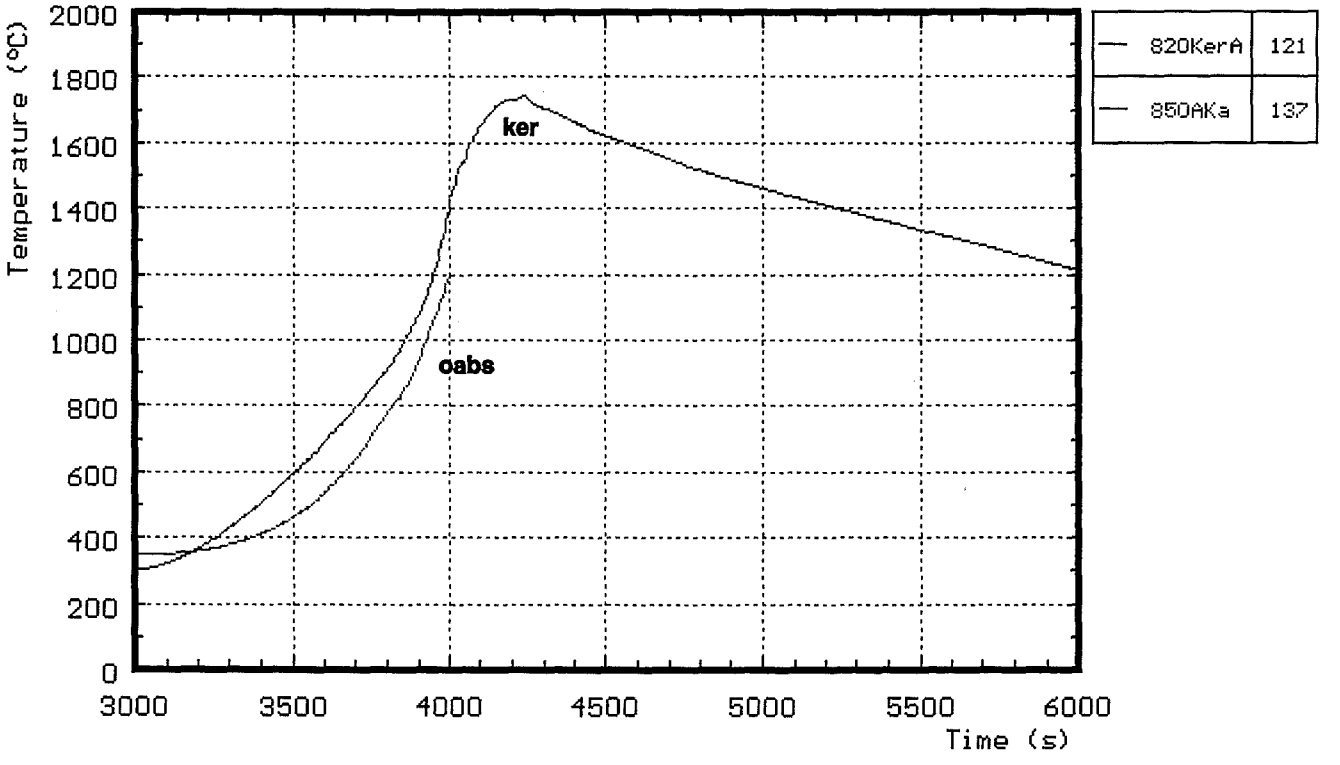

ker: **ceramic protected termocouples** **oabs:** **on absorberblade**

Fig.46: CORA-18; Temperatures at elevations given (850 - 820 mm)

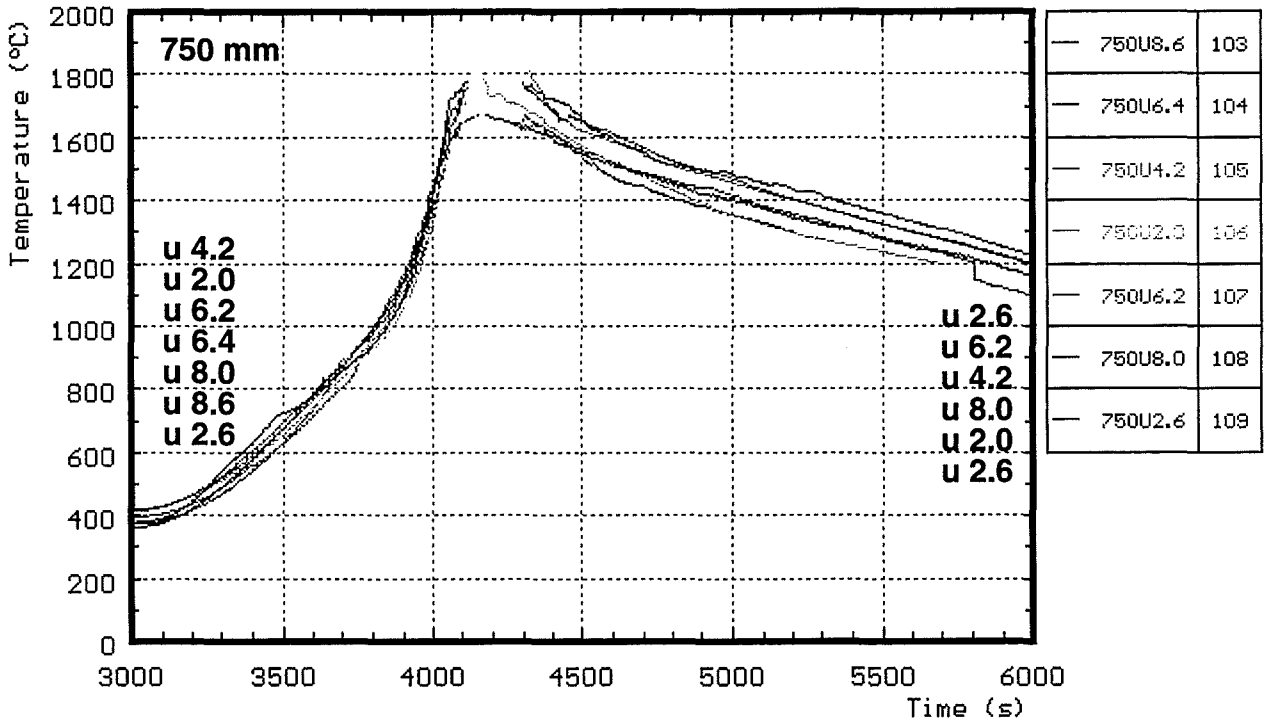

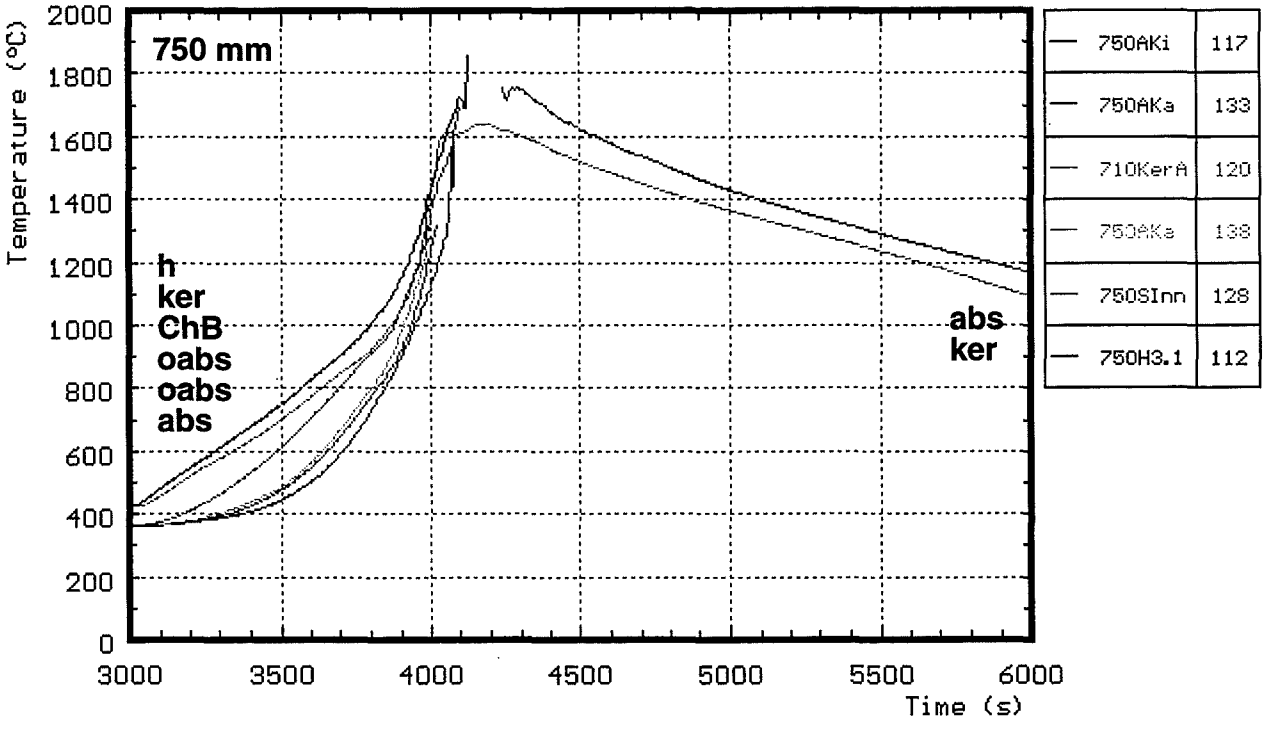

u: unheated rods
h: heated rods
ChB: Channel box wall
abs: in absorber blade
oabs: on absorber blade
ker: ceramic protected thermocouples

Fig. 47 : CORA-18; Temperatures at elevations given (750 - 710 mm)

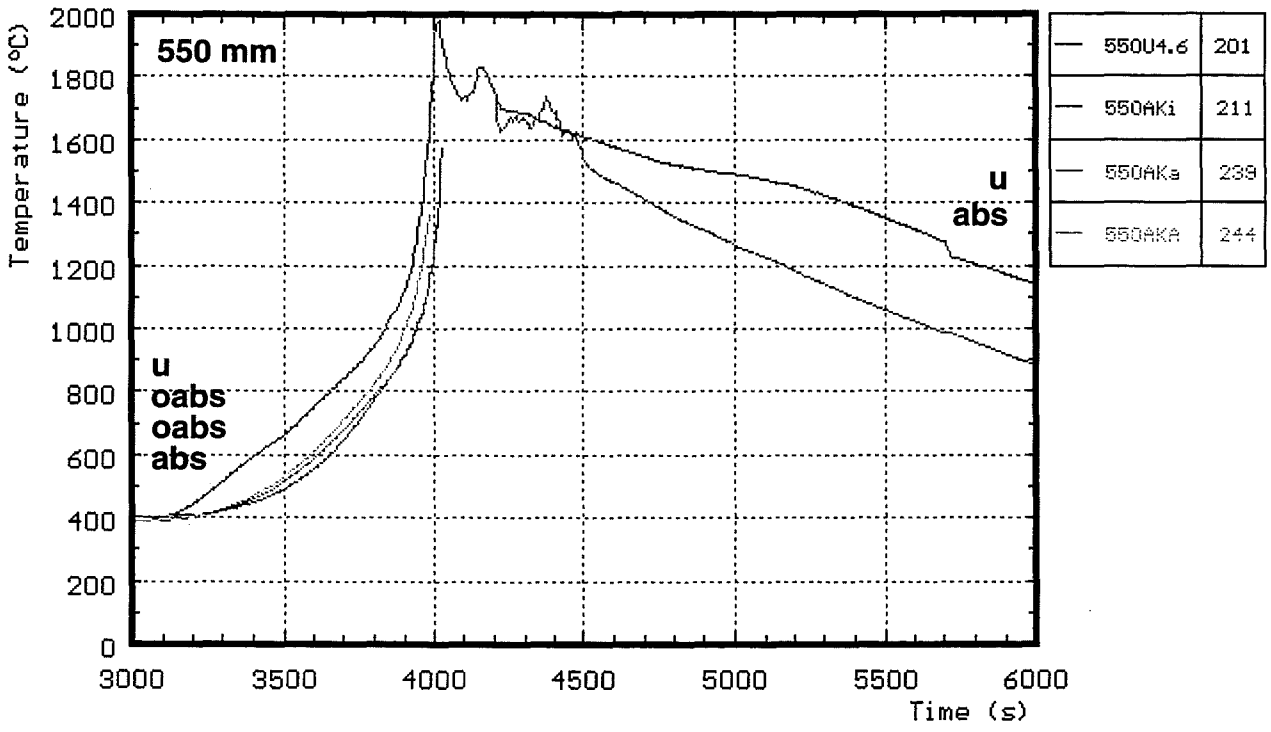

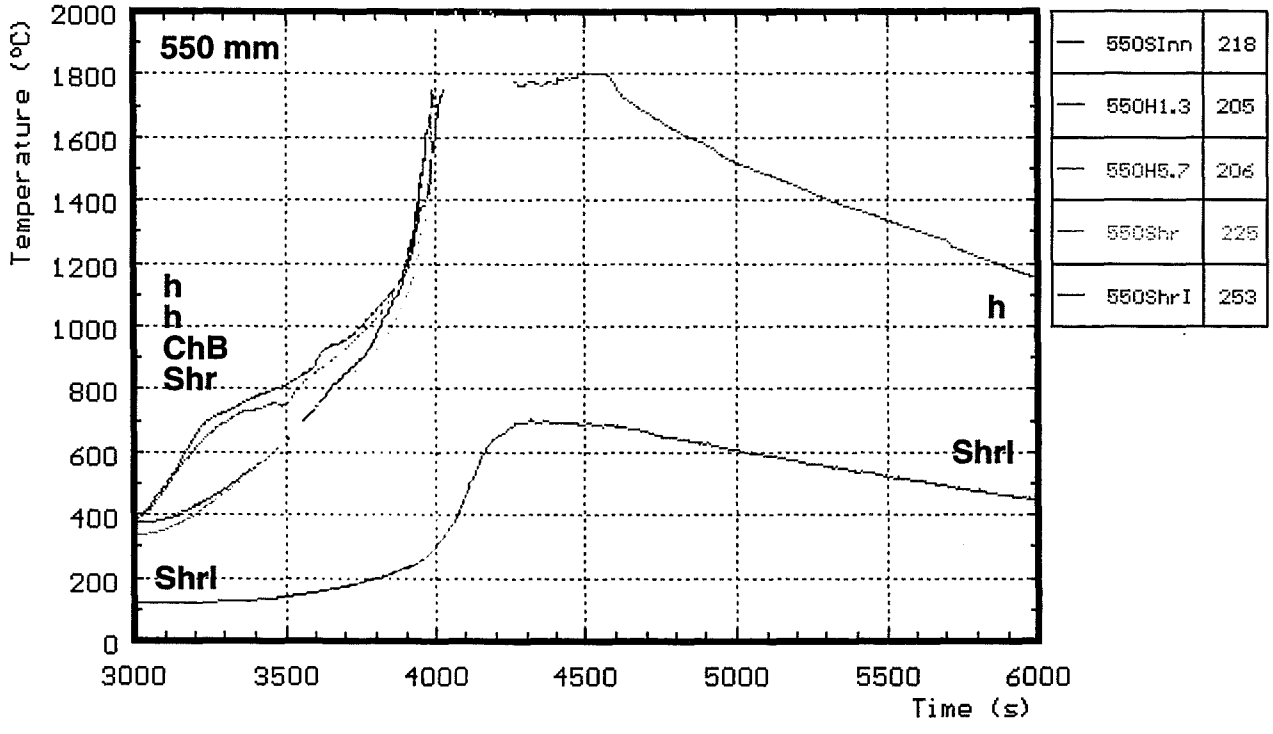

h:	heated rods	ChB:	Channel box wall
u:	unheated rods	Shr:	on shrould
abs:	in absorberblade	Shri:	shrould ins
oabs:	on absorberblade		

Fig.48: CORA-18; Temperatures at elevations given (550 mm)

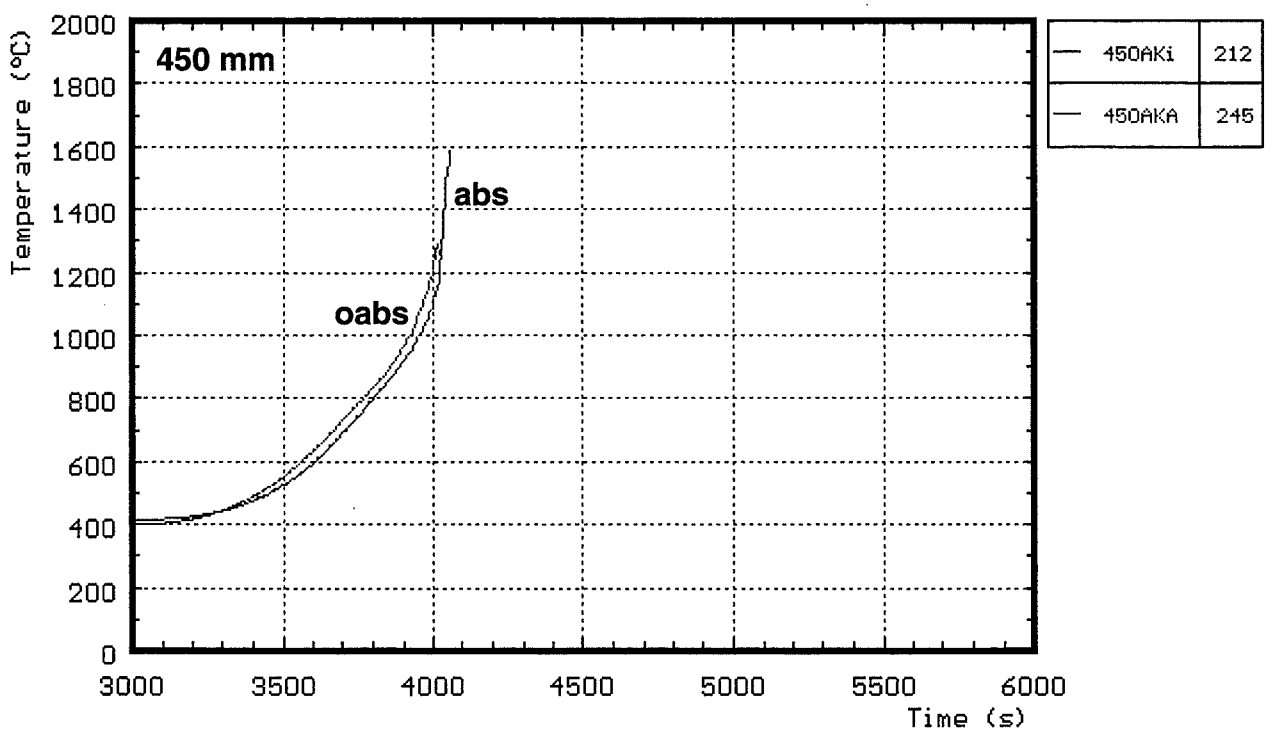

abs: in absorber blade **oabs: on absorber blade**

Fig. 49: CORA-18; Temperatures at elevations given (450mm)

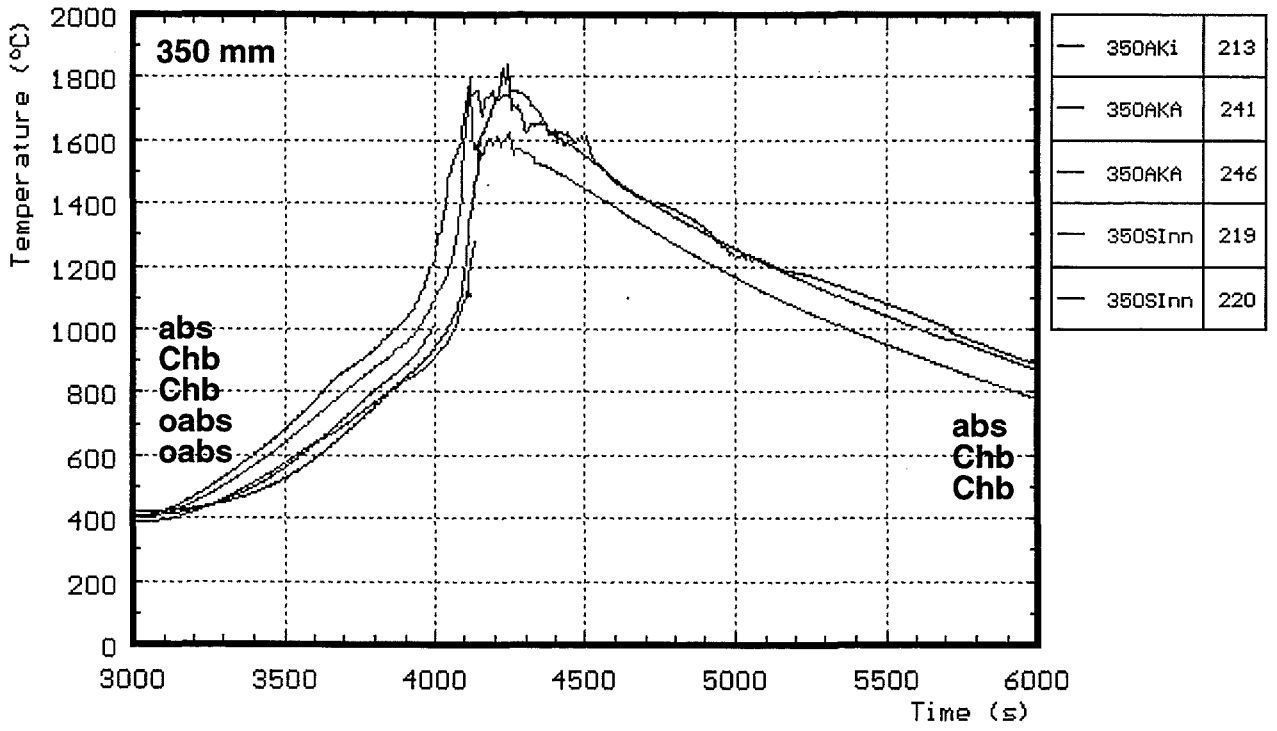

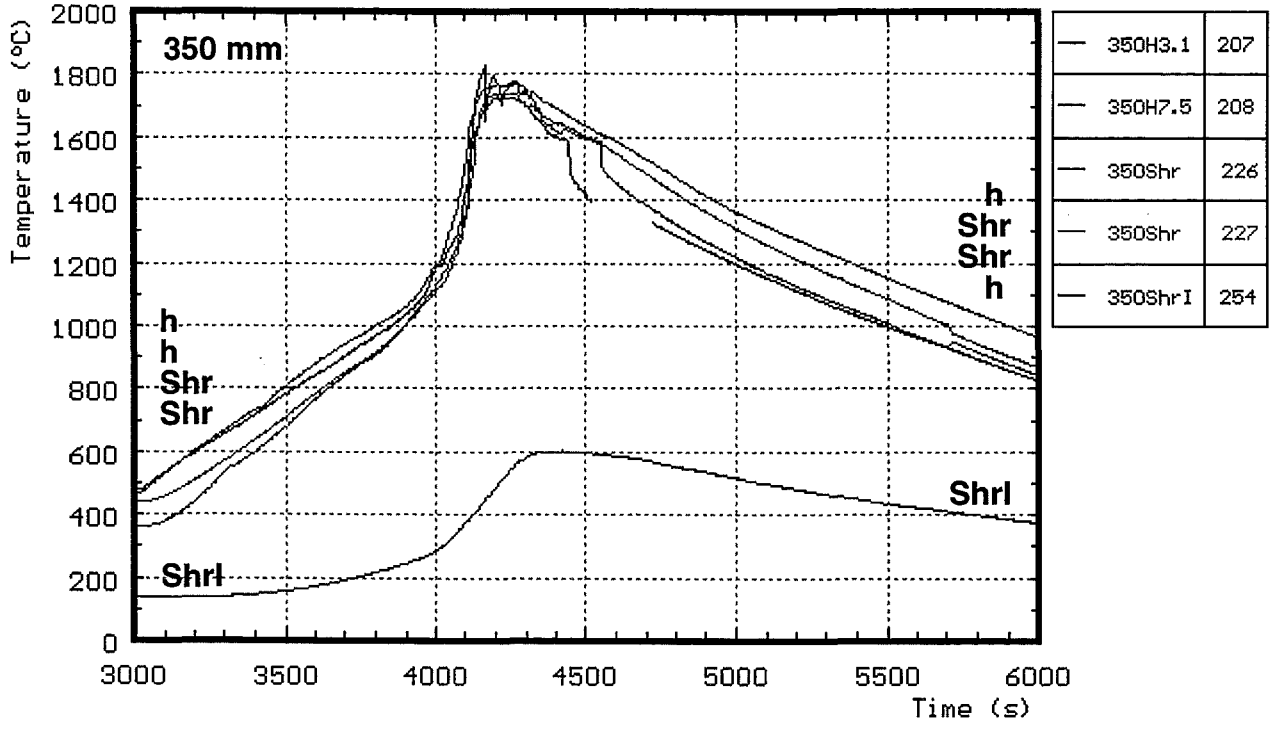

h: heated rods
u: unheated rods
abs: in absorber blade
ChB:Channel box wall
oabs: on absorber blade
Shr: on shrould
Shrl: shrould ins.

Fig.50: CORA-18; Temperatures at elevations given (350mm)

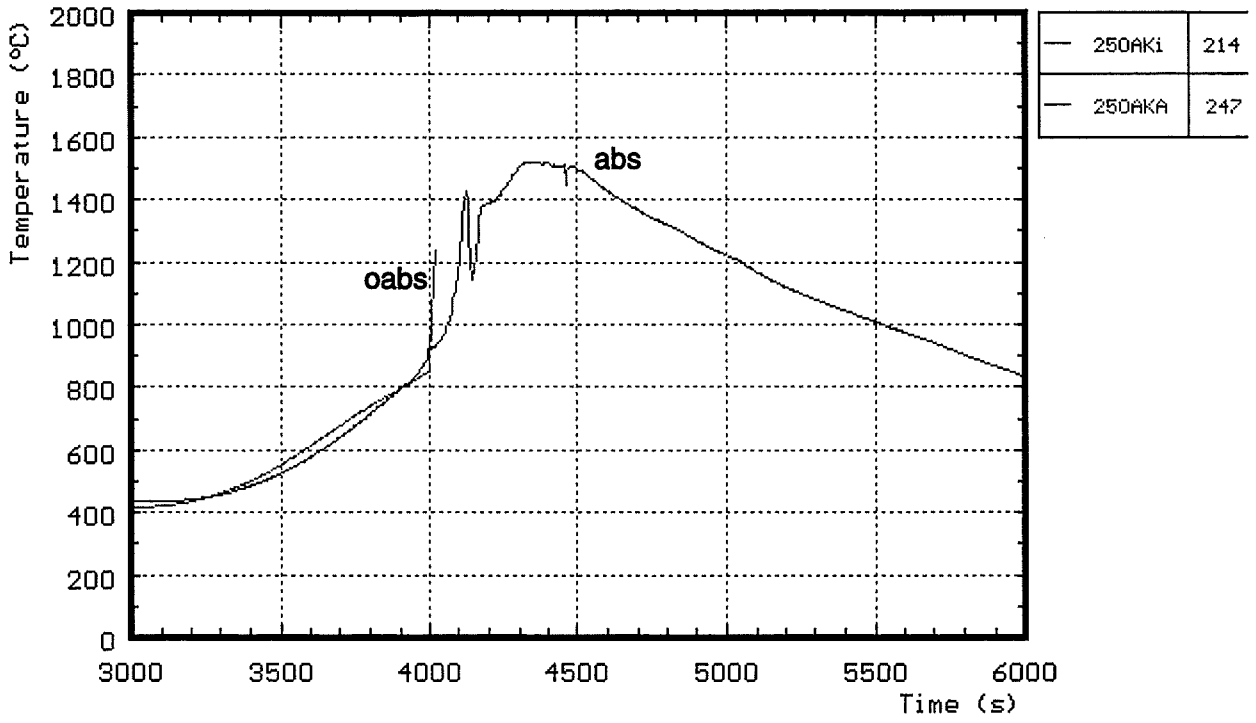

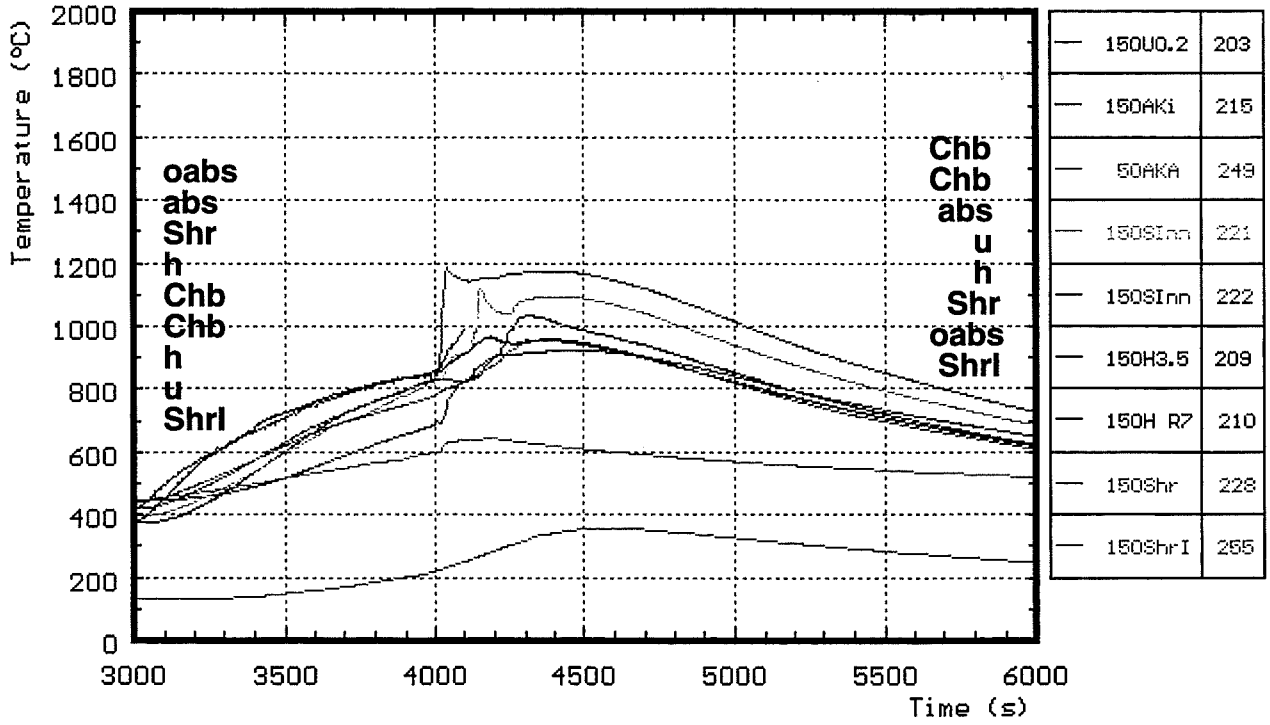

abs:	in absorberblade	h:	heated rods
oabs:	on absorberblade	Shr:	on shroud
ChB:	Channel box wall	Shrl:	shroud insulation

Fig. 51: CORA-18; Temperatures at elevations given (250mm, 150 mm)

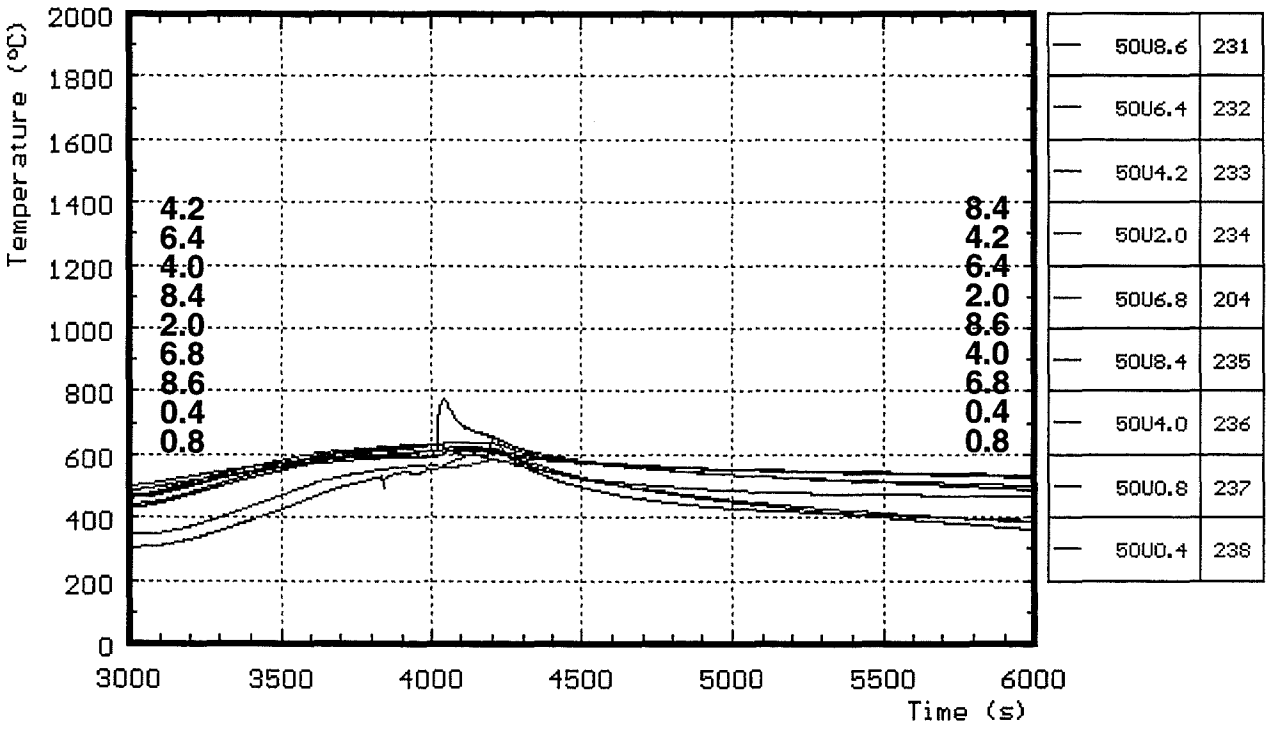

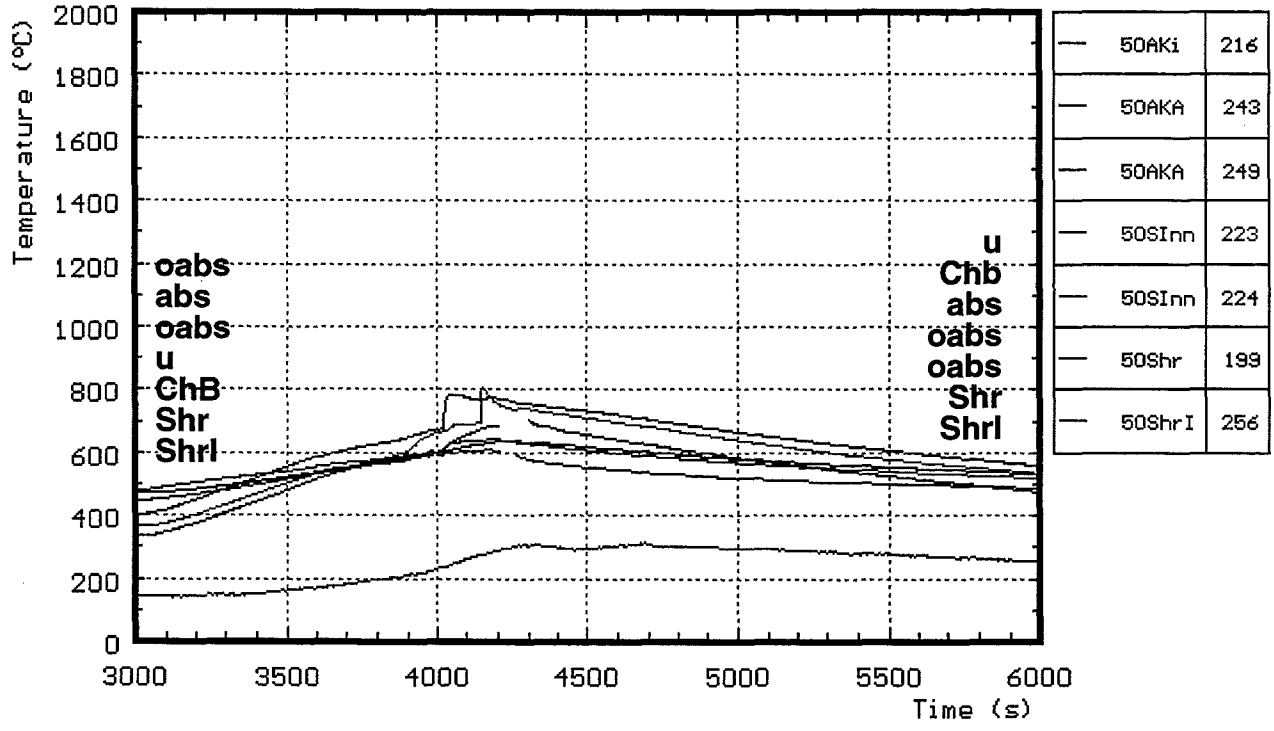

u: unheated rods
abs: in absorberblade
oabs: on absorberblade

ChB: Channel box wall
Shr: on shroud
Shrl: shroud insulation

Fig. 52: CORA-18; Temperatures at elevations given (50 mm)

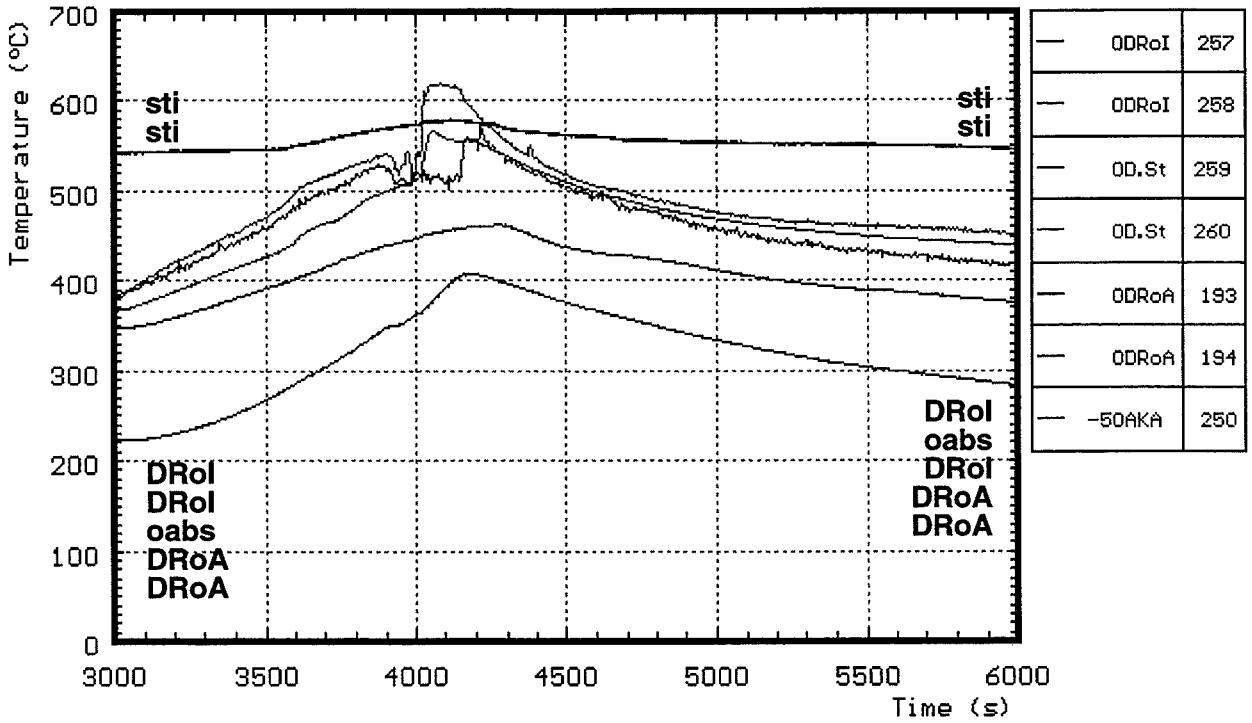

DRoI: steam tube, inner side
DRoA: steam tube, outer side
sti: steam inlet
oabs: on absorber blade

Fig. 53: CORA-18; Temperatures at elevations given (0, -50 mm)

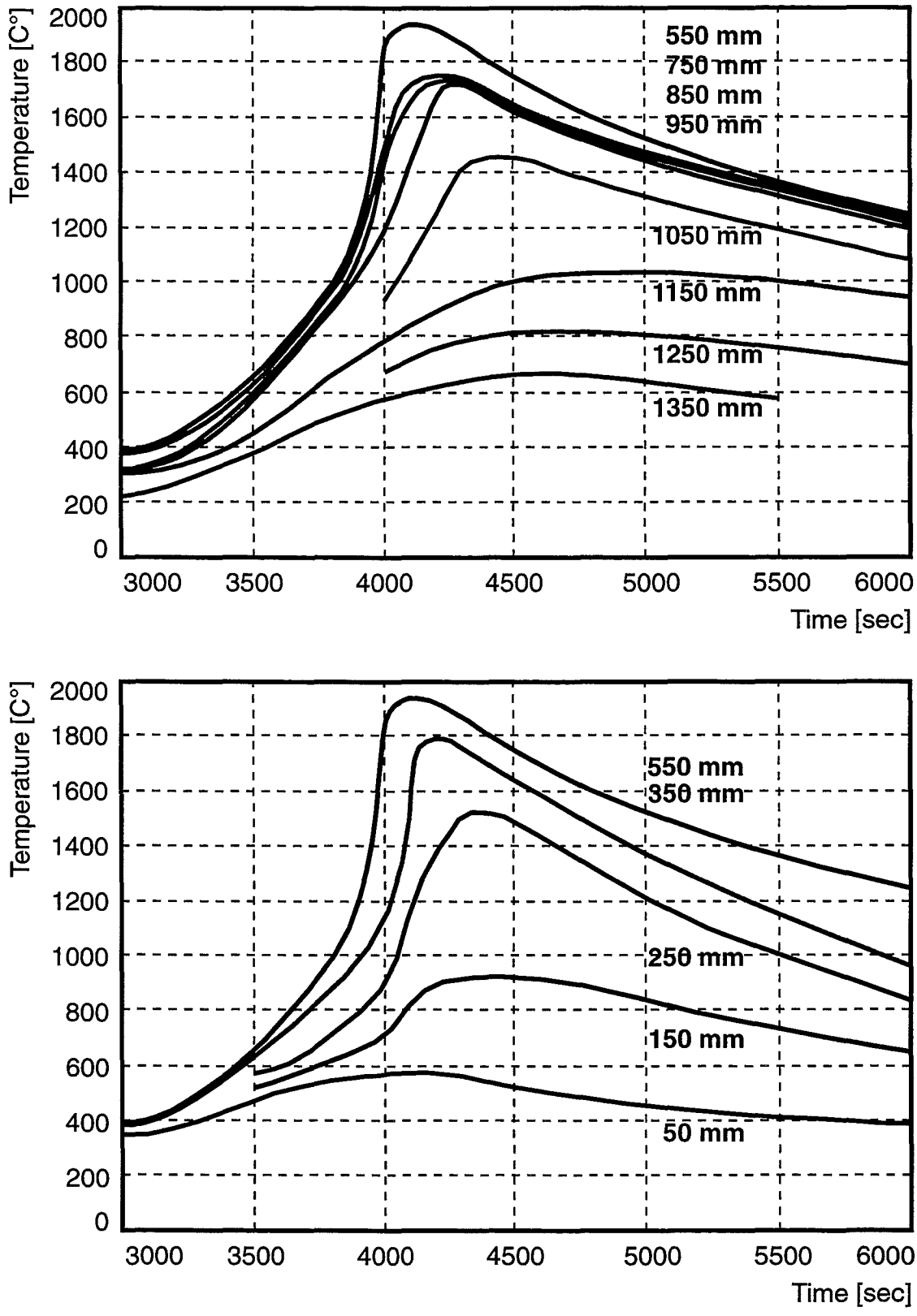

Fig. 54: CORA-18; Best-estimate bundle temperatures at different elevations

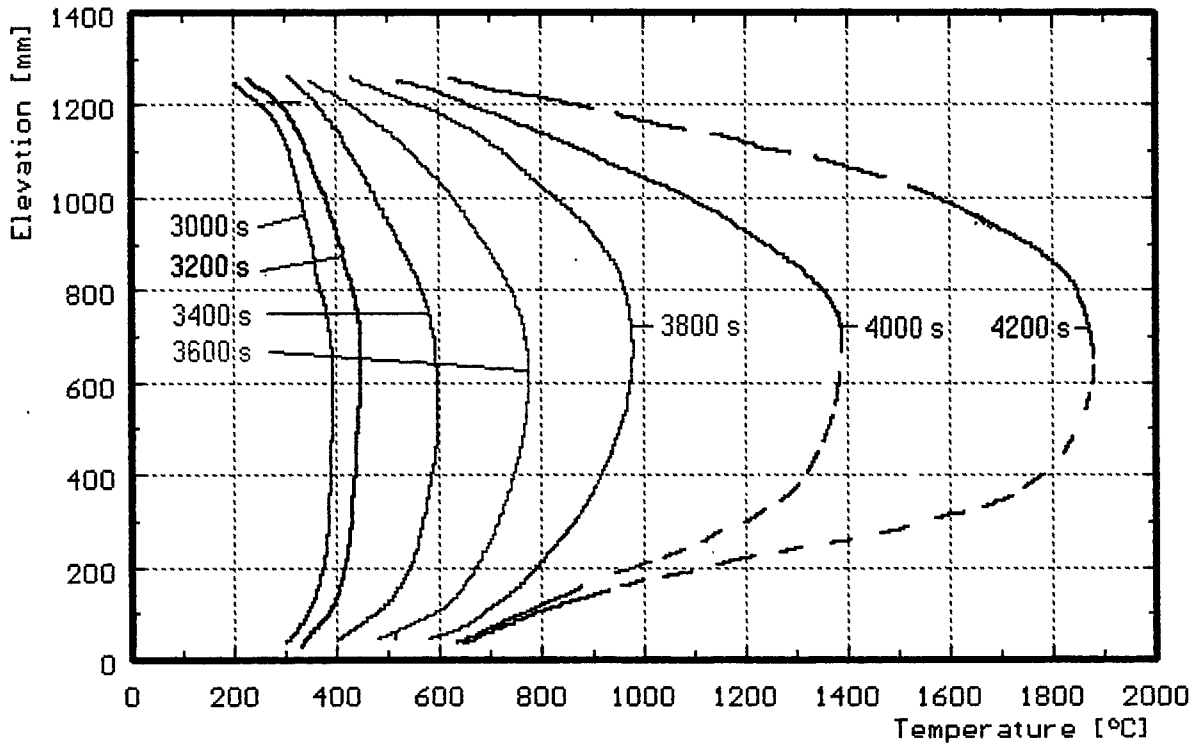

Fig. 54a: Vertical profiles of the best-estimate temperatures (CORA-18)

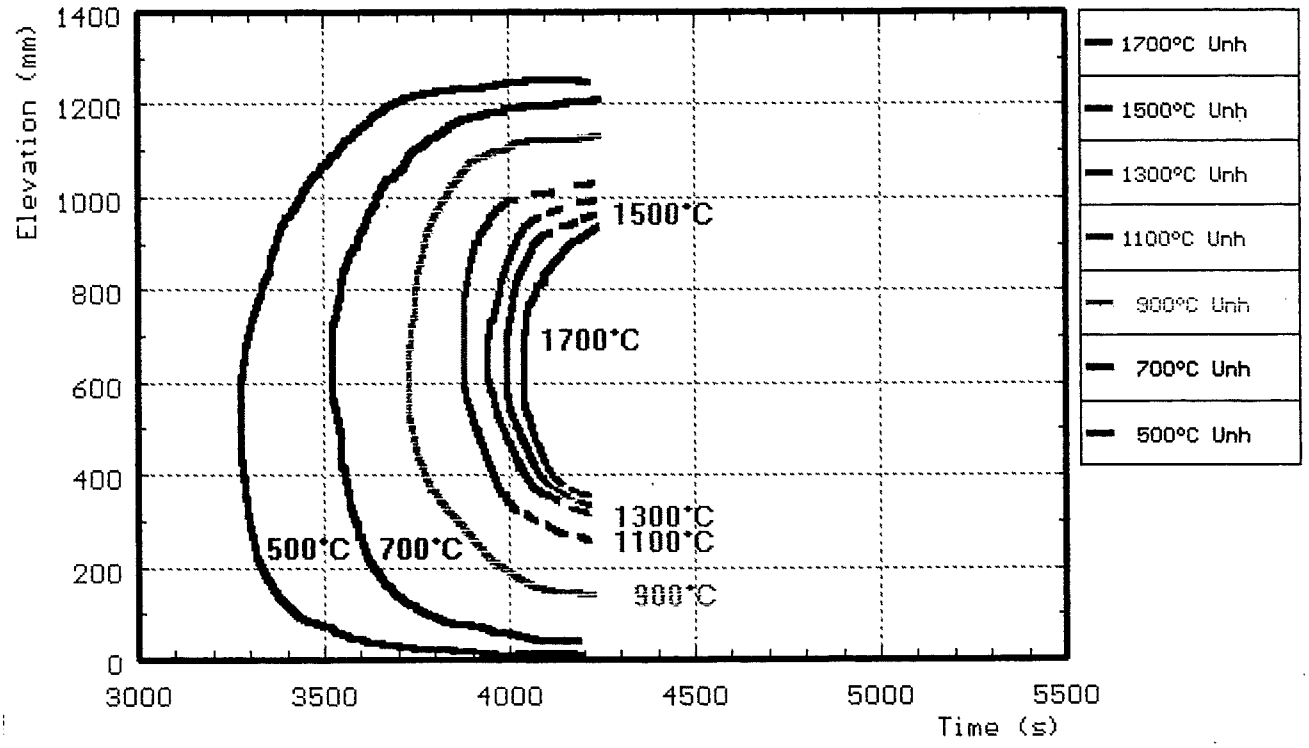

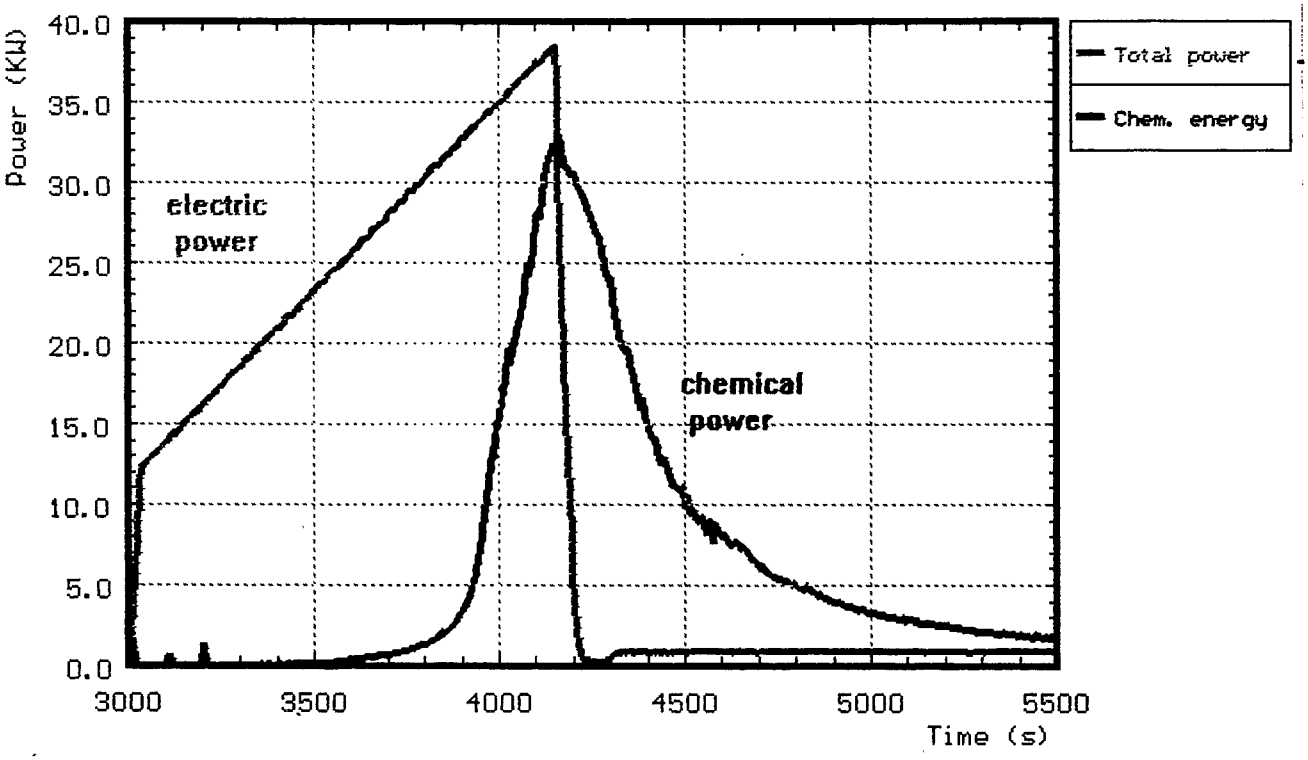

Fig. 54b: Iso-temperature plots of unheated rods in the transient phase compared to electrical and chemical power input (CORA-18)

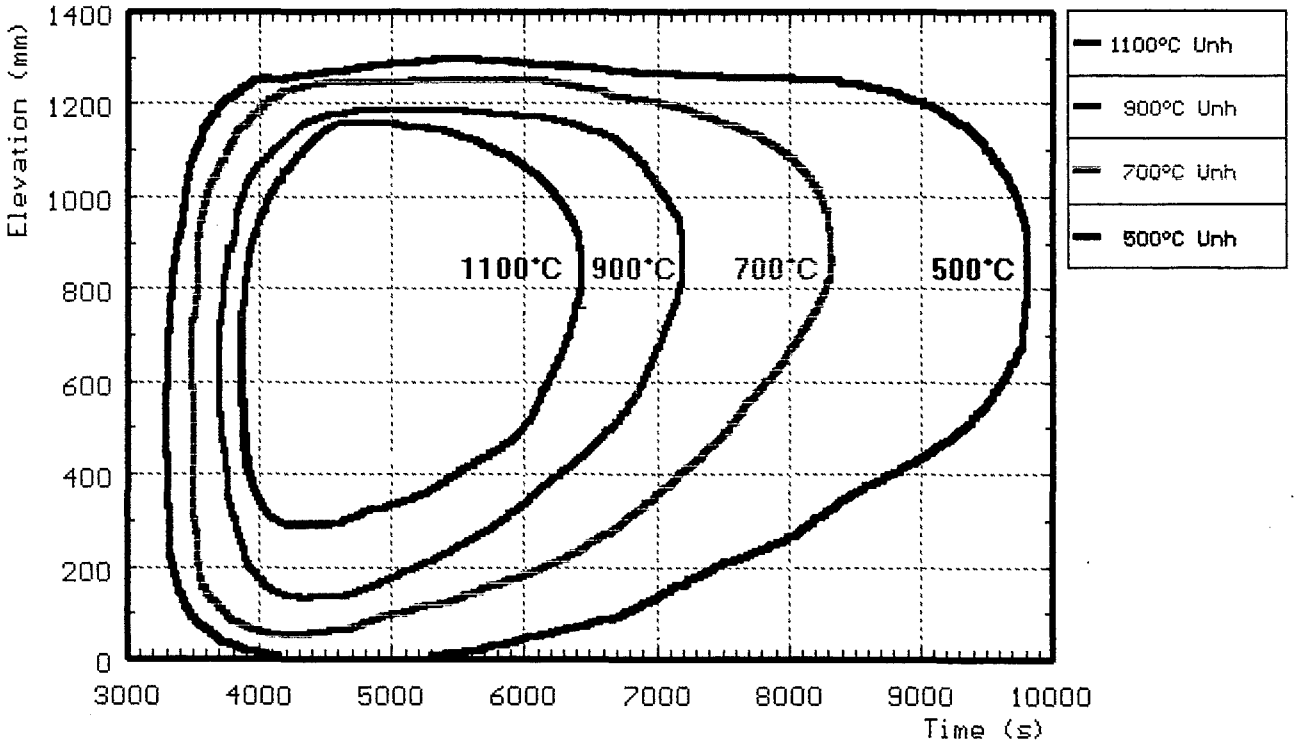

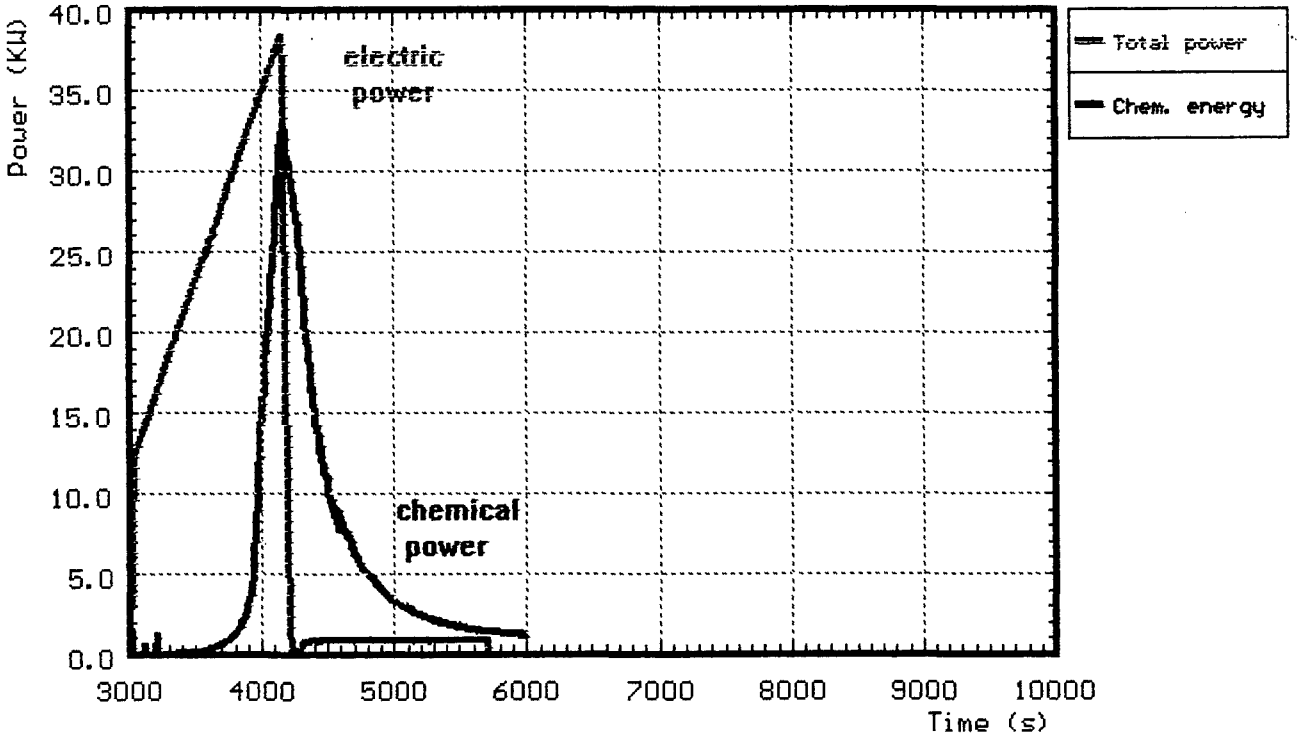

Fig. 54c: Iso-temperature plots of unheated rods for heatup and cooldown compared to electrical and chemical power input (CORA-18)

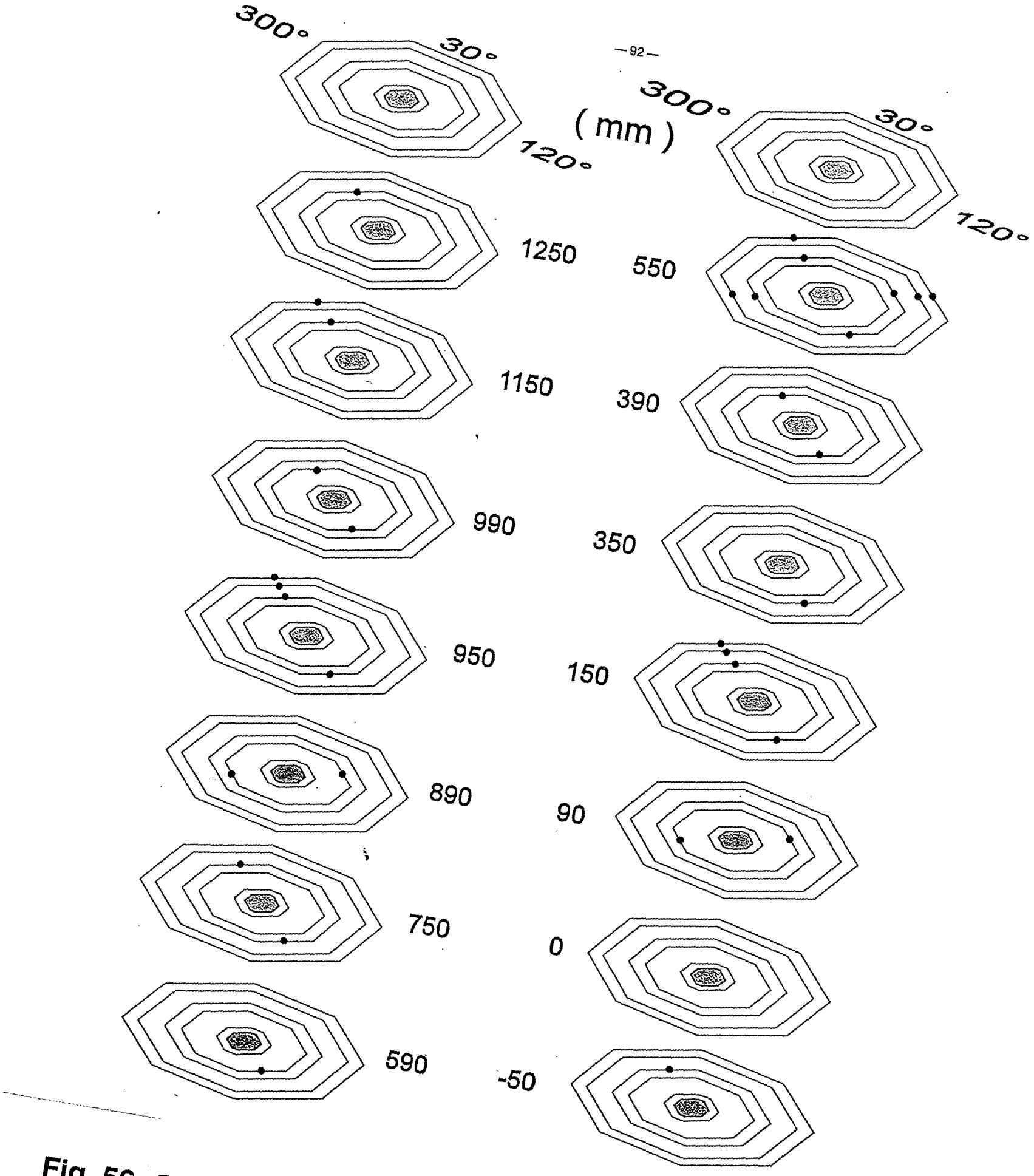

Fig. 56: CORA-18; Locations of thermocouples in the high-temperature shield

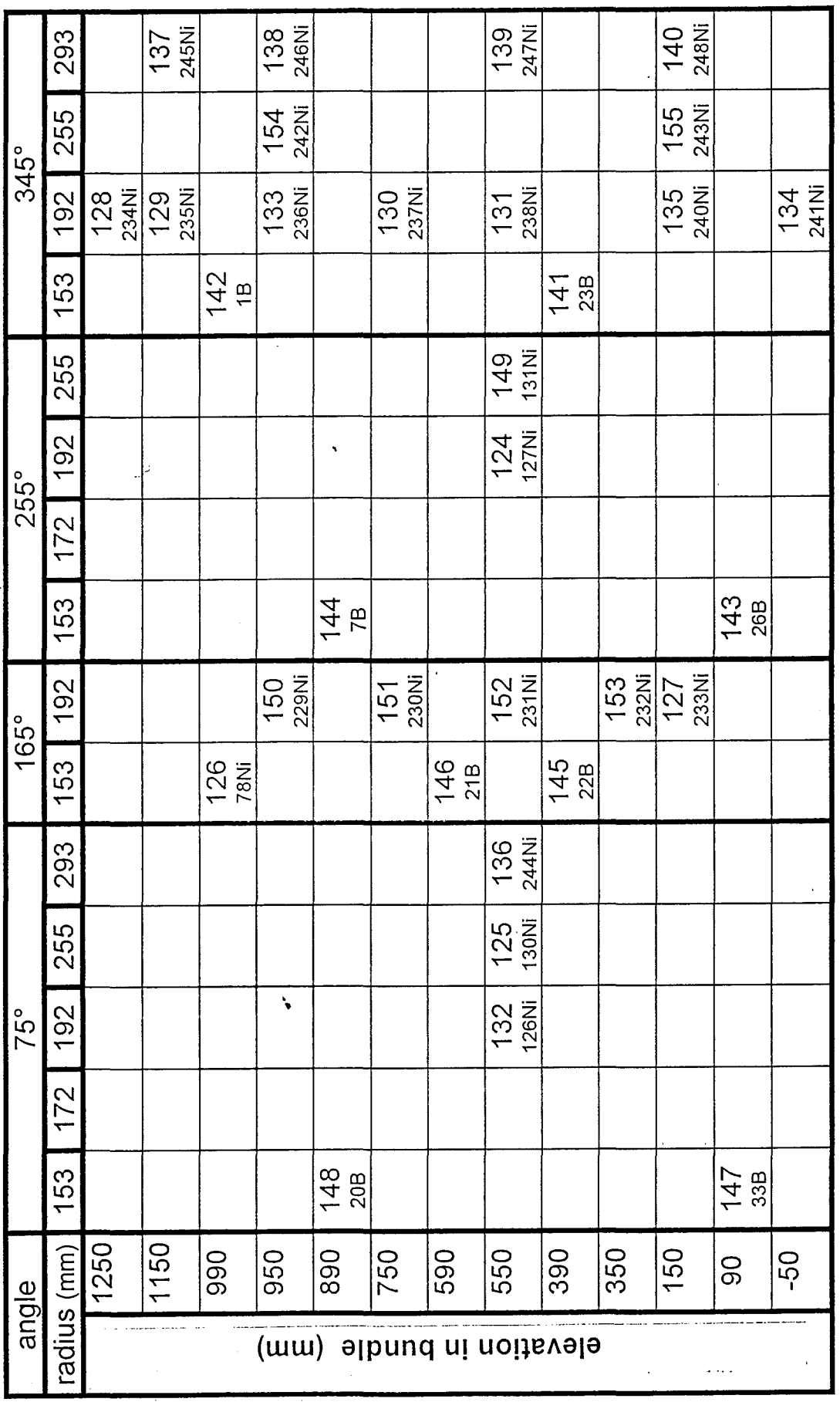

Fig. 57: CORA-18; Positions of thermocouples in the high-temperature shield

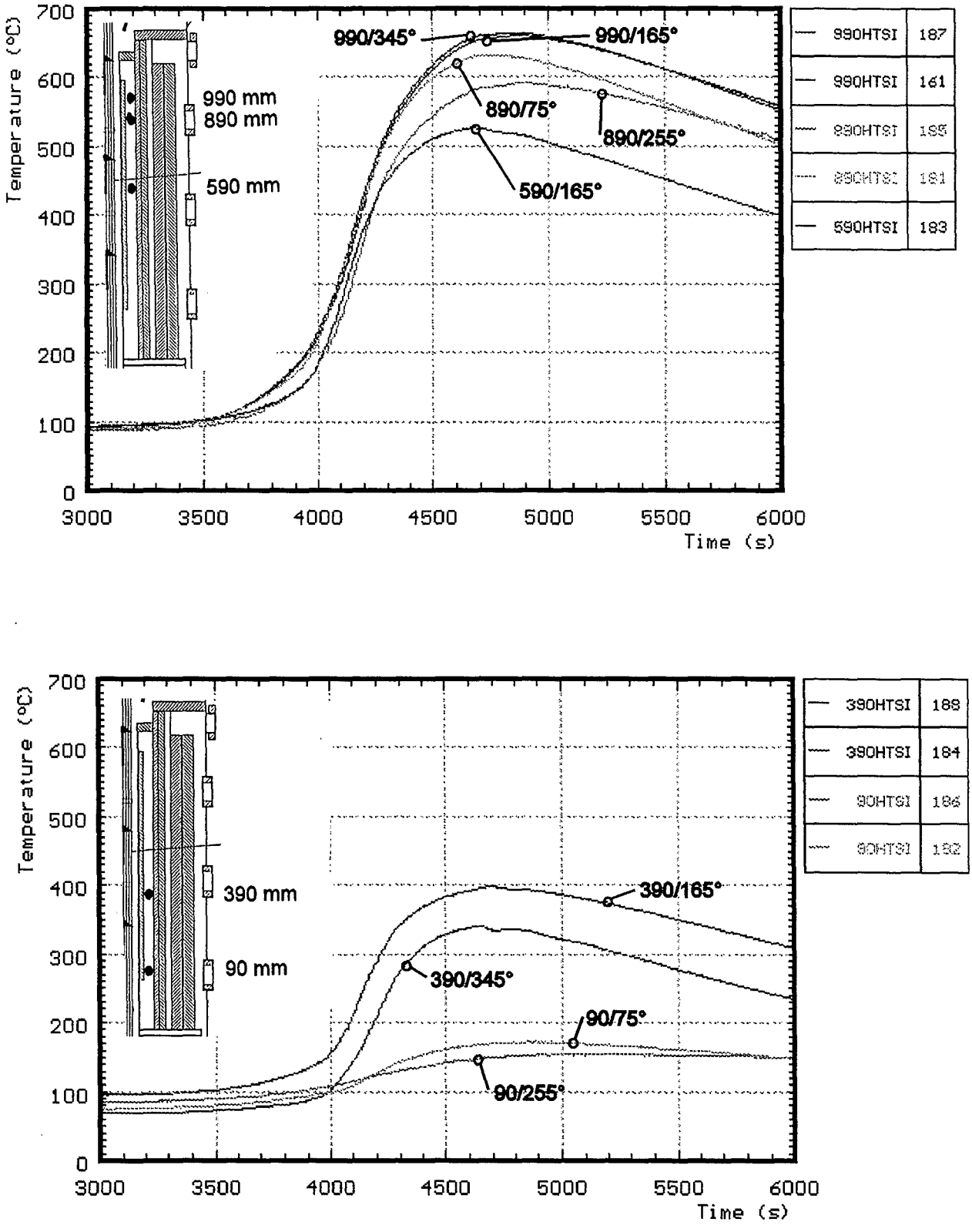

Fig. 58: CORA-18; Temperatures of HTS, inner surface at 153mm radius

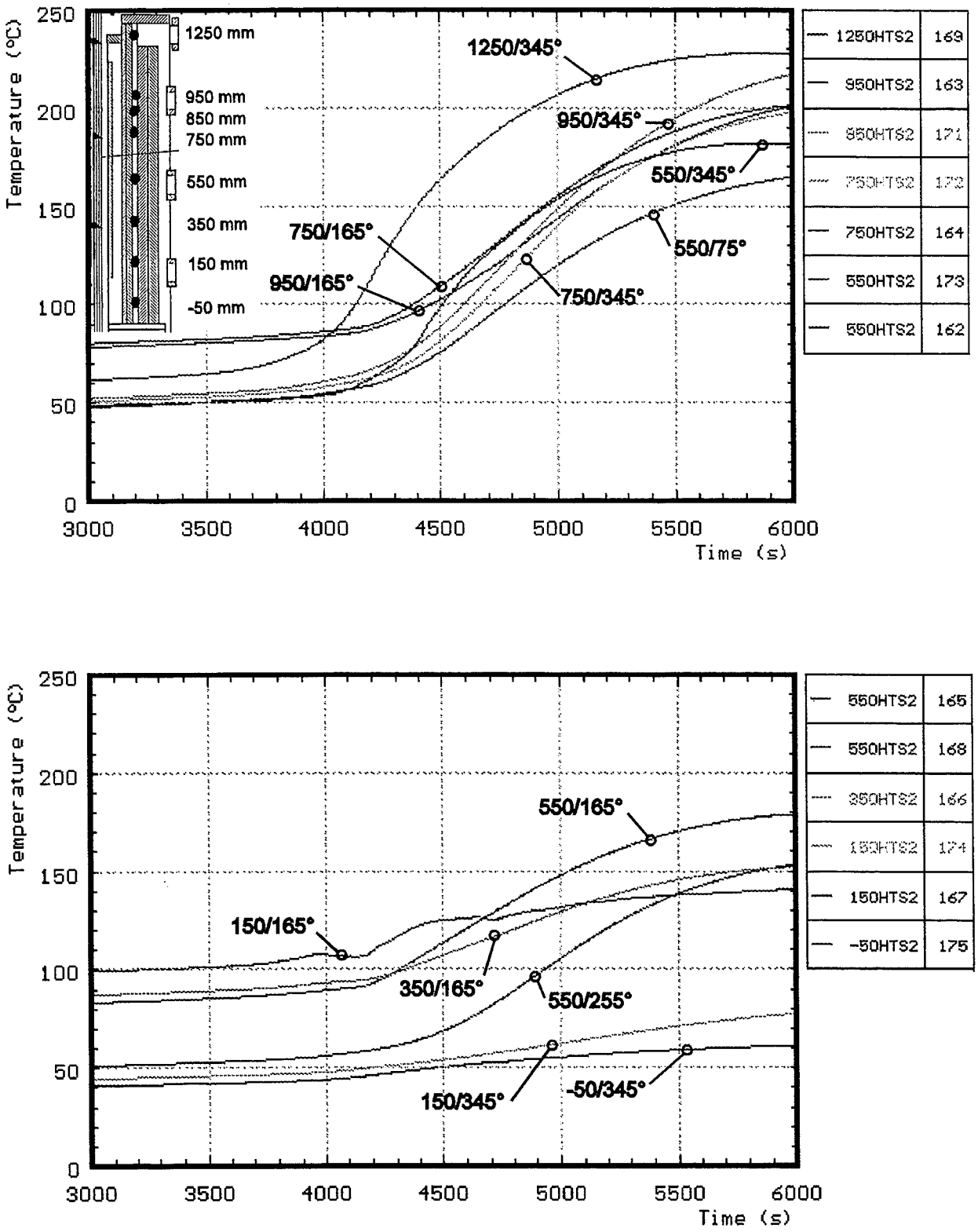

Fig. 59: CORA-18; Temperatures of HTS, Temperatures in HT-shield at 192mm radius

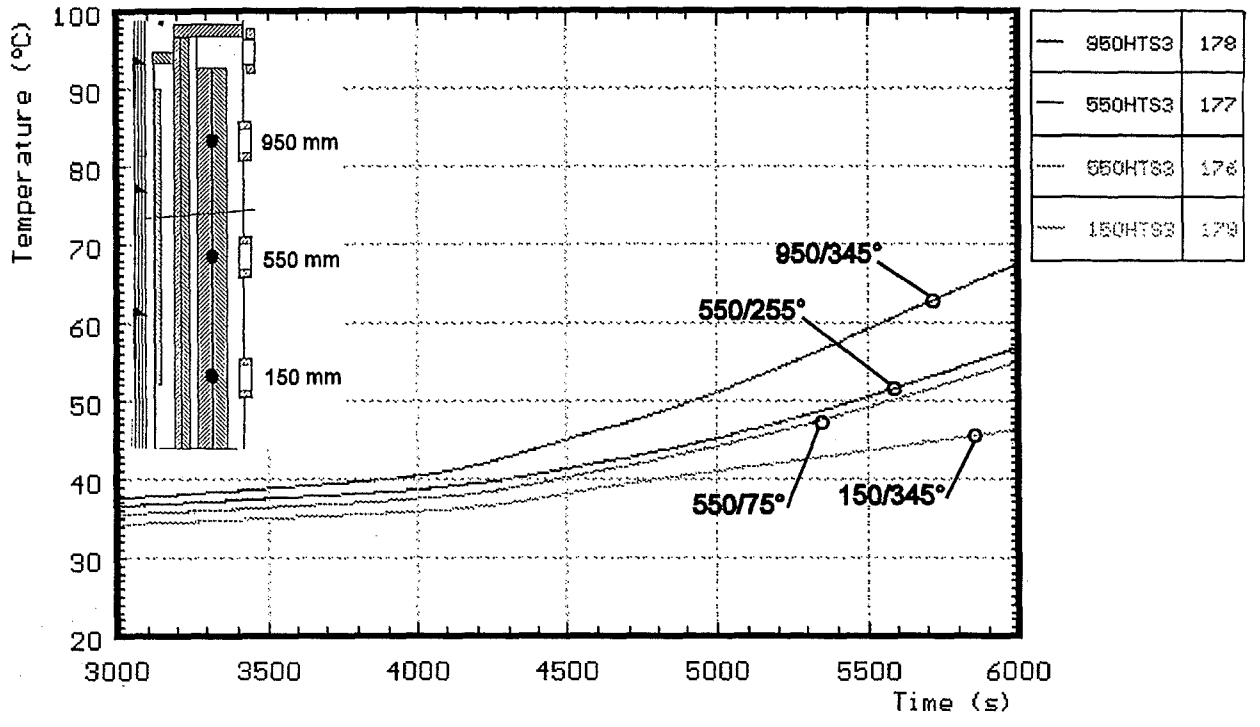

Fig. 60: CORA-18; Temperatures of HTS, Temperatures in HT shield at 255mm radius

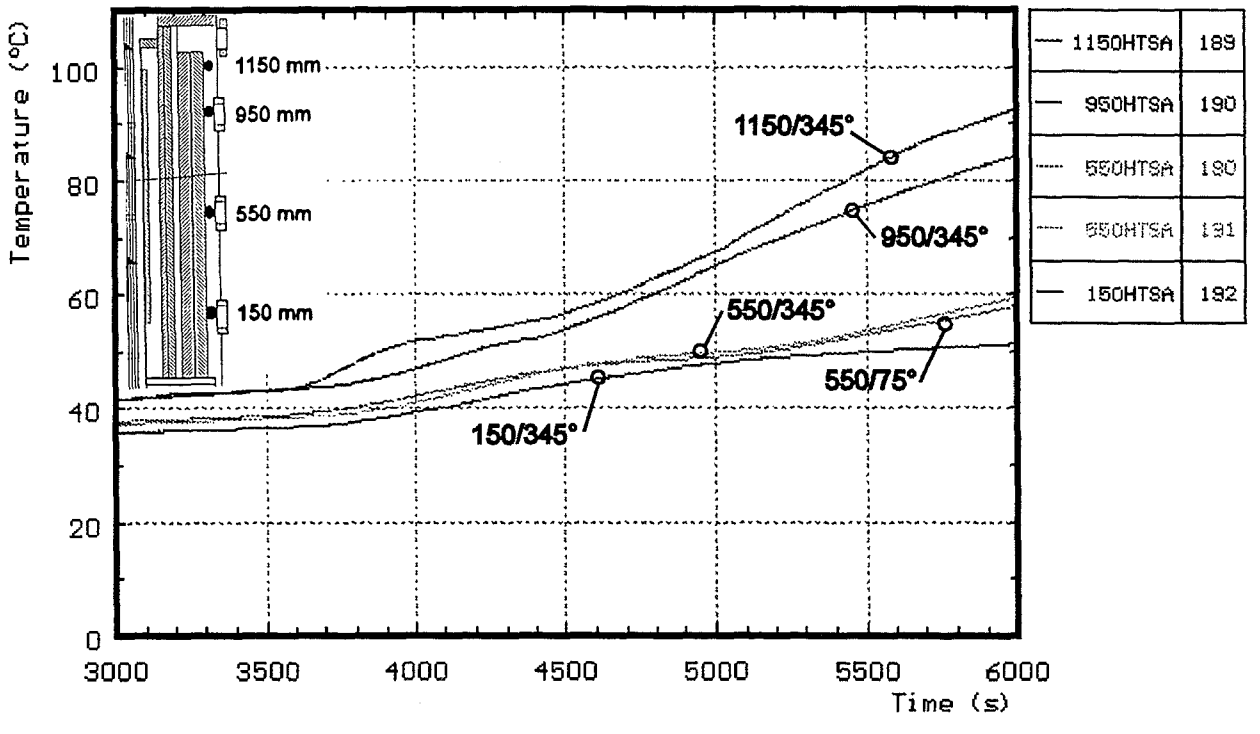

Fig. 61: CORA-18; Temperatures of HTS, outer surface at 293 mm radius

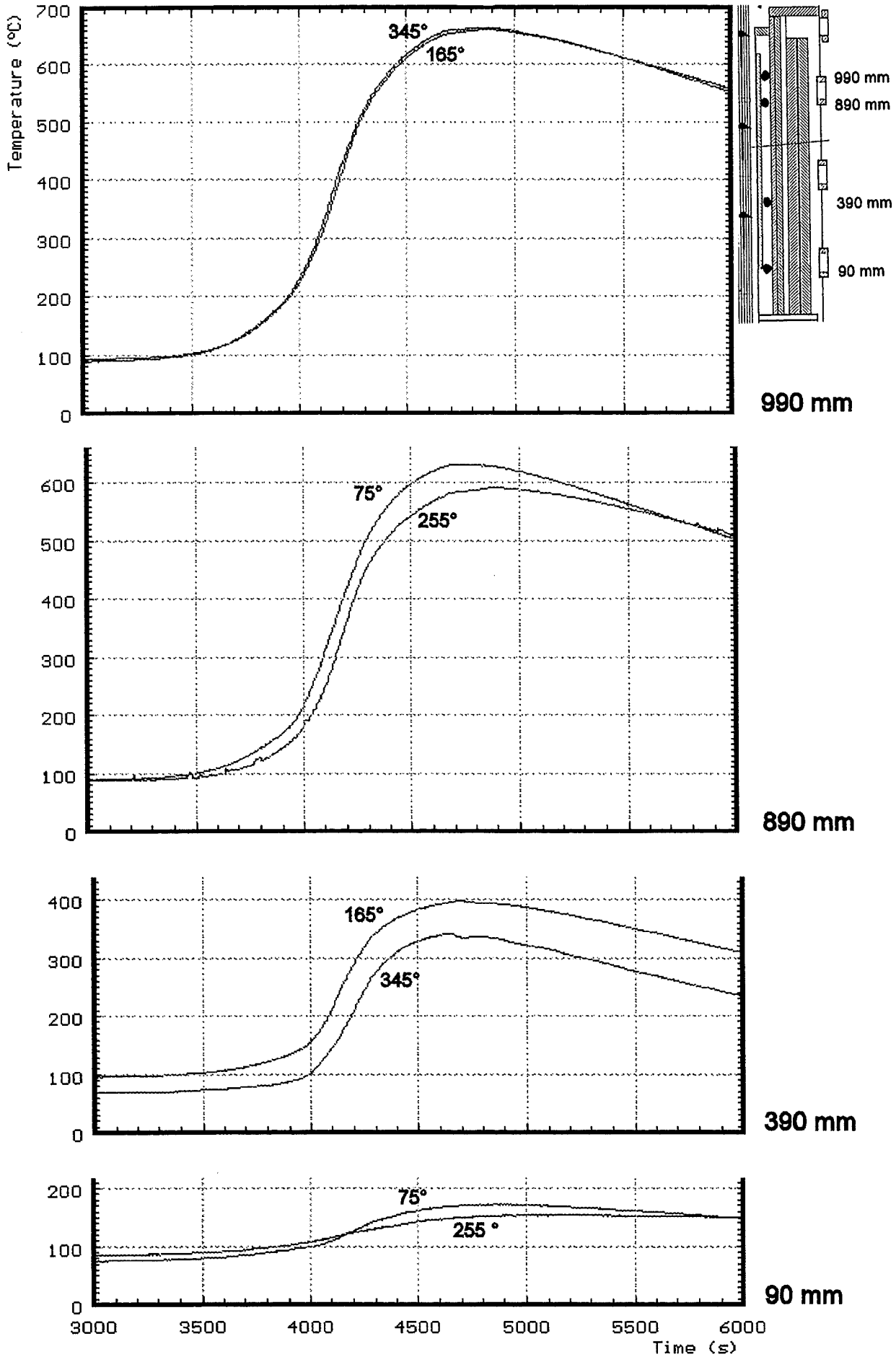

Fig. 62: Temperatures of HTS, Comparsion on inner surface at 153 mm radius

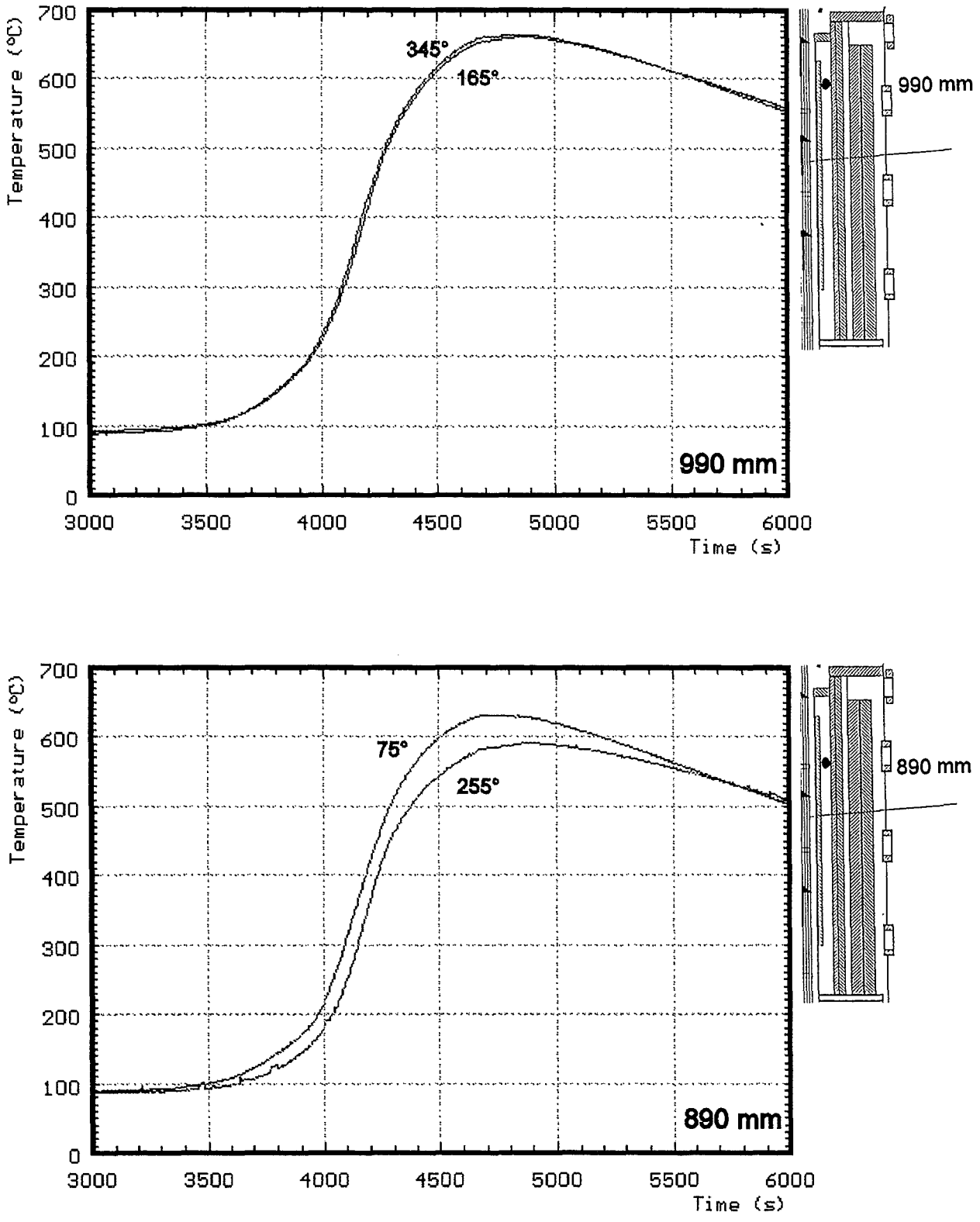

Fig. 63: CORA-18; Temperatures of HTS, Comparsion on inner surface at 153 mm radius, 990 mm and 890 mm elevation

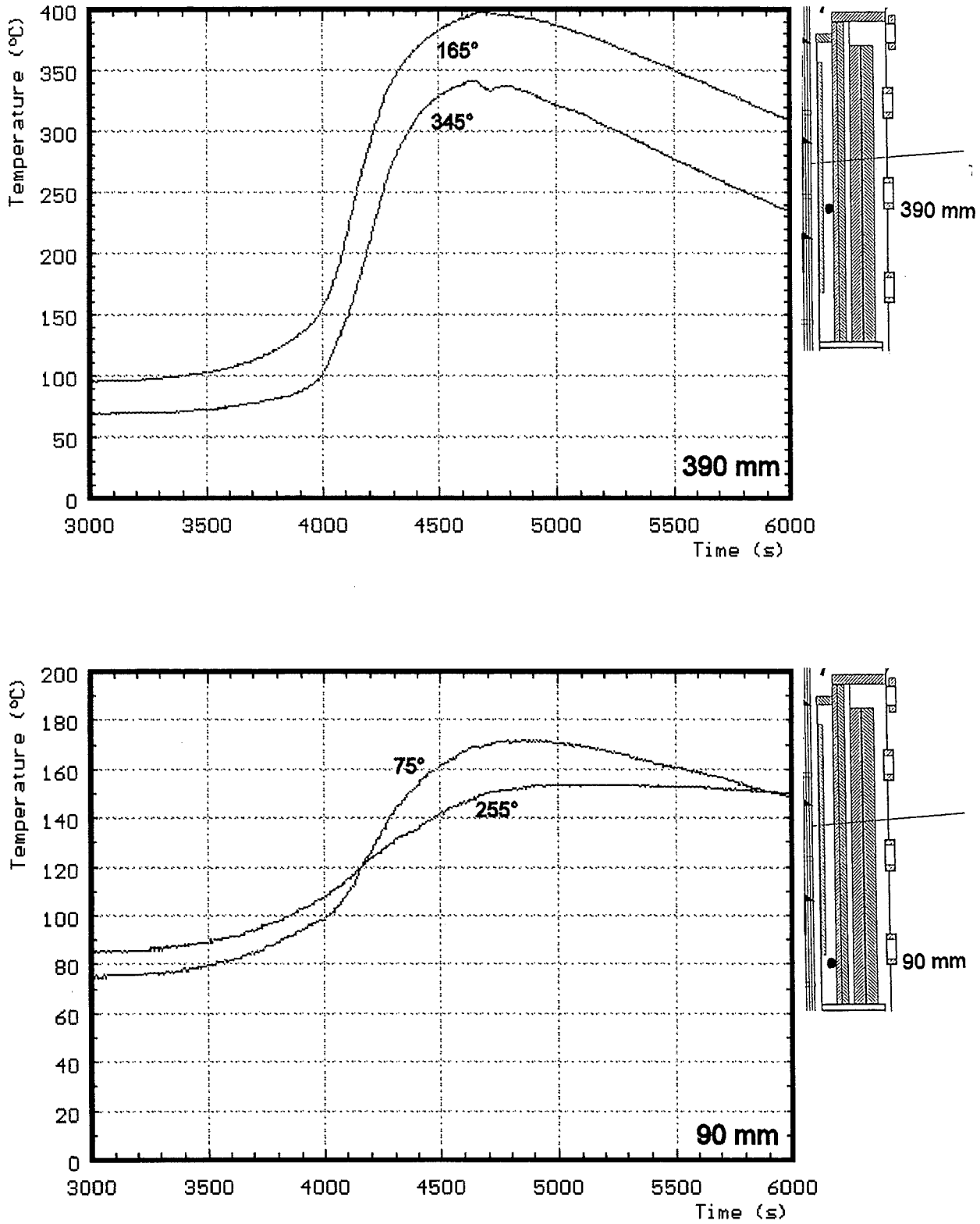

Fig. 64: CORA-18; Temperatures of HTS, Comparsion on inner surface at 153 mm radius, 390 mm and 90 mm elevation

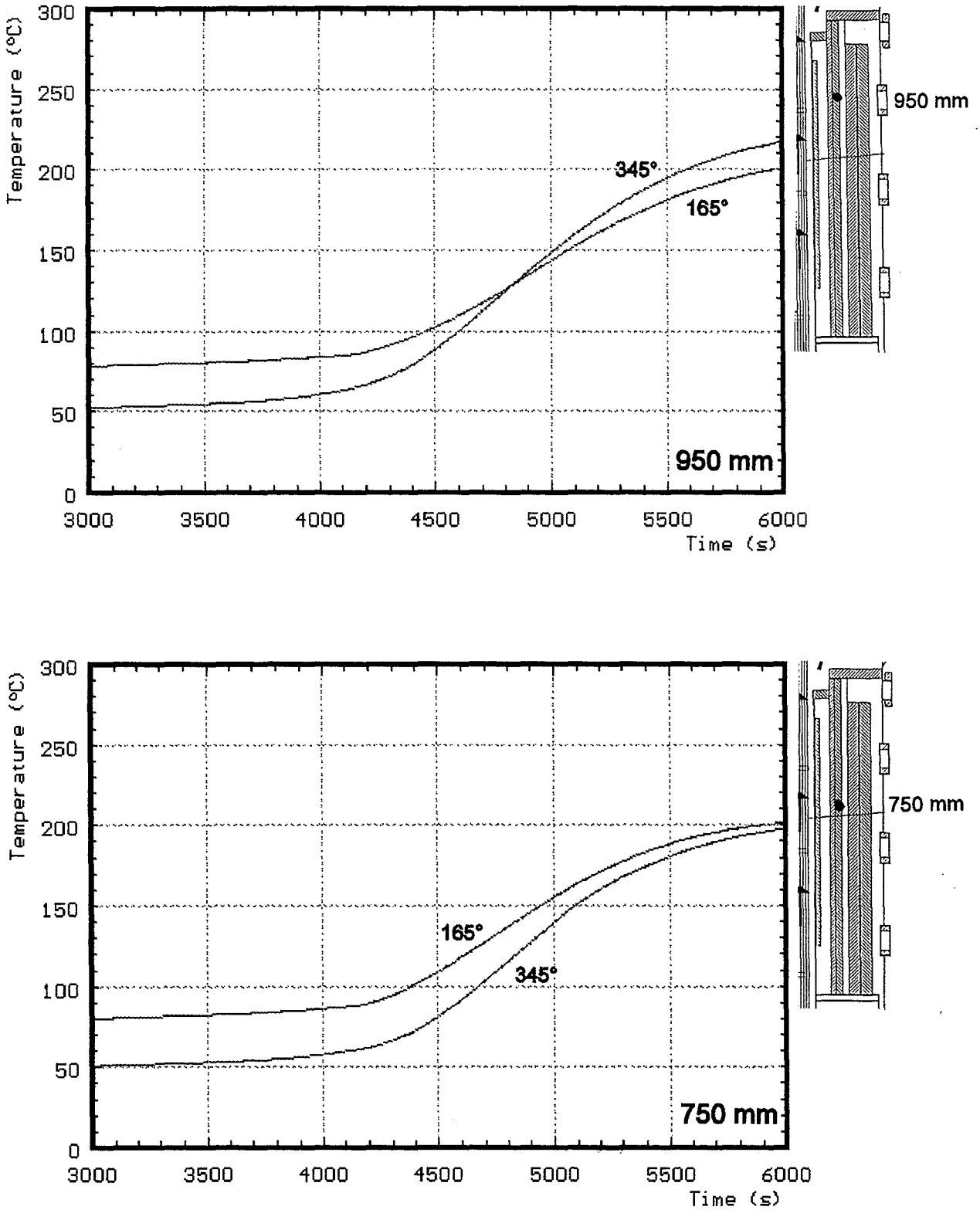

Fig. 65: CORA-18; Temperatures of HTS, Comparsion on inner surface at 192 mm radius, 950 mm and 750 mm elevation

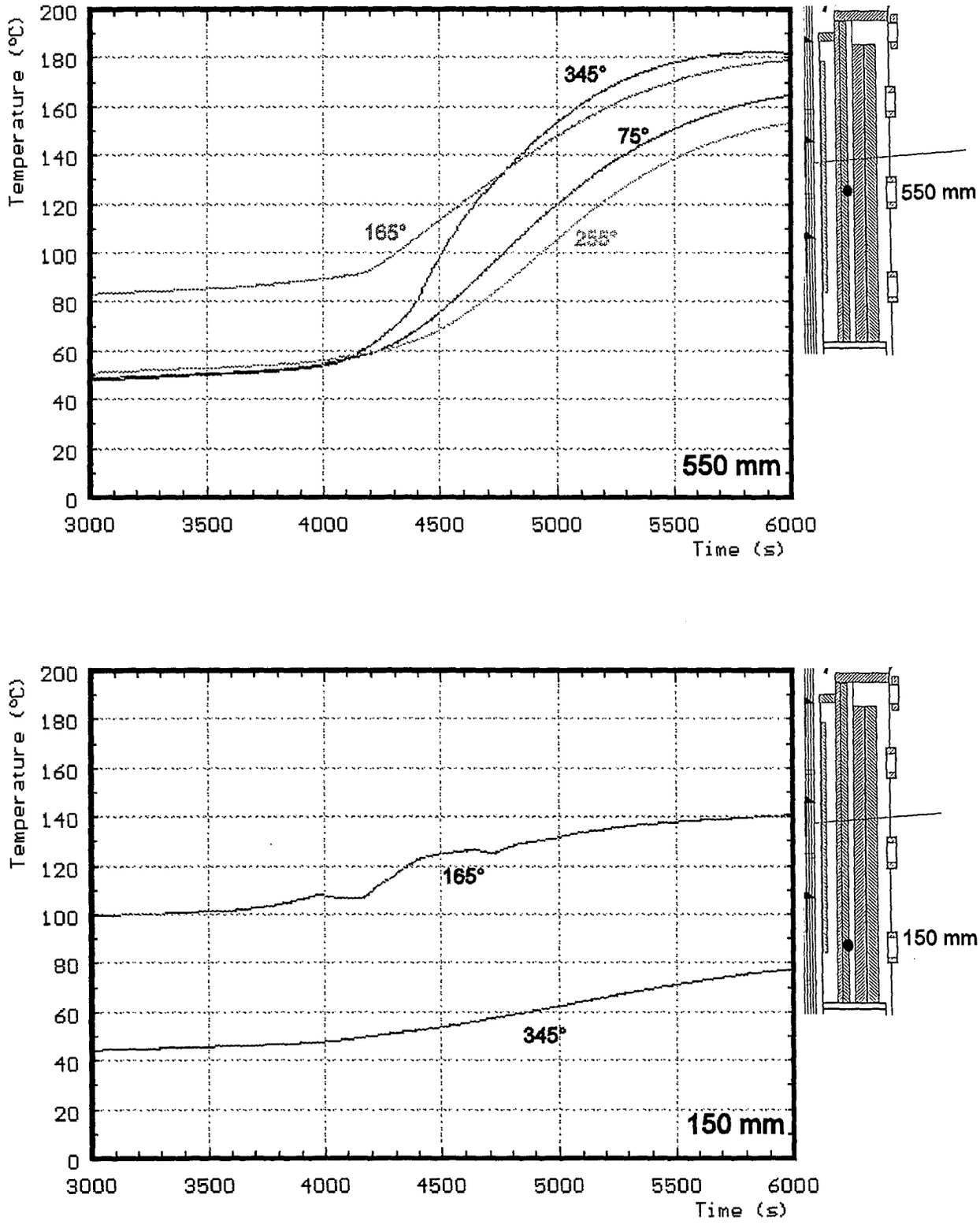

Fig. 66: CORA-18; Temperatures of HTS, Comparsion on inner surface at 192 mm radius, 550 mm and 150 mm elevation

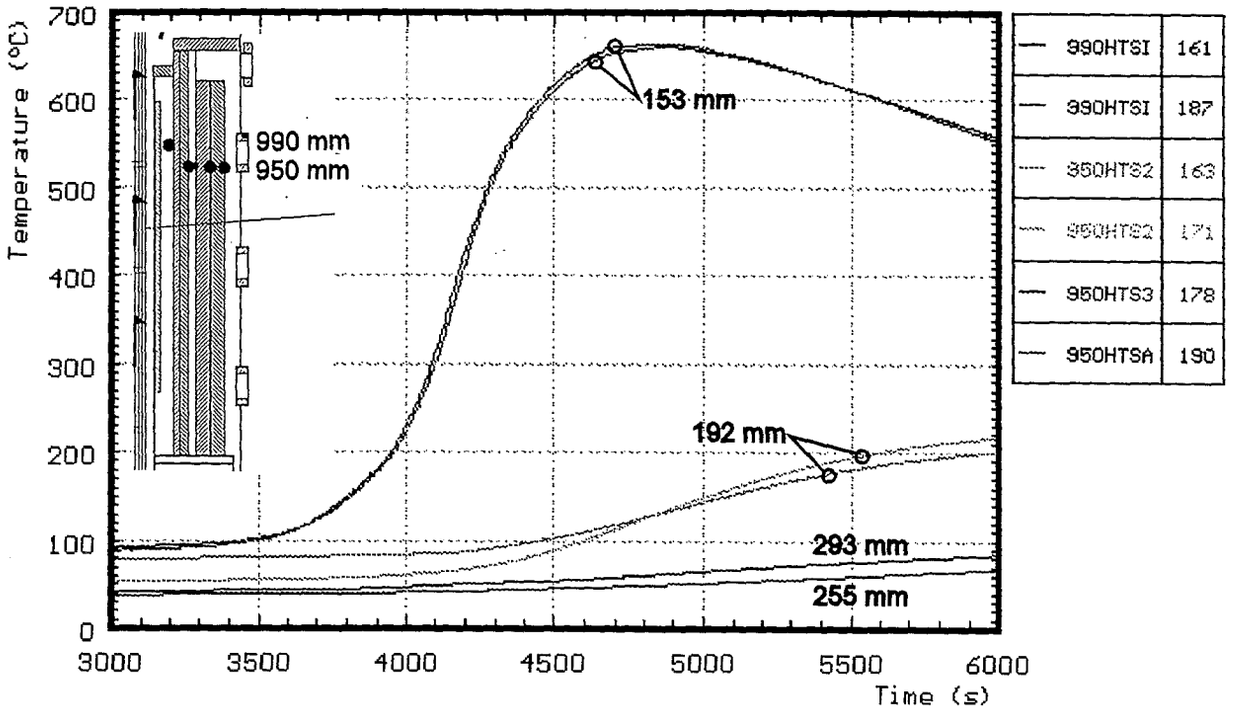

Fig. 67: CORA-18; Temperatures of HTS, Radial dependence at about 950 mm elevation

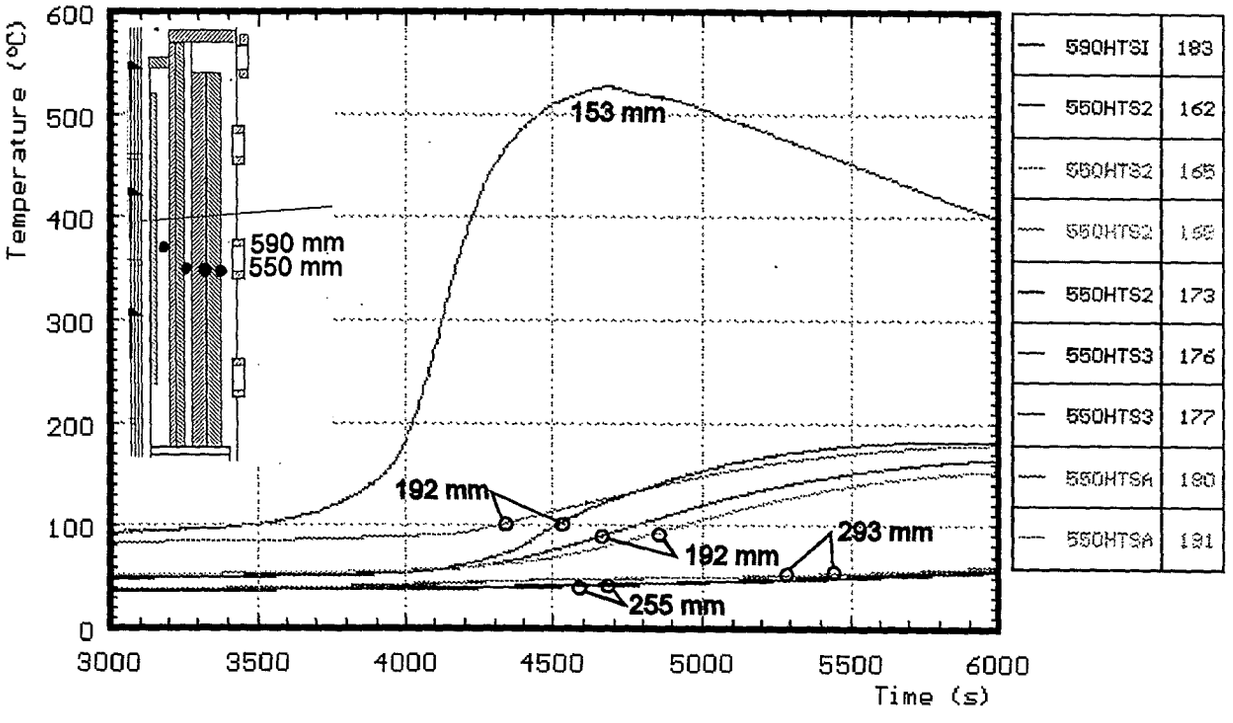

Fig. 68: CORA-18; Temperatures of HTS, Radial dependence at about 550 mm elevation

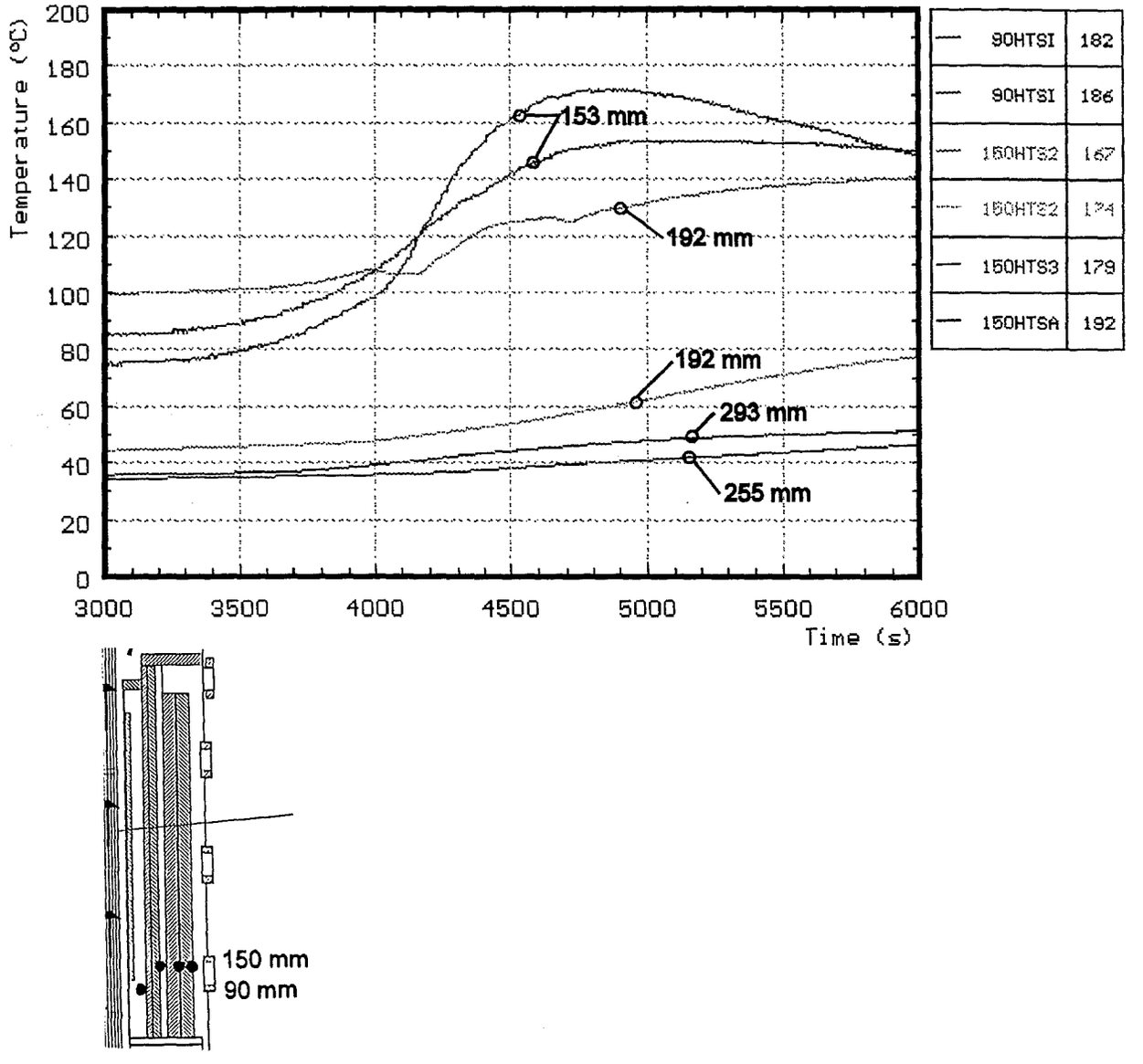

Fig. 69: CORA-18; Temperatures of HTS, Radial dependenc at about 100 mm elevation

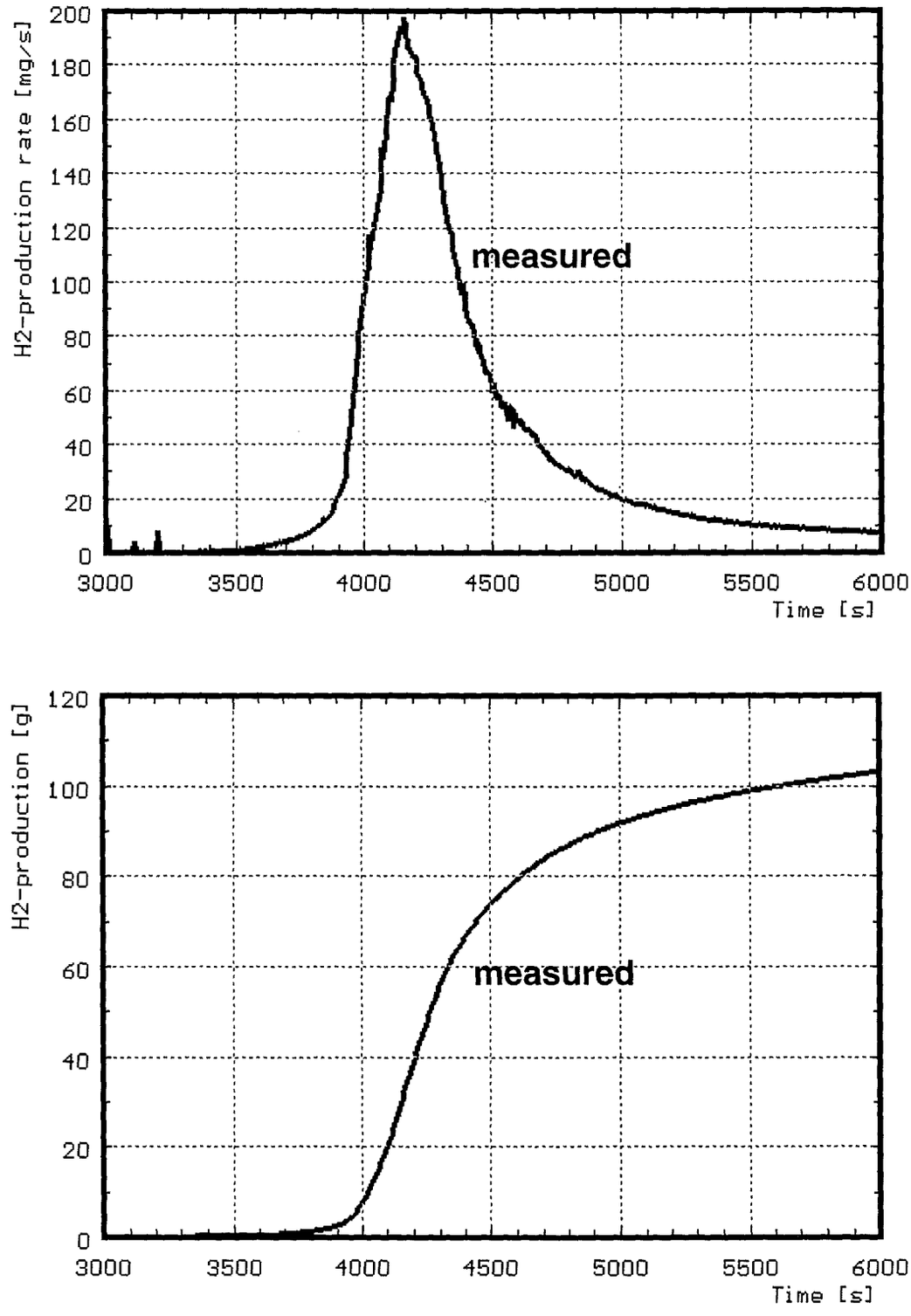

Fig. 70: CORA-18; Measured hydrogen production (uncorrected values); production rate (top) and integrations values (bottom)

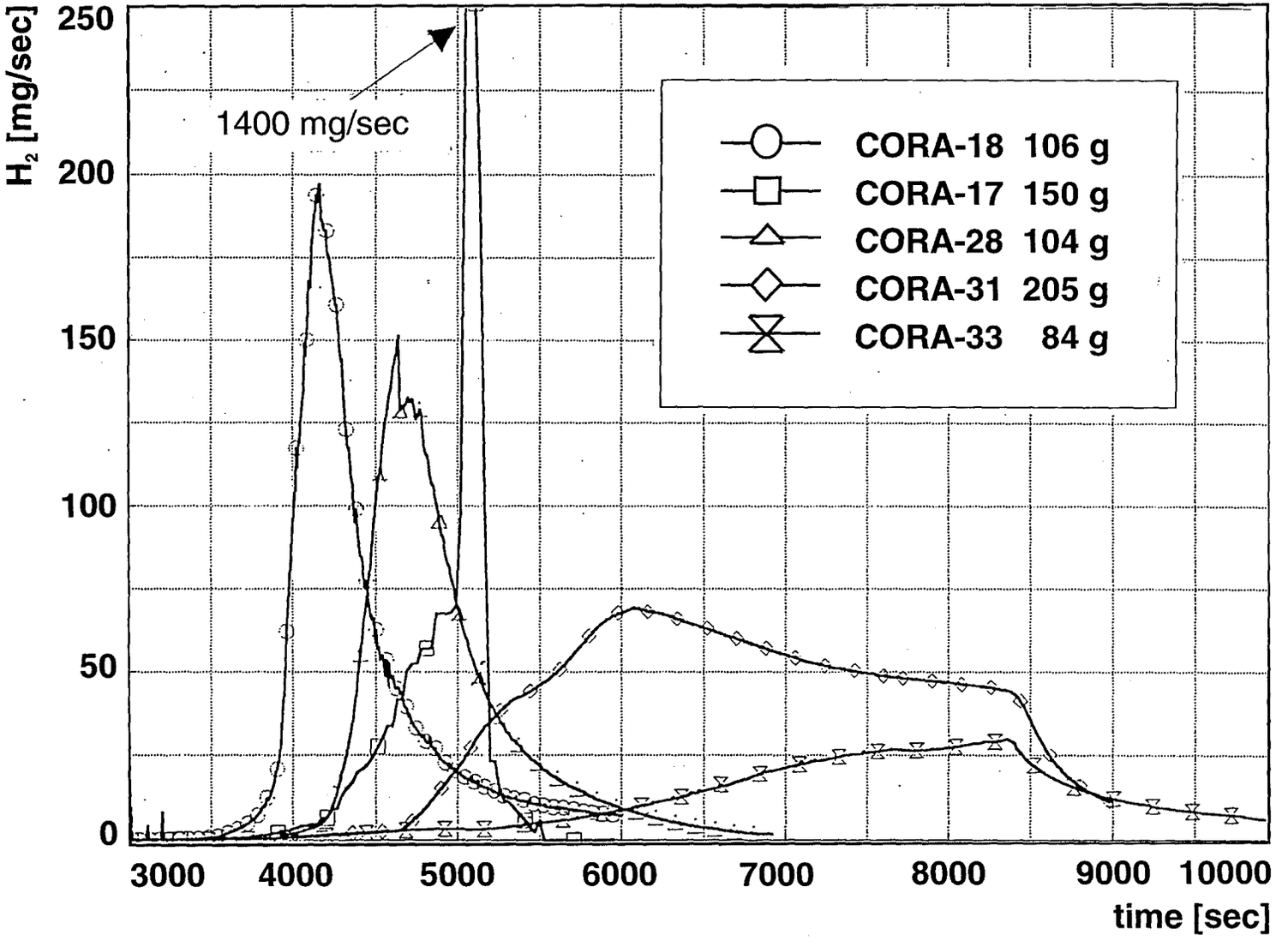

Fig. 71: Comparison of hydrogen production rate of test CORA-18 to the other BWR CORA-tests

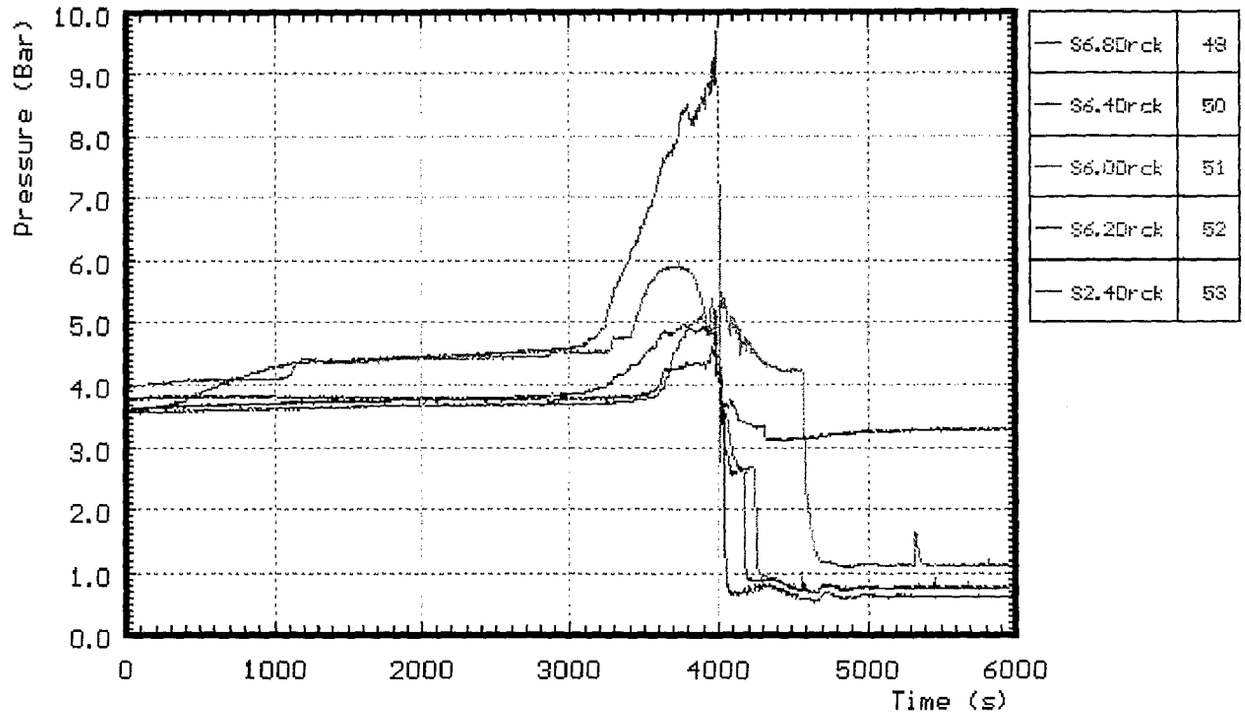

Fig. 73: CORA-18; Internal pressure of fuel rod simulators

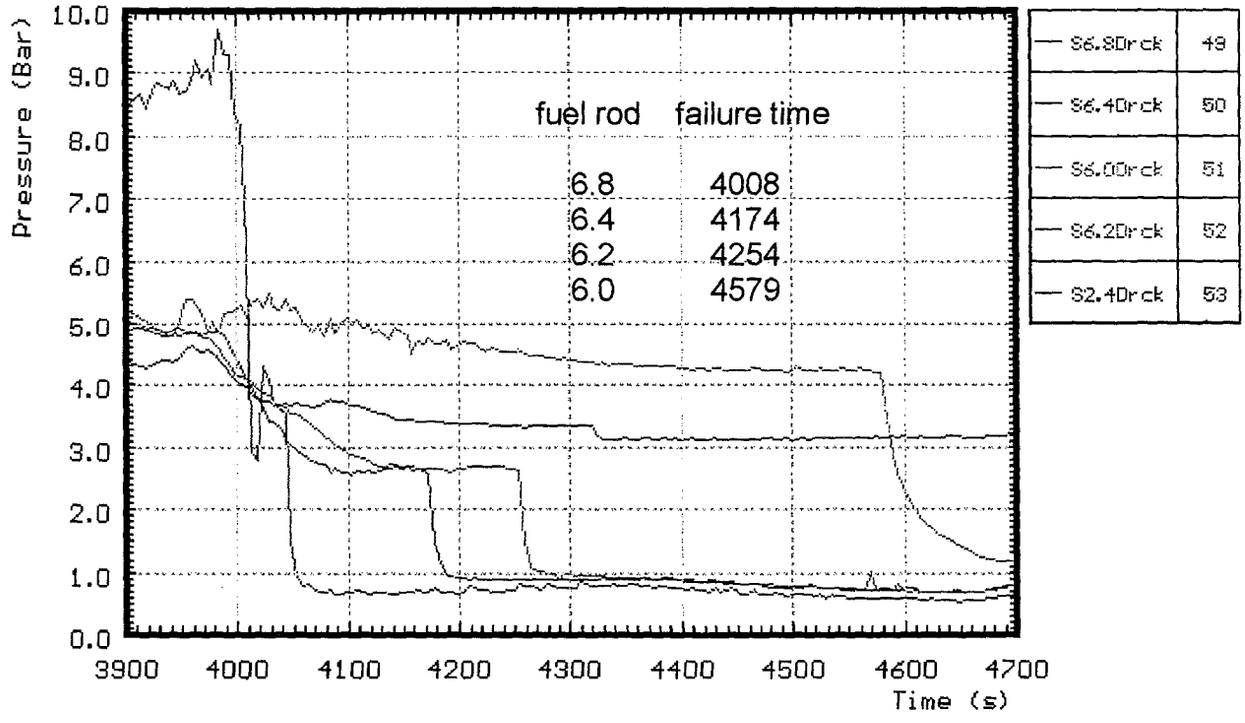

Fig. 74: CORA-18; Measurement of failure time by pressure loss determination

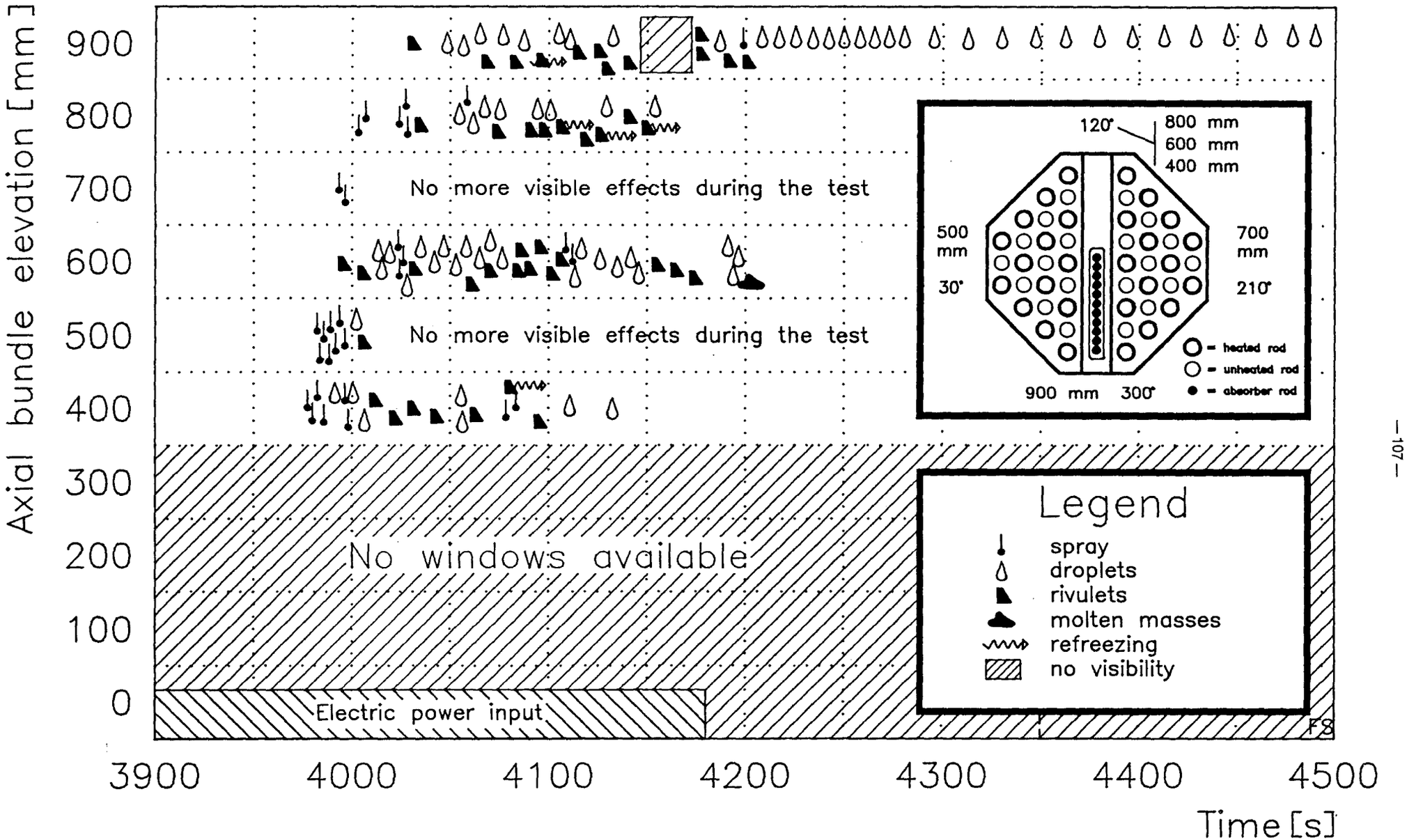

Fig. 76: CORA-18; Melt movement as seen by the video system

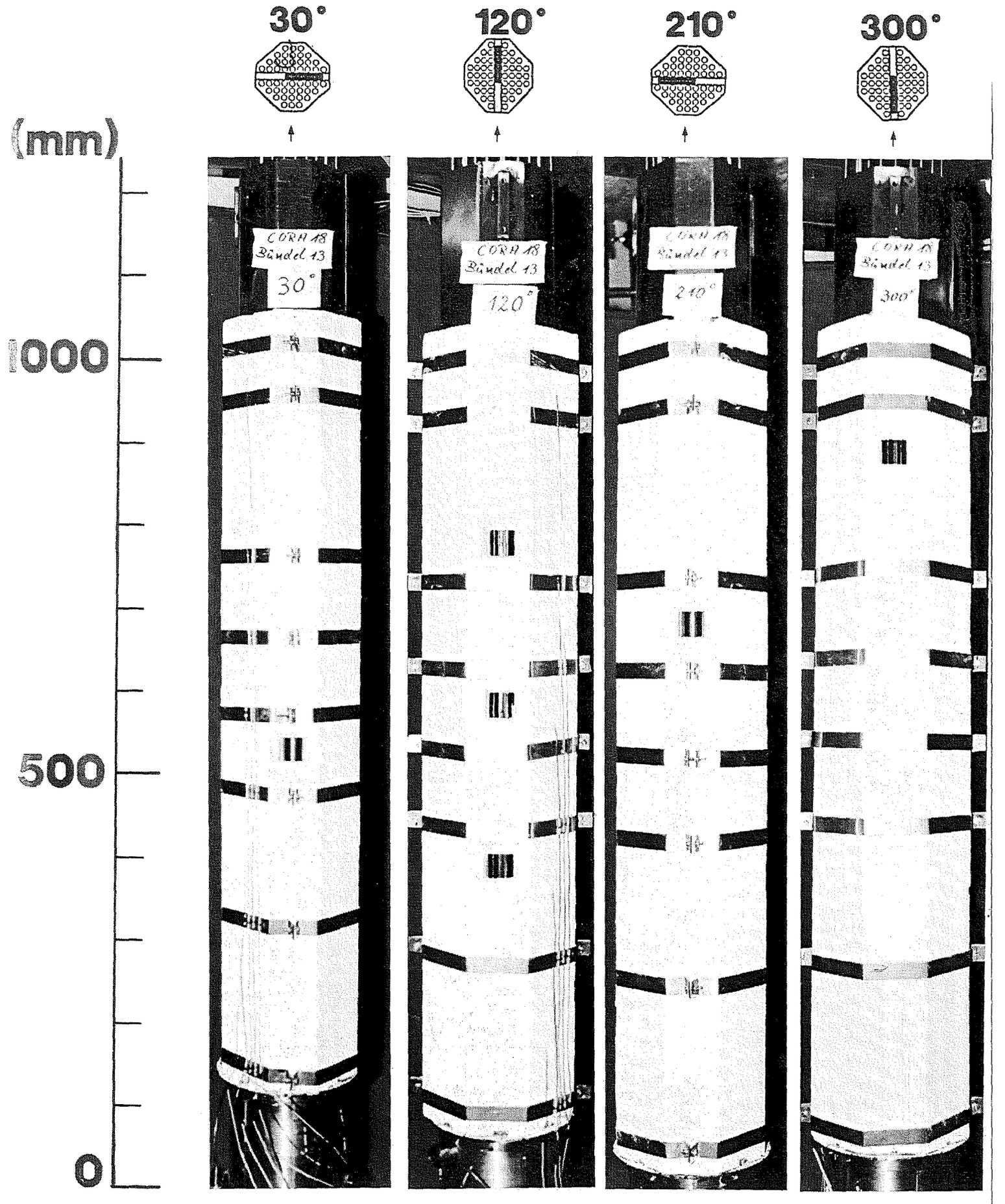

Fig. 80: CORA-18; bundle with insulation before test

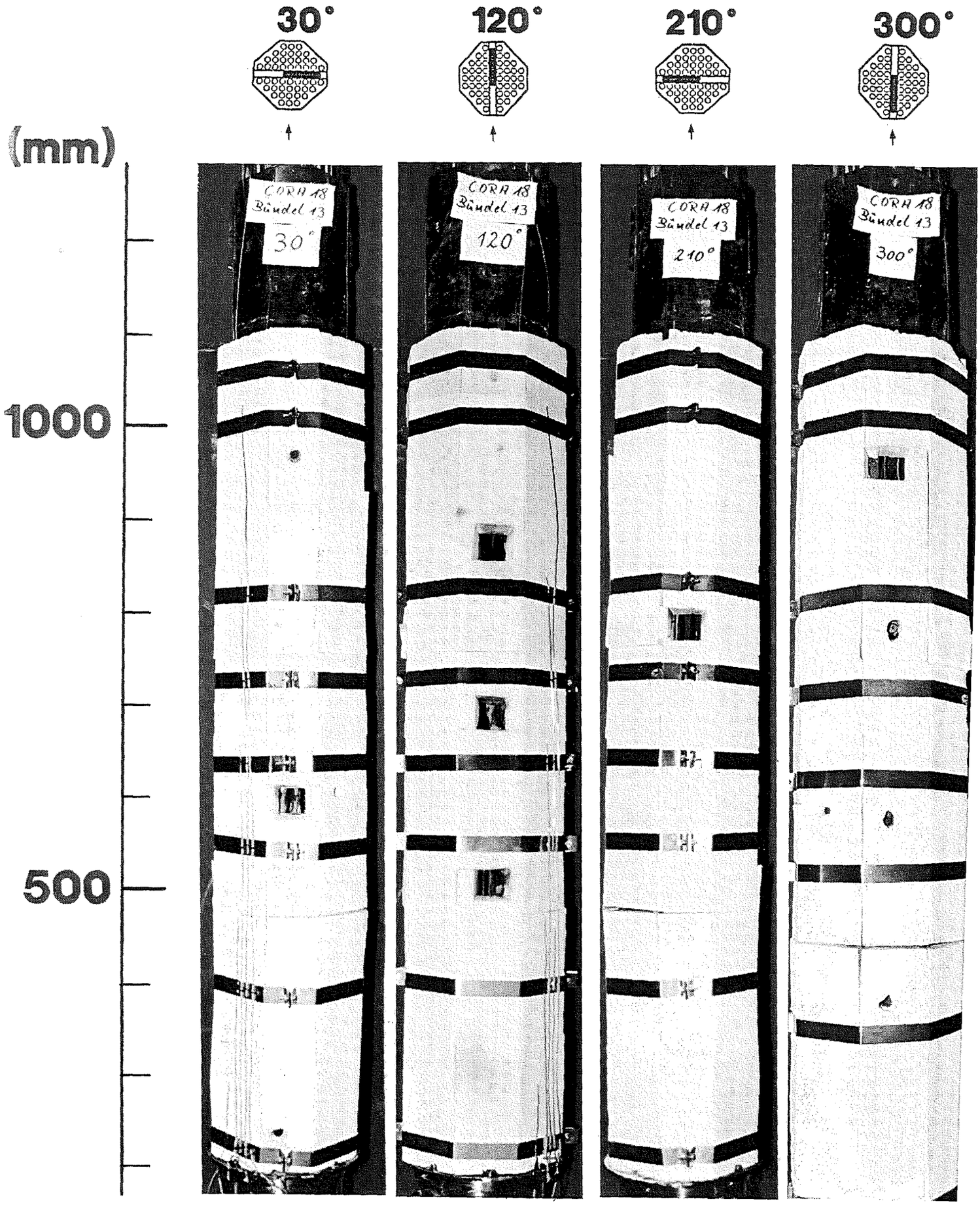

Fig. 81: CORA-18; posttest appearence of the bundle with shroud and insulation

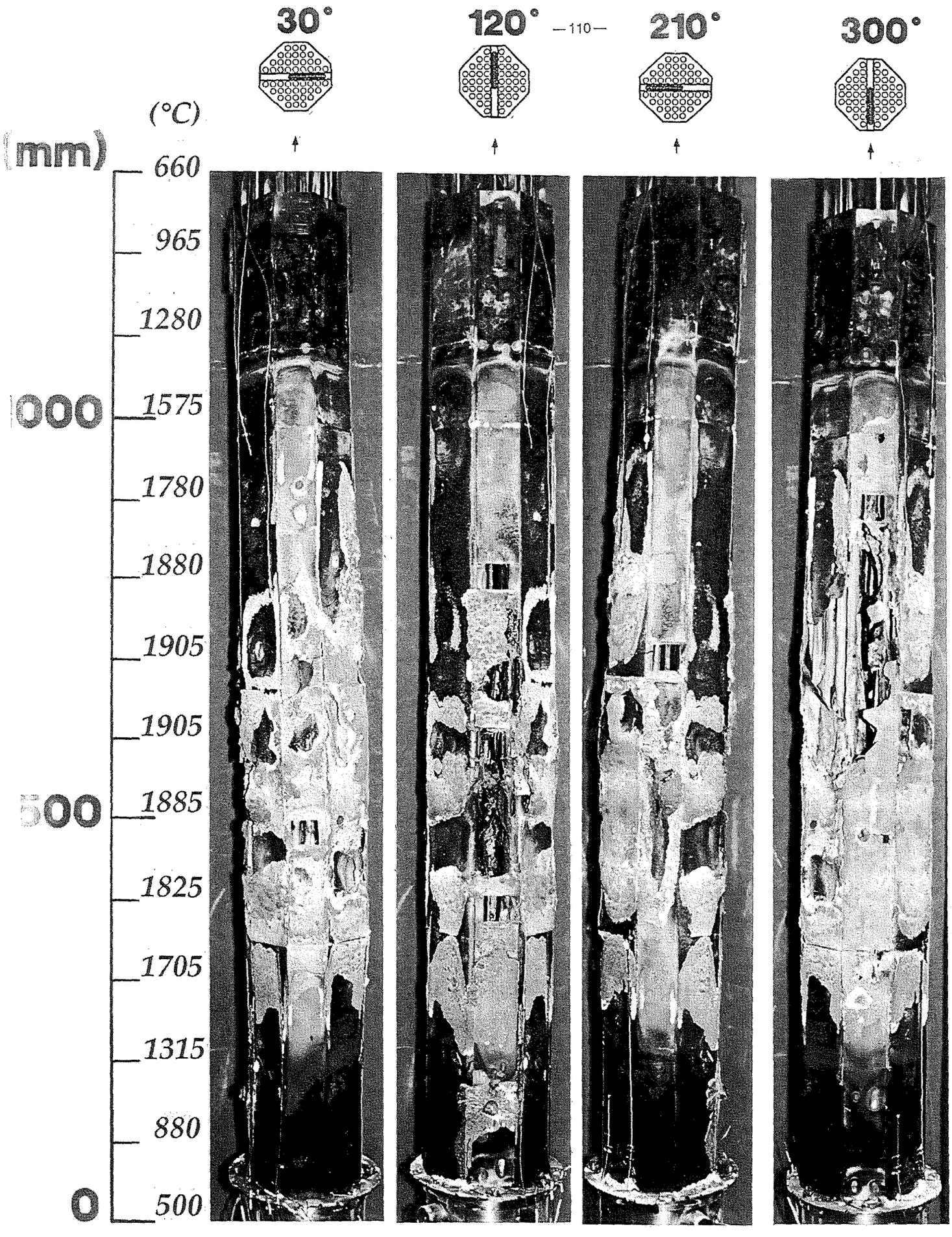

Fig. 82: CORA-18; posttest appearence of the shroud after removal of the insulation

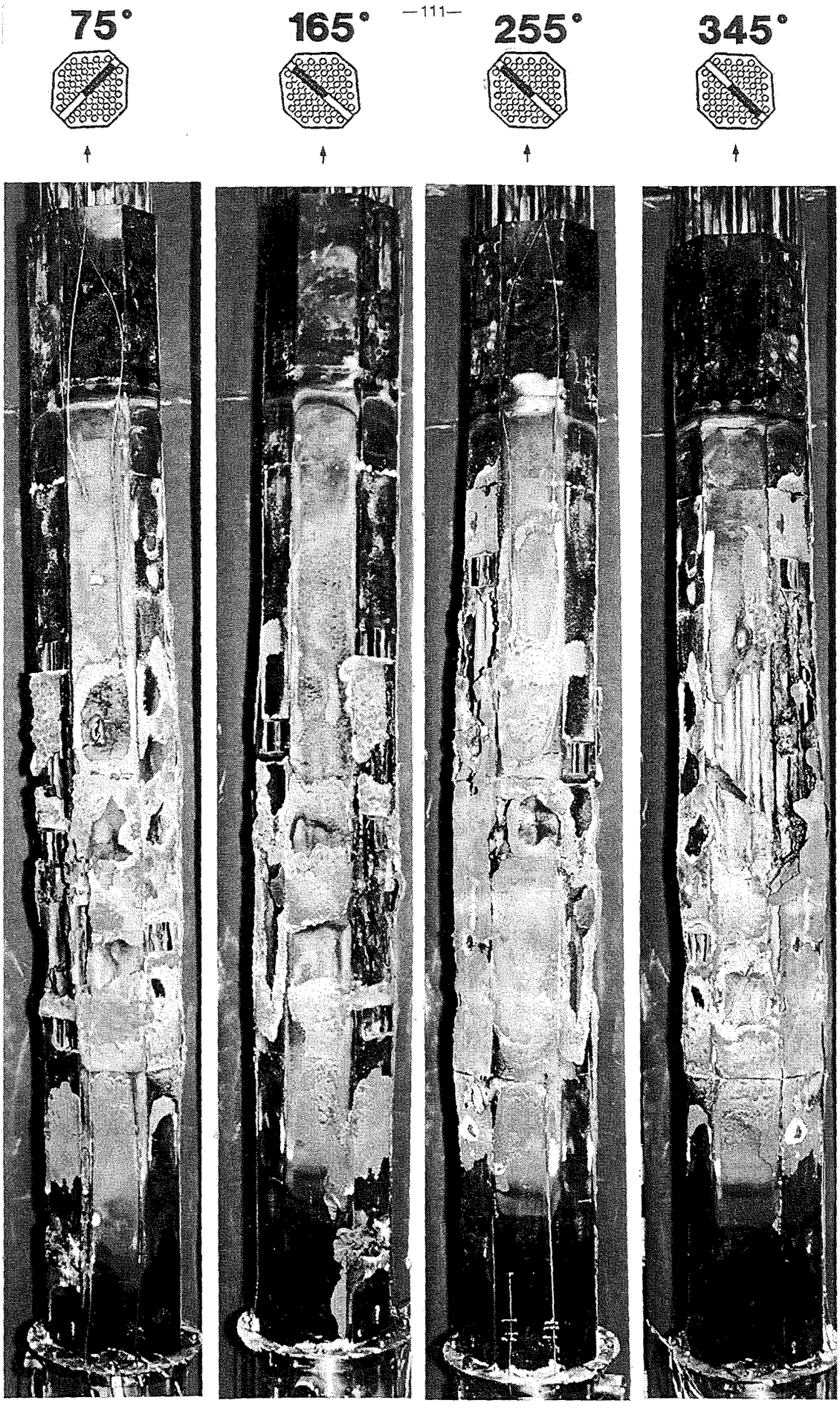

Fig. 83: CORA-18; posttest appearence of the shroud after removal of the insulation

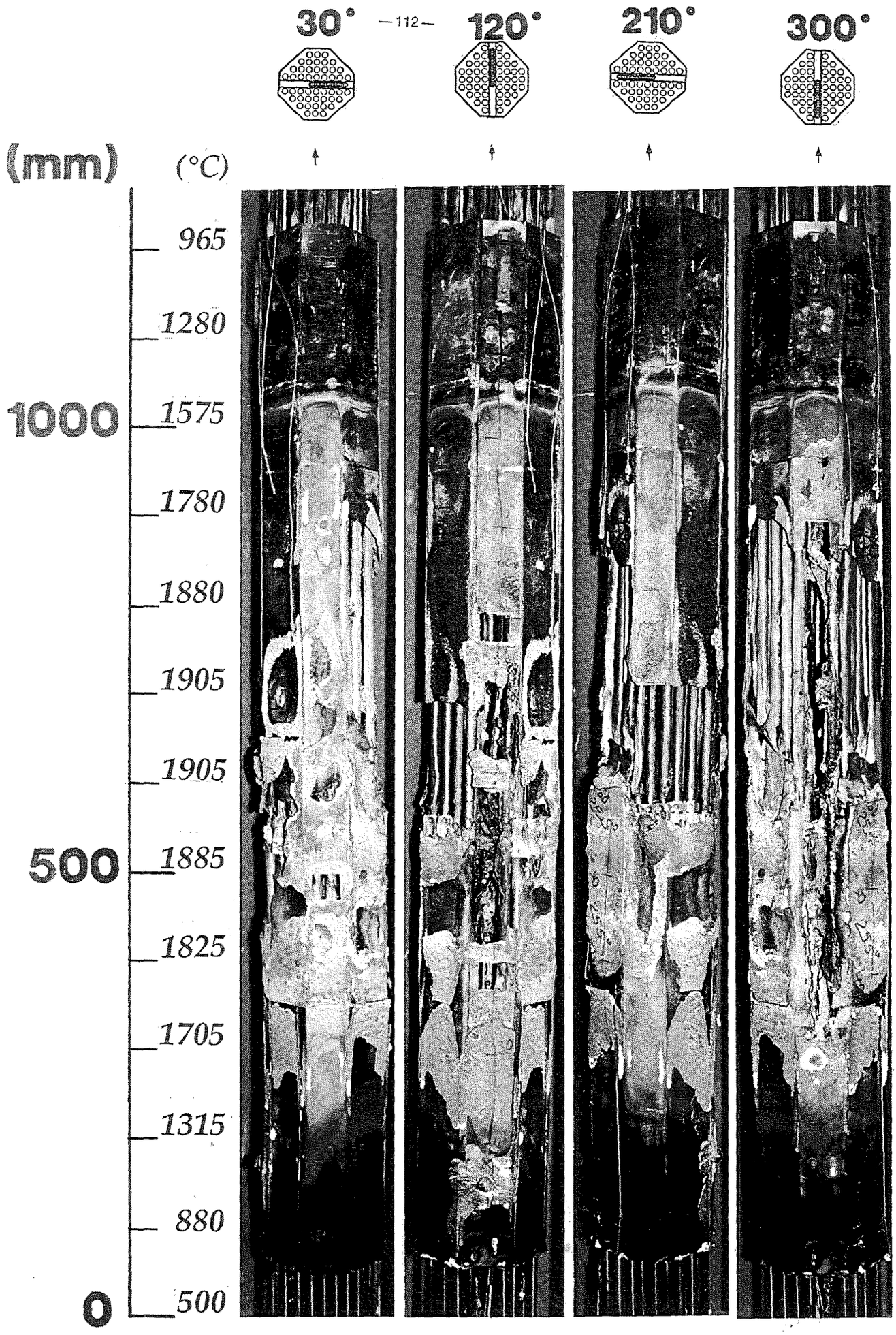

Fig. 84: CORA-18; posttest appearence of the bundle after partial removal of the shroud

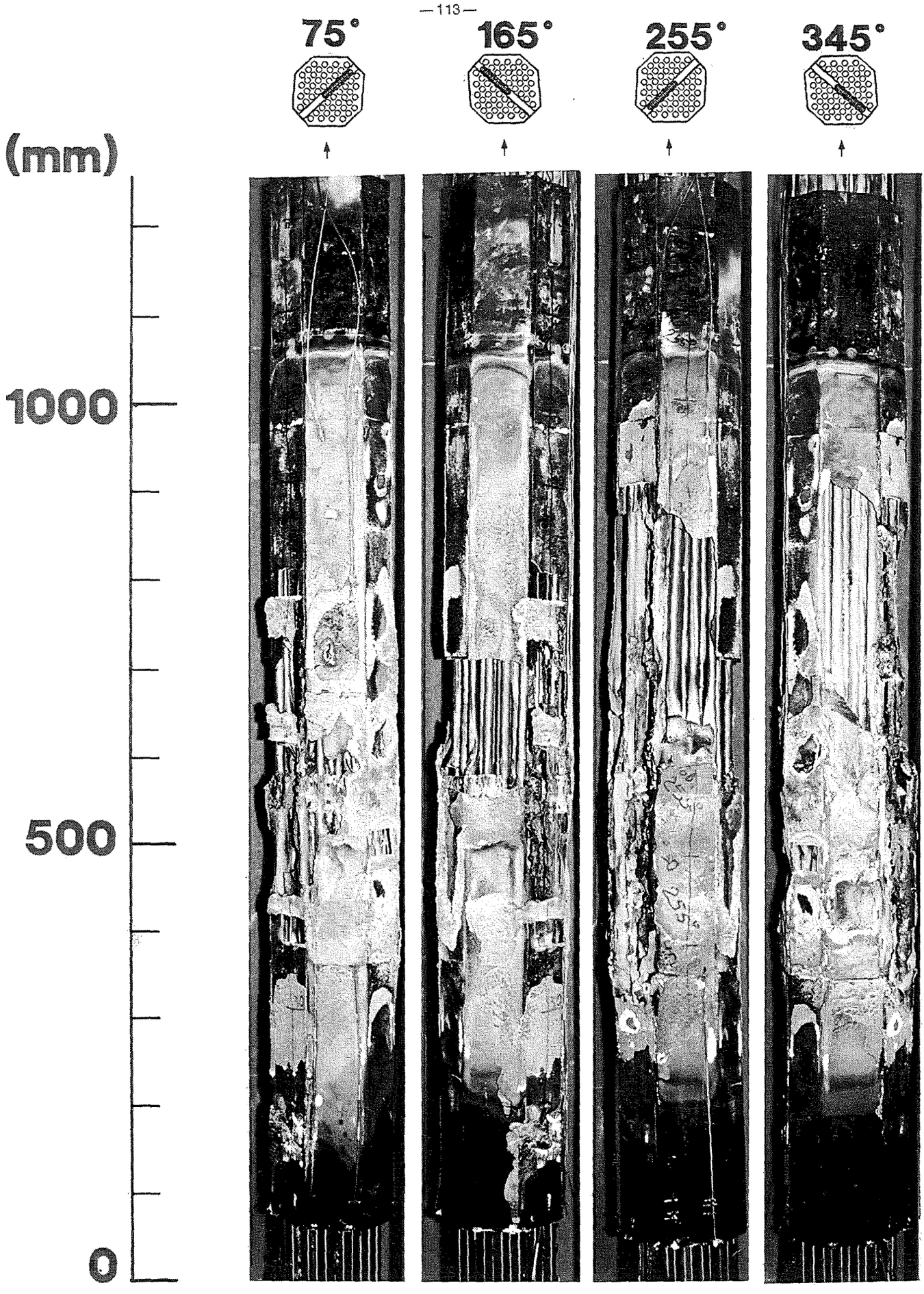

Fig. 85: CORA-18; posttest appearence of the bundle after partial removal of the shroud

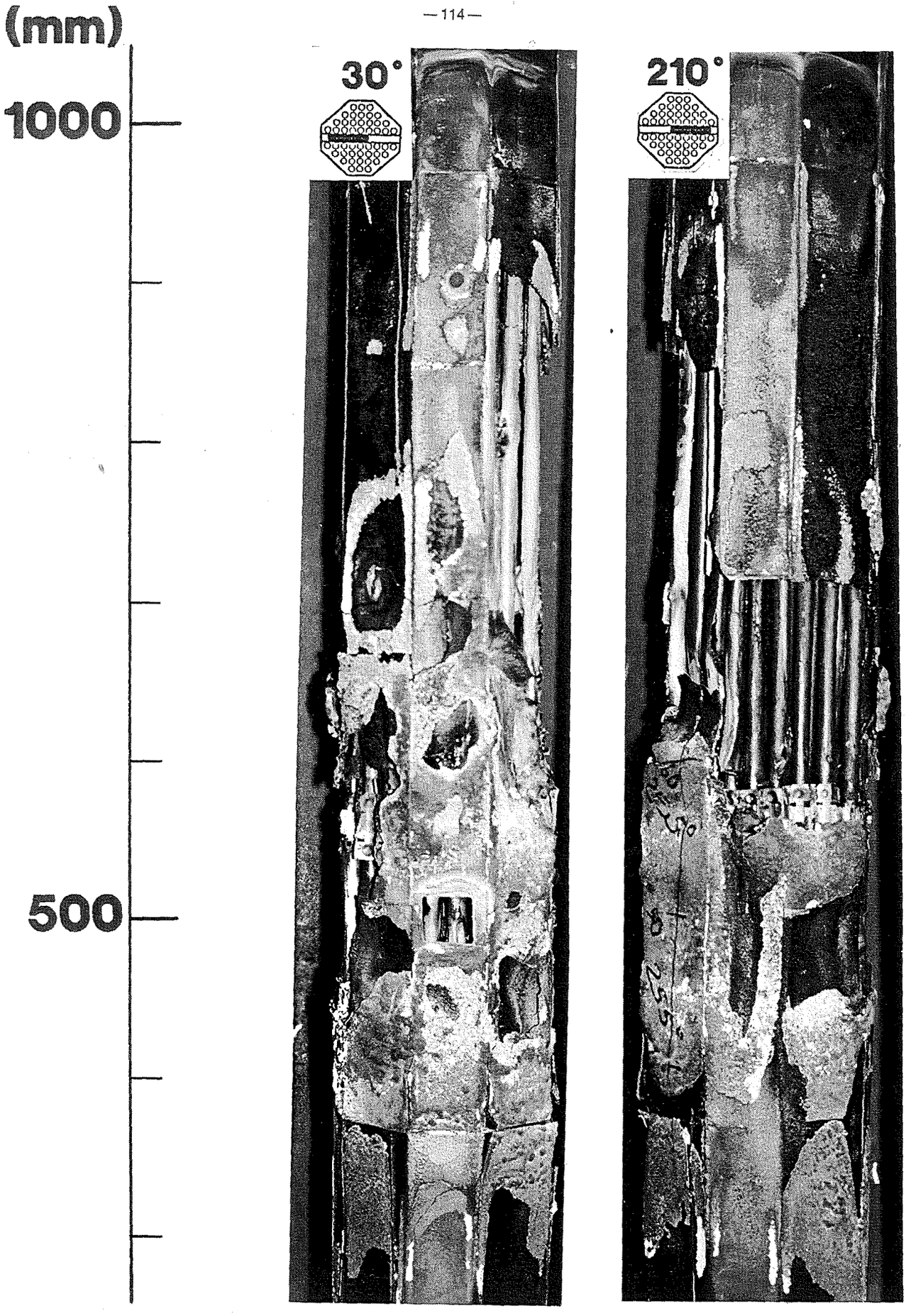

Fig. 86: CORA-18; posttest partial view at 30° and 210° orientation.

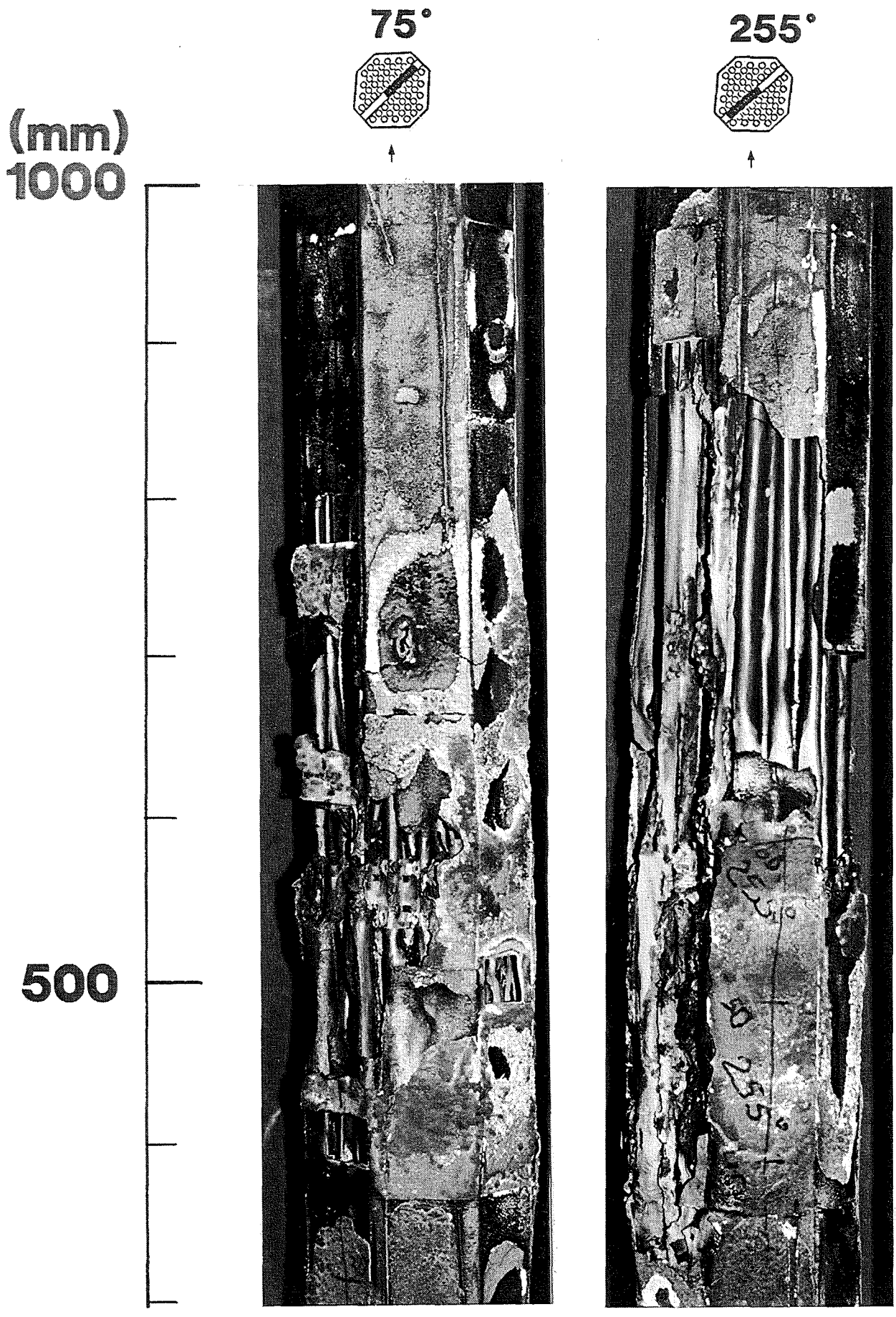

Fig. 87: CORA-18; posttest partial view at 75° and 255° orientation.

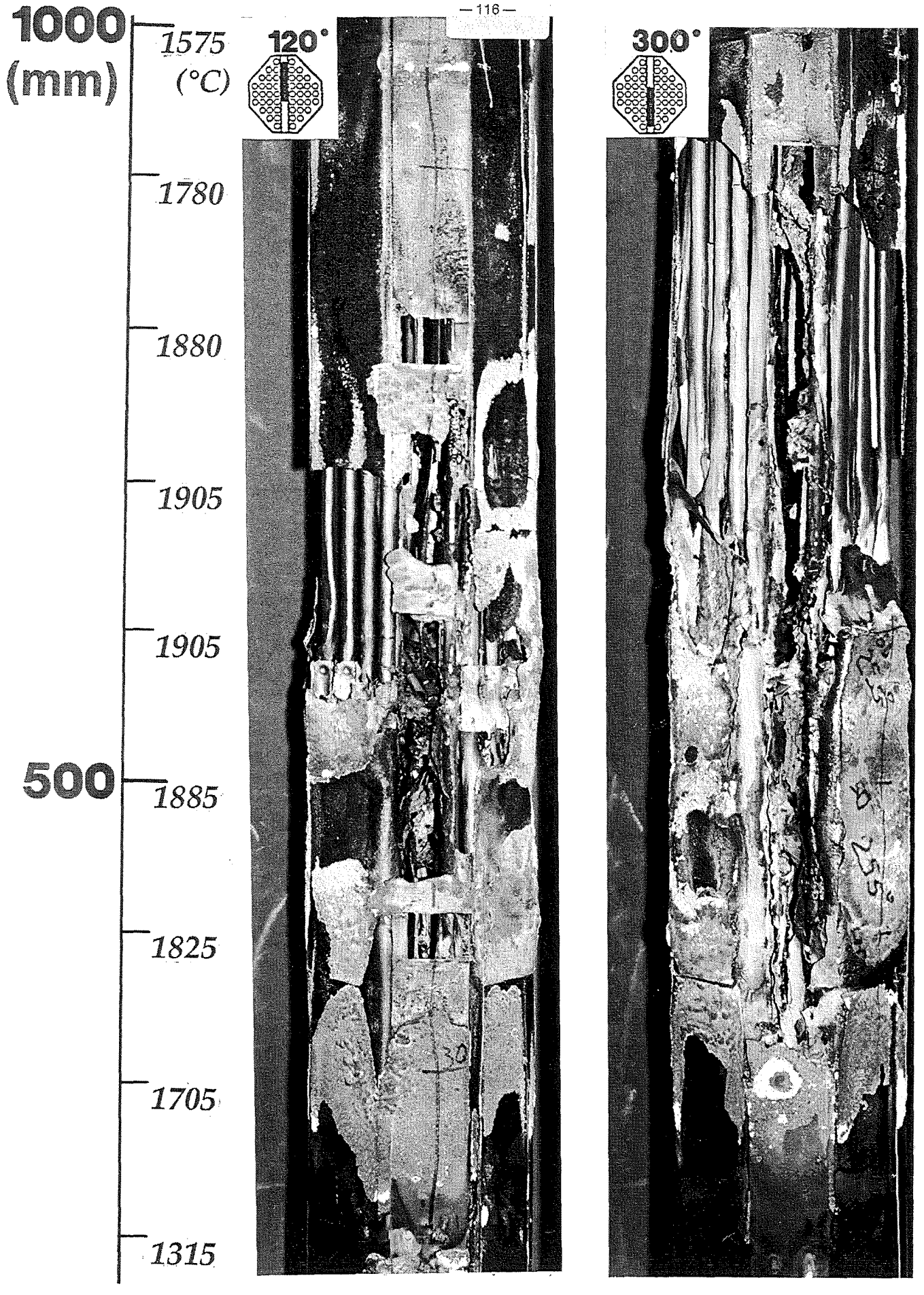

Fig. 88: CORA-18; posttest partial view at 120° and 300° orientation.

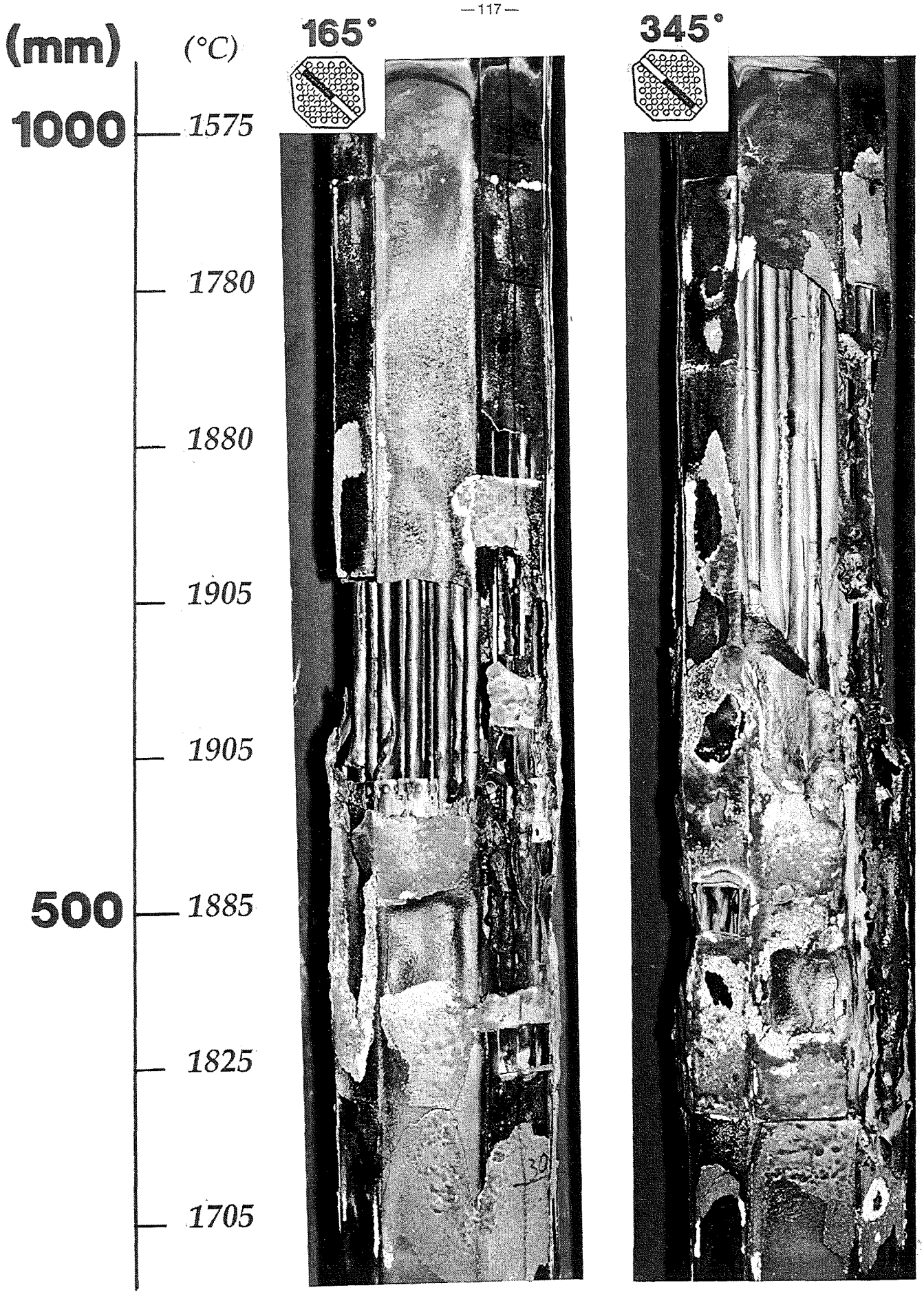

Fig. 89: CORA-18; posttest partial view at 165° and 345° orientation.

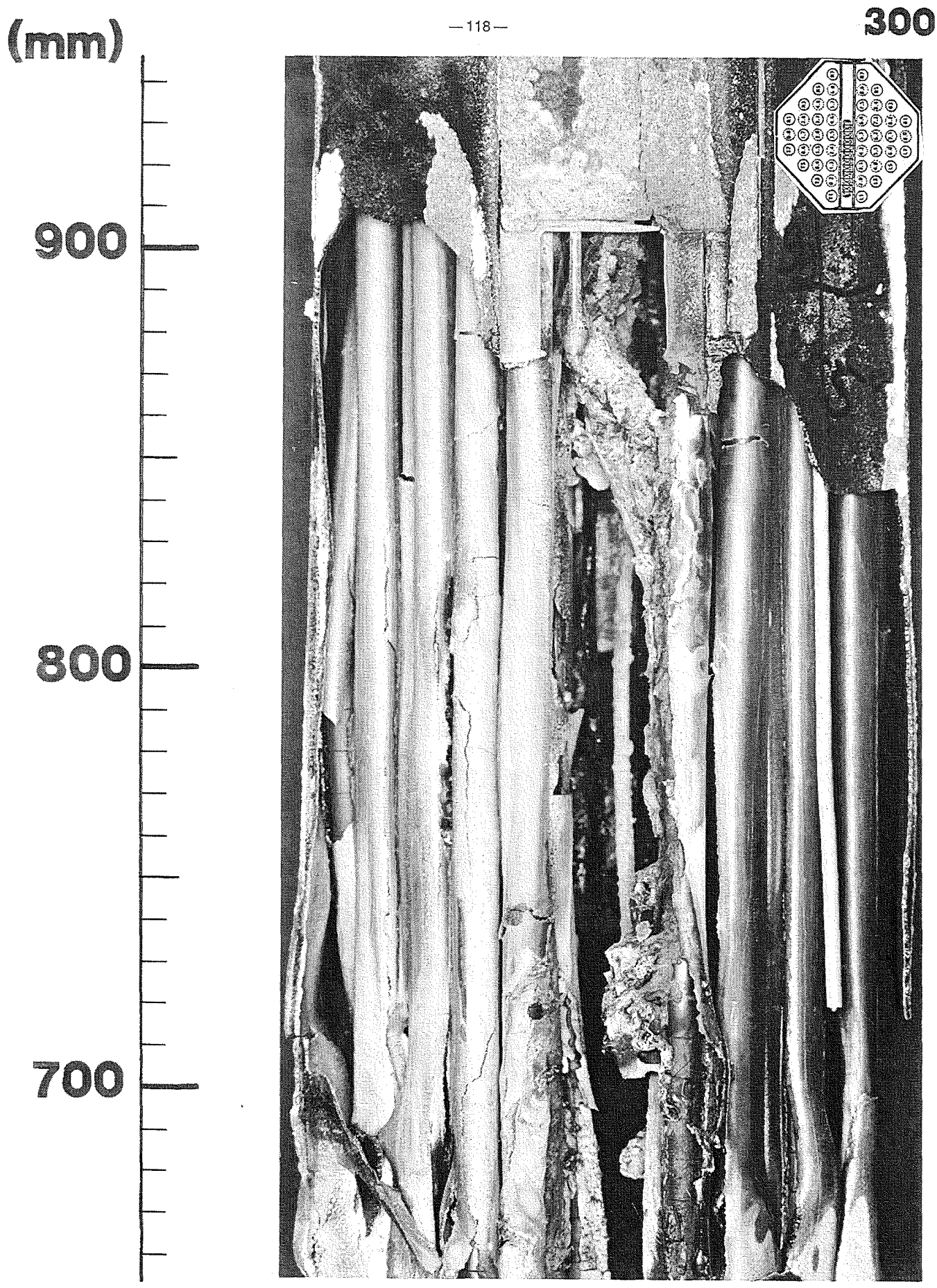

Fig. 90: CORA-18; posttest partial view at 300° orientatation; 650 - 900 mm elevation.

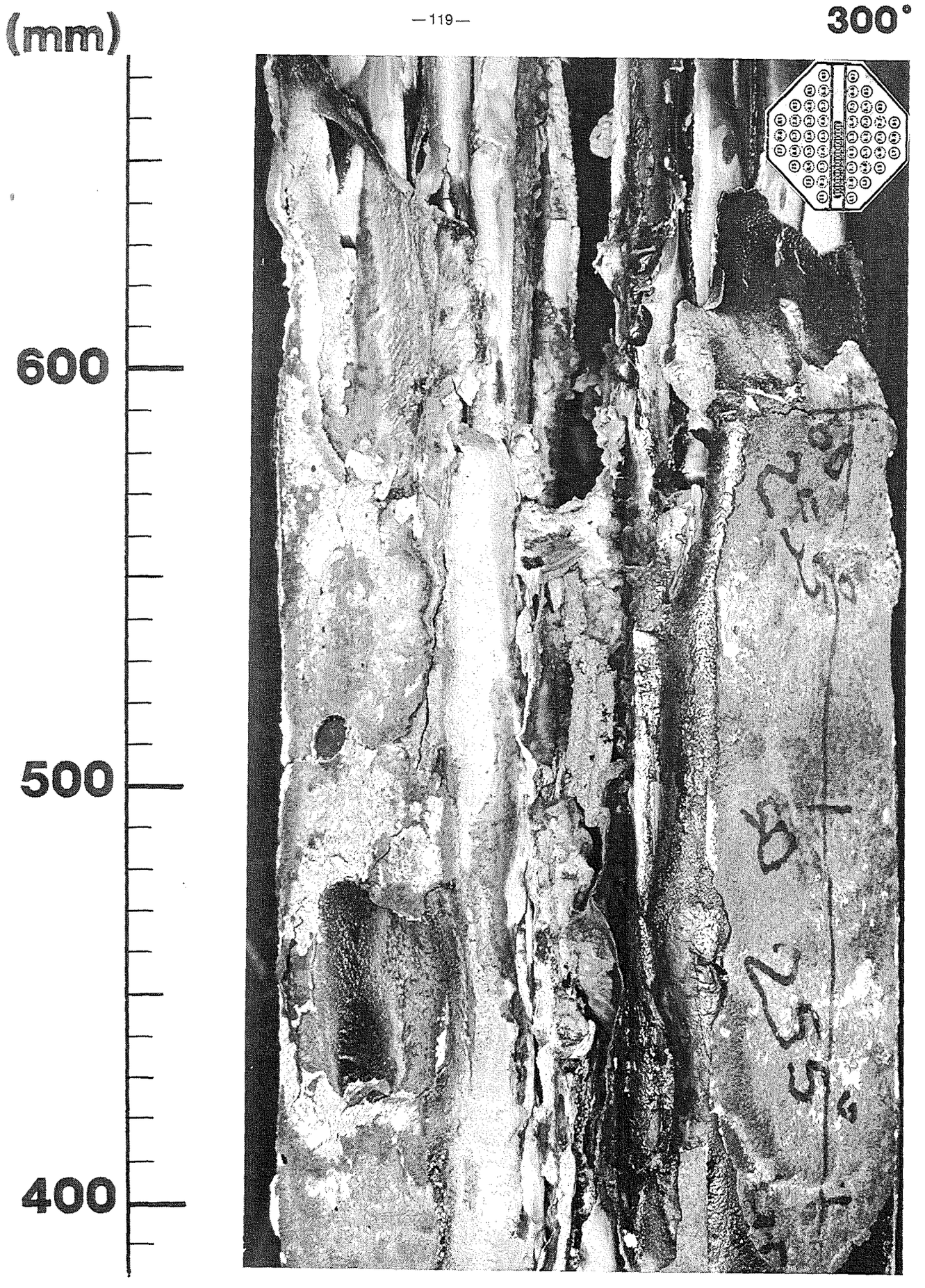

Fig. 91: CORA-18; posttest partial view at 300° orientatation; 400 - 650 mm elevation.

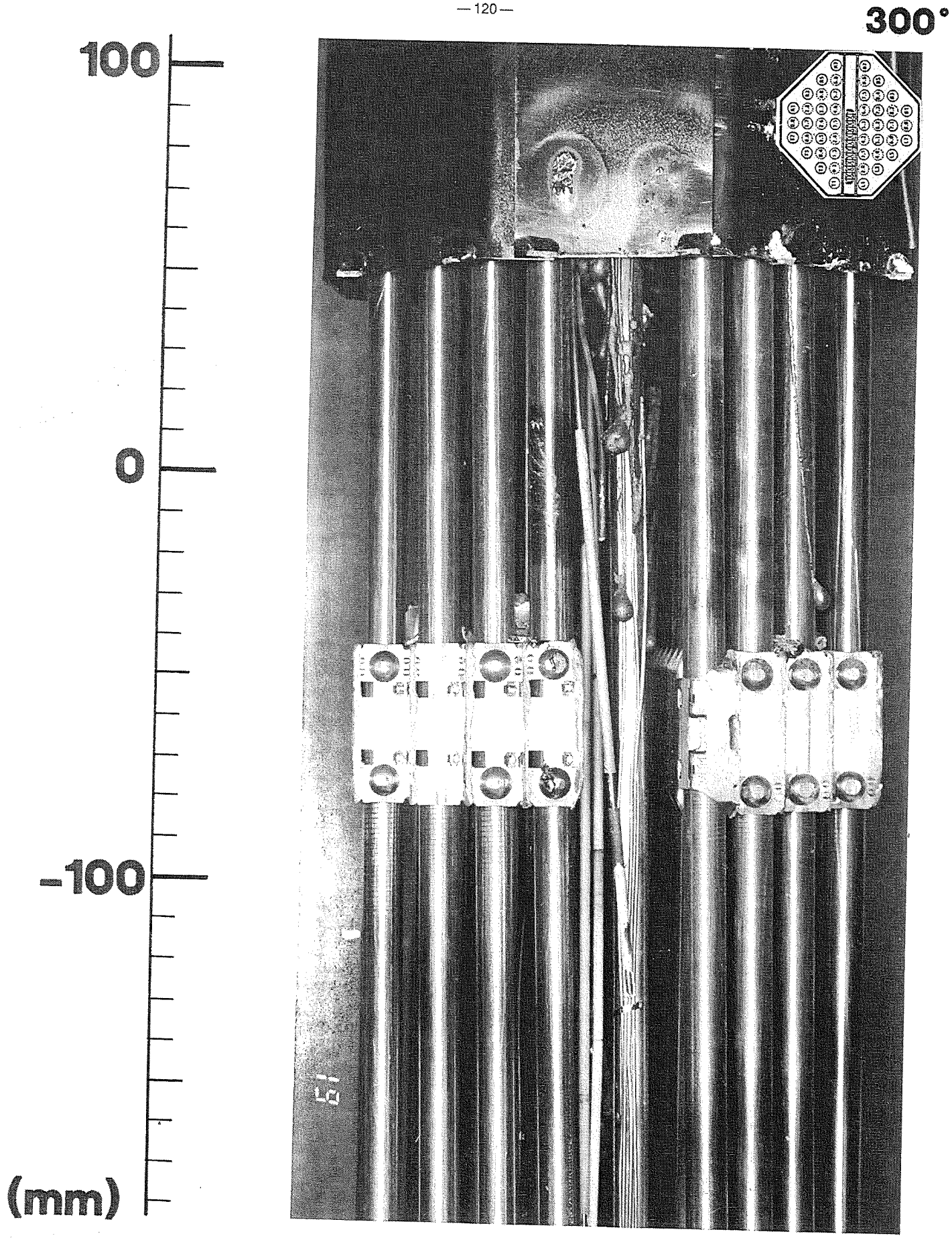

Fig. 92: CORA-18; posttest partial view at 300° orientatation; -150 - 100 mm elevation.

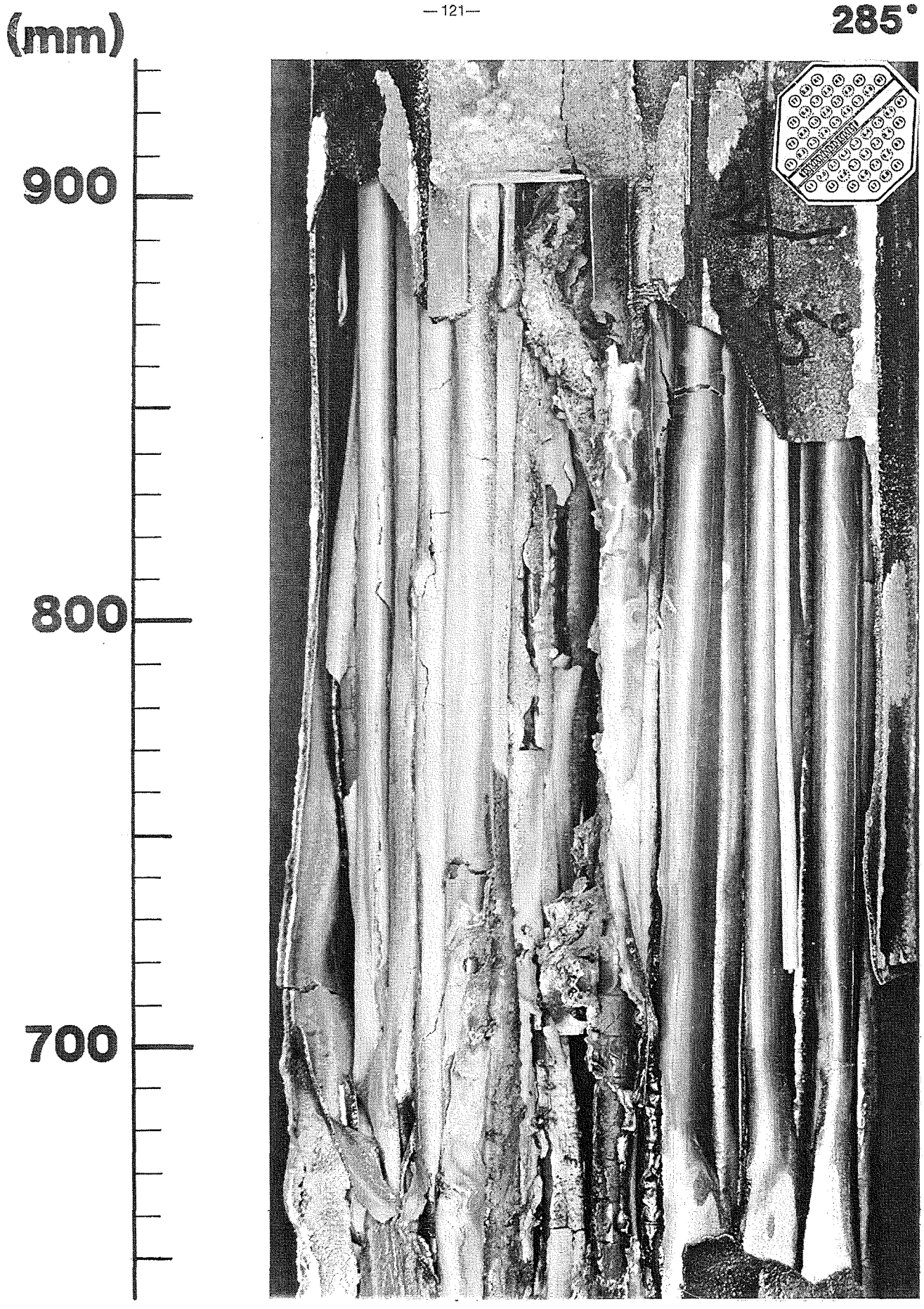

Fig. 93: CORA-18; posttest partial view at 285° orientatation; 650 - 900 mm elevation.

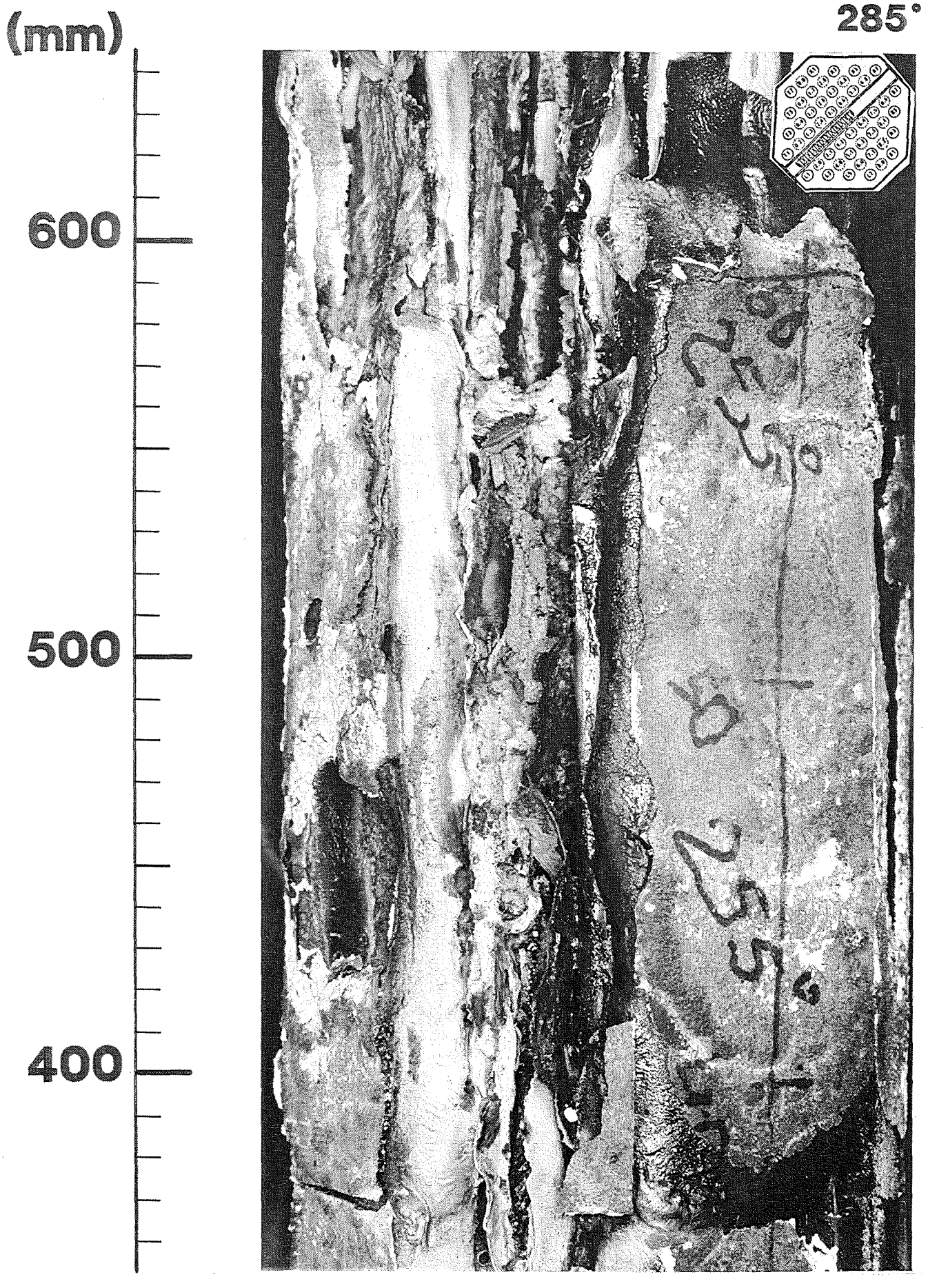

Fig. 94: CORA-18; posttest partial view at 285° orientatation; 350 - 650 mm elevation.

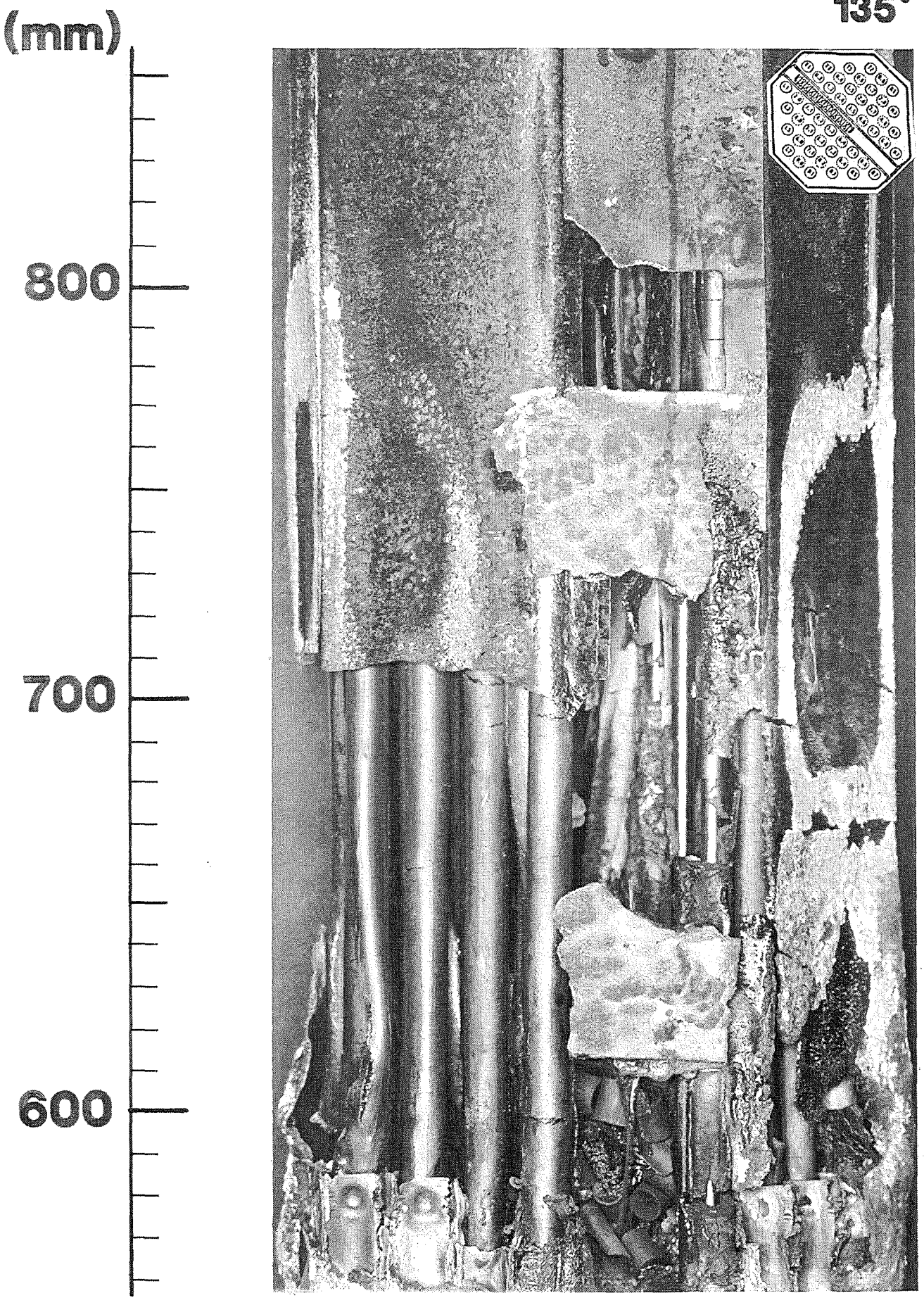

Fig. 95: CORA-18; posttest partial view at 135° orientatation; 650 - 900 mm elevation.

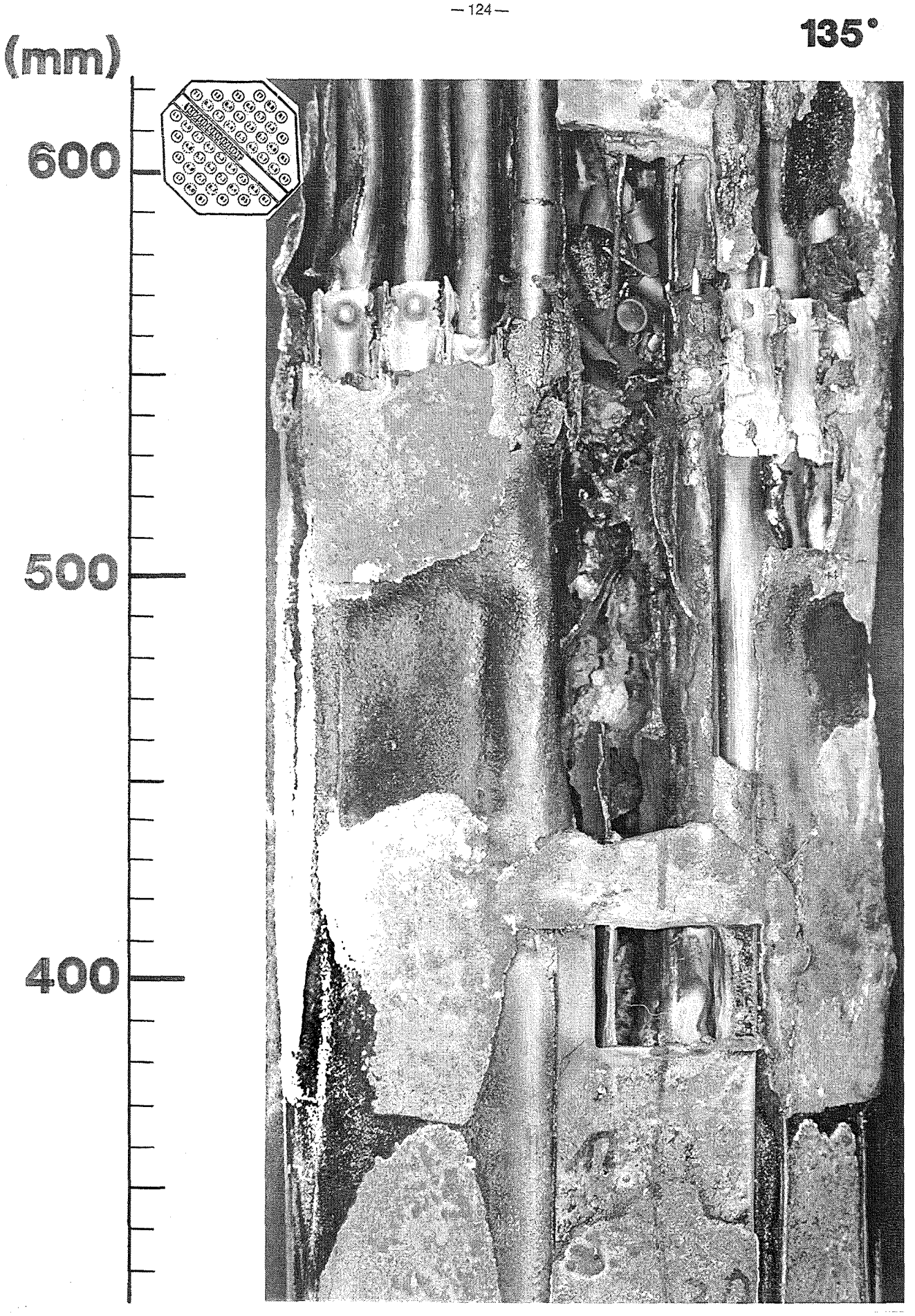

Fig. 96: CORA-18; posttest partial view at 135° orientatation; 350 - 600 mm elevation.

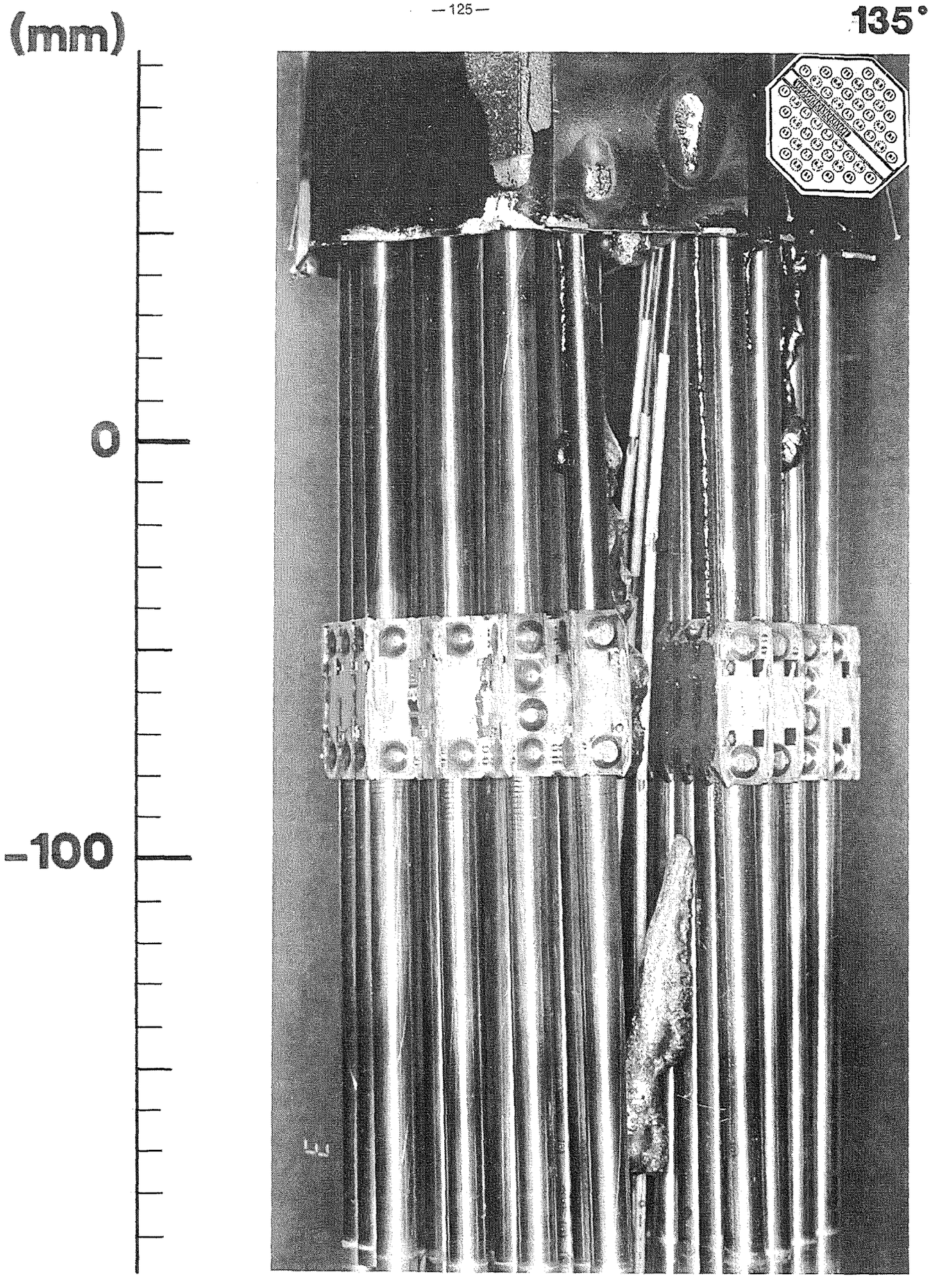

Fig. 97: CORA-18; posttest partial view at 135° orientatation; -200 - 100 mm elevation.

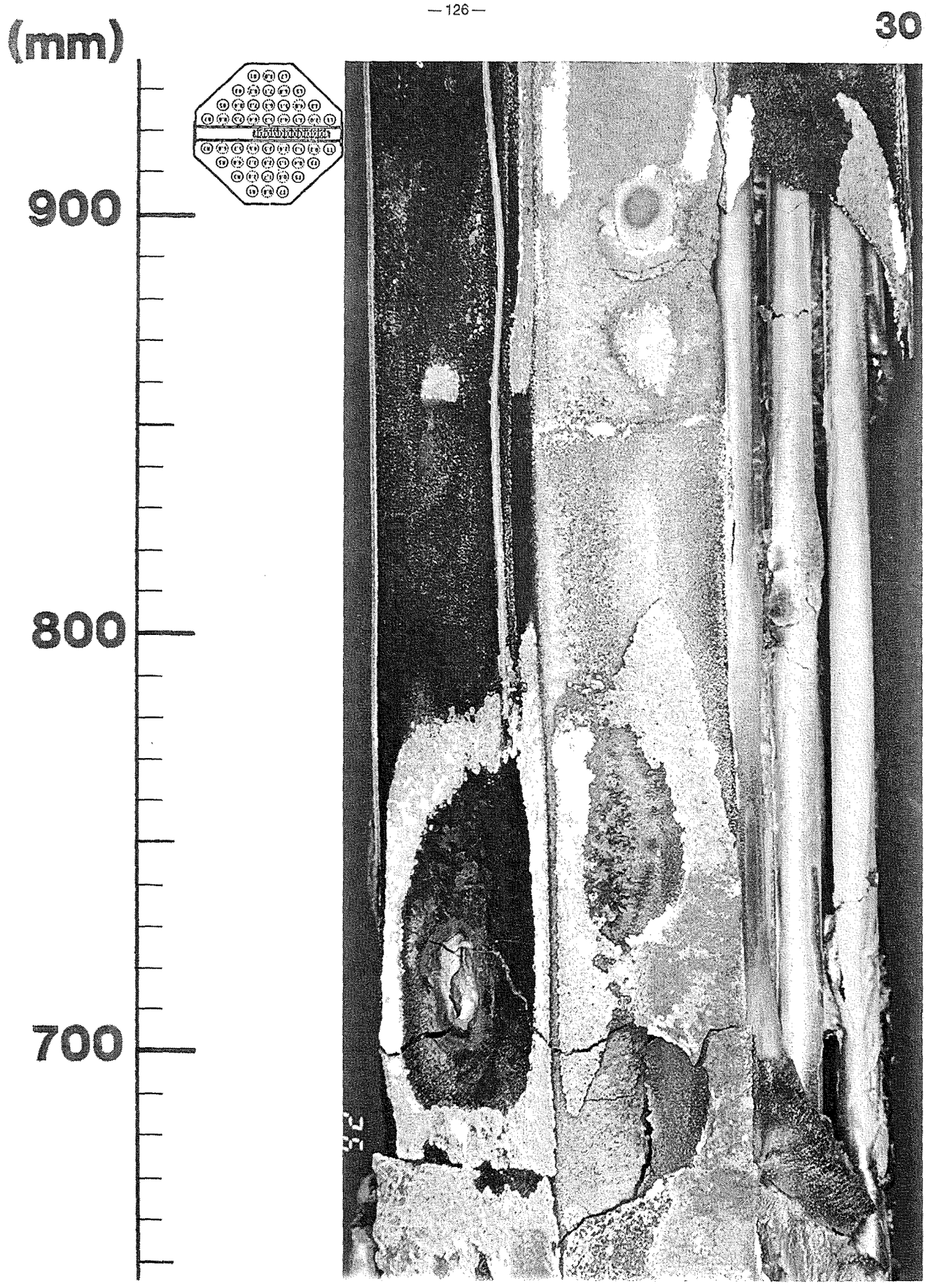

Fig. 98: CORA-18; posttest partial view at 30° orientatation; 650 - 900 mm elevation.

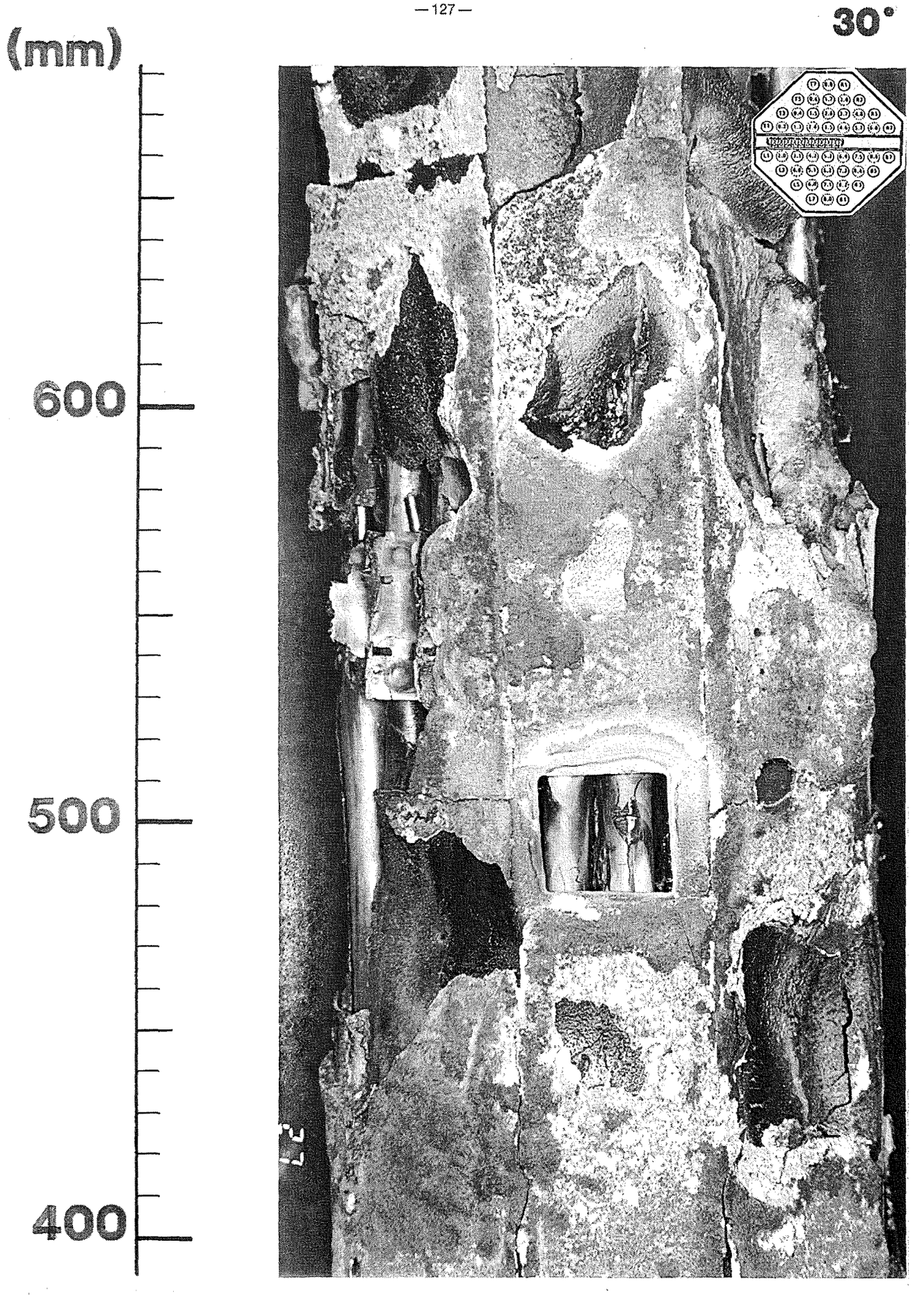

Fig. 99: CORA-18; posttest partial view at 30° orientatation; 400 - 650 mm elevation.

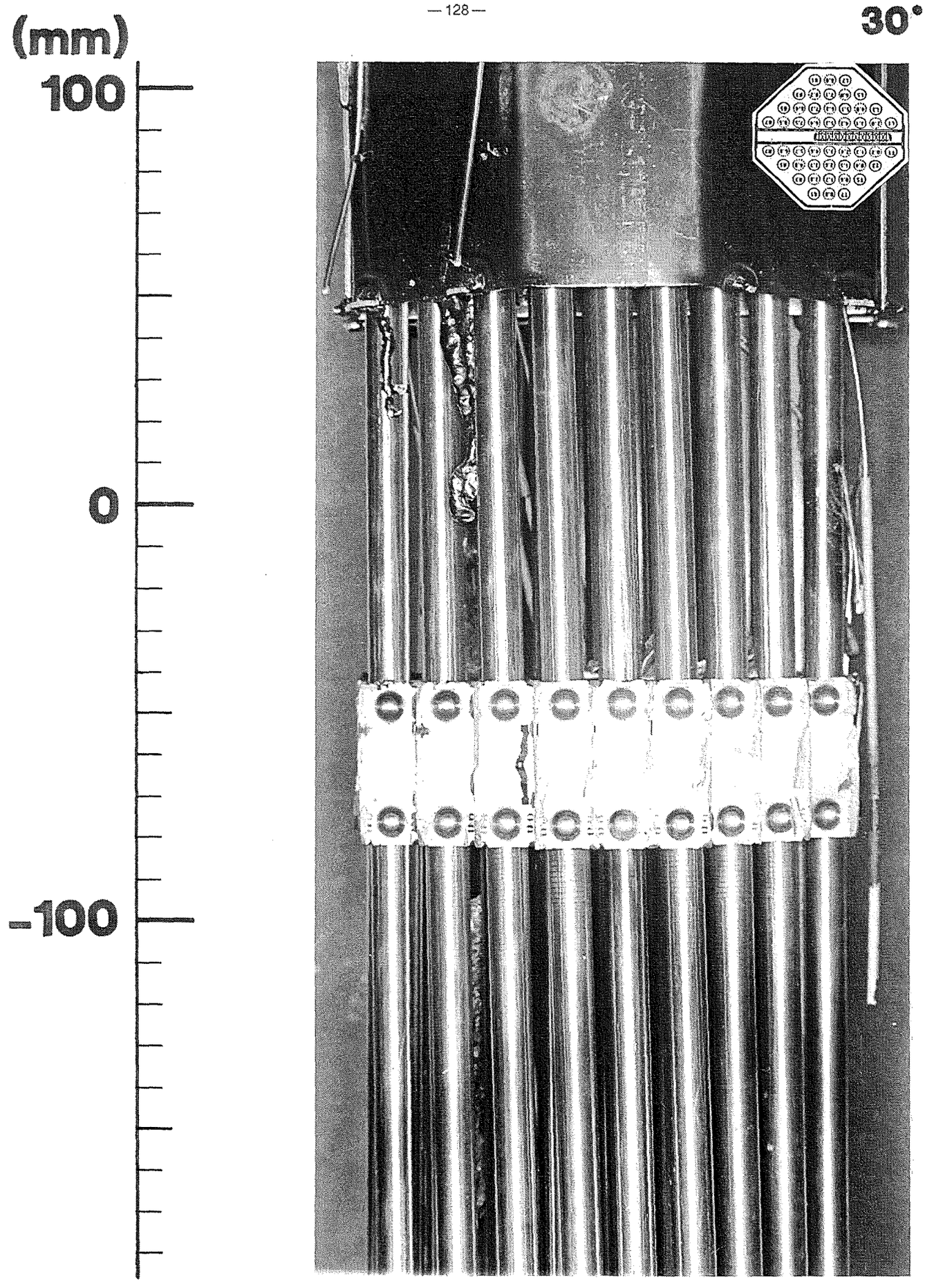

Fig. 100: CORA-18; posttest partial view at 30° orientatation; -50 to 100 mm elevation.

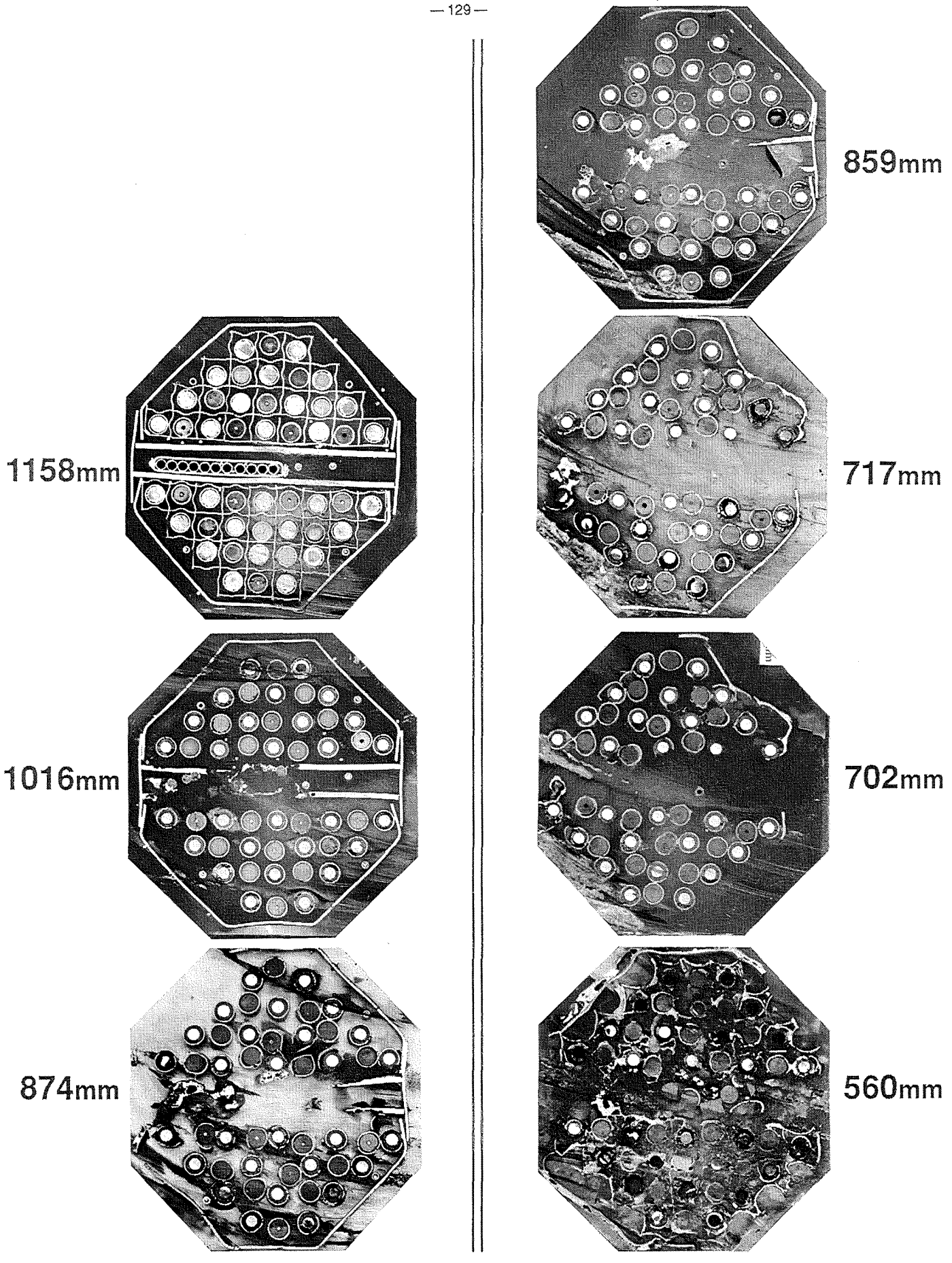

Fig. 101: CORA-18; horizontal cross-sections;
1158 - 560 mm elevations

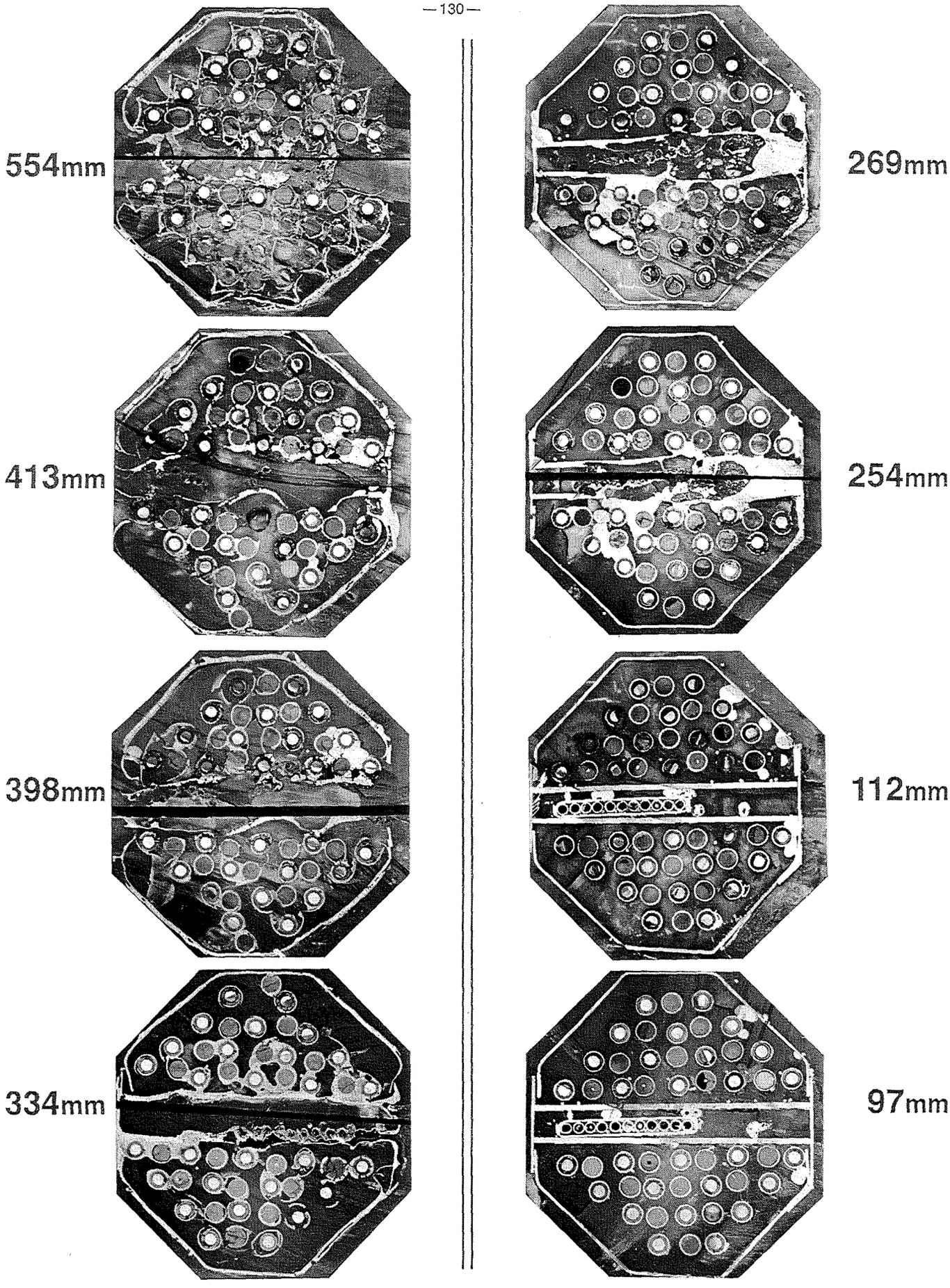

Fig. 102: CORA-18; horizontal cross-sections;
554 - 97 mm elevations

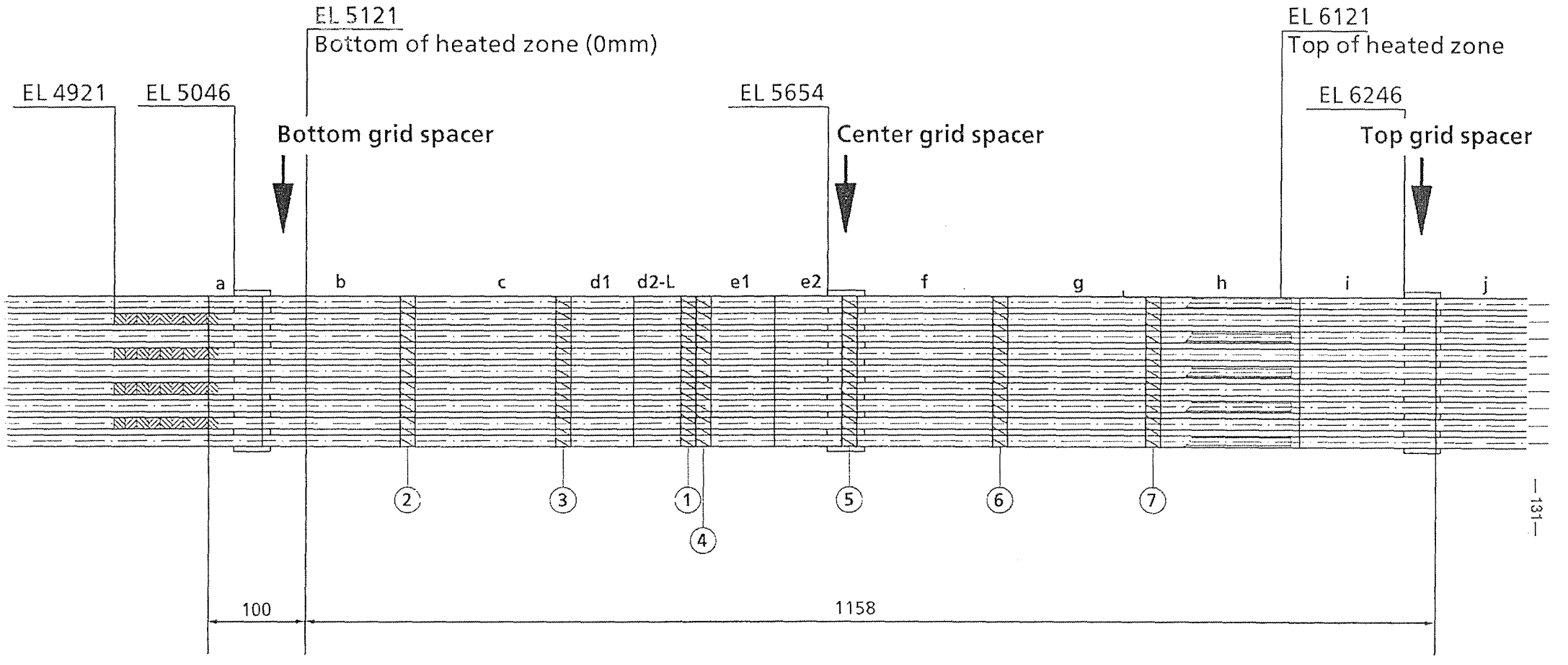

Vertical sections of remnants c, d, e,

Height of horizontal sample : 13mm (marking distance = 15mm)

Bundle viewed from 30° and 210°, respectively

Fig. 102a: Bundle Sectioning

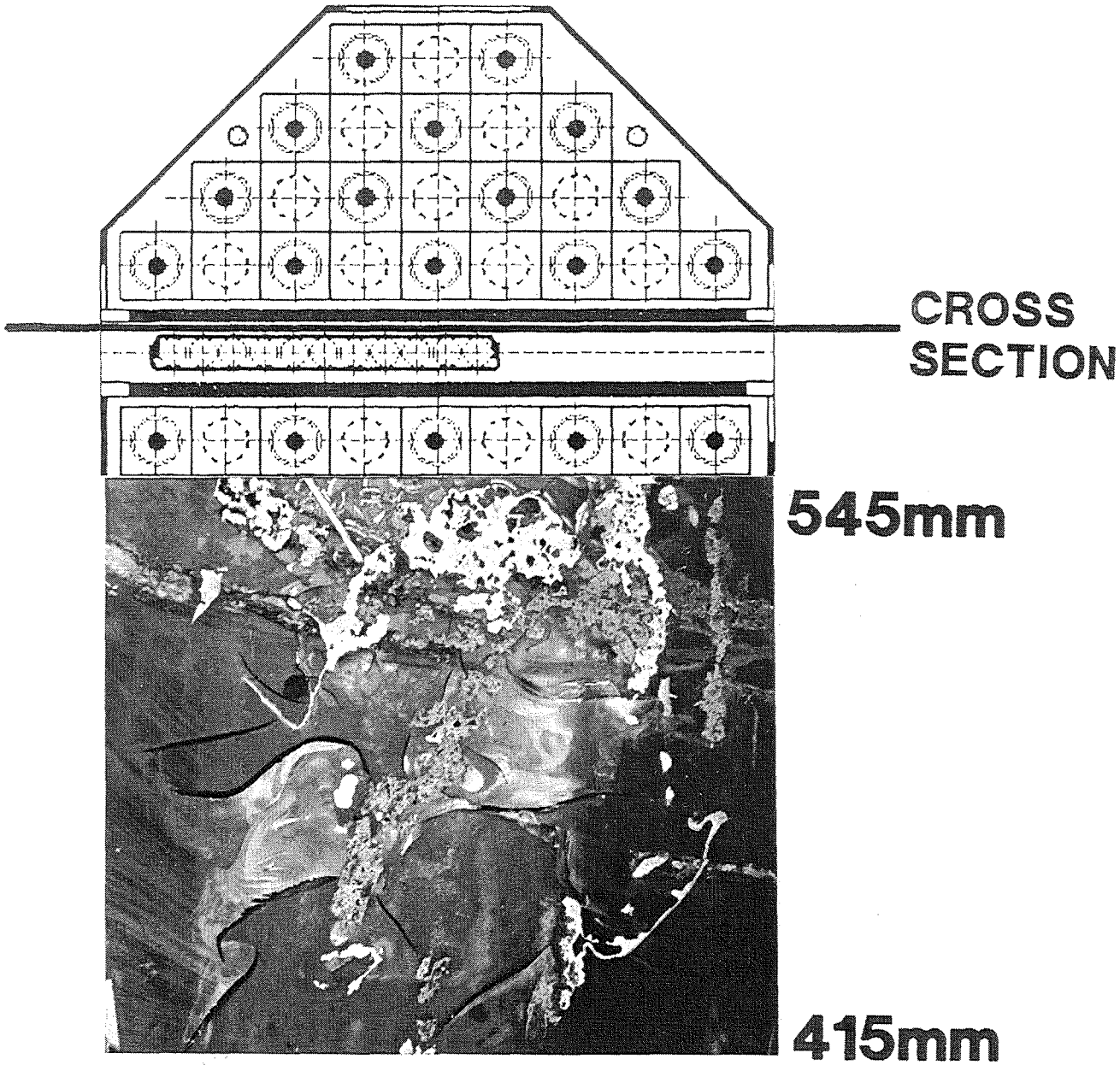

Fig. 103: CORA-18; vertical cross-section;
in absorber region, 415 - 545 mm

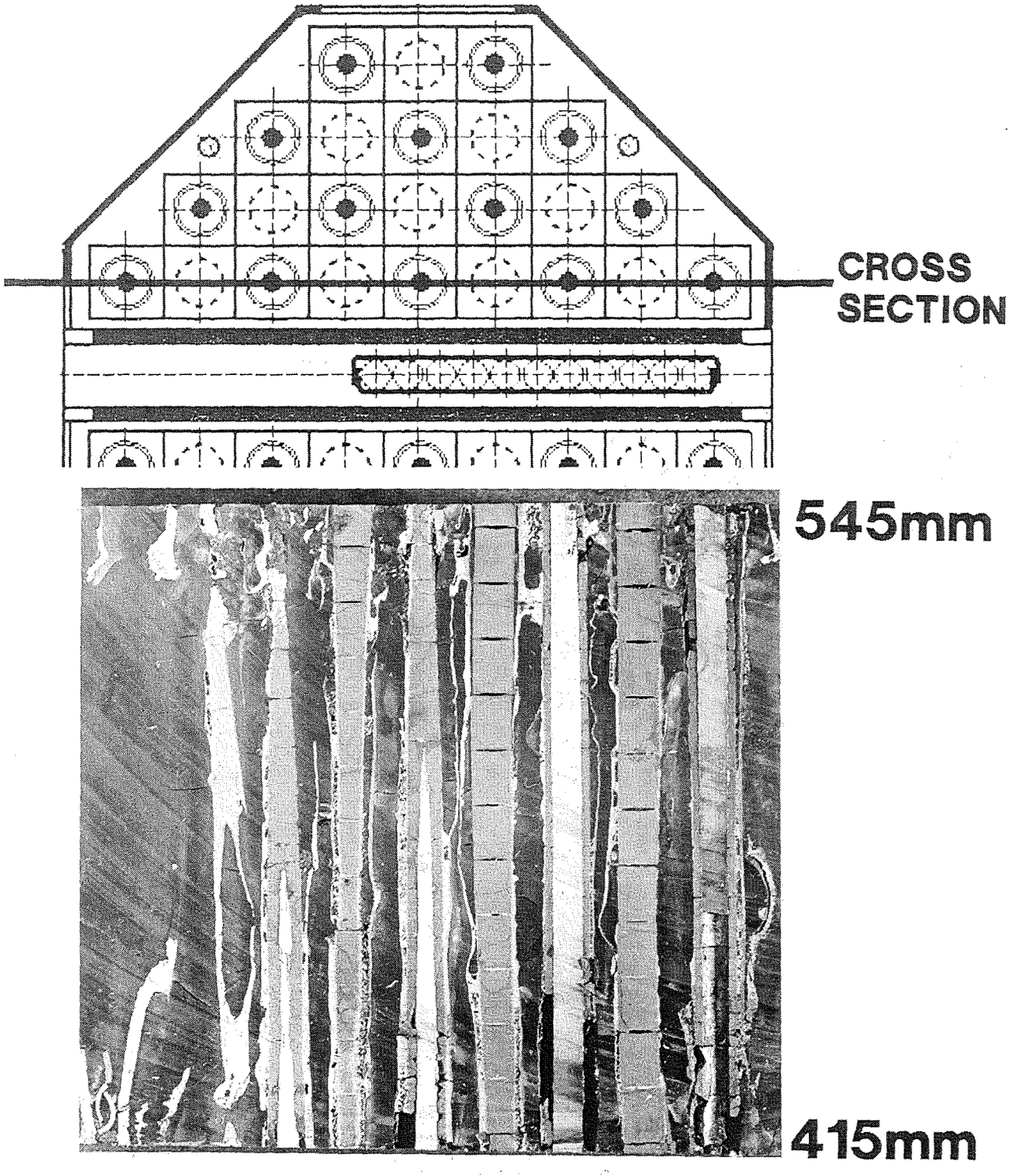

Fig. 104: CORA-18; vertical cross-section;
in simulator region, 415 - 545 mm

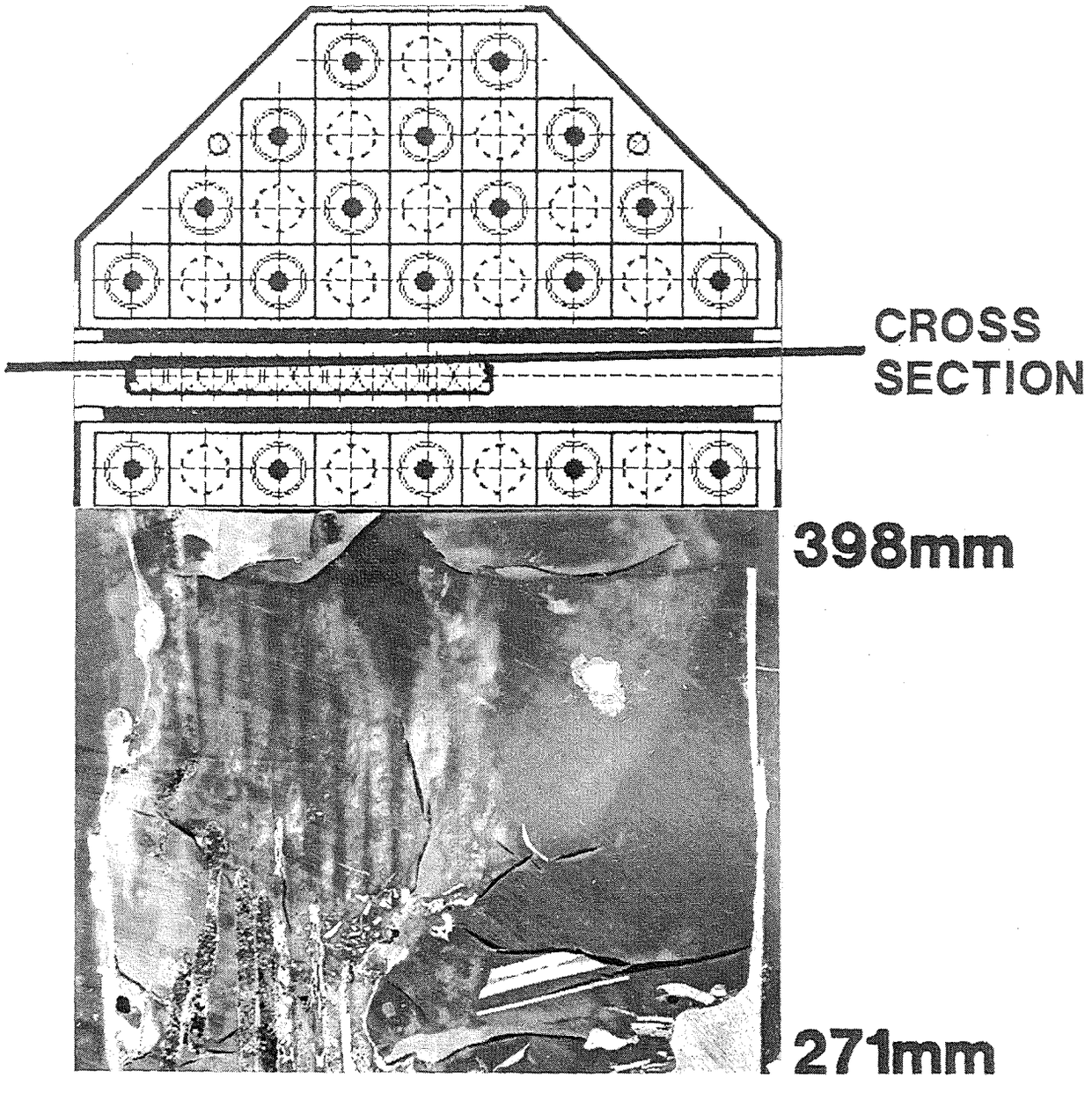

Fig. 105: CORA-18; vertical cross-section;
in absorber region, 271 - 398 mm

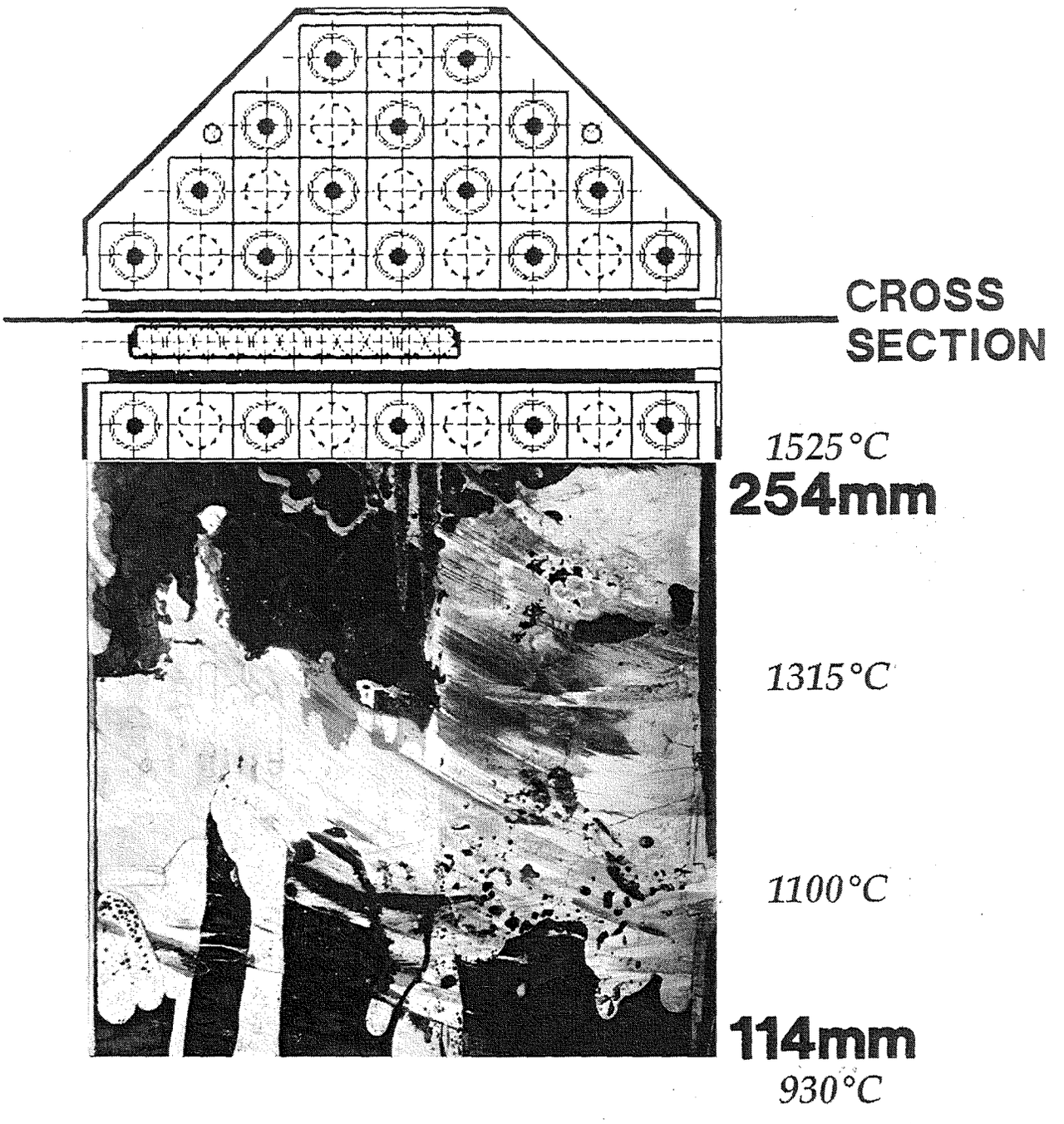

Fig. 106: CORA-18; vertical cross-section;
in absorber region, 114 - 254 mm

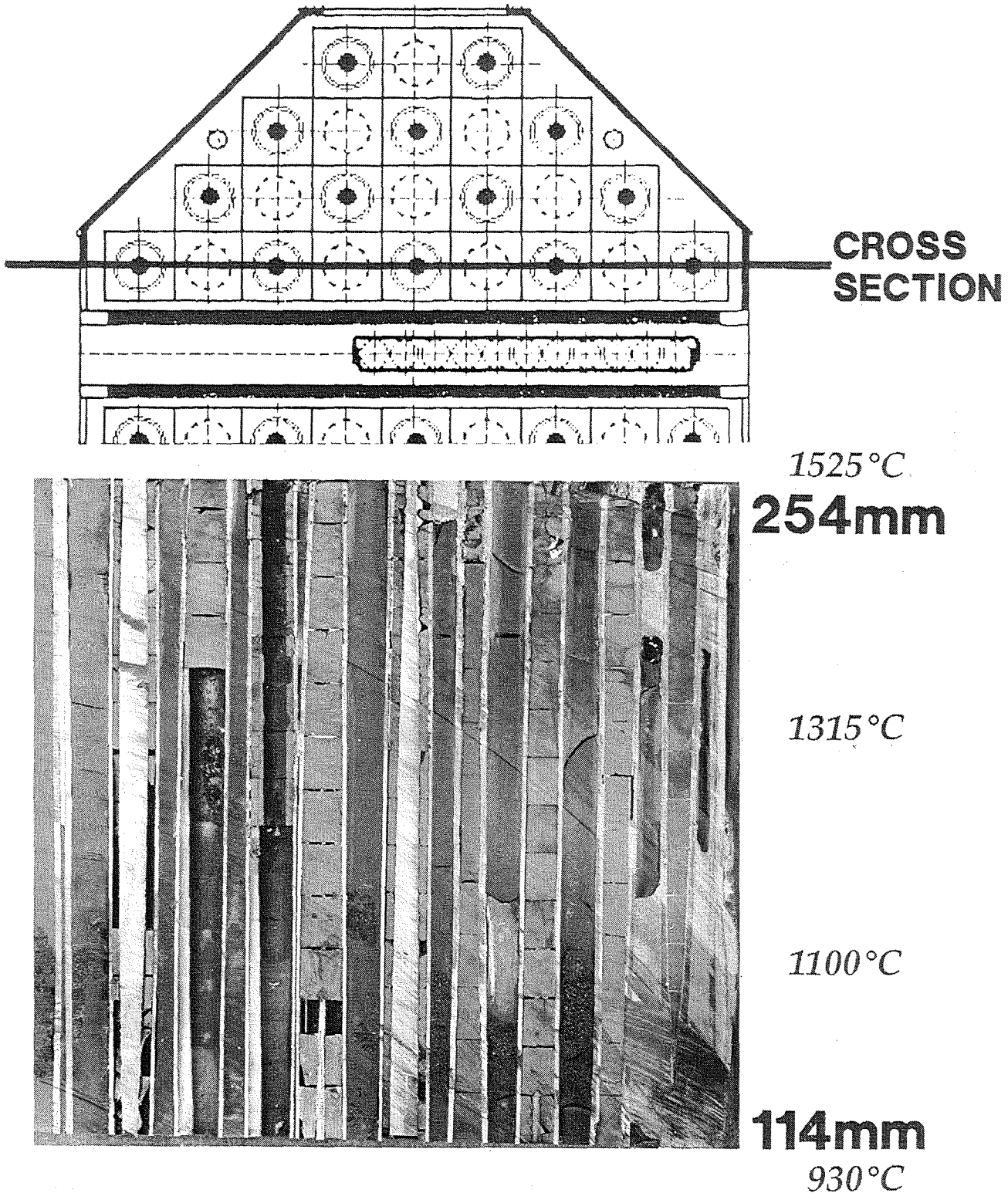

Fig. 107: CORA-18; vertical cross-section; in simulator region, 114 - 254 mm elevation

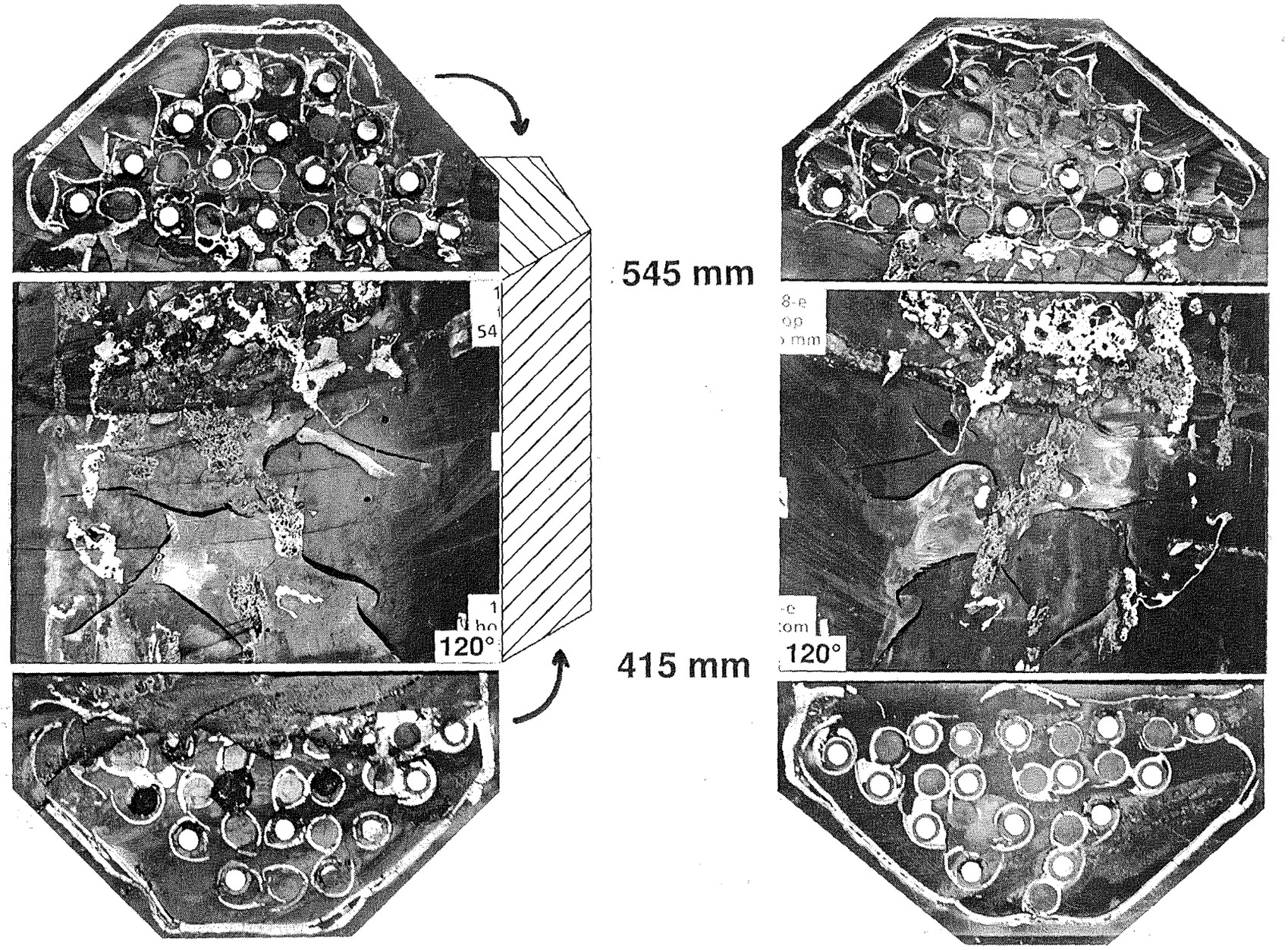

Fig. 108: CORA-18; two sides of vertical cross-section; in absorber region, 415 - 545 mm elevation

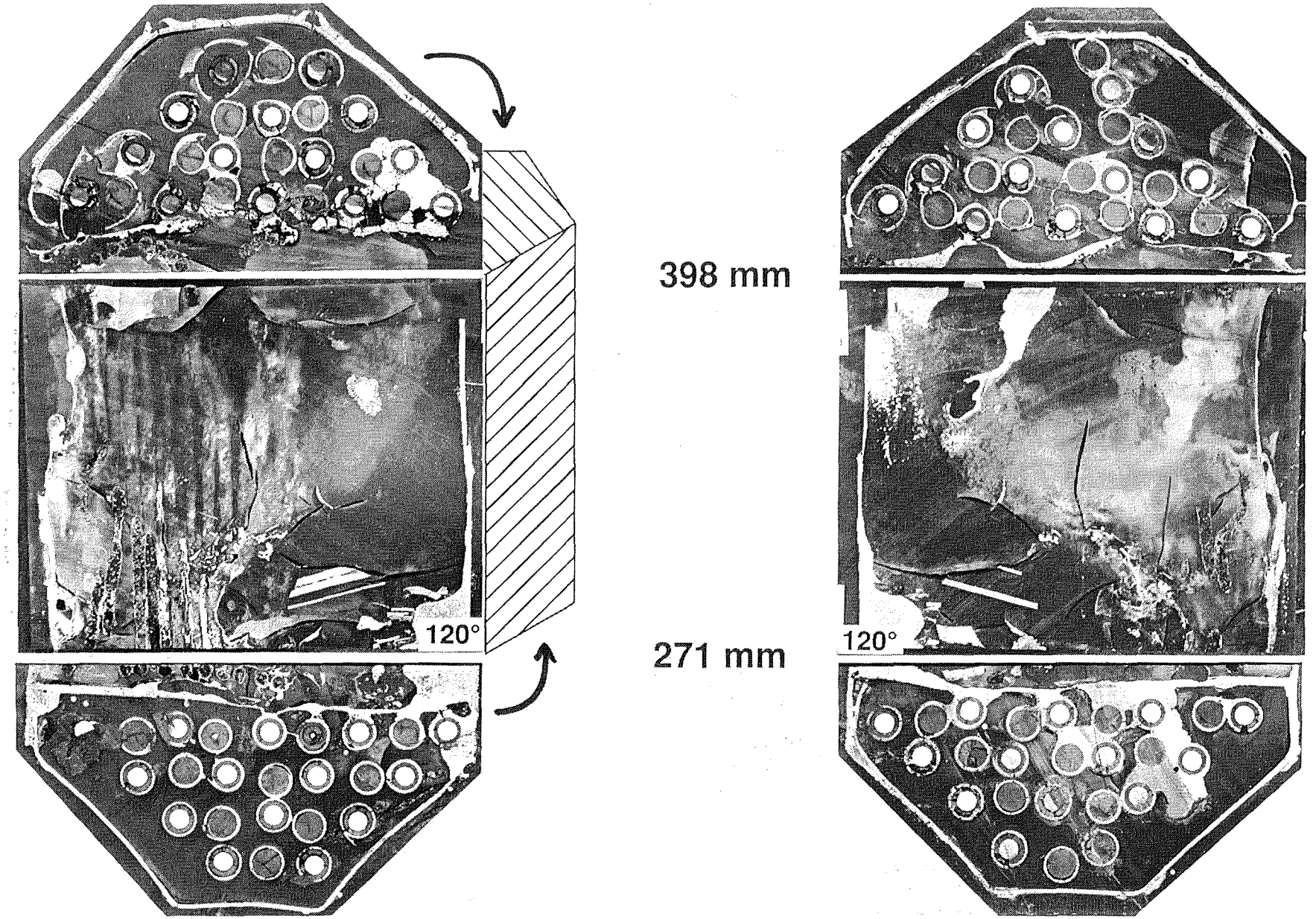

Fig. 109: CORA-18; two sides of vertical cross-section; in absorber region, 271 - 398 mm elevation

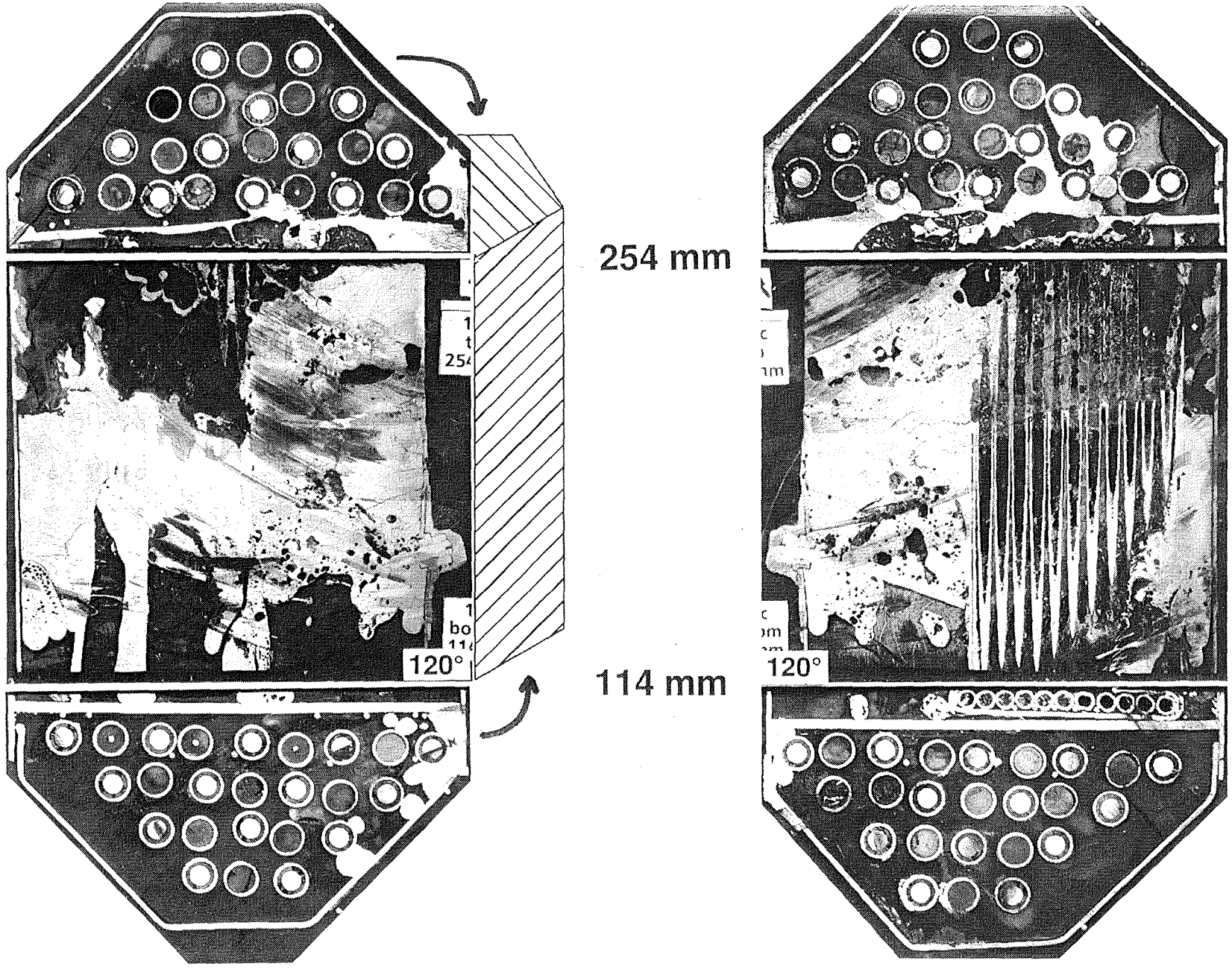

Fig. 110: CORA-18; two sides of vertical cross-section; in absorber region, 114 - 254 mm elevation

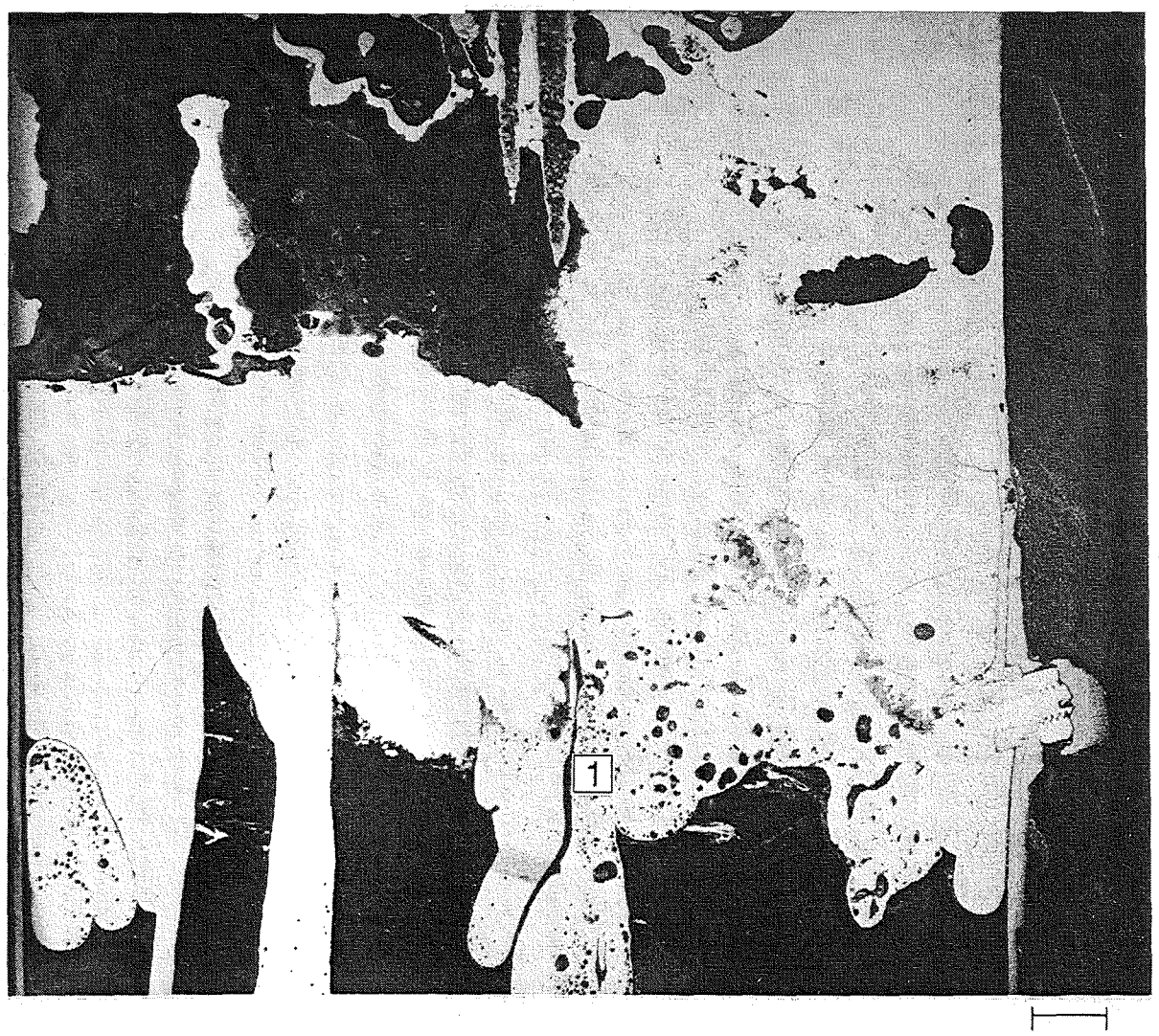

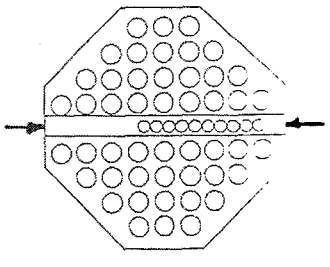

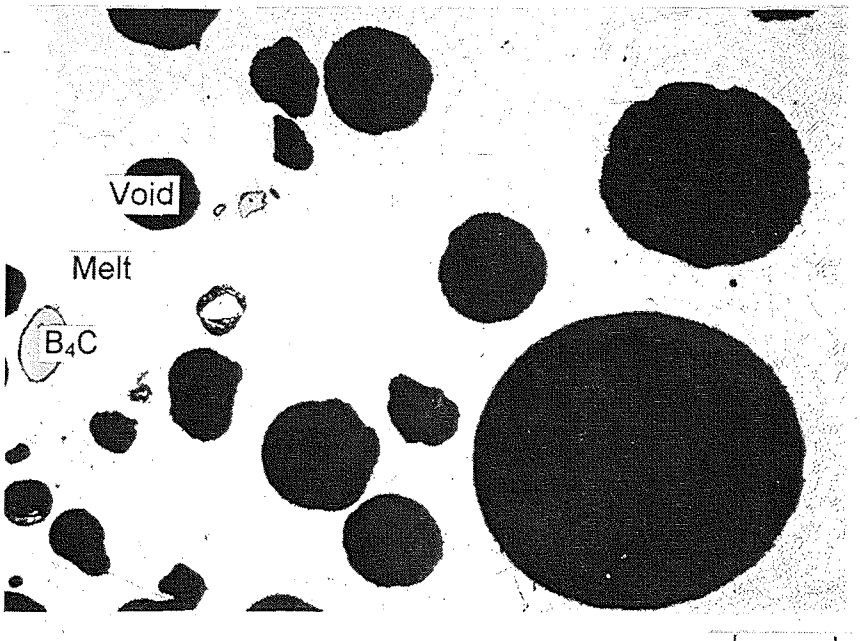

Early formed melt with closed porosity and some residual B_4C particles

Fig. 111:
Vertical Section CORA-18-c-L, Elevation 114-254 mm Overview and Detail of Melt within Absorber Channel

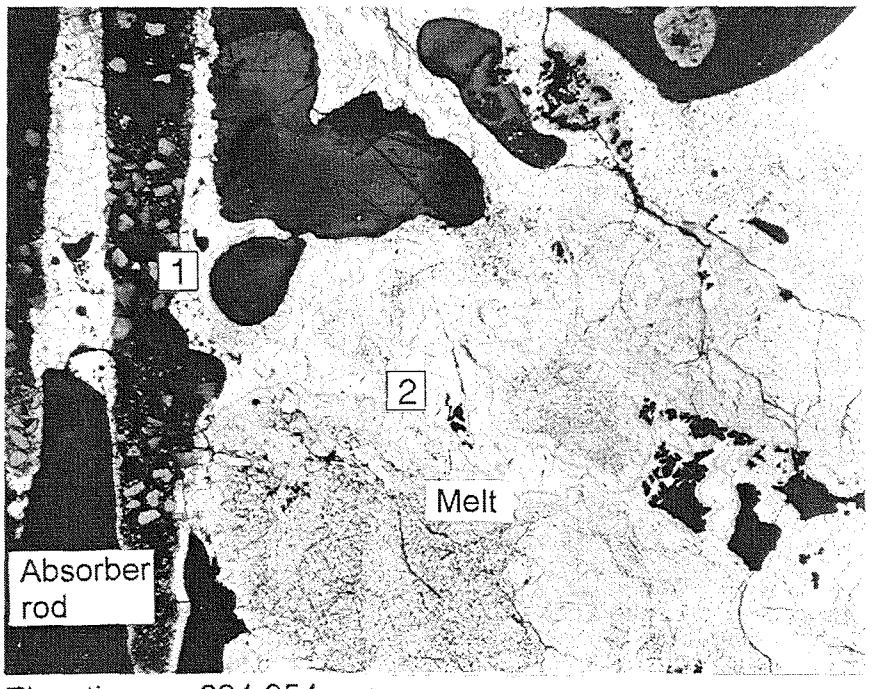

Elevation ca. 224-254 mm

5 mm

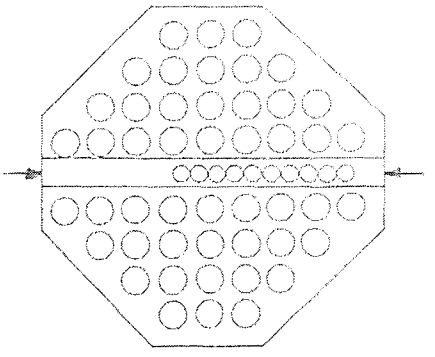

Melt Pos 2

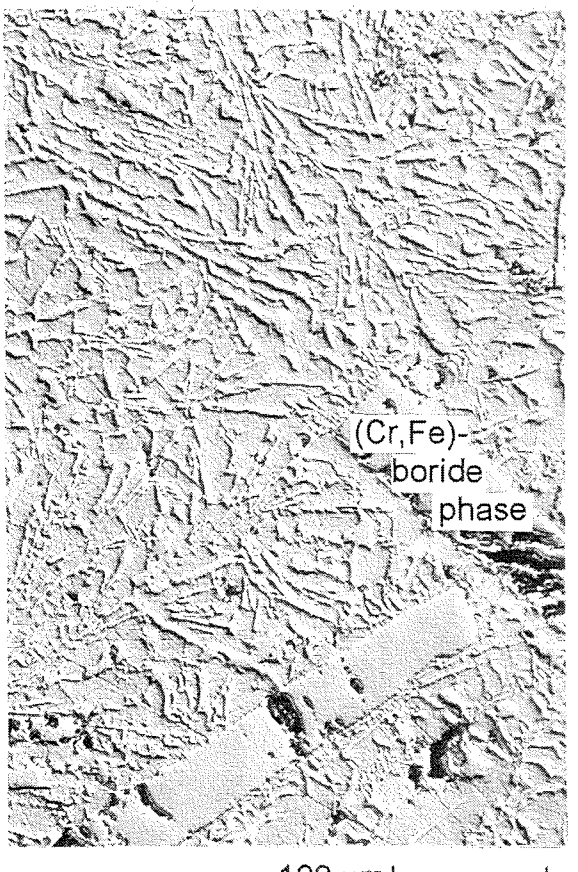

100 µm

Absorber rod Pos 1

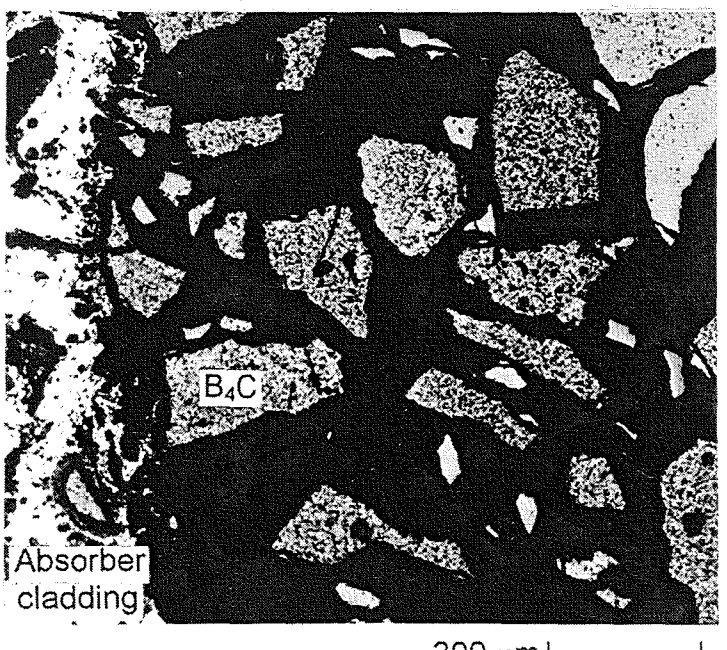

300 µm

Fig. 112:
Vertical Section CORA-18-c-L, Elevation 114-254 mm
Absorber Blade Remnants, Embedded by Melt

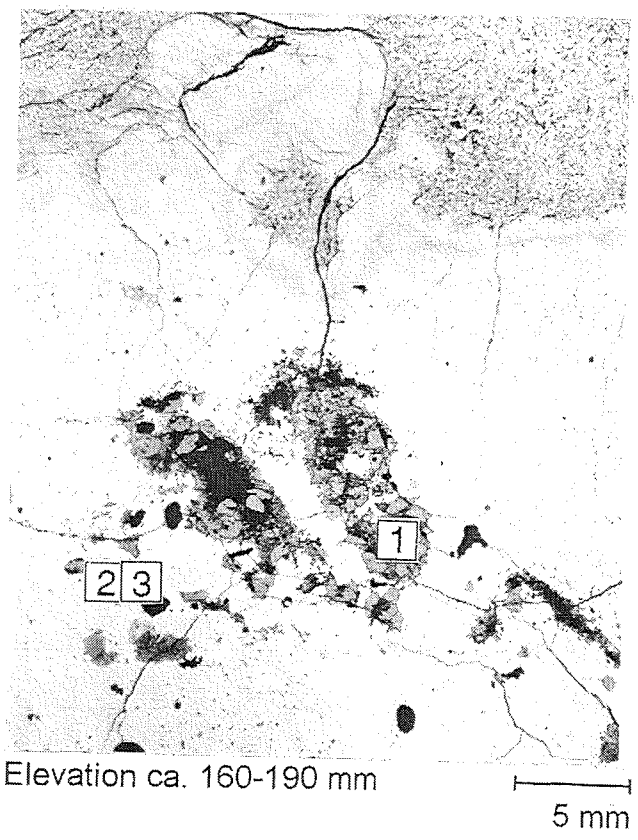

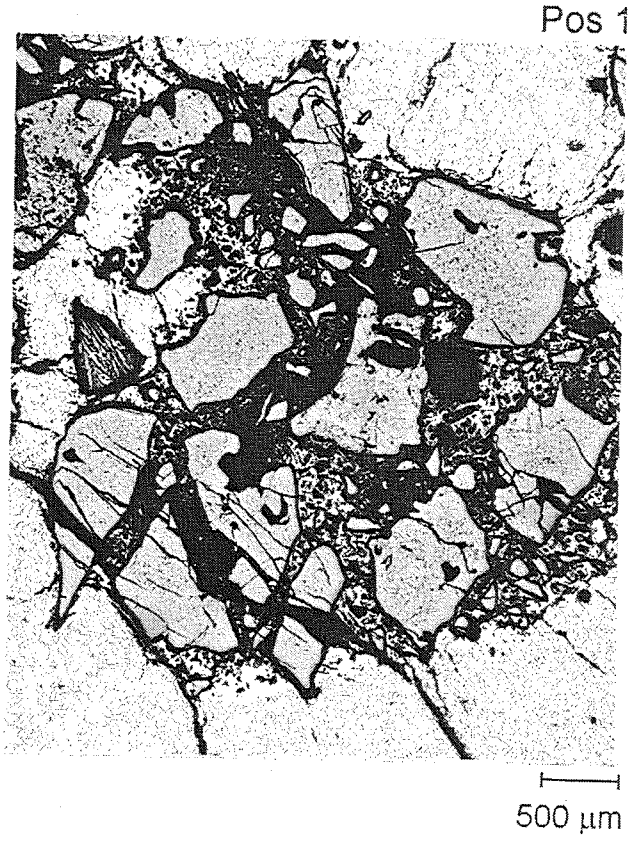

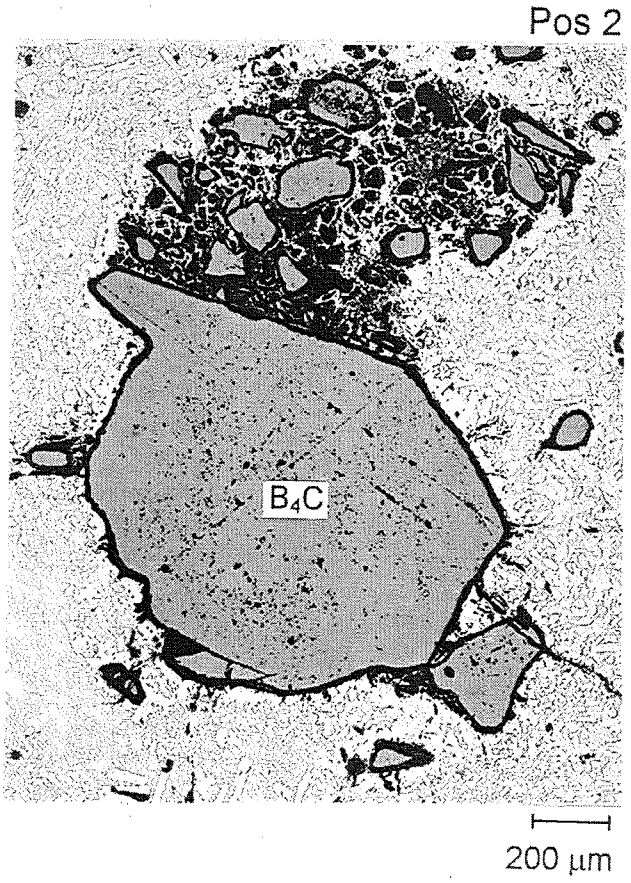

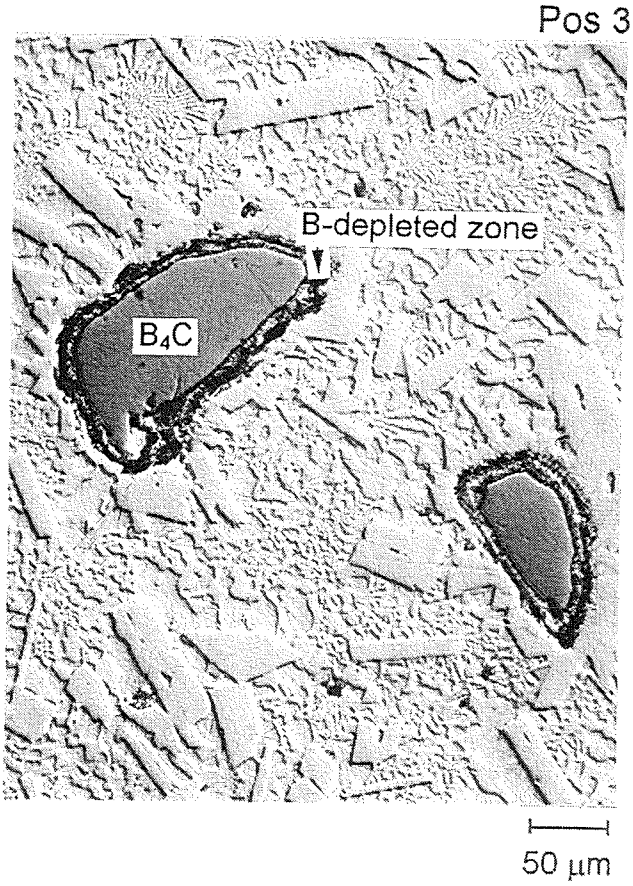

Fig. 113:
Vertical Section CORA-18-c-L, Elevation 114-254 mm
B_4C Particles, Embedded by Melt; Start of Dissolution

Selective forms of melt surface oxidation

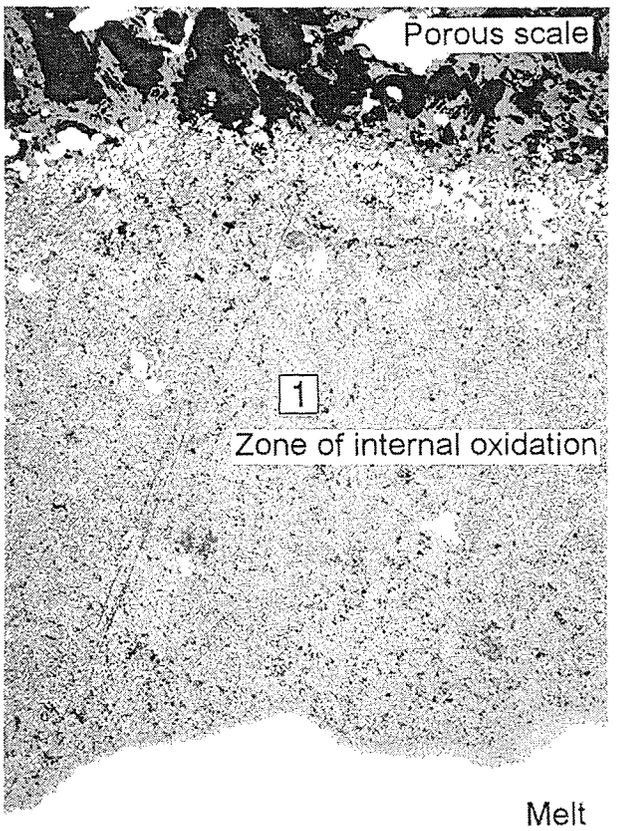

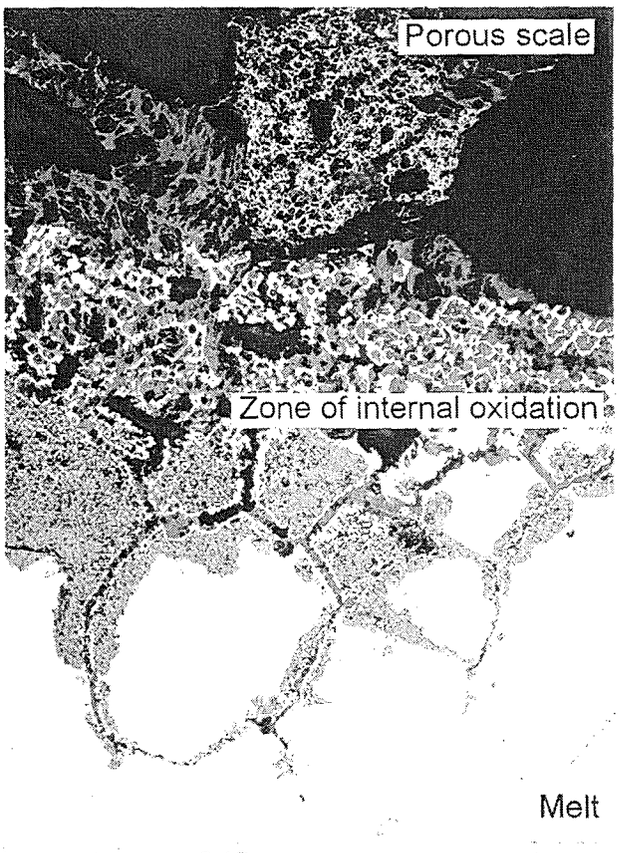

Oxidation zone metallic/ceramic

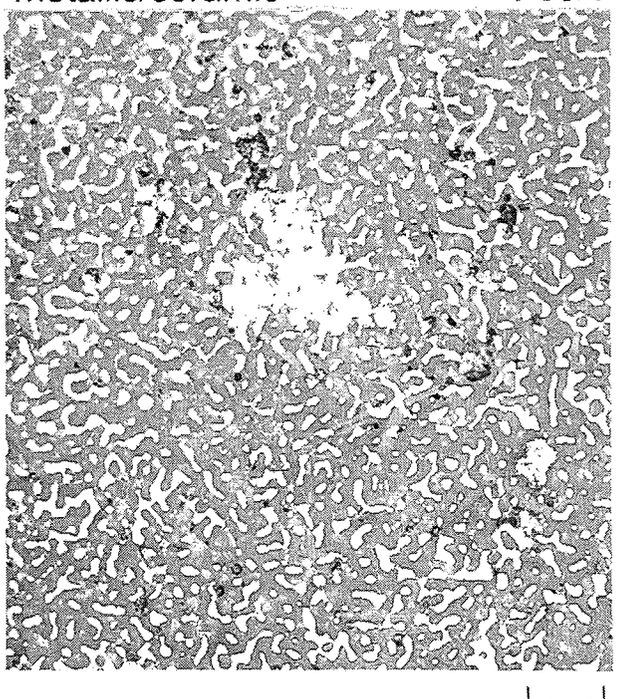

Transition between duplex and single phase melt microstructure

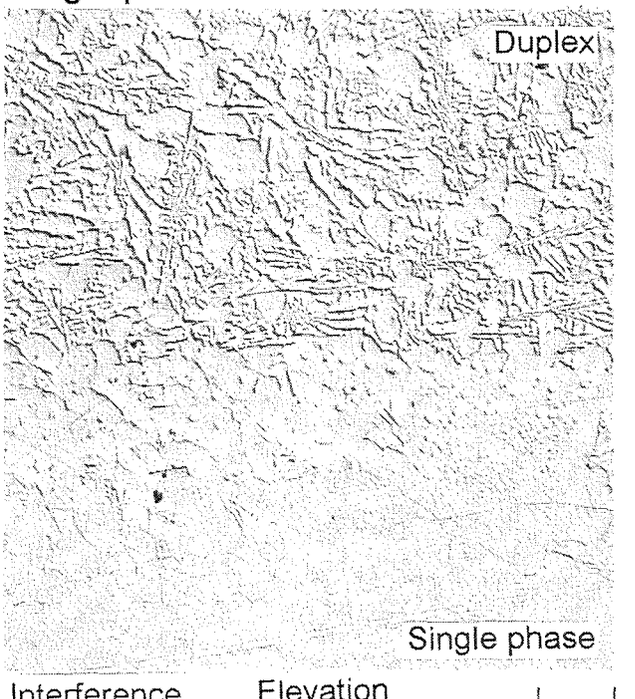

Fig. 114:
Vertical Section CORA-18-c-L, Elevation 114-254 mm
Melt Microstructure, Oxidation

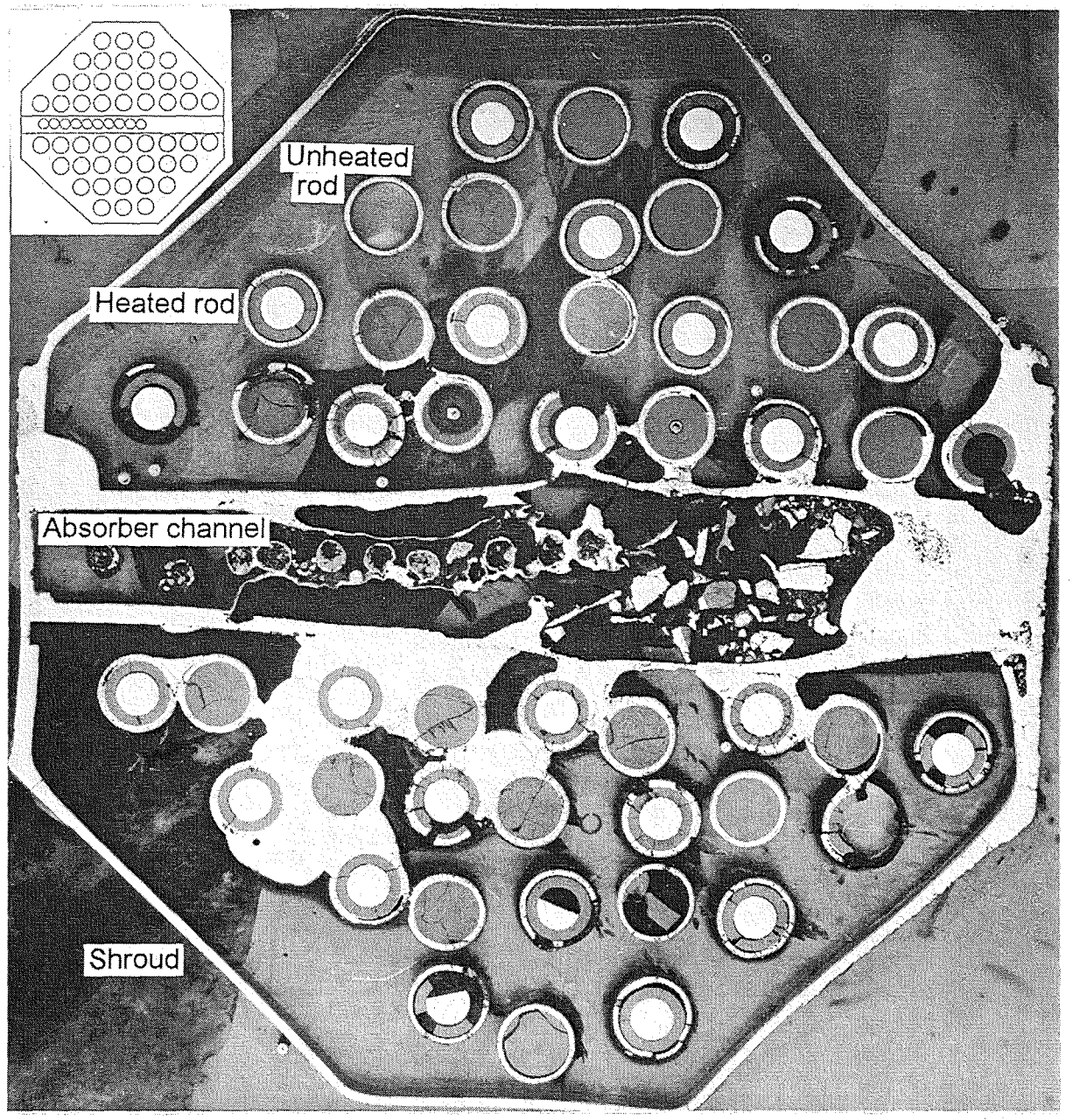

Fig. 115:
Cross Section CORA-18-03 (top), Elevation 269 mm Overview

Metallic melt between fuel rods

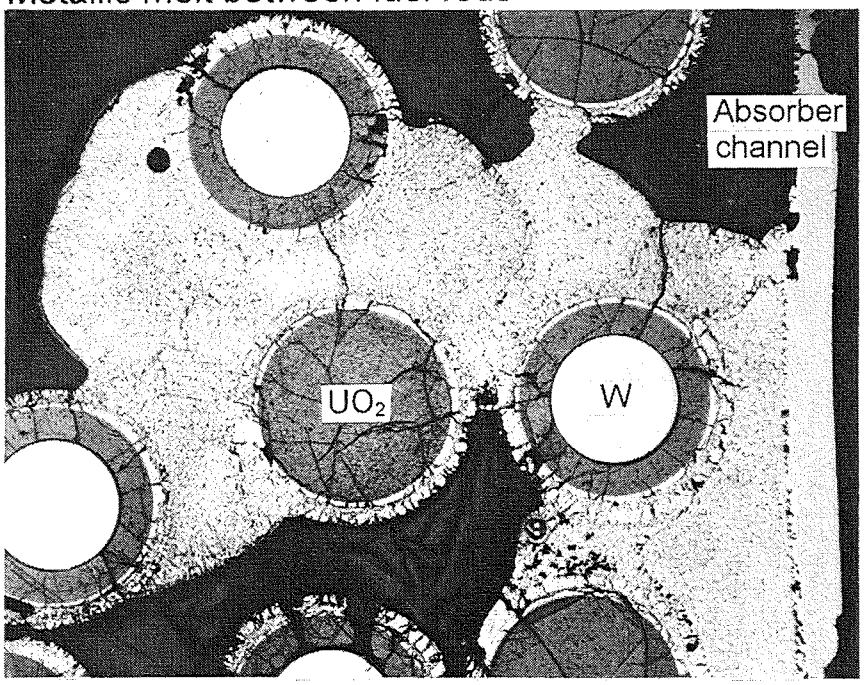

Pos. 1

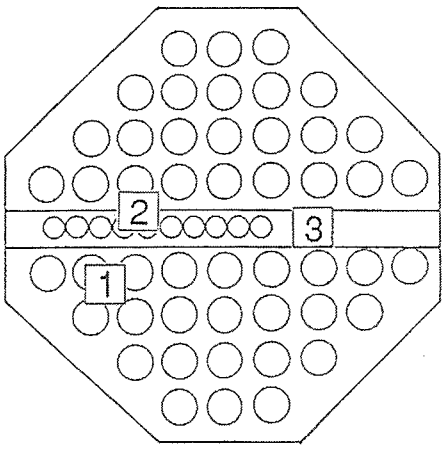

5 mm

Residues of absorber blade

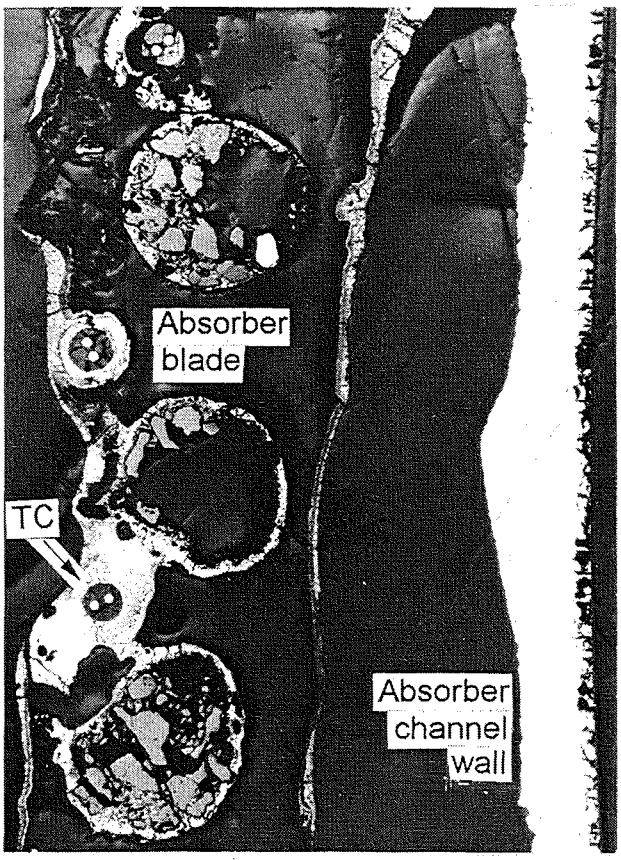

Pos. 2

3 mm

Rubble within absorber channel

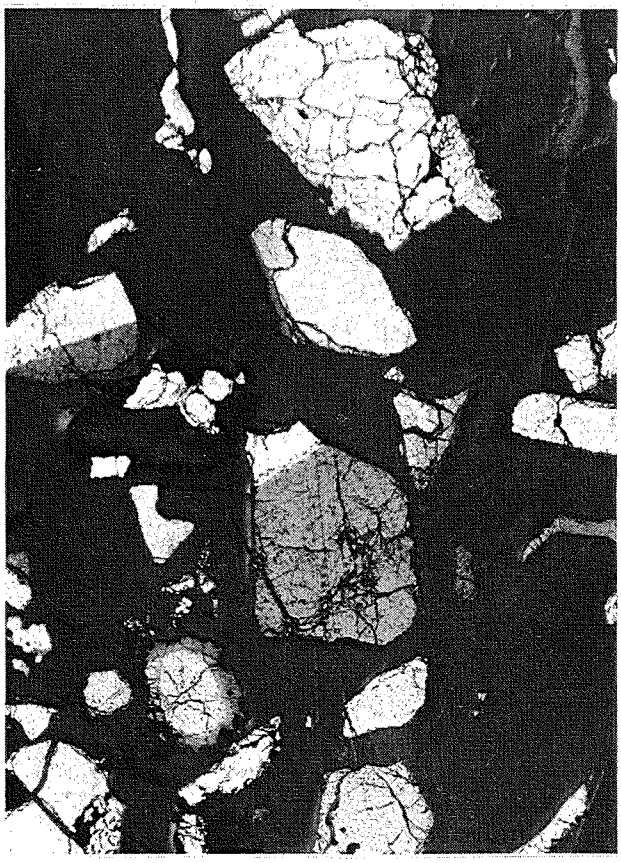

Pos. 3

3 mm

Fig. 116:
Cross Section CORA-18-03 (top), Elevation 269 mm
Macrographs of Absorber Blade, Melt and Fragments

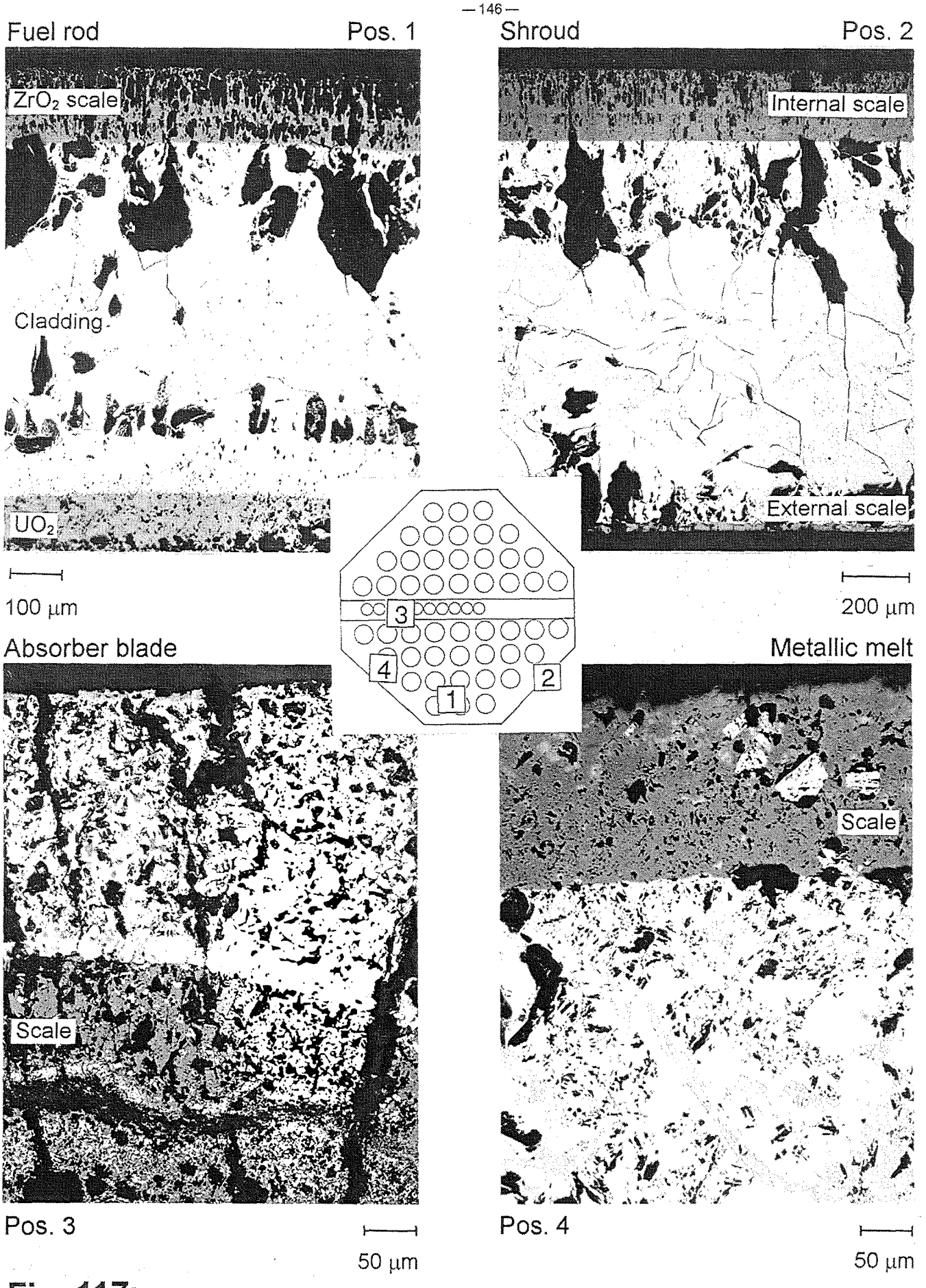

Fig. 117:

Cross Section CORA-18-03 (top), Elevation 269 mm
Oxidation Status of Bundle Components and Products

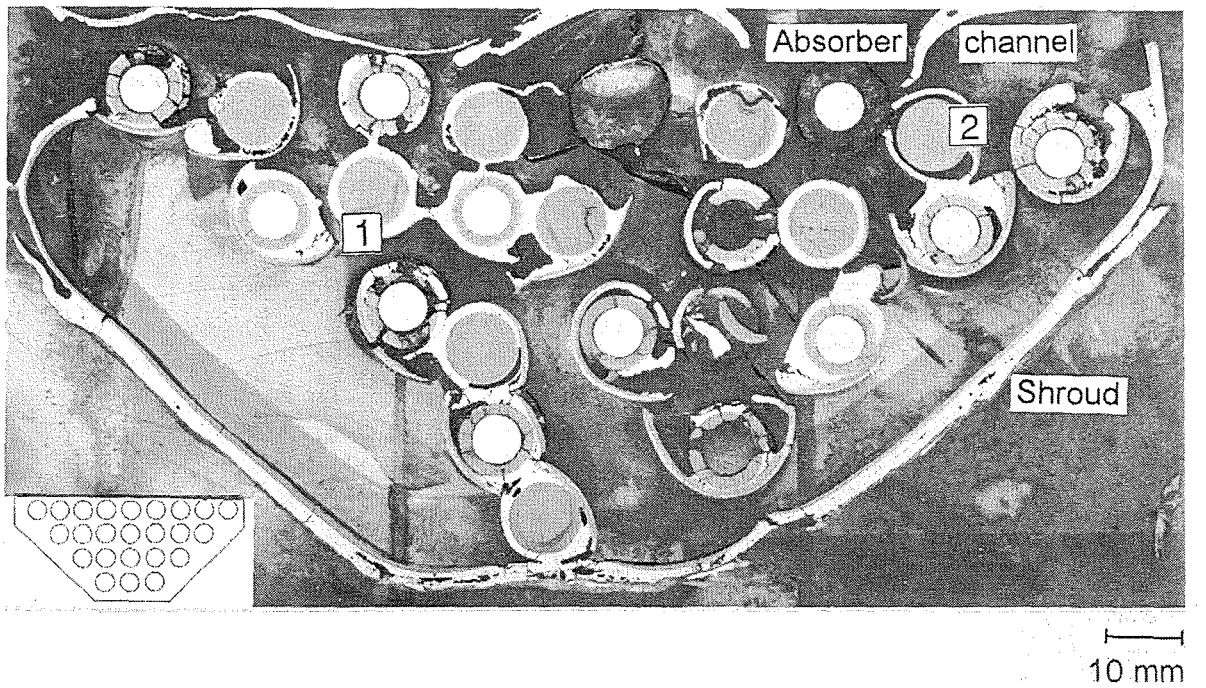

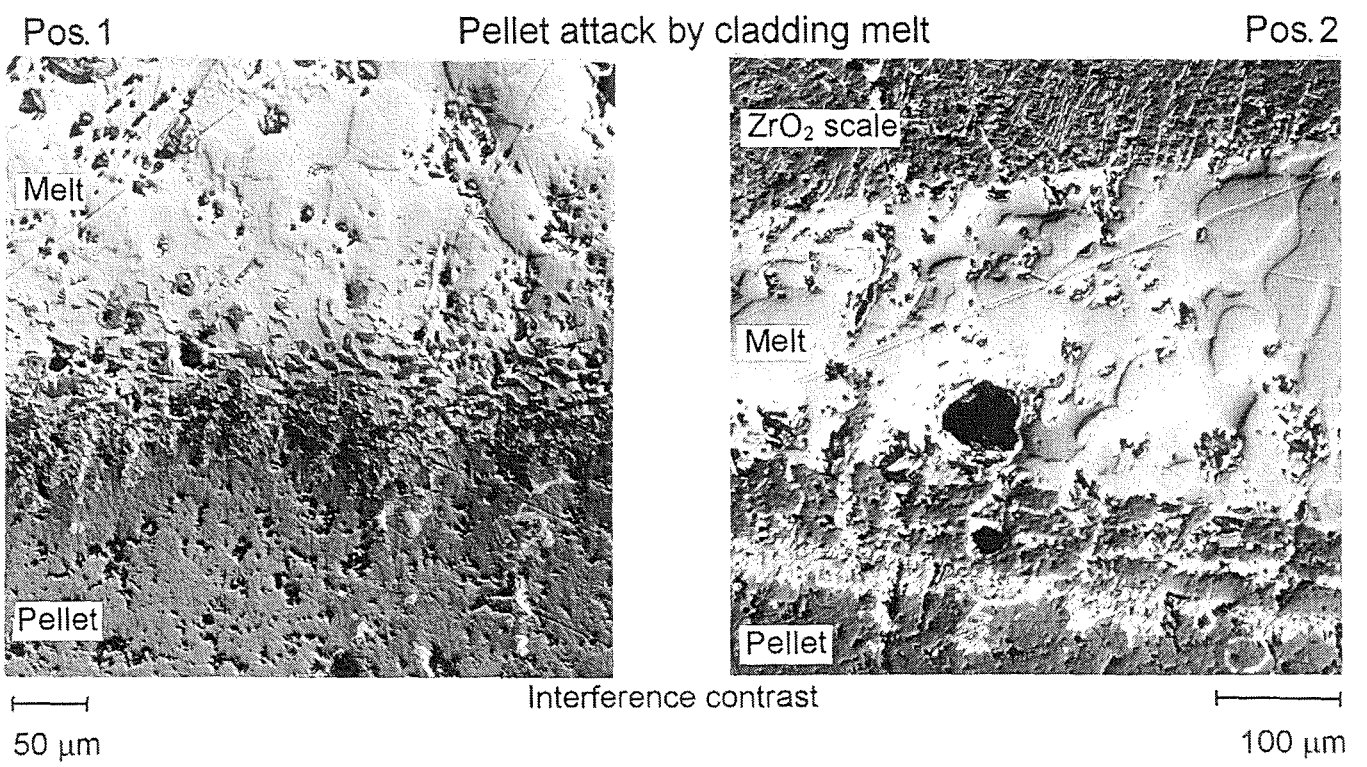

Fig. 118:
Cross Section CORA-18-04 (top), Elevation 413 mm Overview; Detectable Fuel Pellet Dissolution

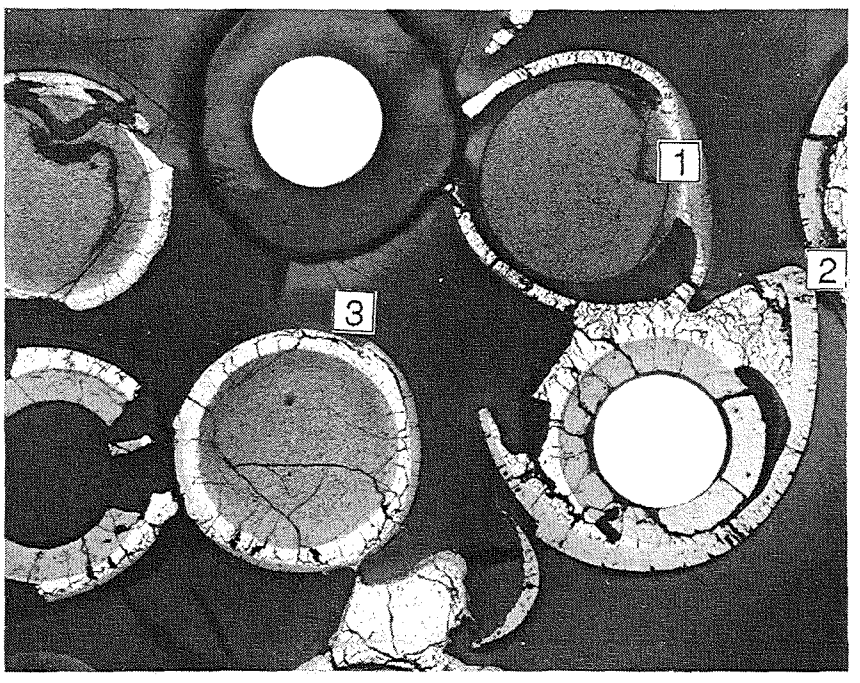

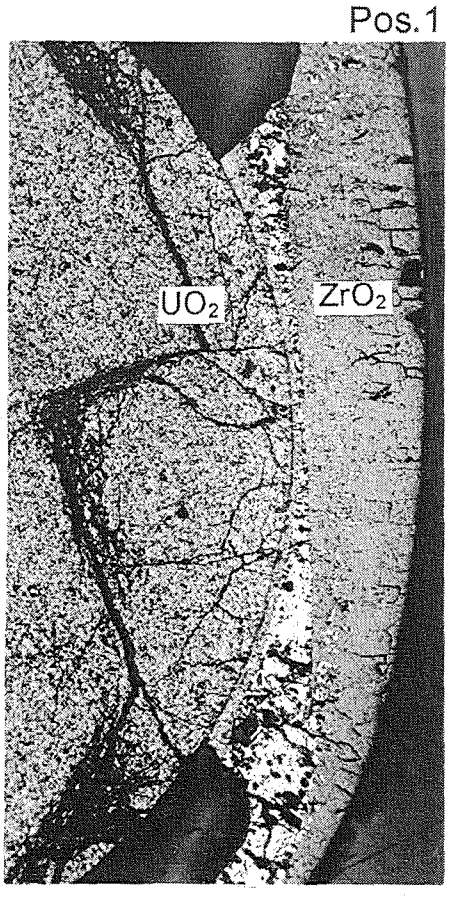

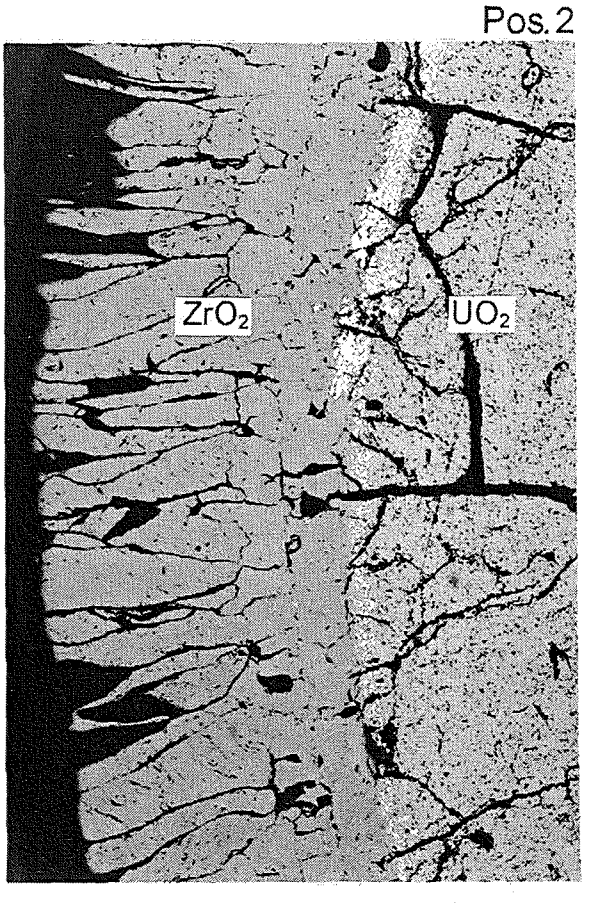

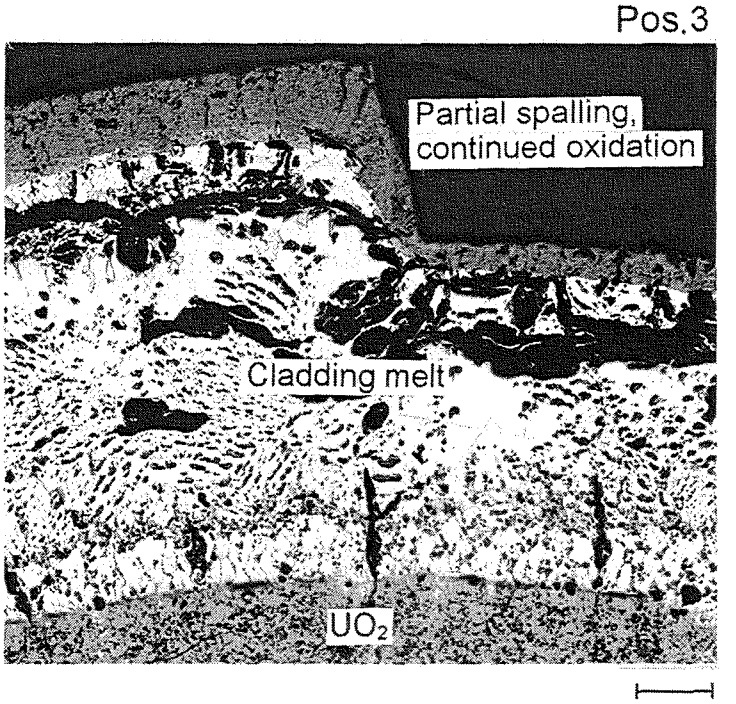

Fig. 119:
Cross Section CORA-18-04 (top), Elevation 413 mm
Cladding Oxidation

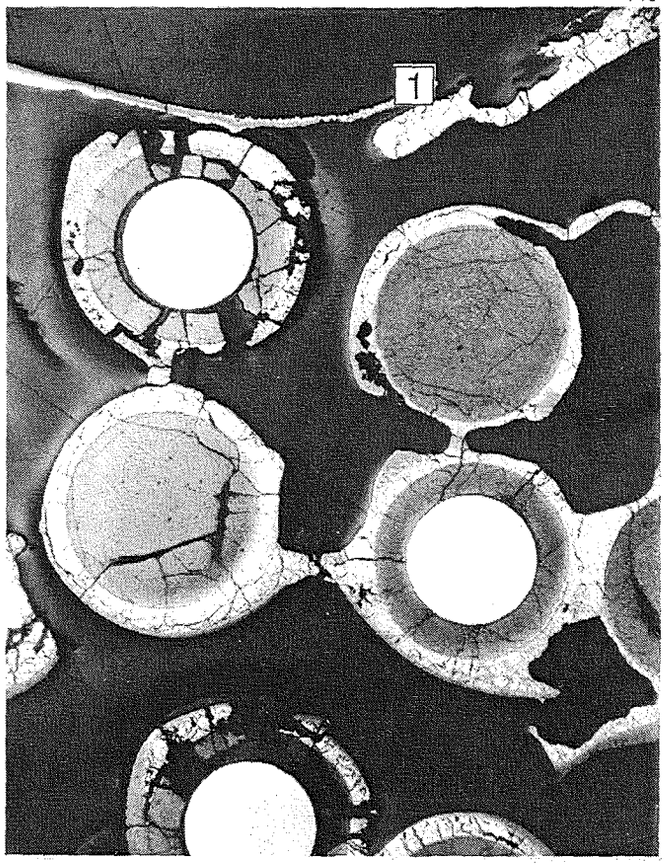

Channel box Pos 1

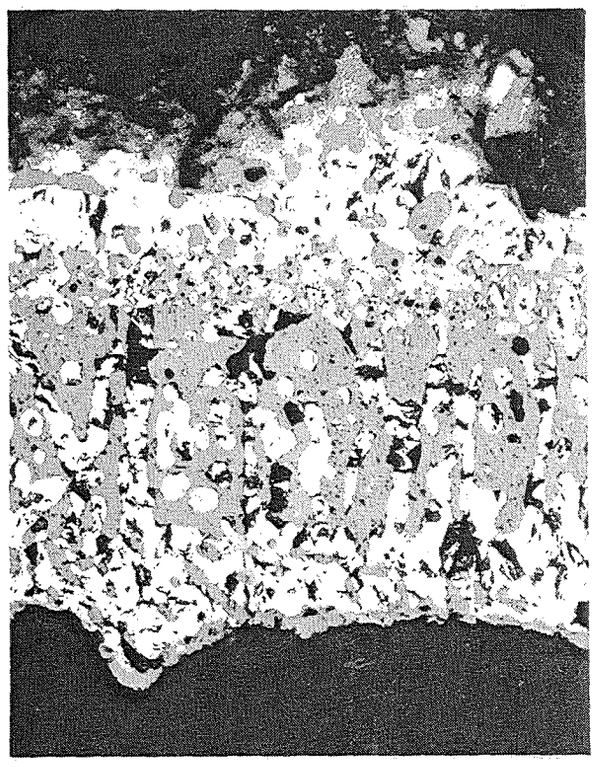

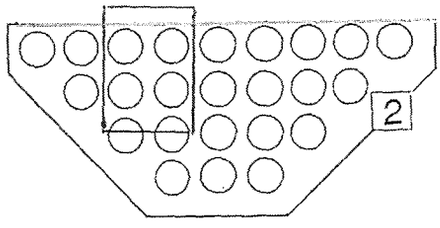

Shroud Pos 2

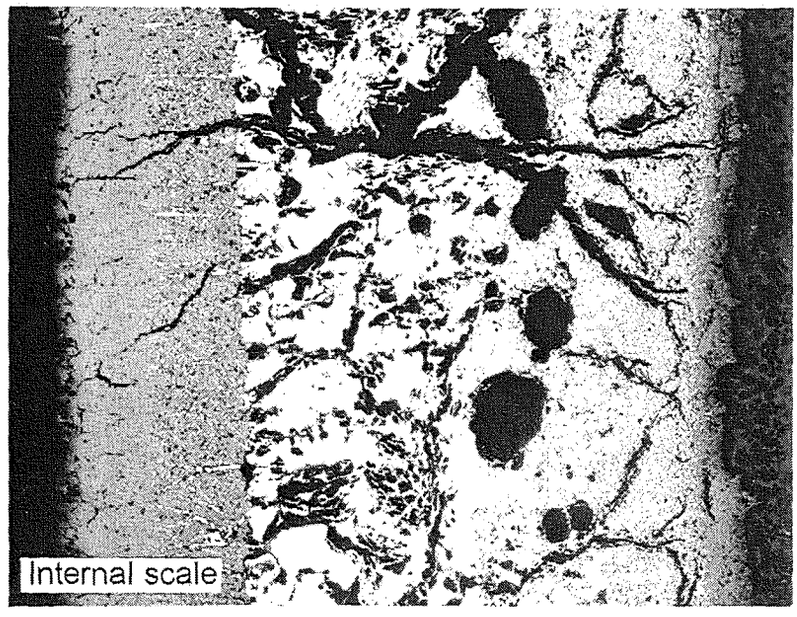

Fig. 120:
Cross Section CORA-18-04 (top), Elevation 413 mm
Components Oxidation

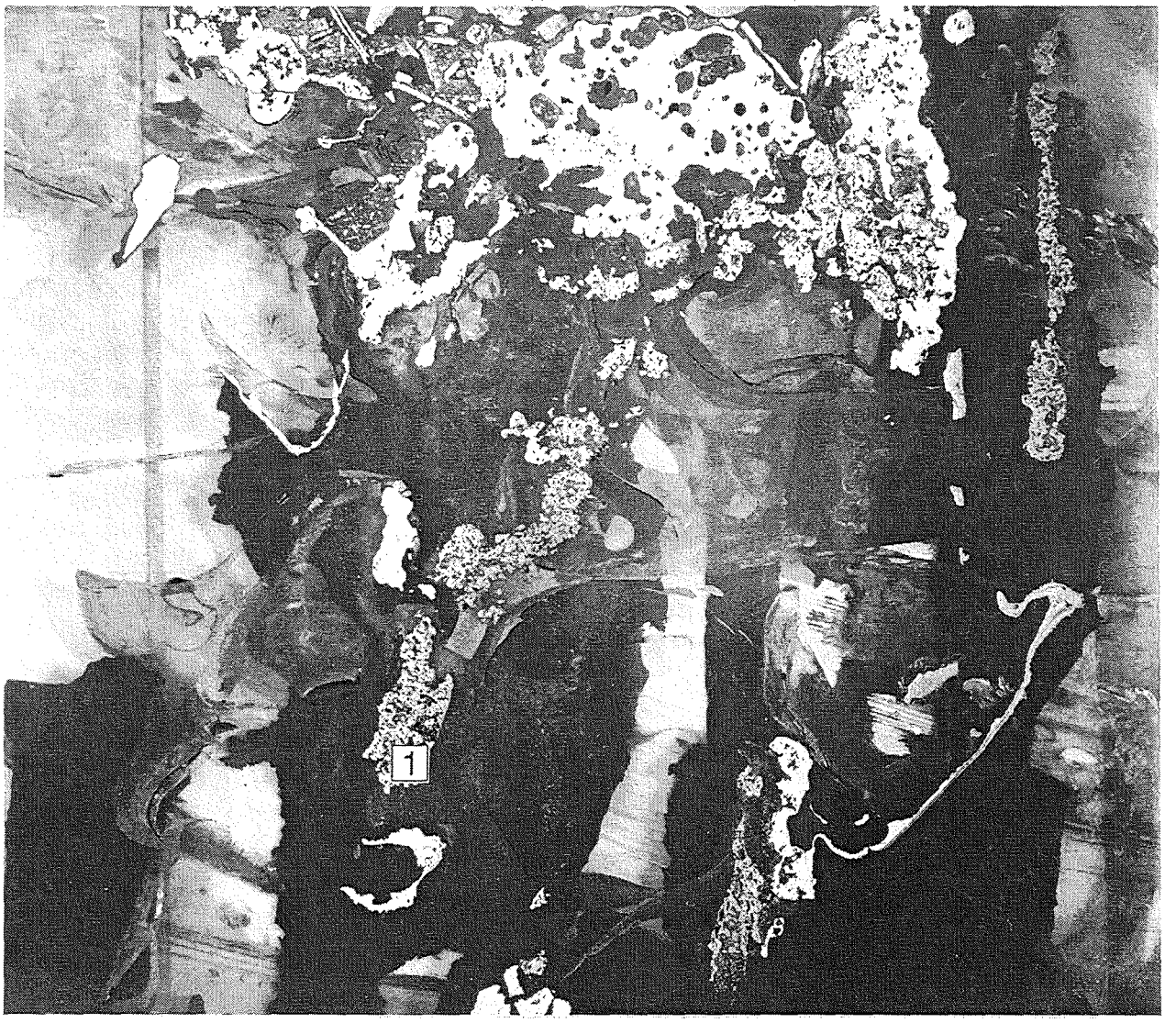

10 mm

Pos.1

Example of absorber melt microstructure

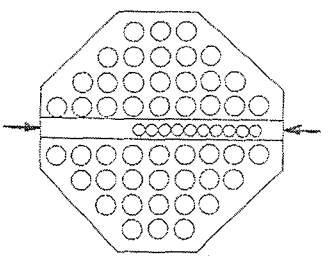

100 µm

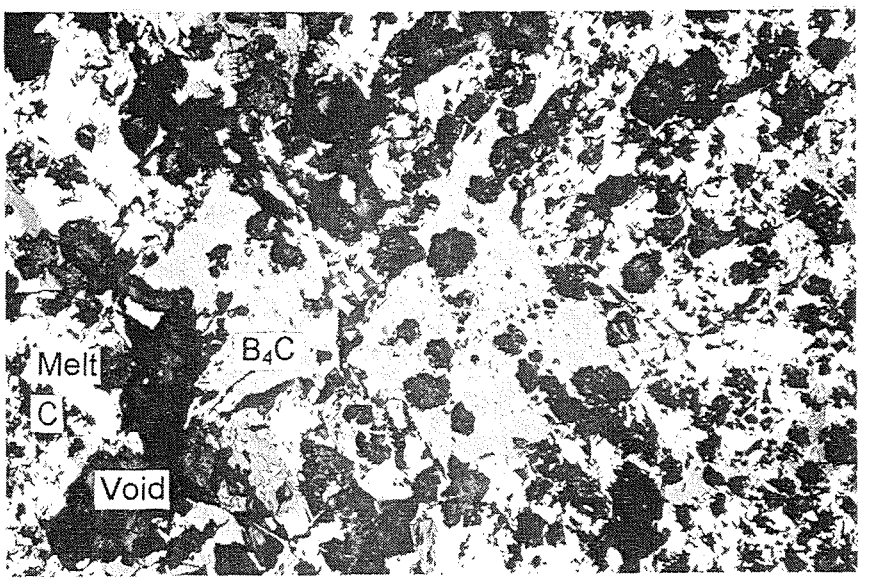

Fig. 121:
Vertical Section CORA-18-e-L, Elevation 415-545 mm
Overview on Absorber Channel; Typical Absorber Melt

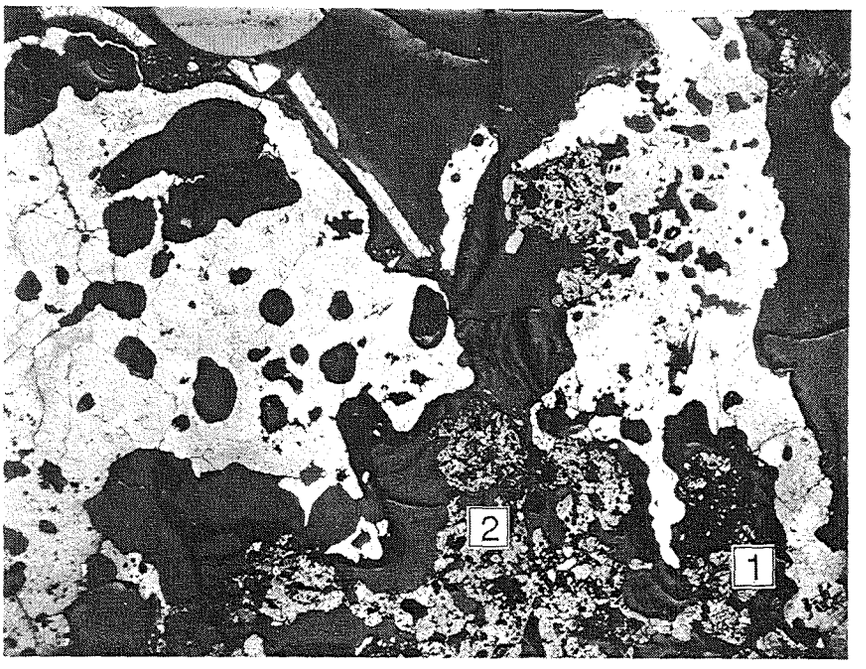

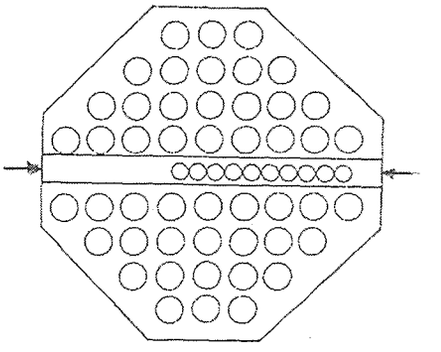

Elevation ca. 515-545 mm

5 mm

Residual boron carbide
in modified steel melt

Pos. 1

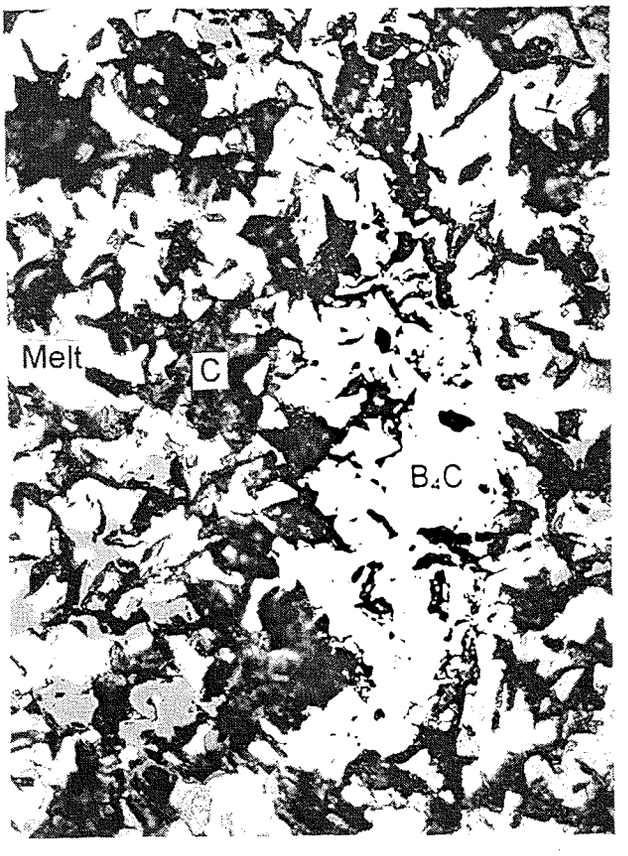

20 µm

Residual carbon
in acicular form

Pos. 2

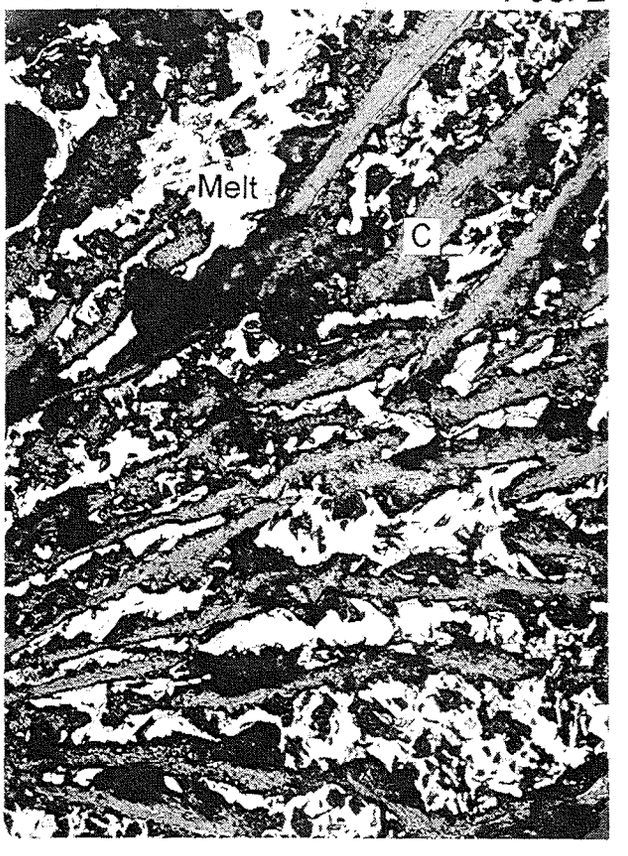

50 µm

Fig. 122:
Vertical Section CORA-18-e-L, Elevation 415-545 mm
Morphologies of Absorber Melt

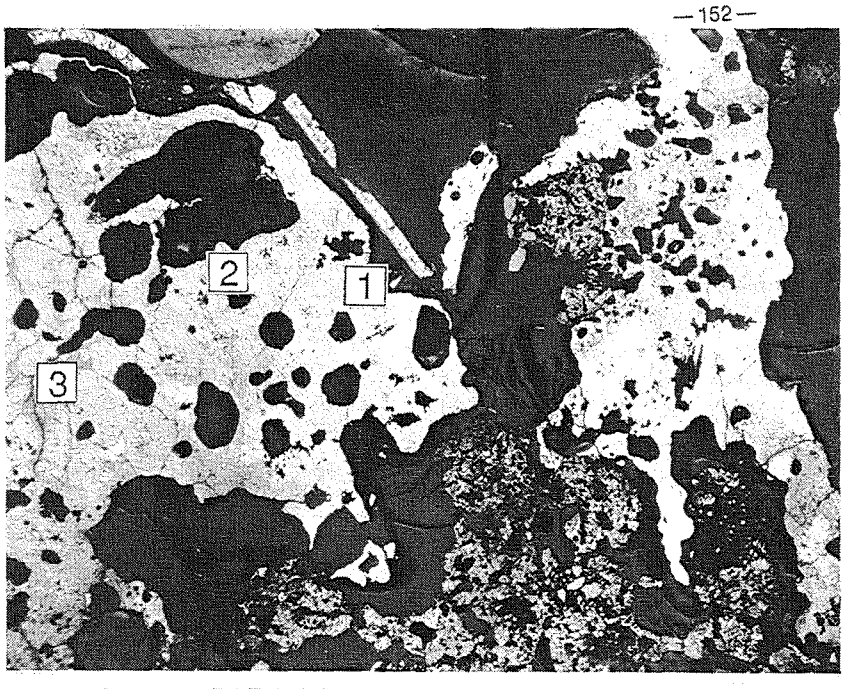

Elevation ca. 515-545 mm

5 mm

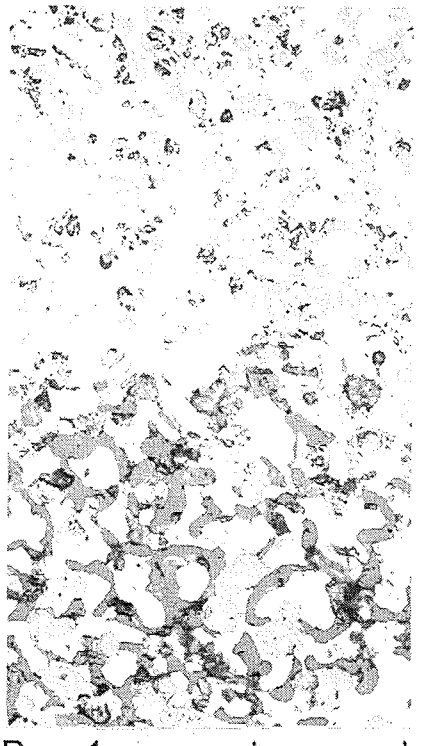

Pos. 1

40 µm

Pos. 2

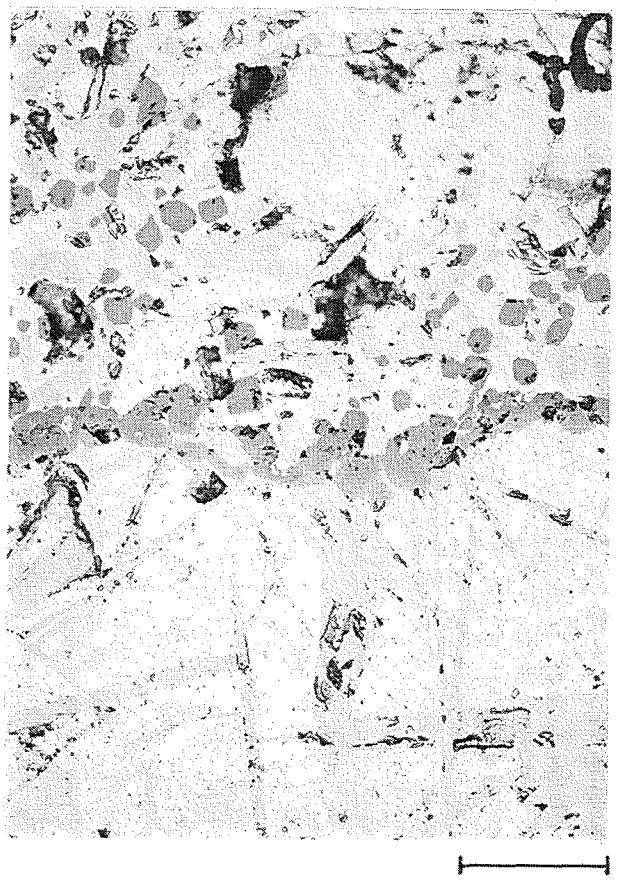

40 µm

Pos. 3

40 µm

Fig. 123:
Vertical Section CORA-18-e-L, Elevation 415-545 mm
Morphologies of Melt within Absorber Channel

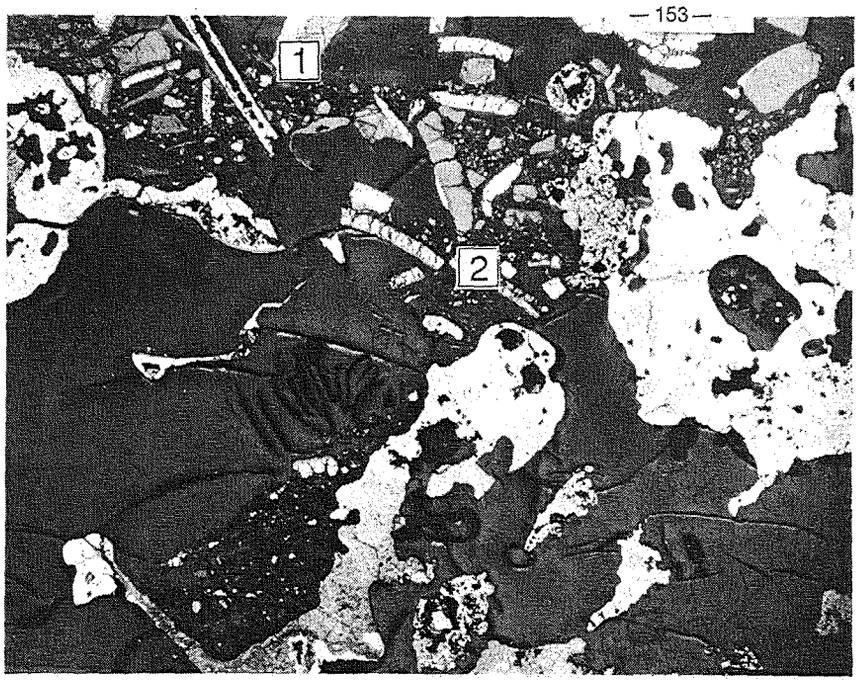

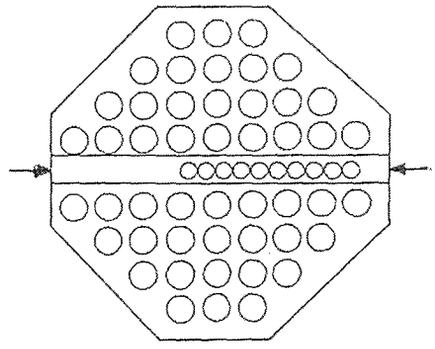

Elevation ca. 515-545 mm

5 mm

Fuel pellet fragment
in contact with melt

Pos. 1

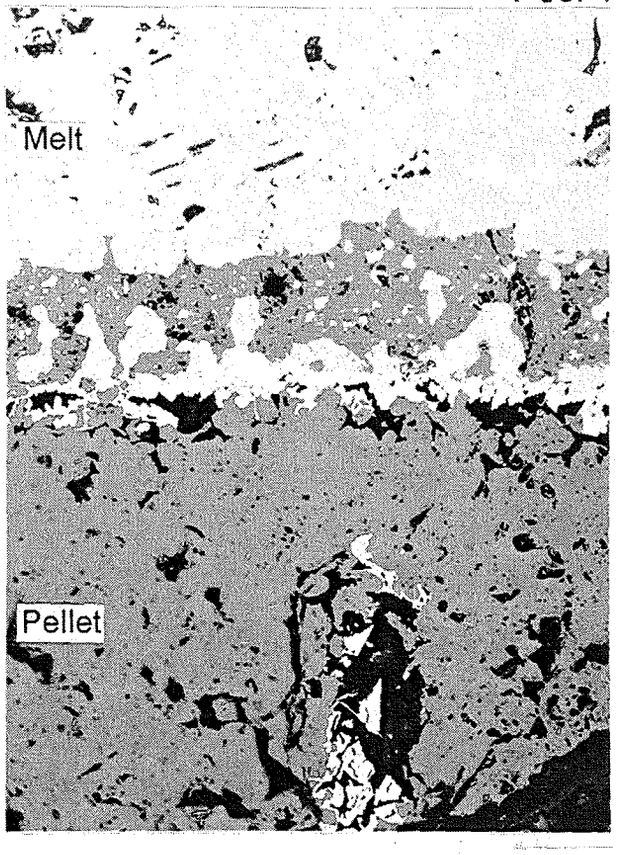

50 µm

Fuel cladding fragment

Pos. 2

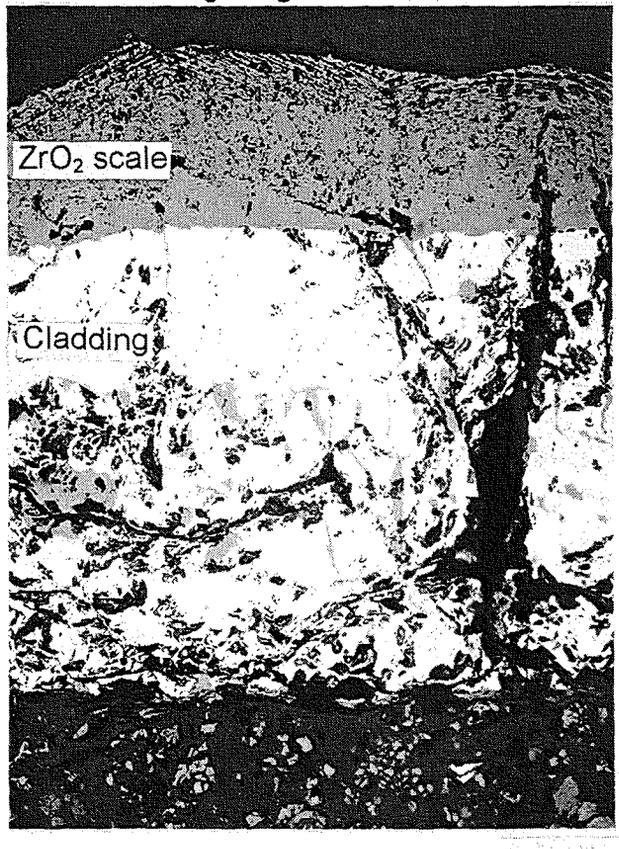

100 µm

Fig. 124:

Vertical Section CORA-18-e-L, Elevation 415-545 mm Rubble Fragments After Relocation Within Absorber Channel

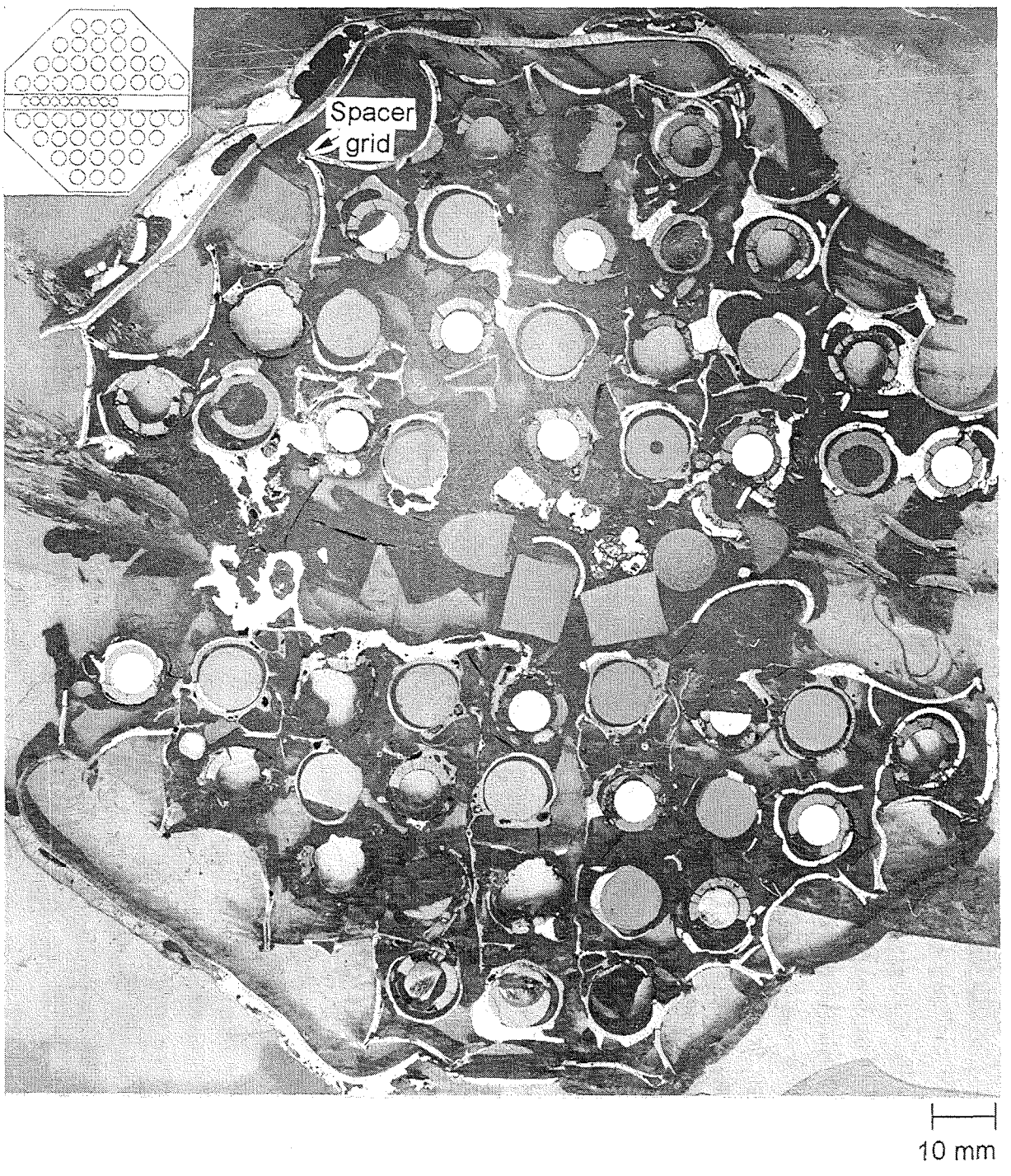

Fig. 125:
Cross Section CORA-18-05 (top), Elevation 560 mm Overview

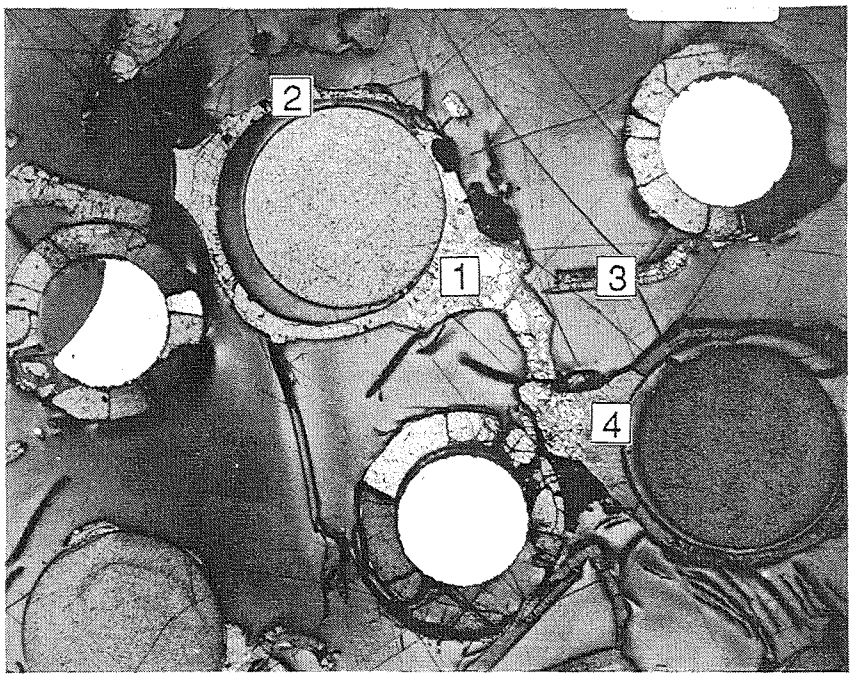

Melt microstructure Pos. 1

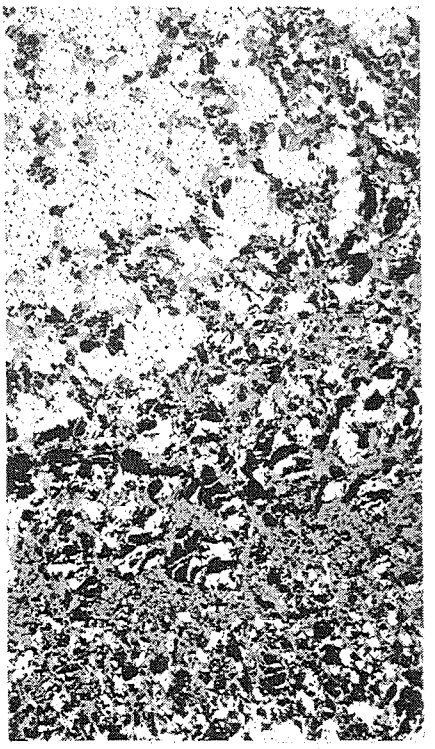

Oxidized fuel rod cladding Pos. 2

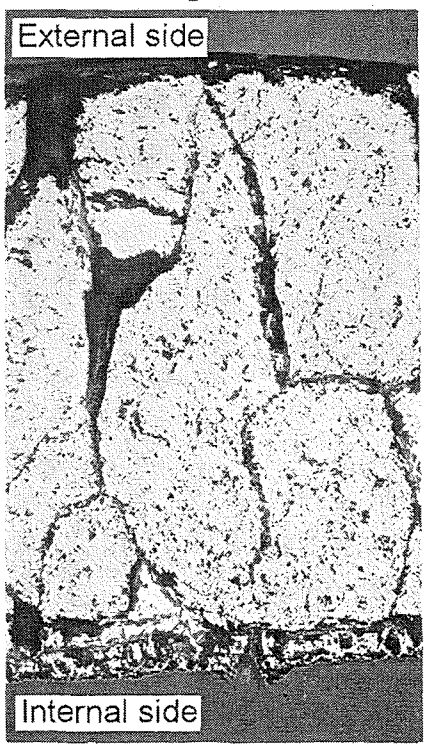

Oxidized fragment Pos. 3

Melt microstructure Pos. 4

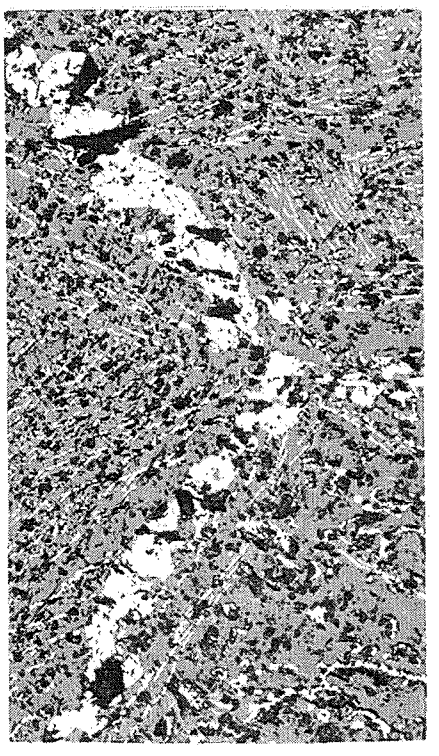

Fig. 126:
Cross Section CORA-18-05 (top), Elevation 560 mm
Details of Fuel Rod Region

Oxidized spacer grid Pos.1

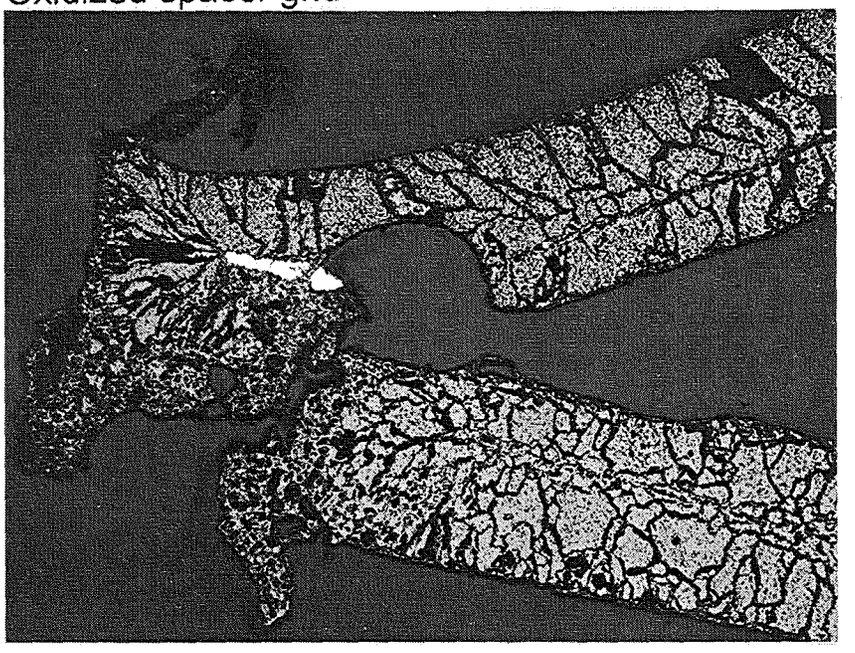

500 µm

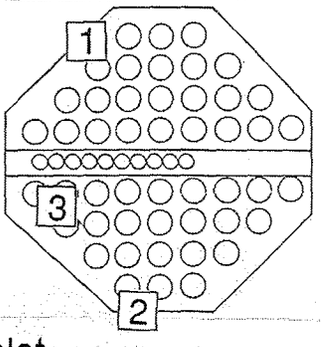

Oxidizing Zry structure after partial scale spalling during deformation Pos.2

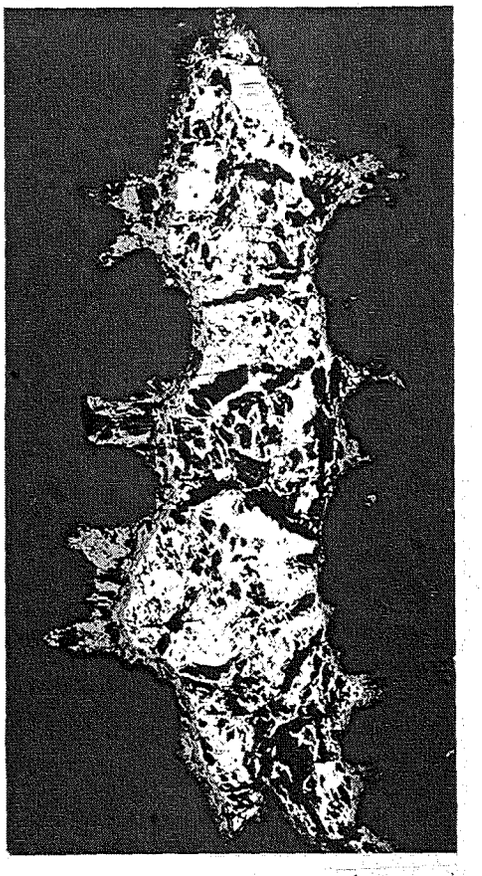

200 µm

Oxidized melt droplet Pos.3

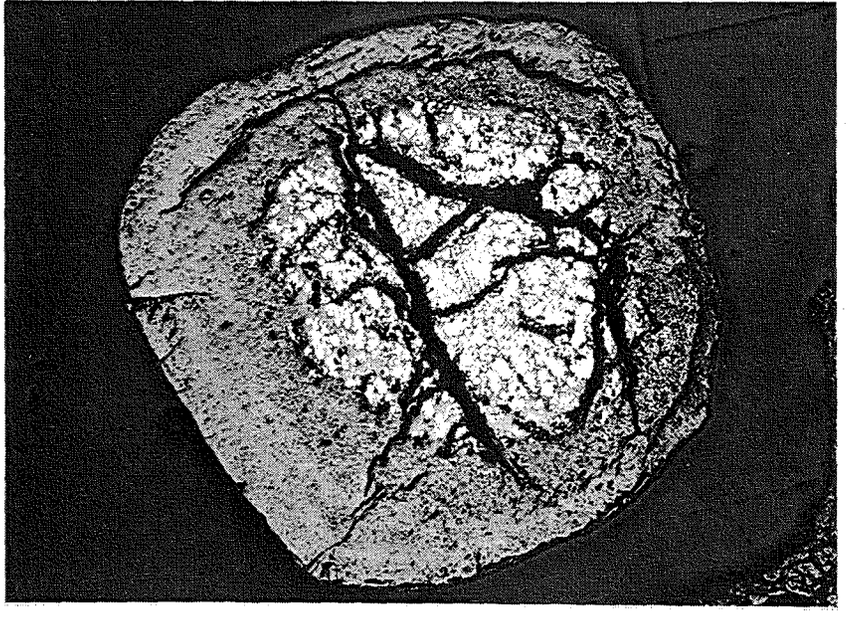

500 µm

Fig. 127:
Cross Section CORA-18-05 (top), Elevation 560 mm
Morphologies of Oxide Scales

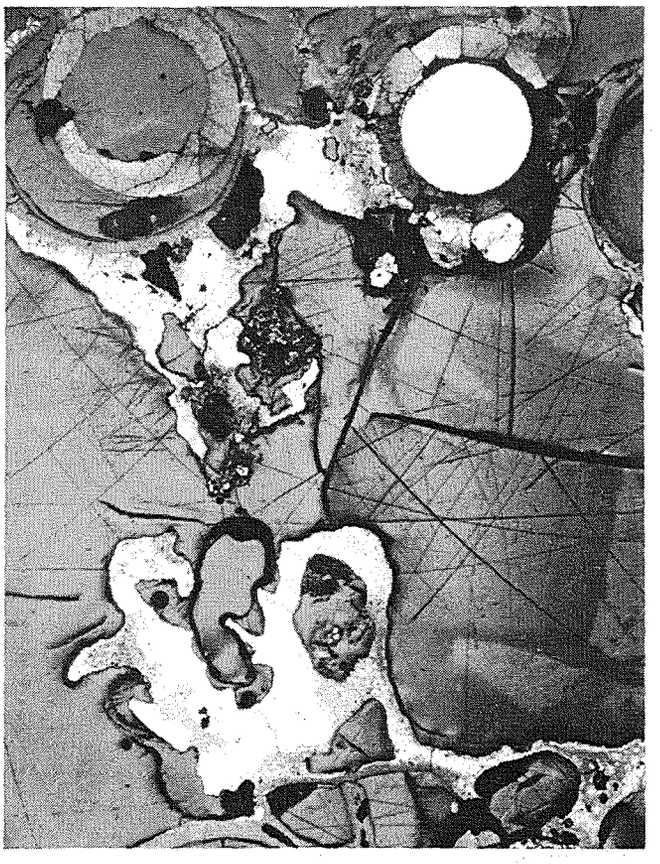

5 mm

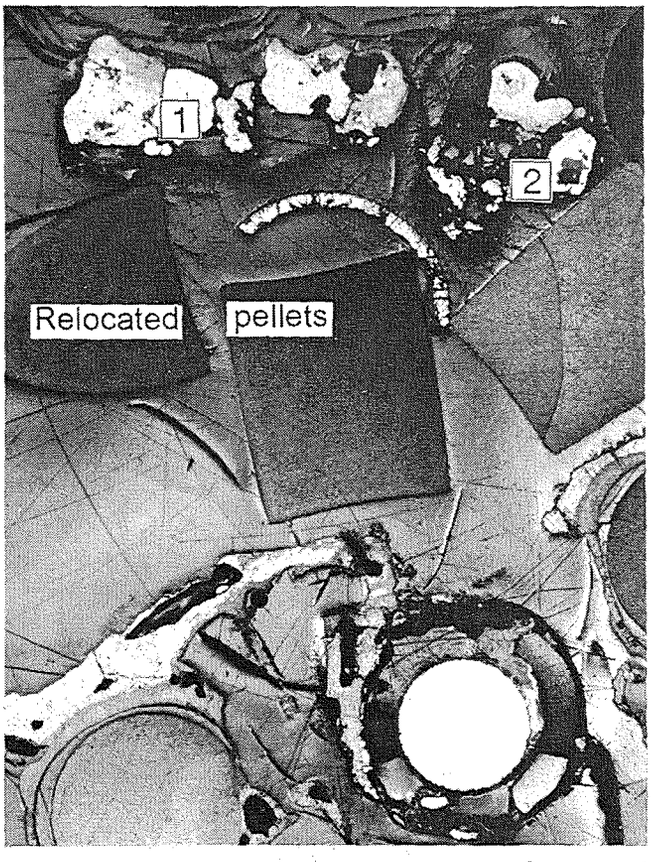

5 mm

Embedded and partly dissolved B_4C particle Pos.1

40 µm

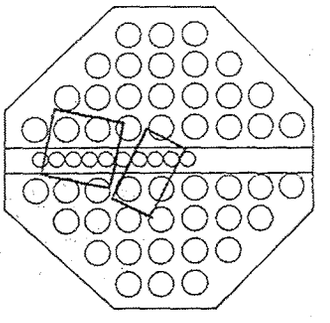

Free surface of non-oxidized melt Pos.2

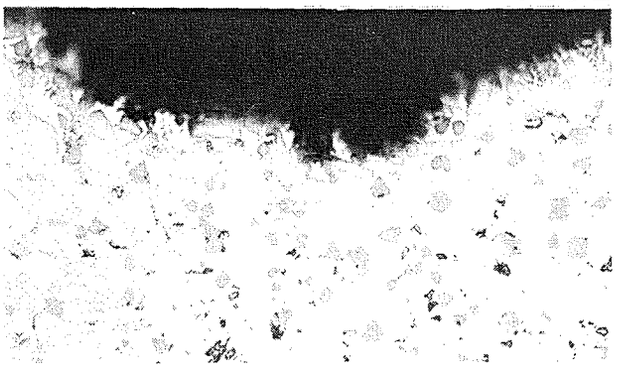

20 µm

Fig. 128:
Cross Section CORA-18-05 (top), Elevation 560 mm
Details of Absorber Blade Region

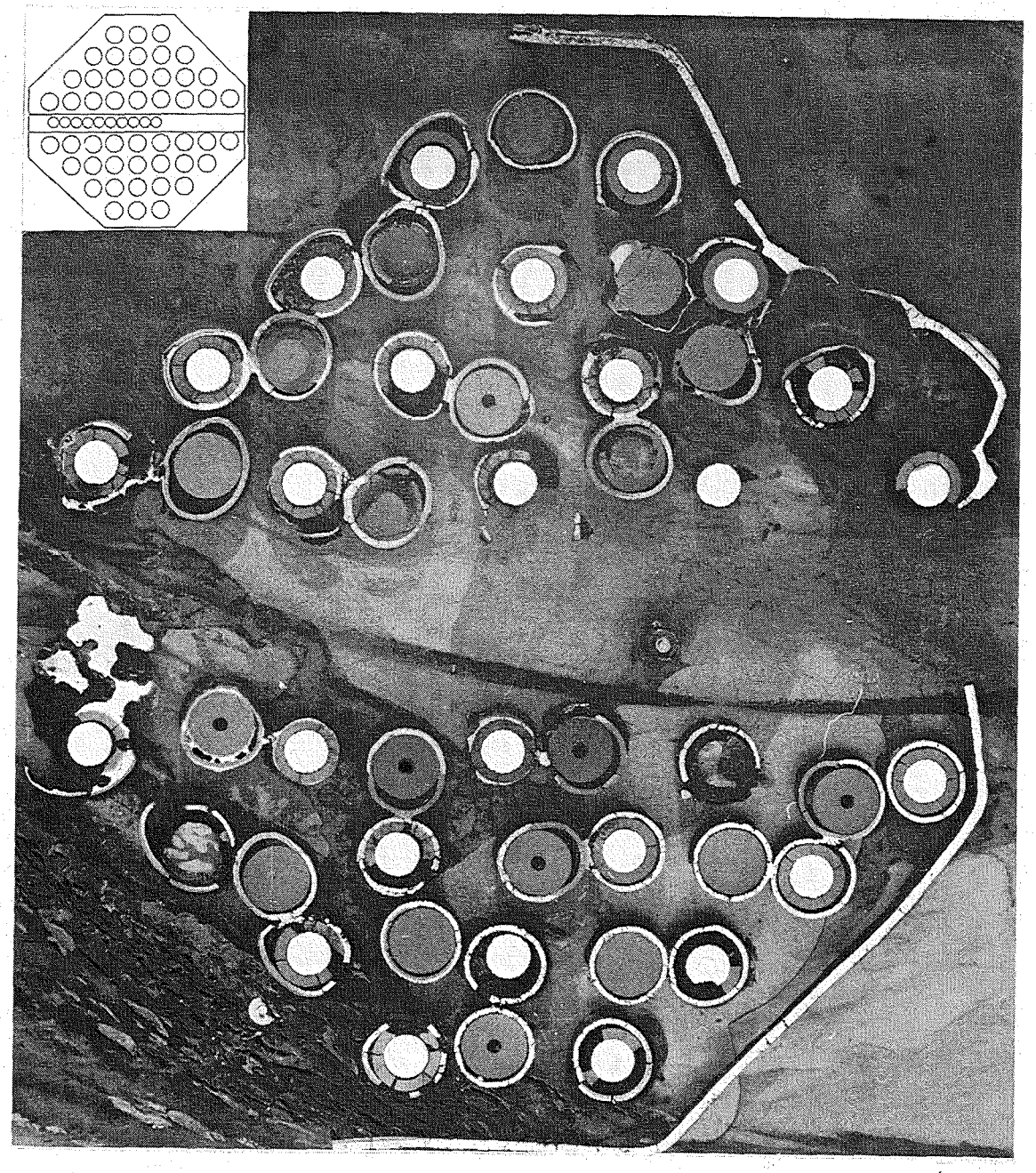

Fig. 129:
Cross Section CORA-18-06 (top), Elevation 717 mm
Overview on Remaining Fuel Rod Regions

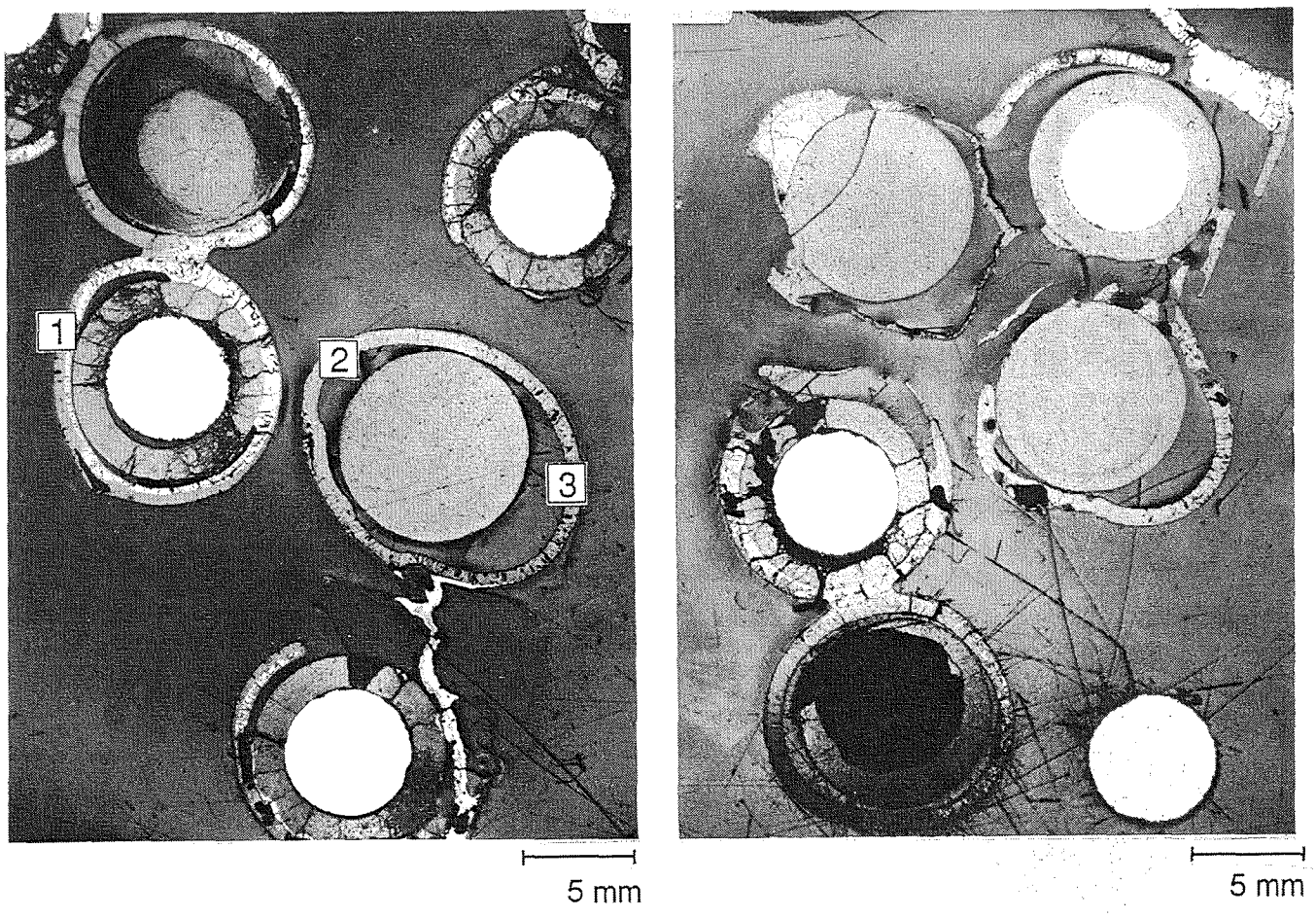

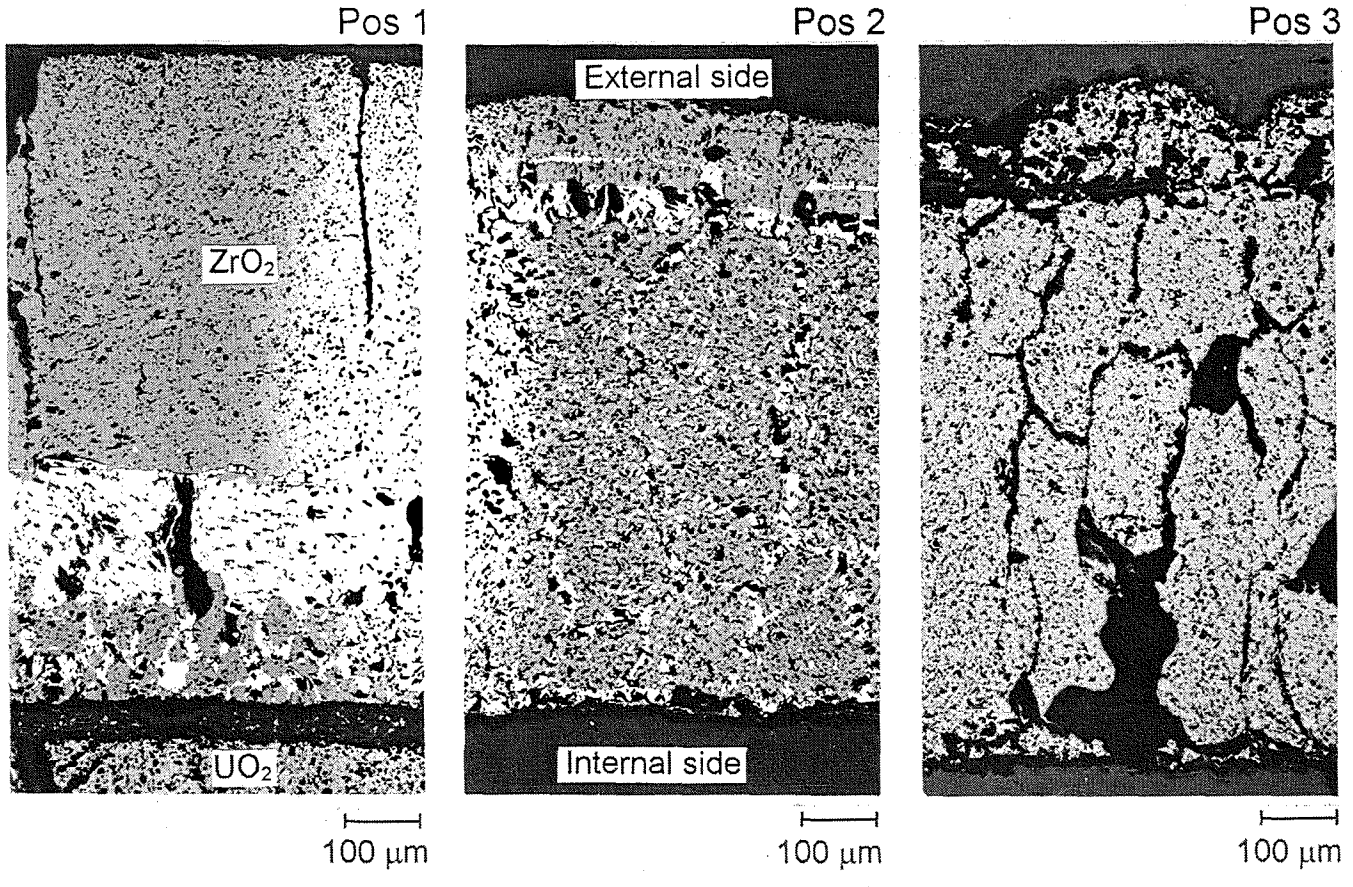

Fig. 130:
Cross Section CORA-18-06 (top), Elevation 717 mm
Extent of Cladding Oxidation

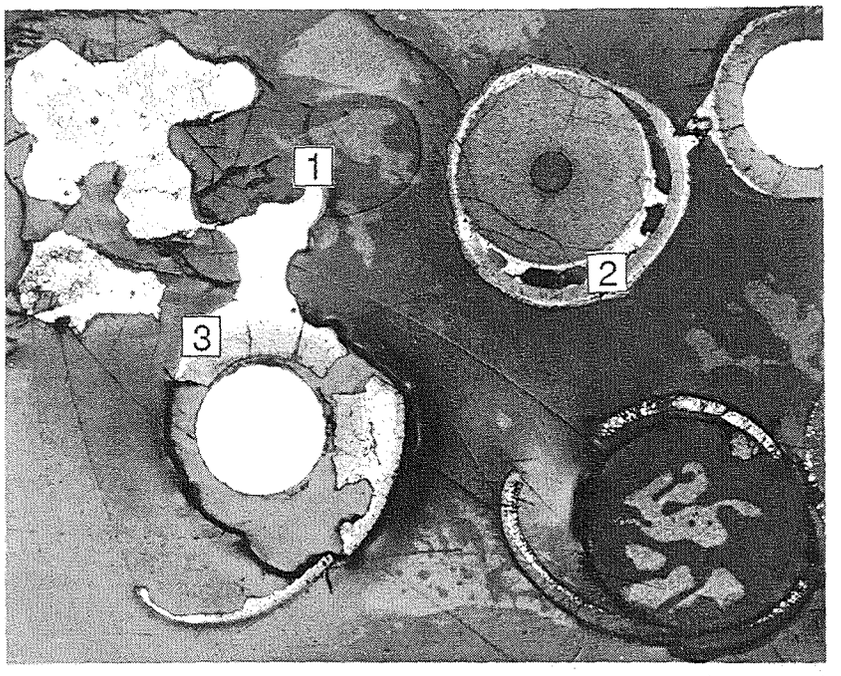

Melt oxidation Pos.1

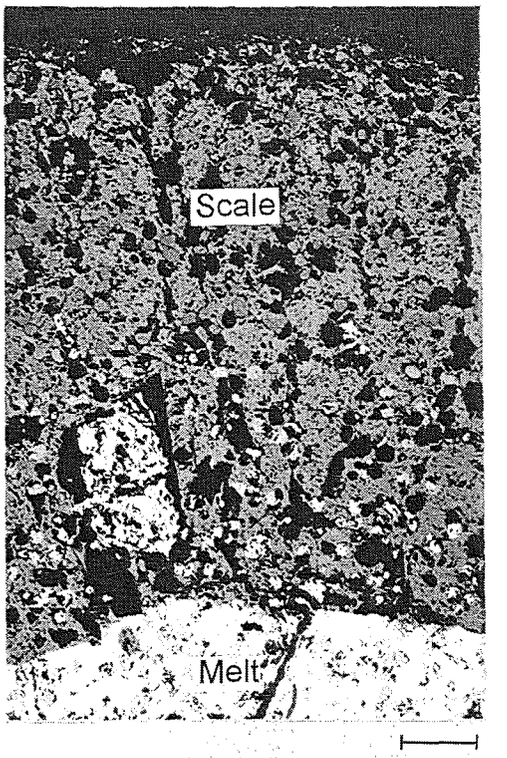

Fuel rod with adhering melt
and internal melting Pos.2

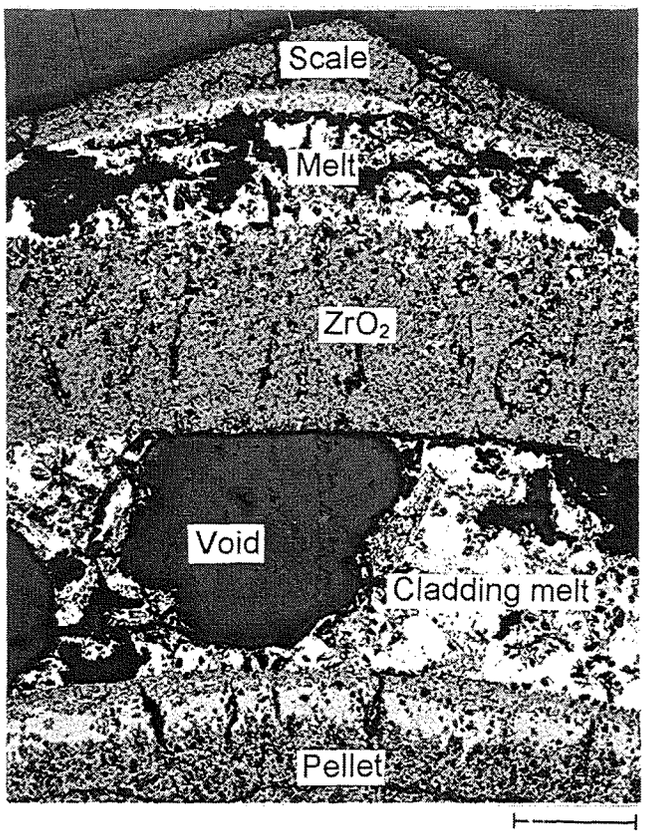

Pellet/melt interaction
after cladding dissolution Pos.3

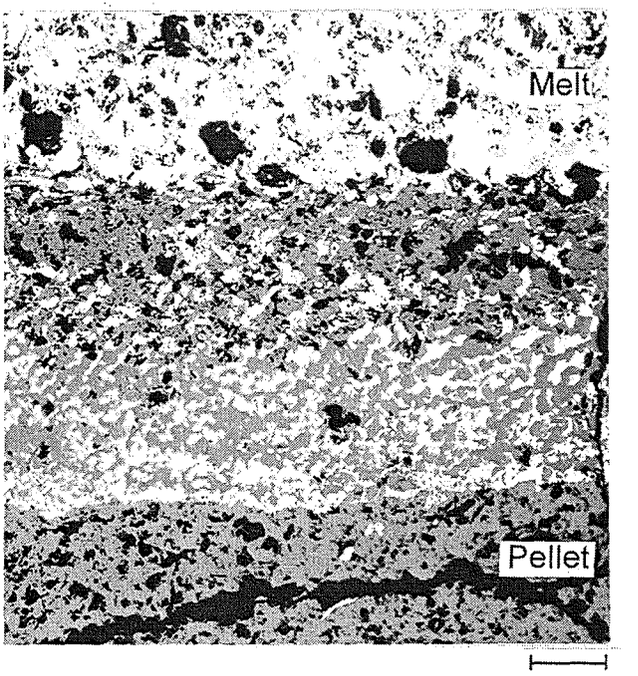

Fig. 131:
Cross Section CORA-18-06 (top), Elevation 717 mm
Oxidation versus Melting and Interactions

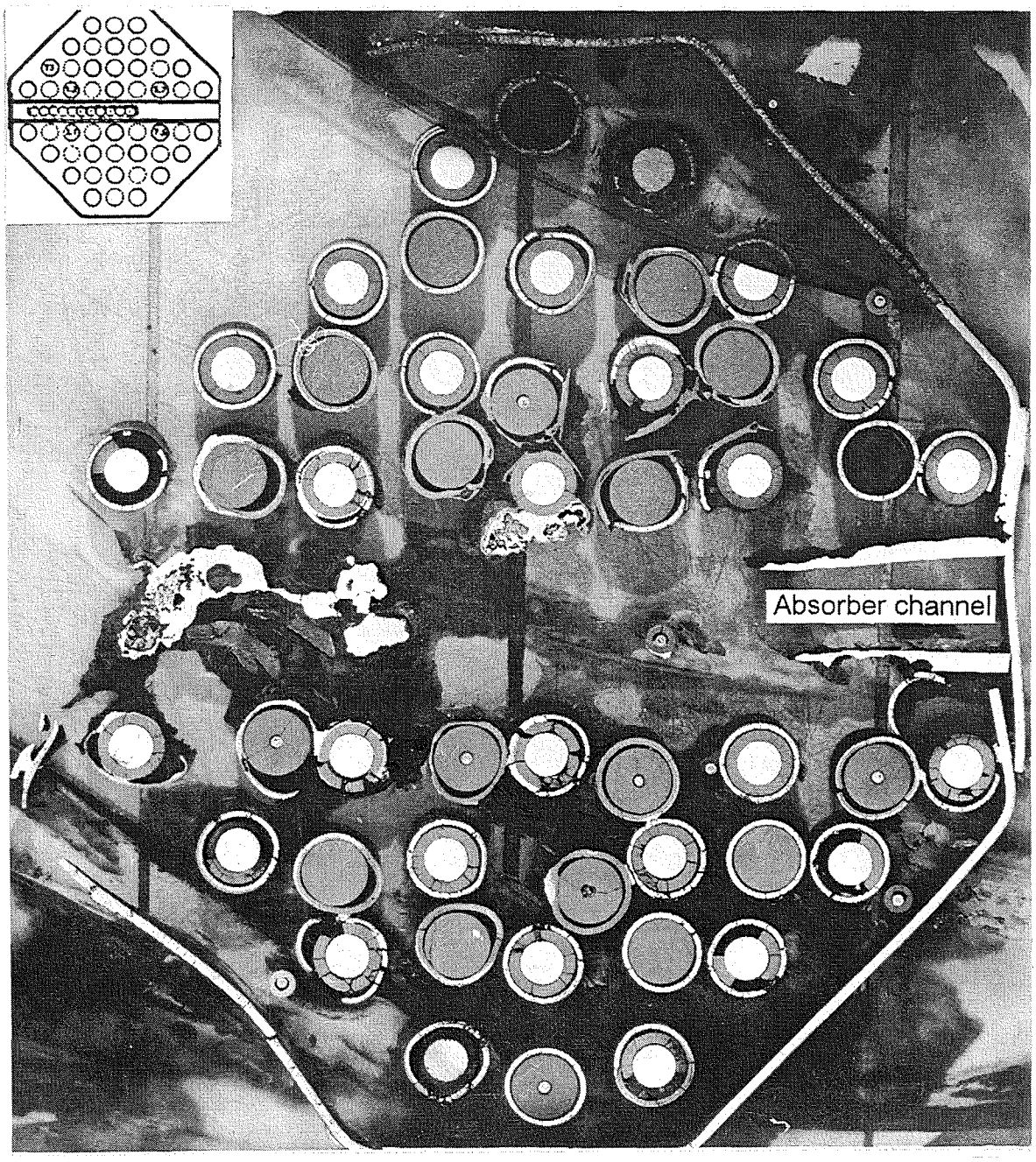

Fig. 132:
Cross Section CORA-18-07 (top), Elevation 874 mm
Overview

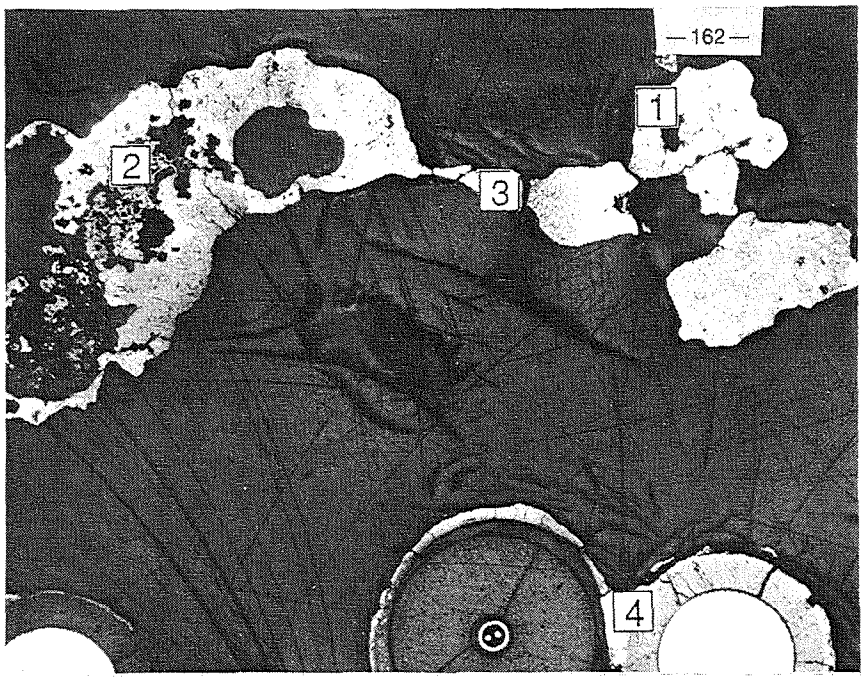

5 mm

Oxidized surface of absorber melt Pos.1

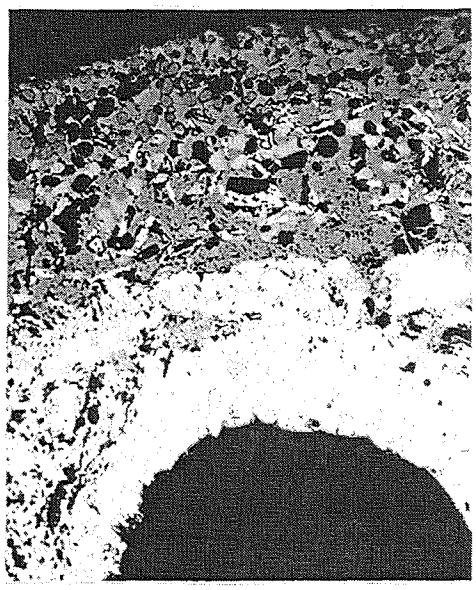

50 µm

Free carbon, embedded by boron - rich melt Pos.2

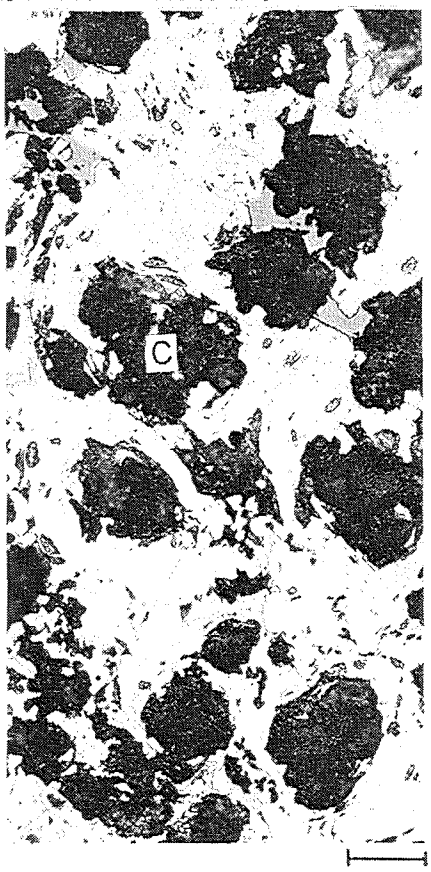

20 µm

Absorber melt Pos.3

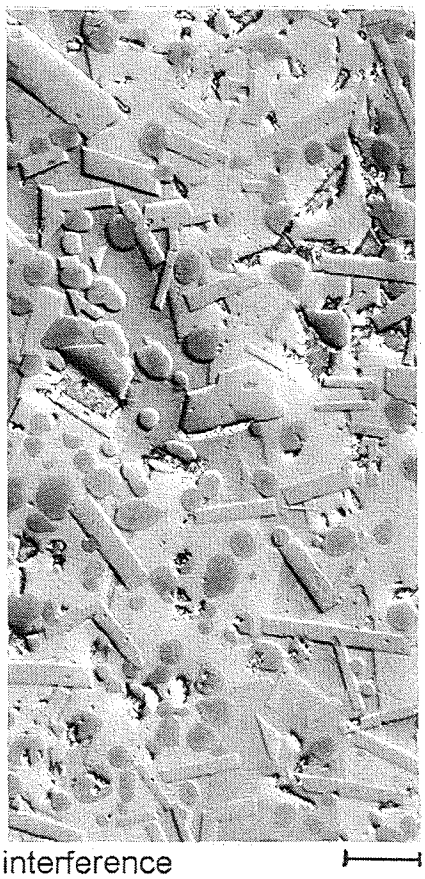

interference contrast

20 µm

Absorber melt in contact with pellet Pos.4

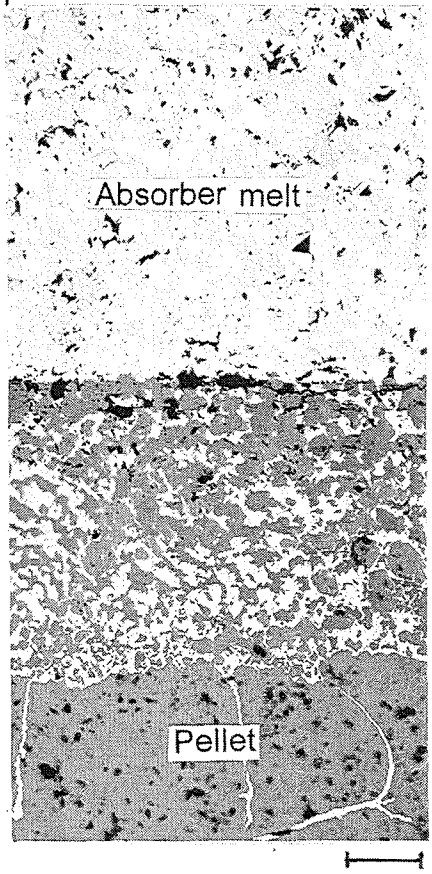

50 µm

Fig. 133:
Cross Section CORA-18-07 (top), Elevation 874 mm
Morphologies of Absorber Relicts

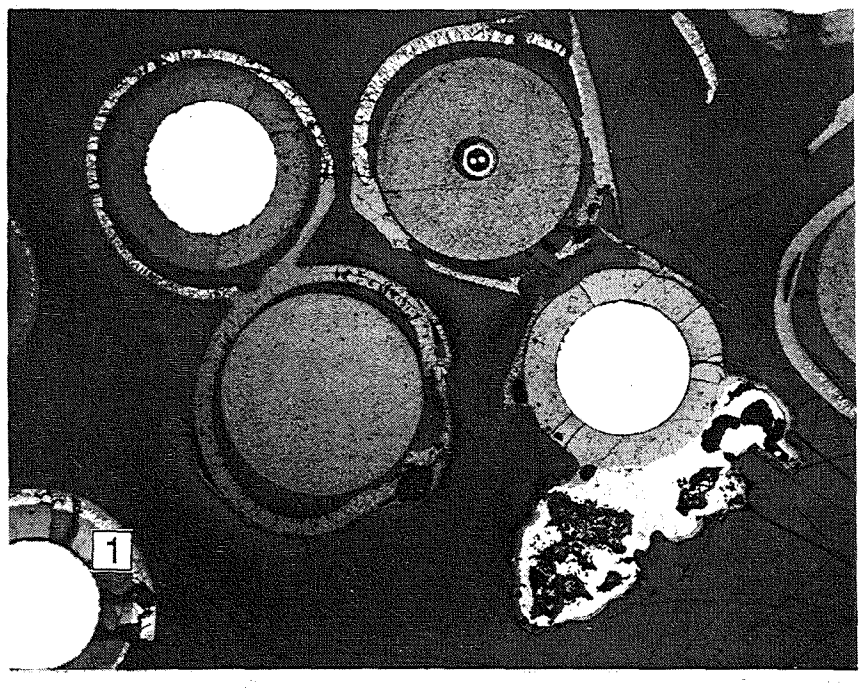

5 mm

Residual metallic cladding Pos.1

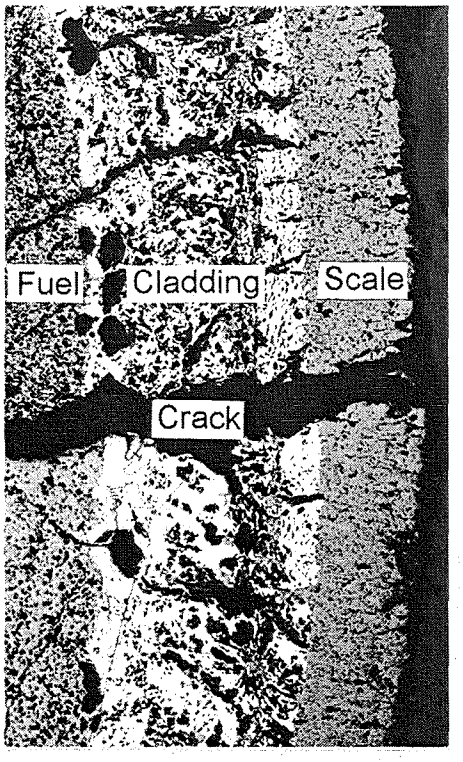

200 µm

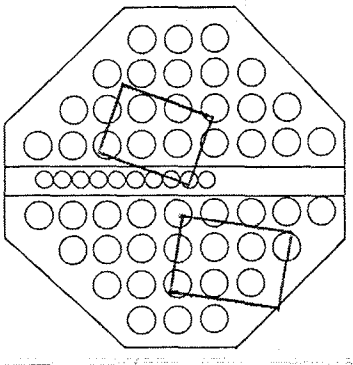

Pellet desintegration Pos.2

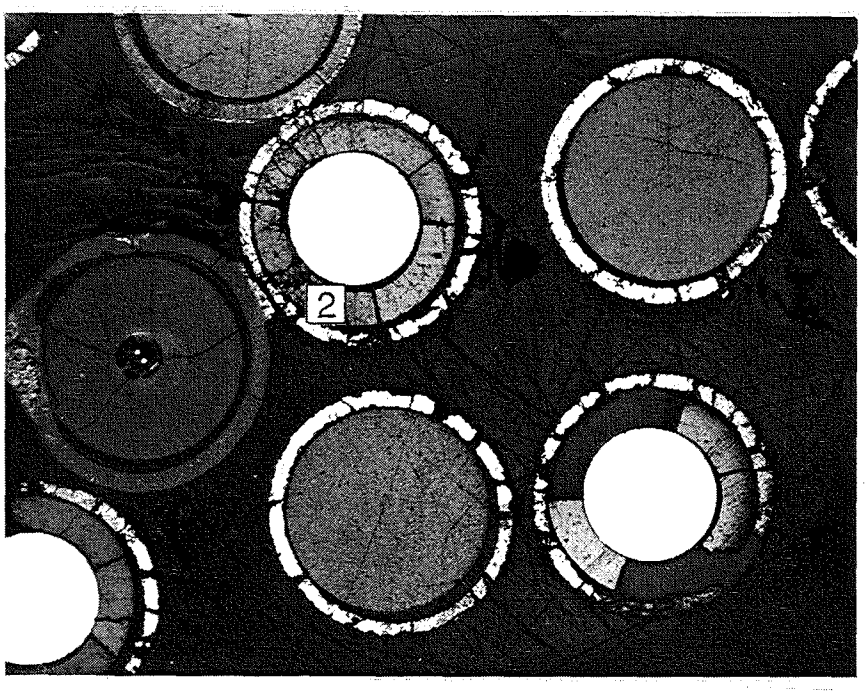

5 mm

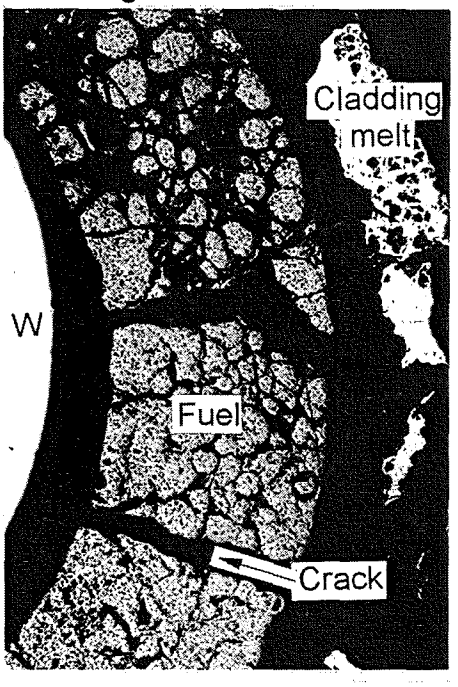

500 µm

Fig. 134:
Cross Section CORA-18-07 (top), Elevation 874 mm
Fuel Rod Degradation Status

Appendix A

Test Data of the pre-heating phase

Figures A1 - A20

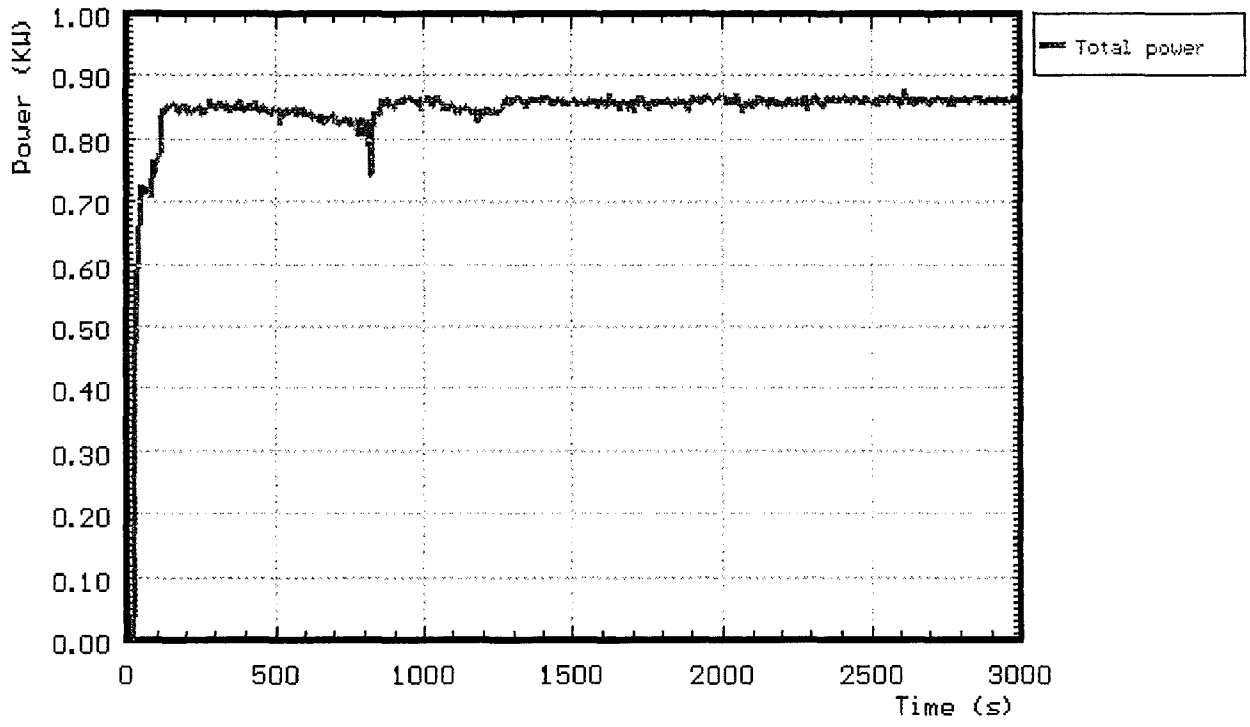

Fig. A1: CORA-18; Power input during pre-heat phase

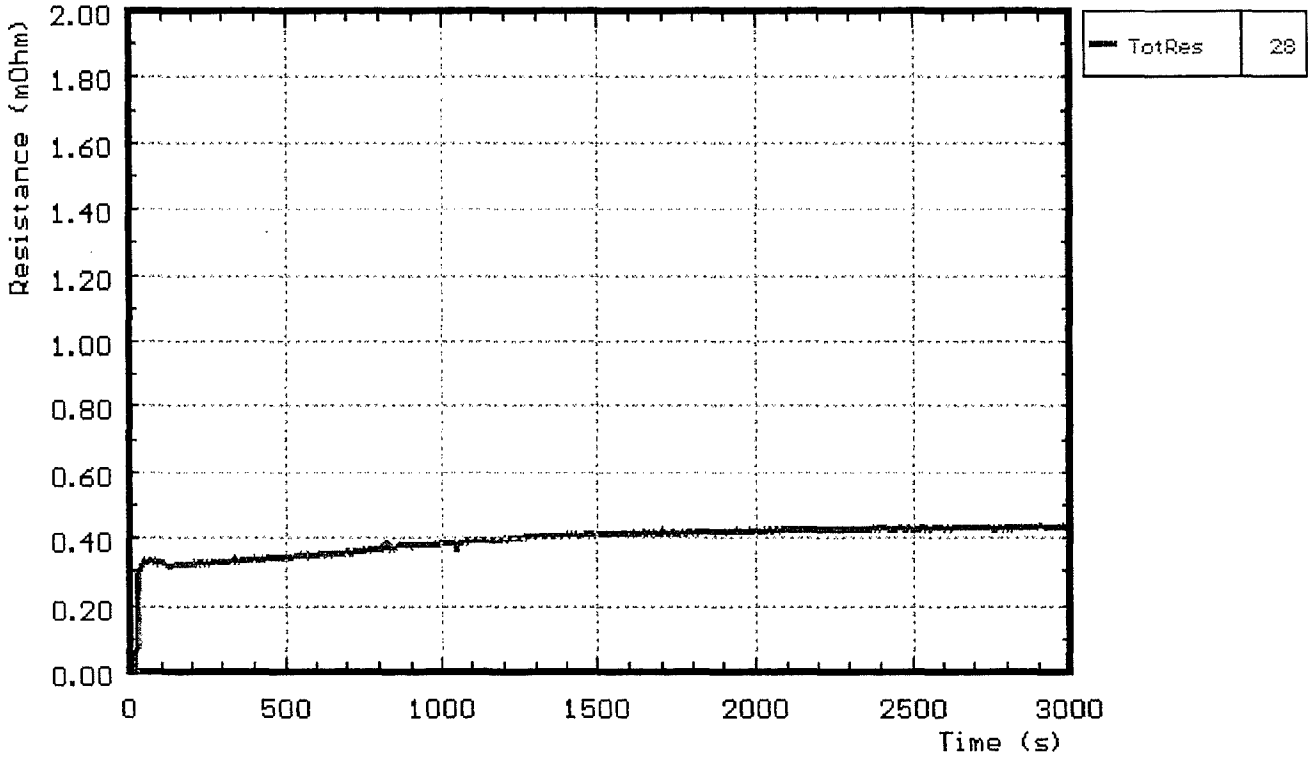

Fig. A2: CORA-18; Resistance of bundle during pre-heat phase

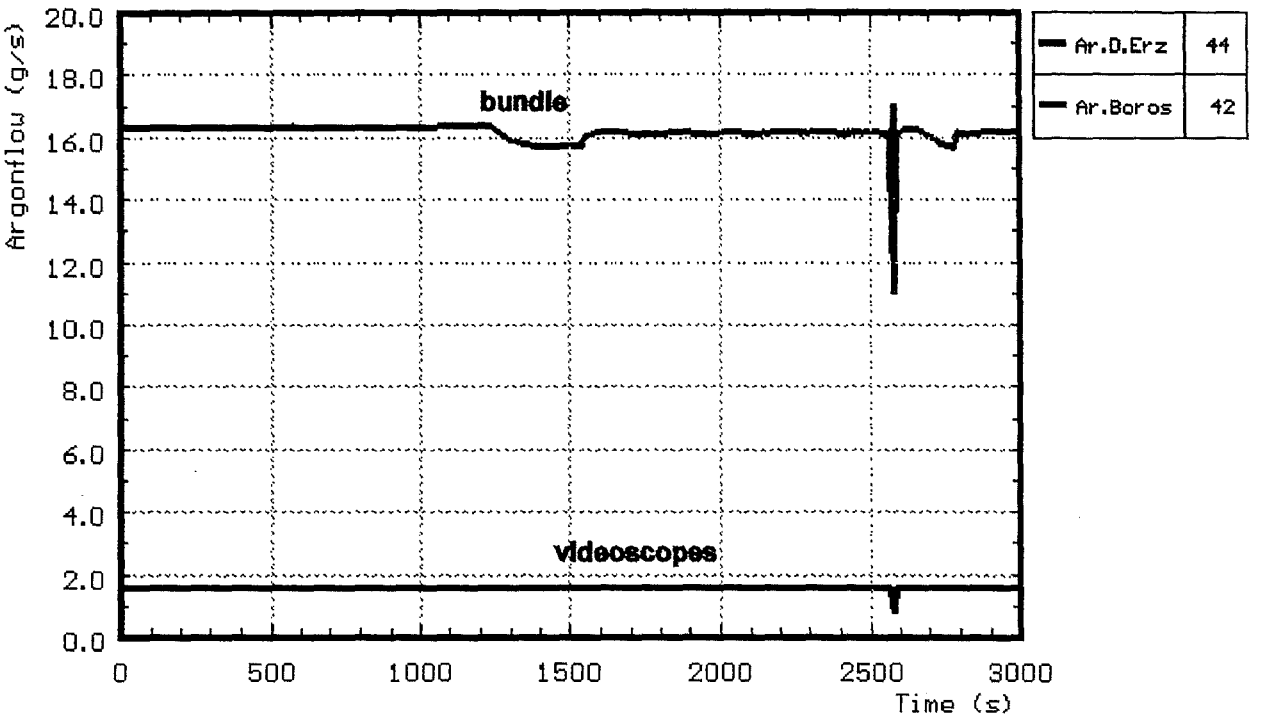

Fig. A3: CORA-18; Argon input prior to test

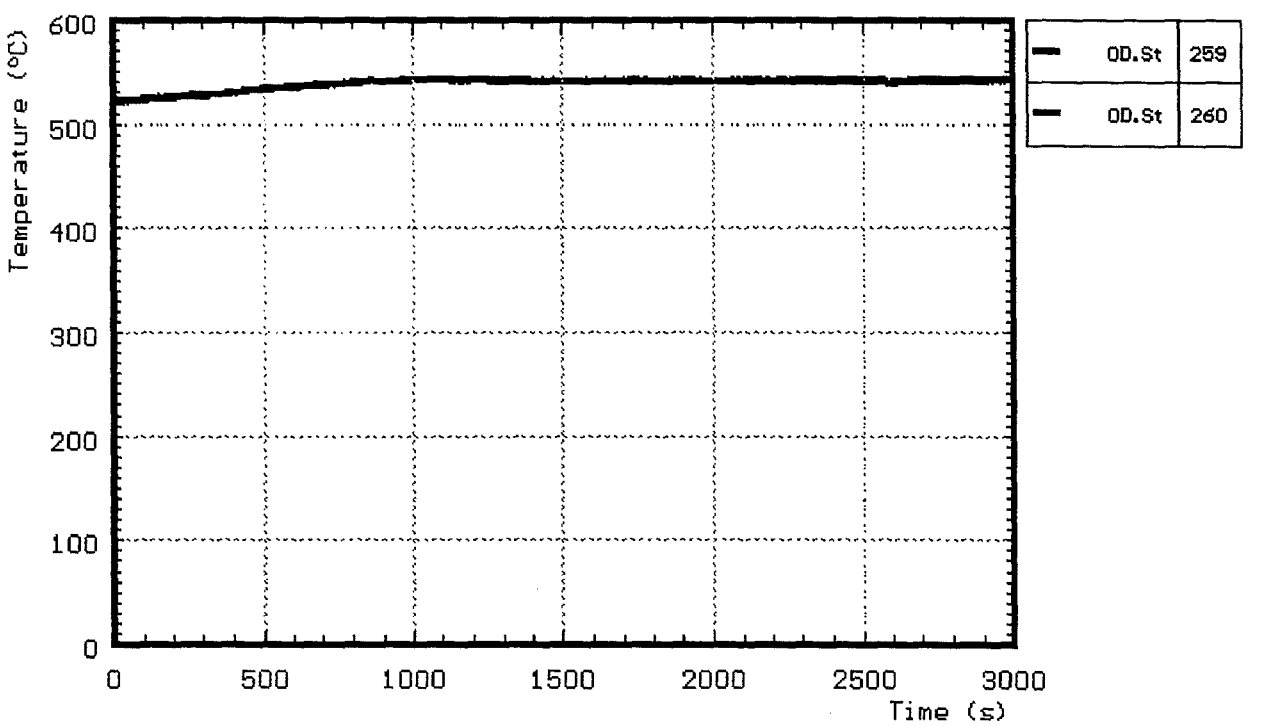

Fig. A4: CORA-18; Temperatures at steam inlet; pre-heat phase

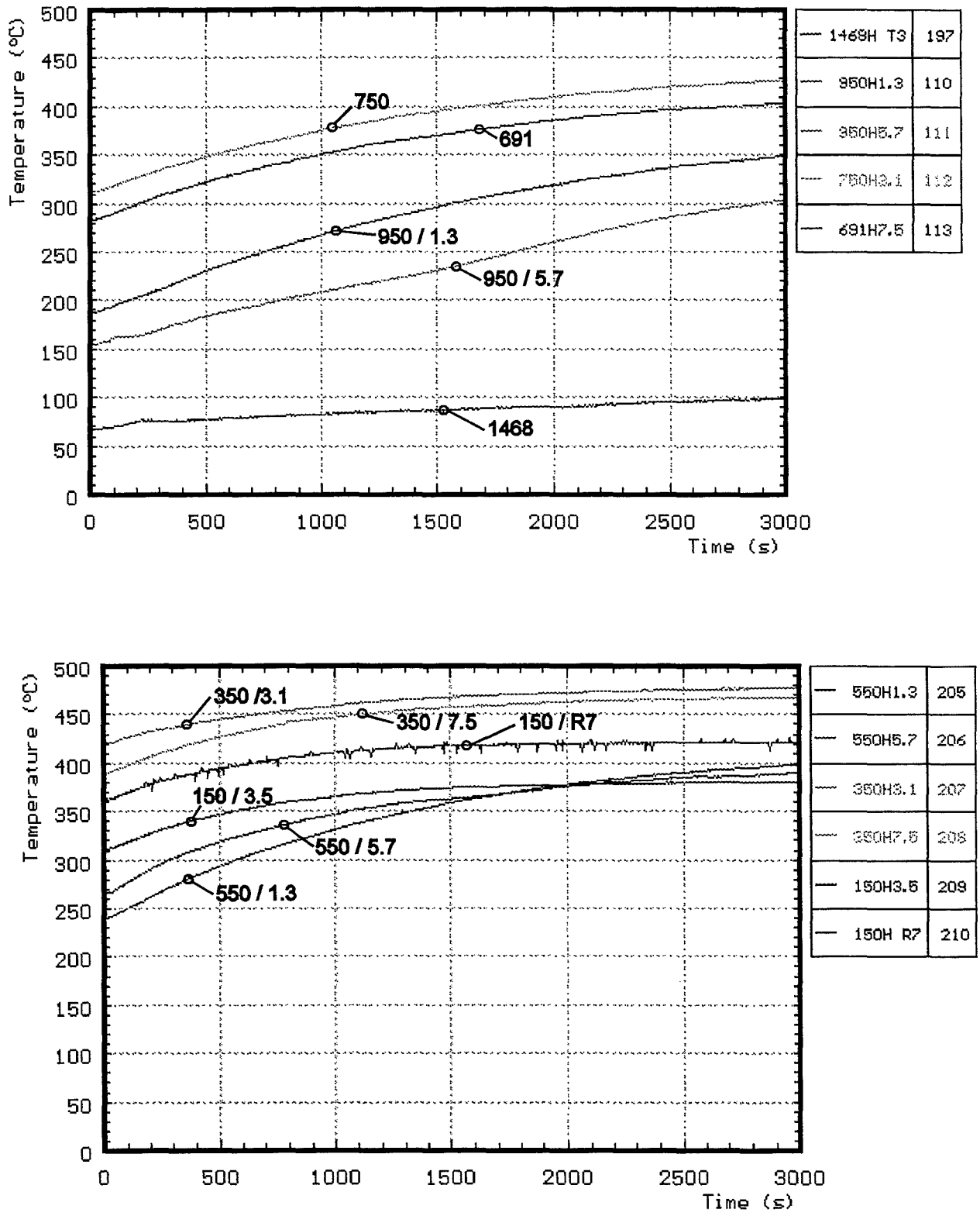

Fig. A5: CORA-18; Temperatures of heated rods

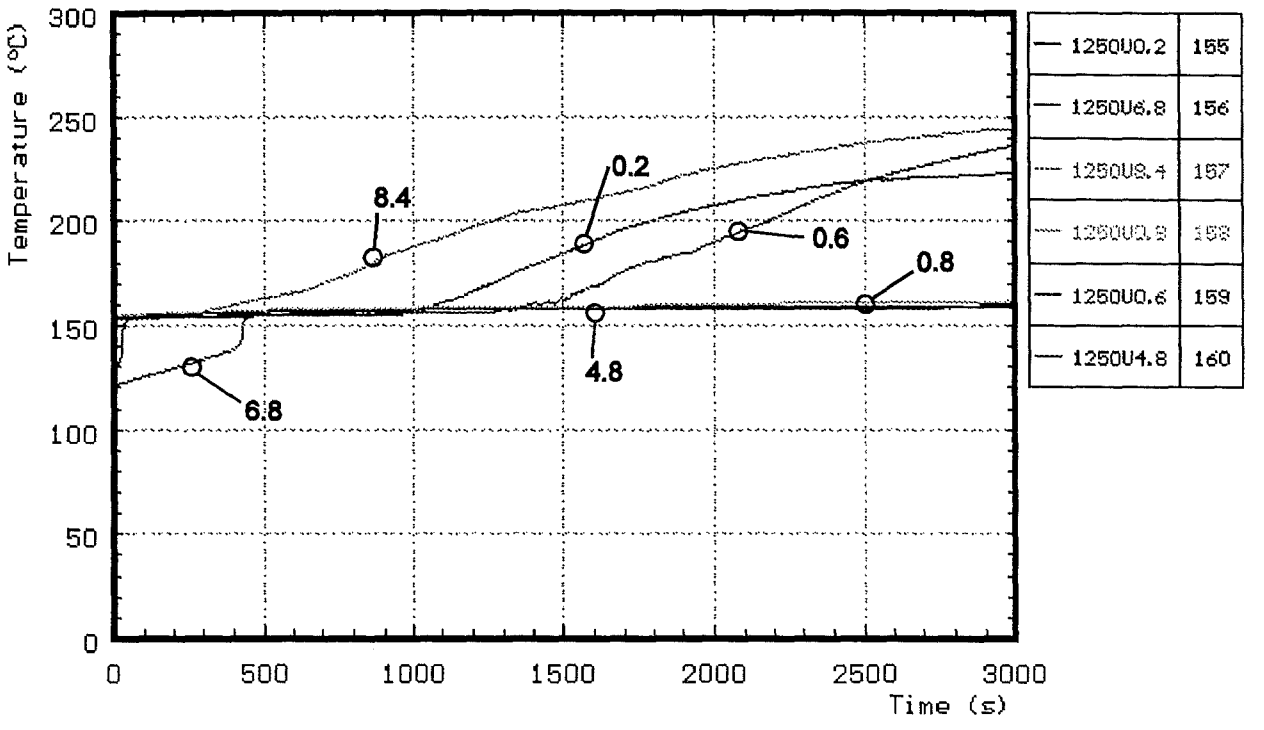

Fig. A6: CORA-18; Temperatures of unheated rods, 1250 mm elevation

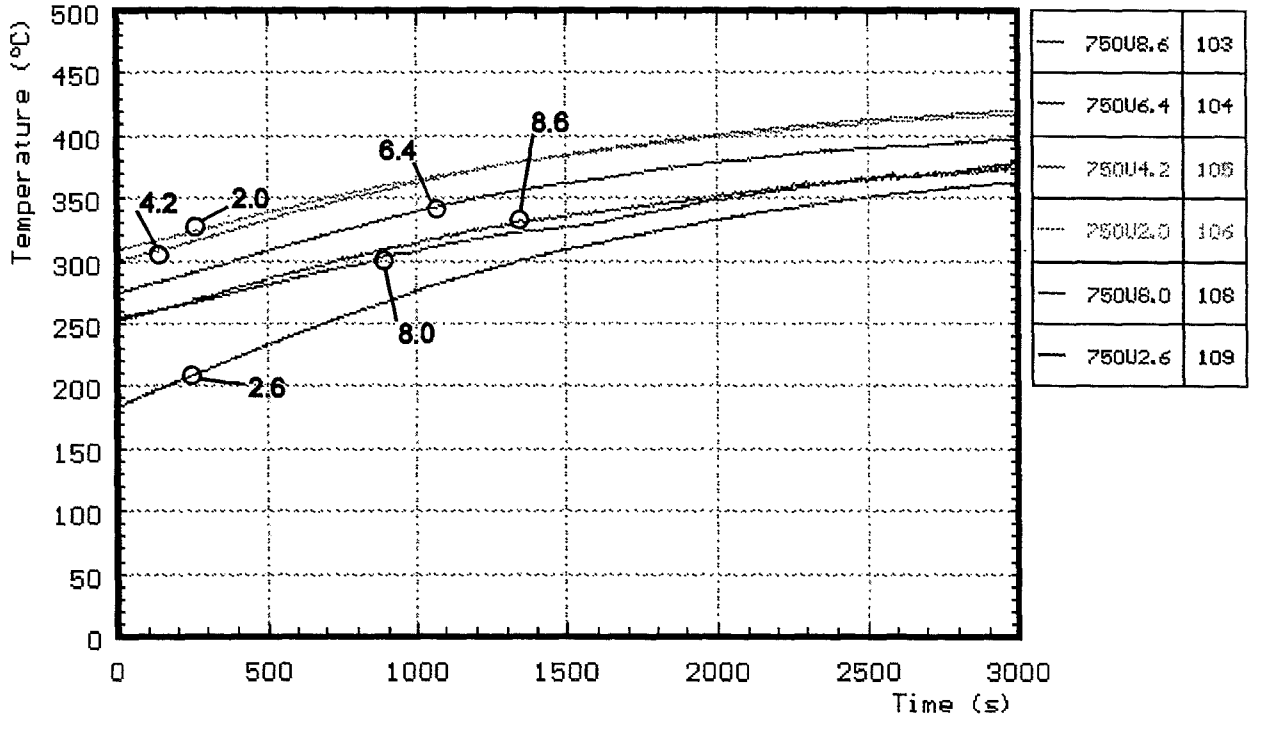

Fig. A7: CORA-18; Temperatures of unheated rods, 750 mm elevation

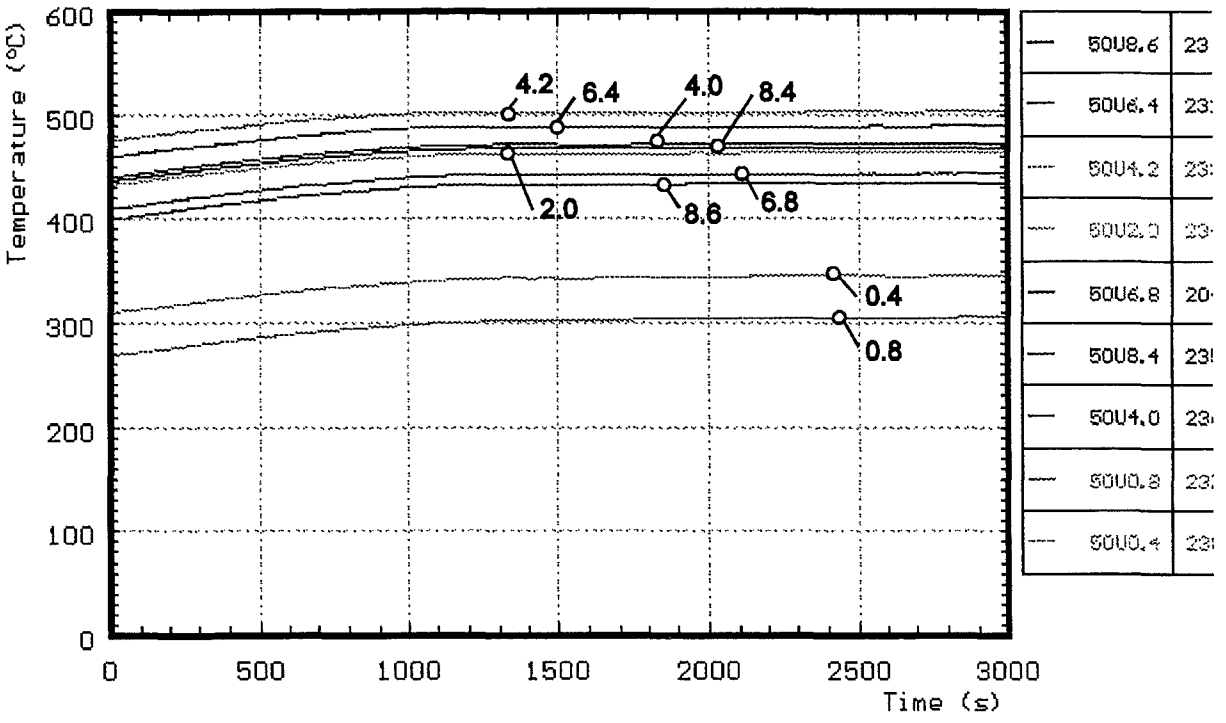

Fig. A8: CORA-18, Temperatures of unheated rods, 50 mm elevation

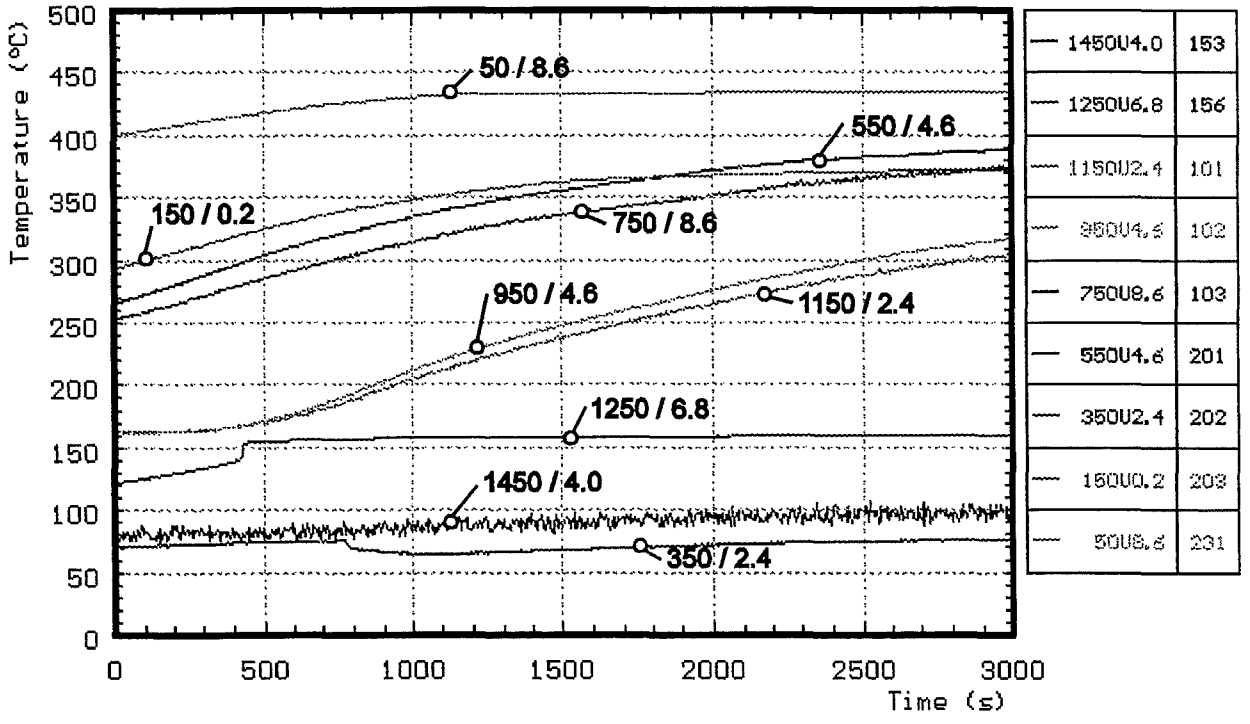

Fig. A9: CORA-18, Temperatures of unheated rods (TCs in central position)

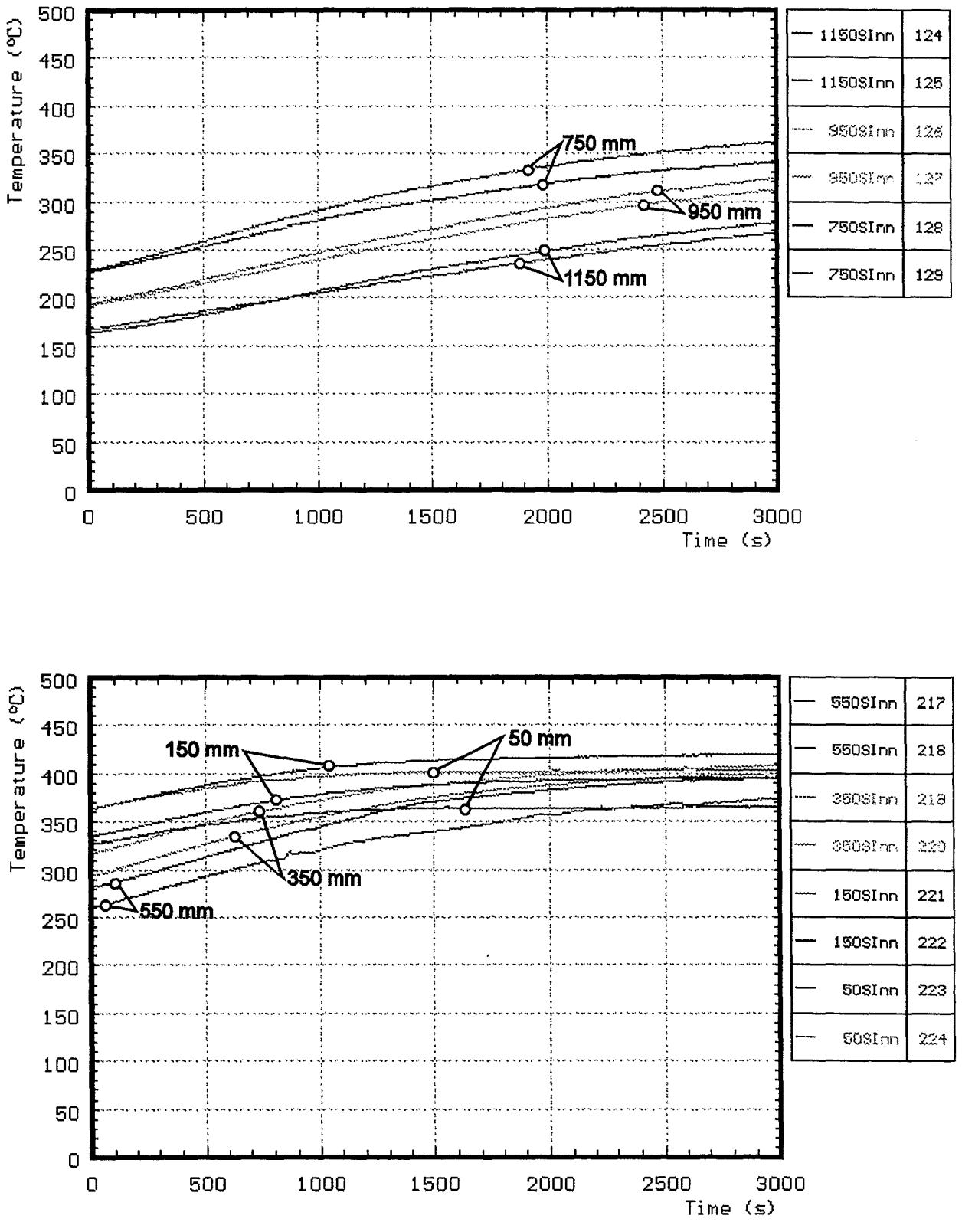

Fig. A10: CORA-18; Temperatures on the channel box wall

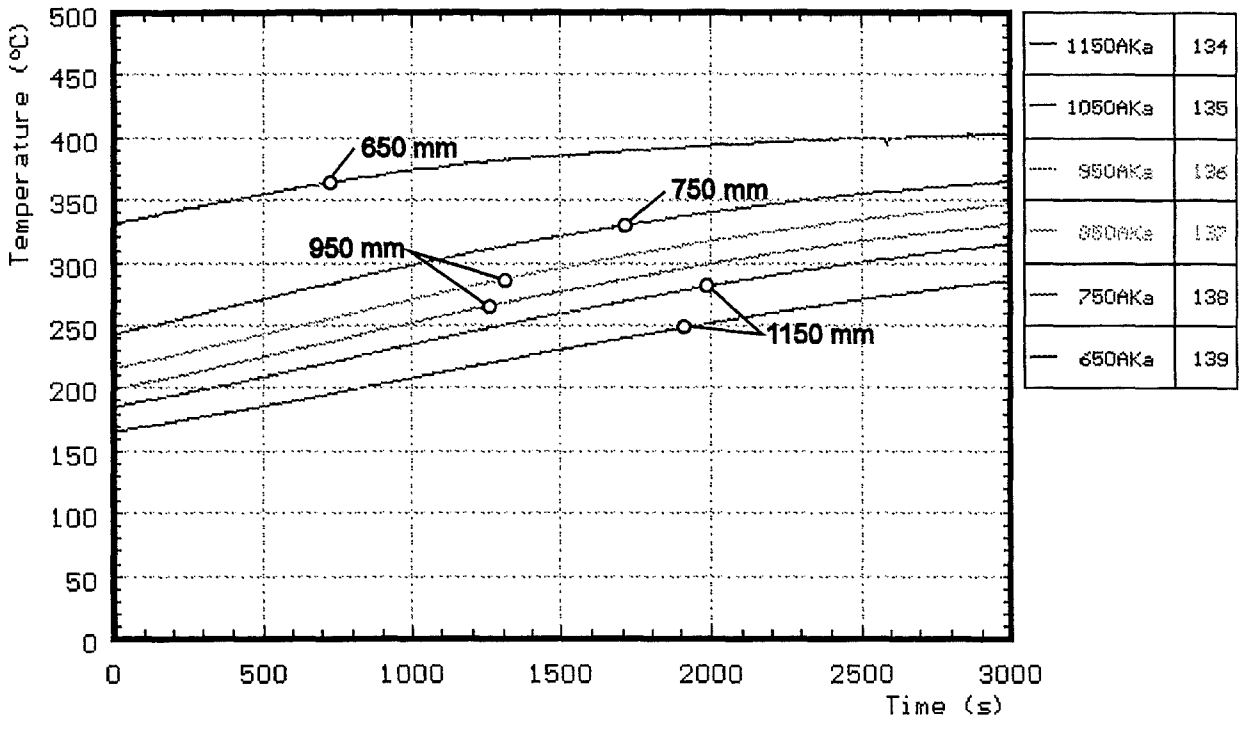

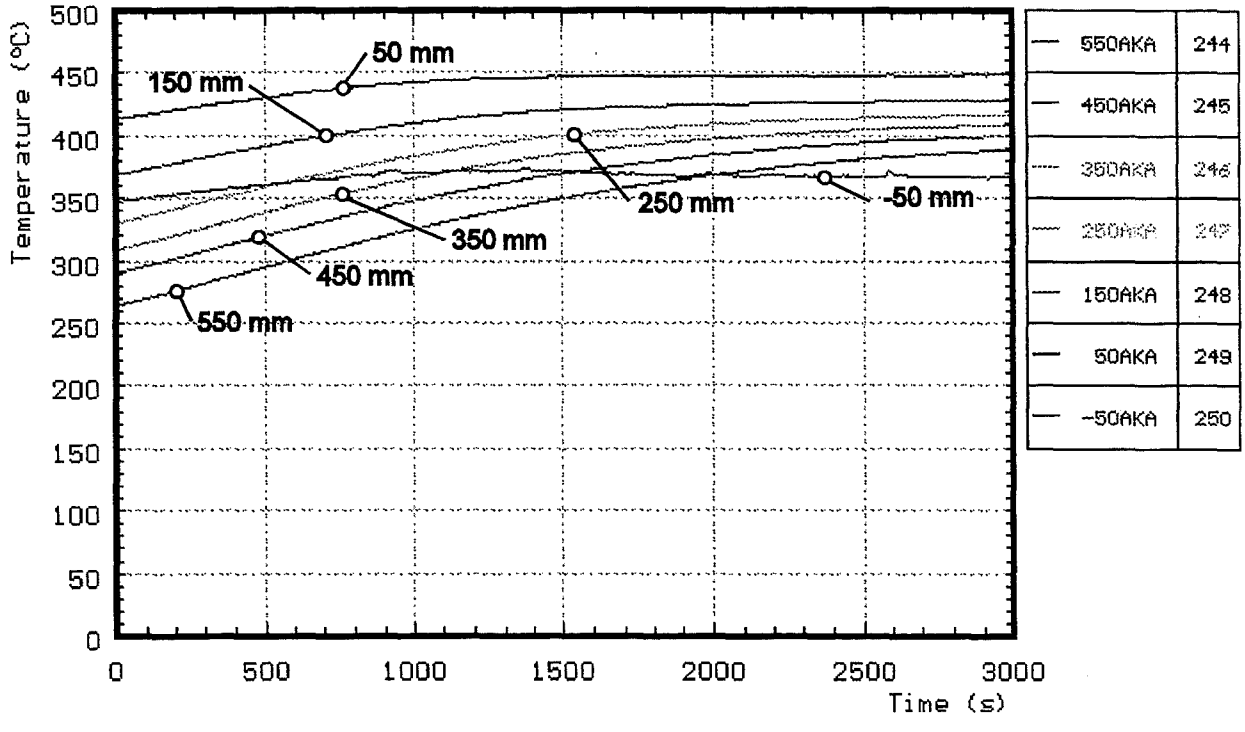

Fig. A11: CORA-18; Temperatures on the absorber blade, 120° orientation

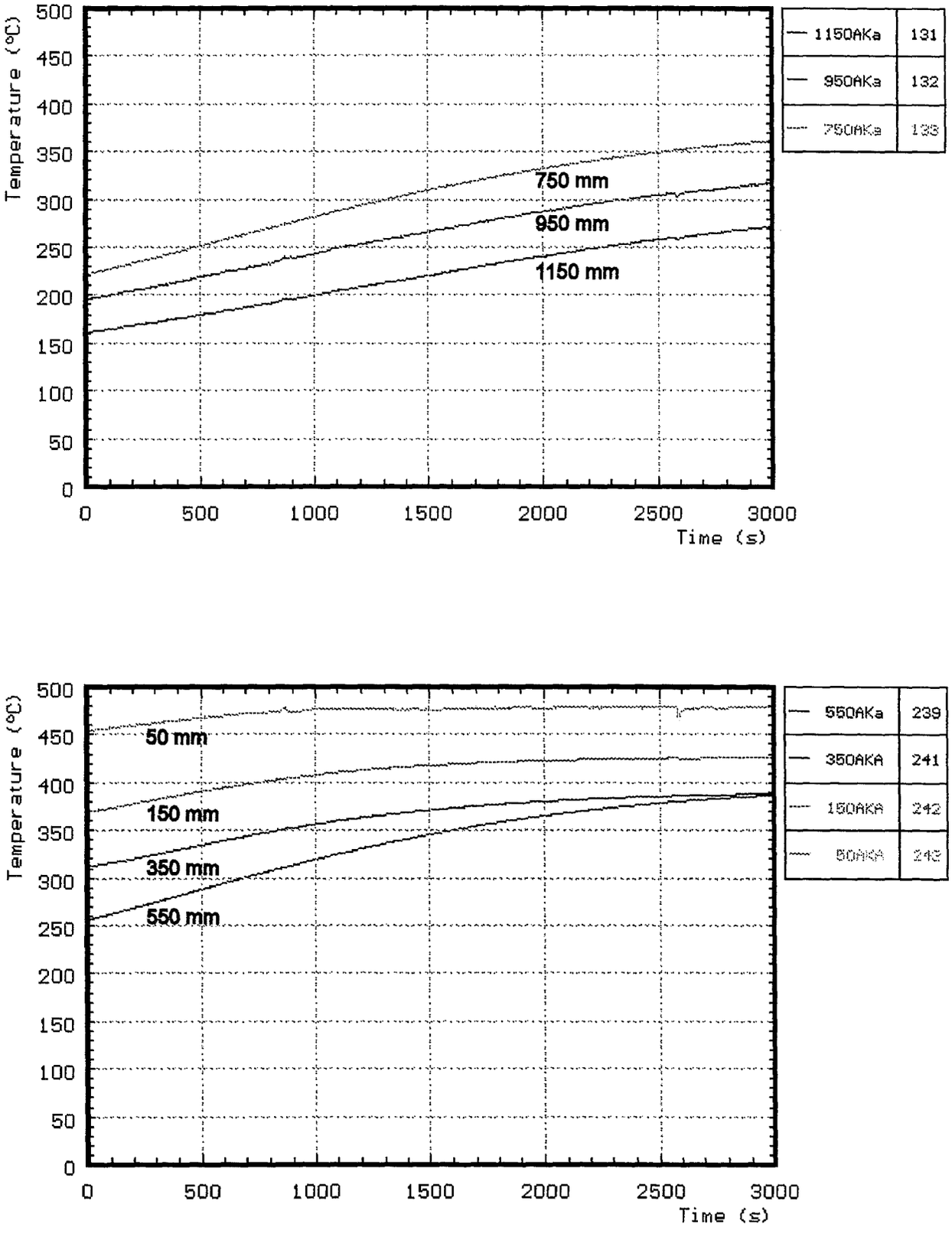

Fig. A12: CORA-18; Temperatures on the absorber blade, 300° orientation

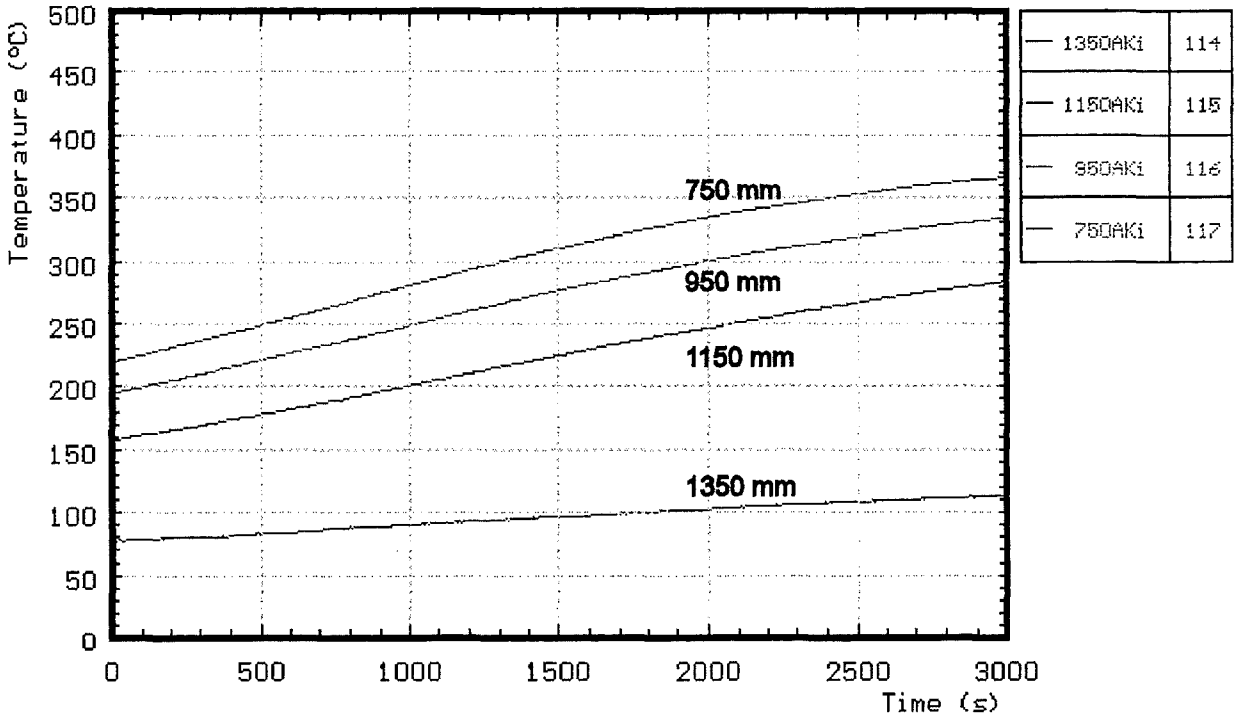

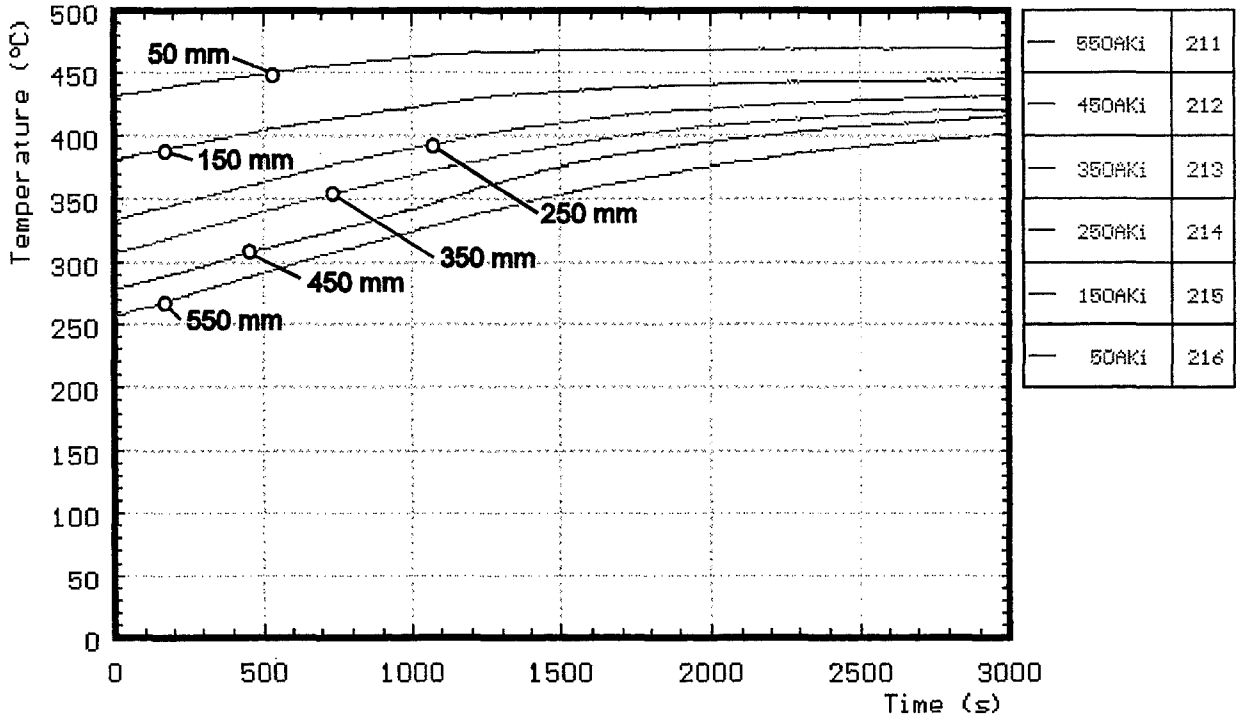

Fig. A13: CORA-18; Temperatures in the absorber blade

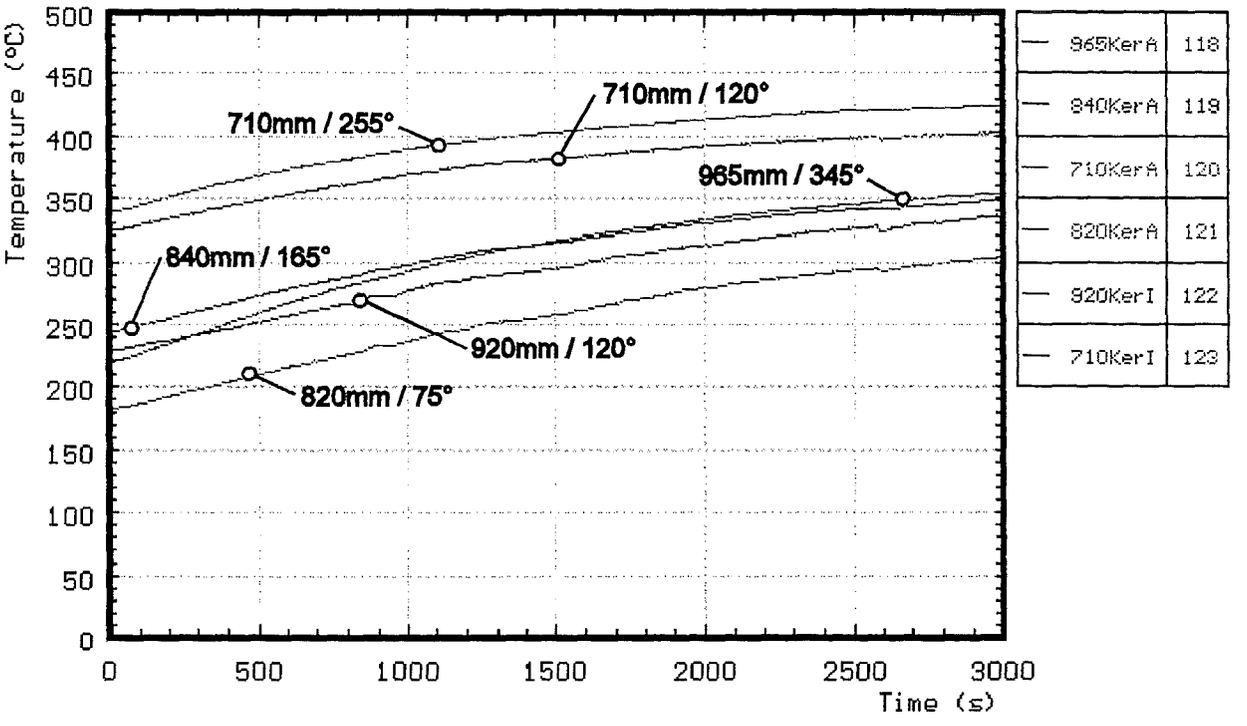

Fig. A14: CORA-18; Temperatures measured with ceramic protected TCs

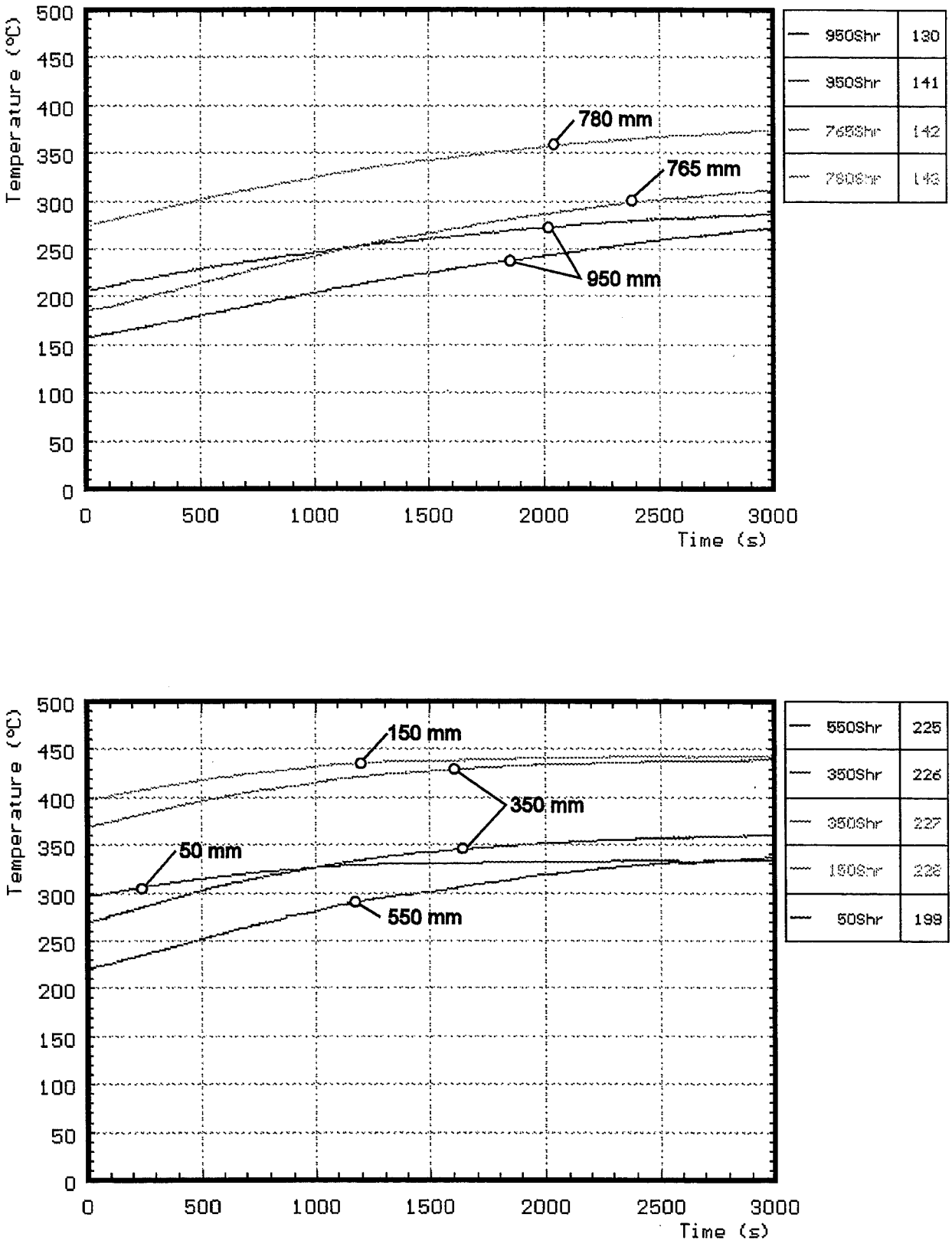

Fig. A16: CORA-18; Temperatures of the outer side of the shroud

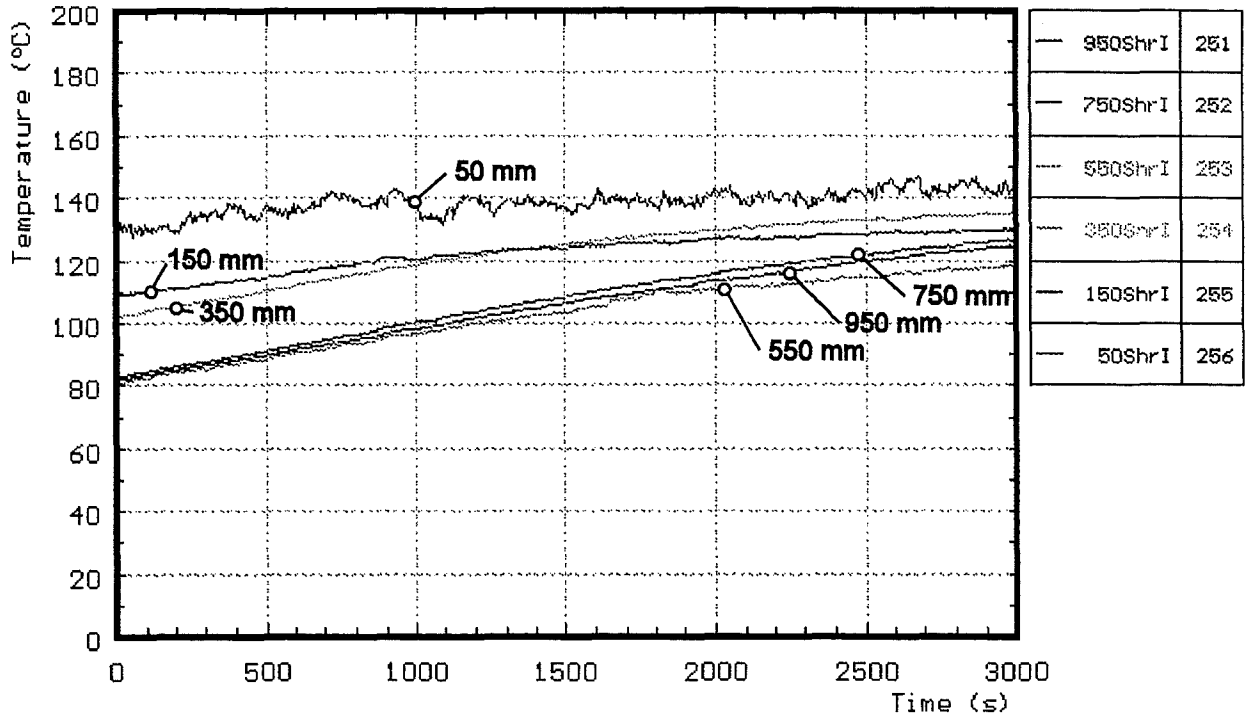

Fig. A17: CORA-18; Temperatures on shroud insulation

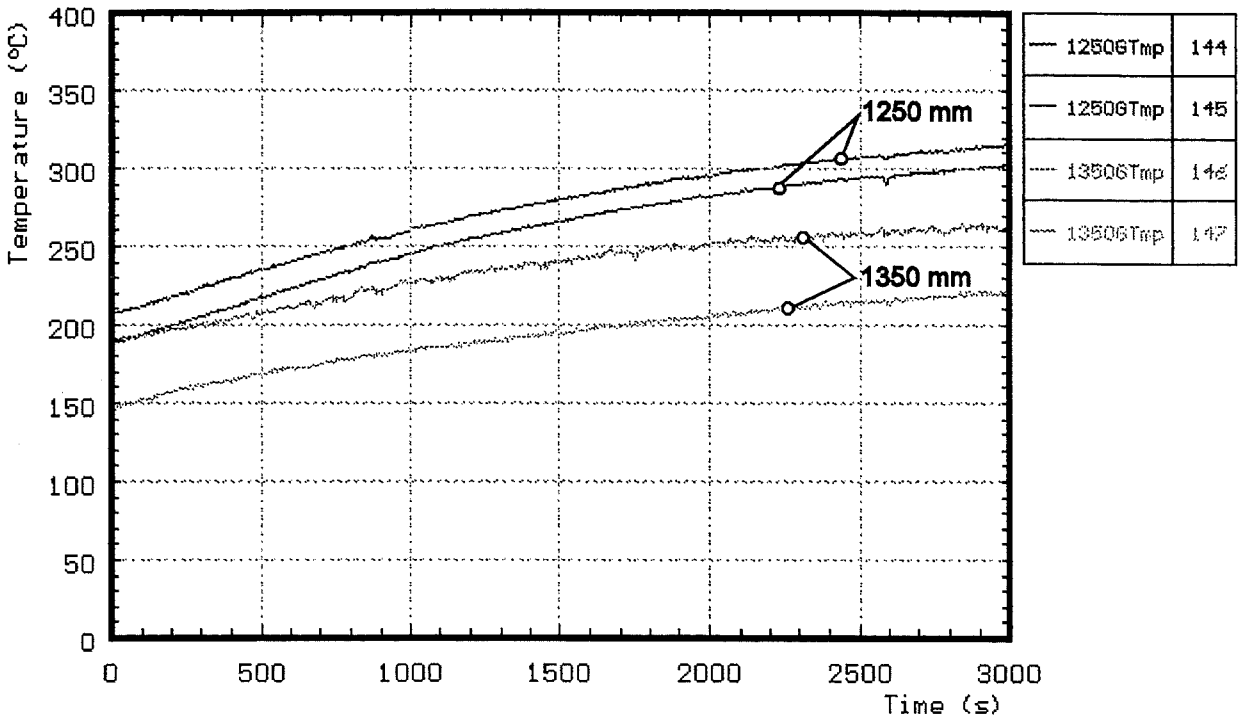

Fig. A18: CORA-18; Gas temperatures above the heated zone

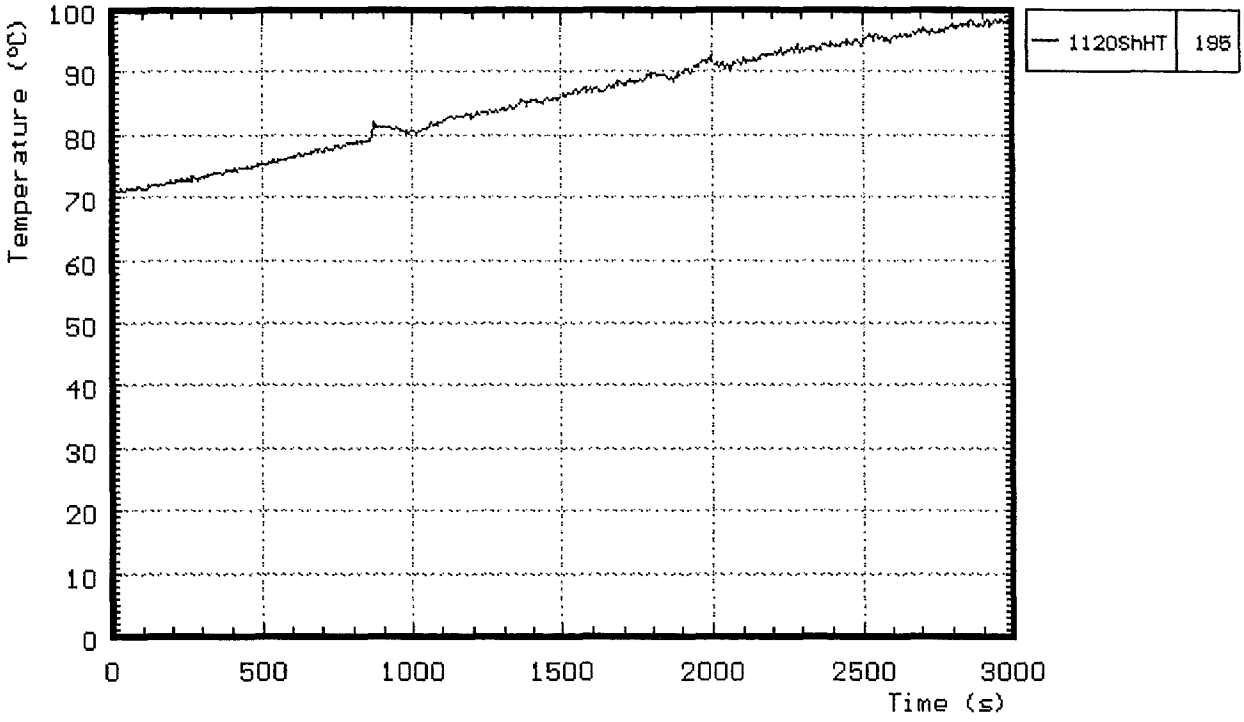

Fig. A19: CORA-18; Gas temperature between shroud and HTS

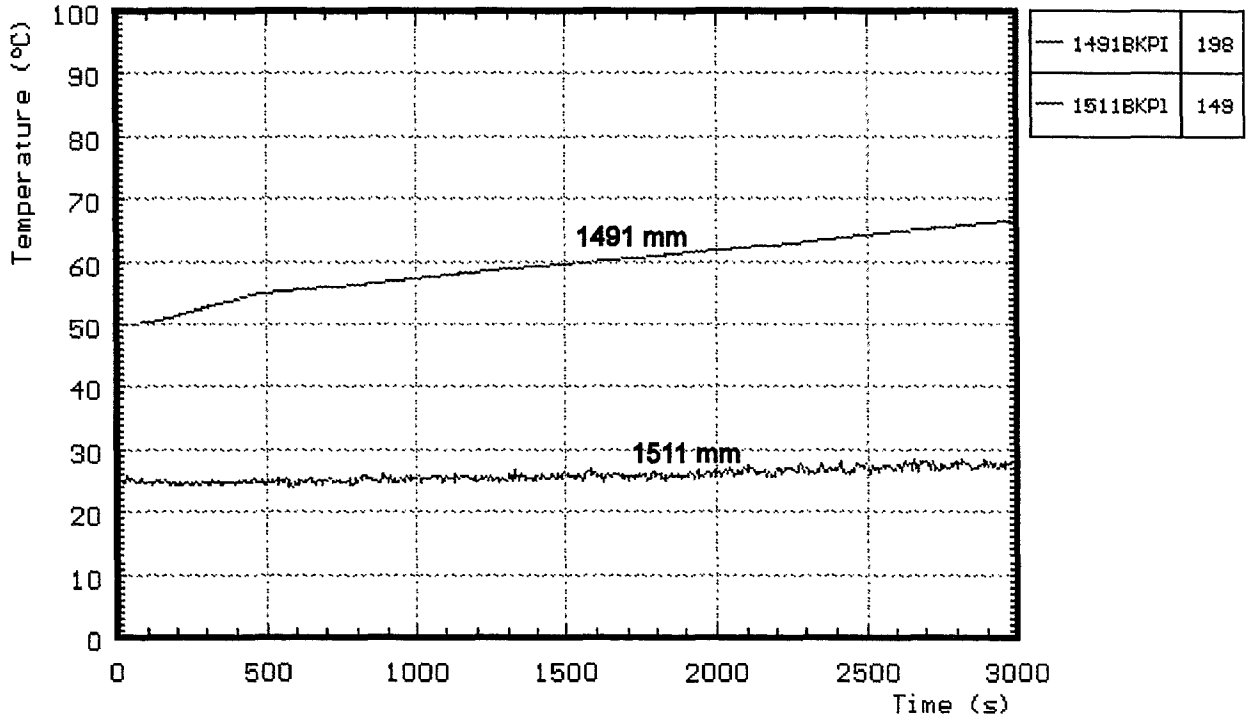

Fig. A20: CORA-18; Gas temperature measured in the bundle head plate

Appendix B

Complete set of cross sections

Figures B1 - B15

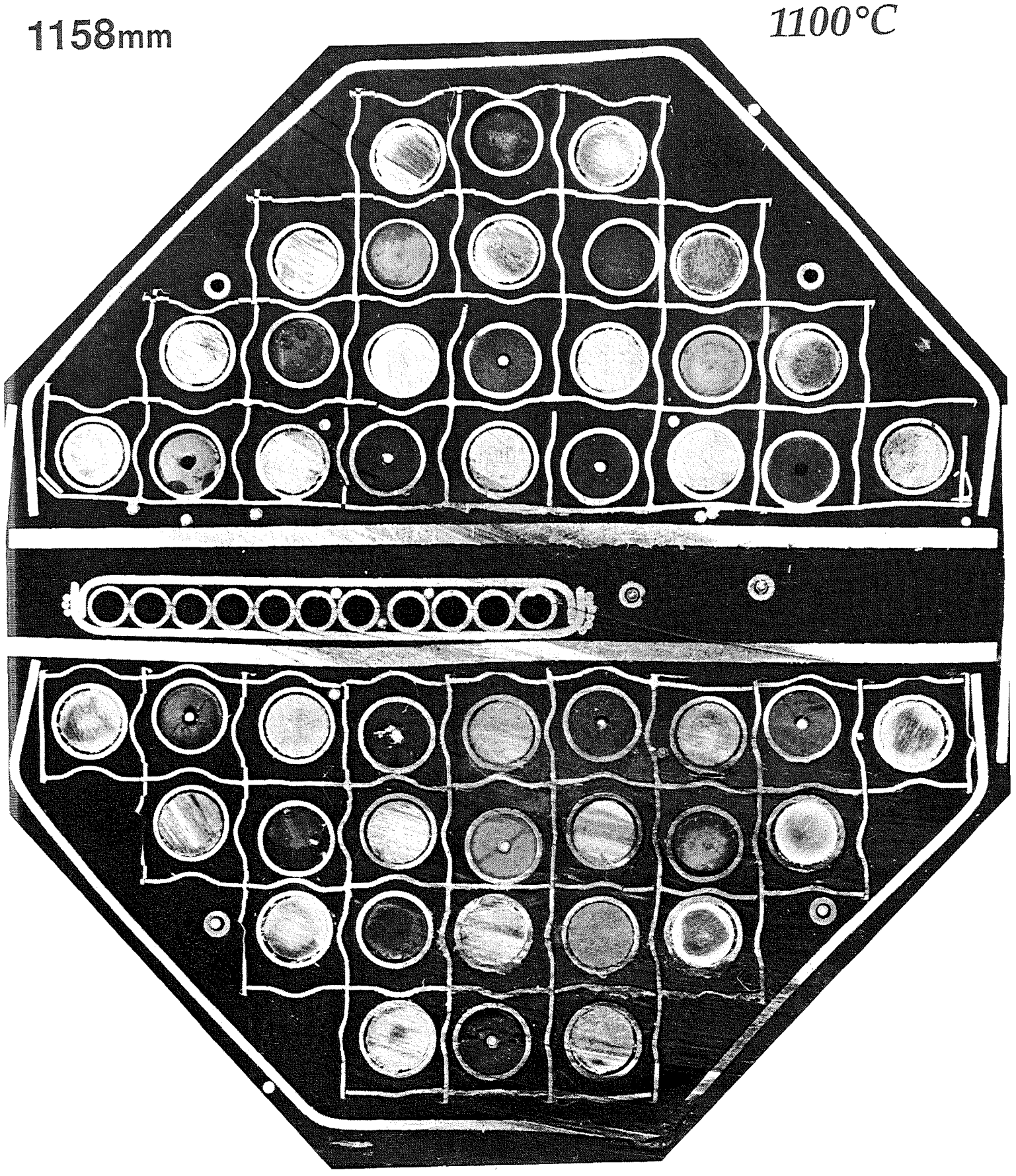

Fig. B1: CORA-18; horizontal cross-section at 1158 mm elevation.

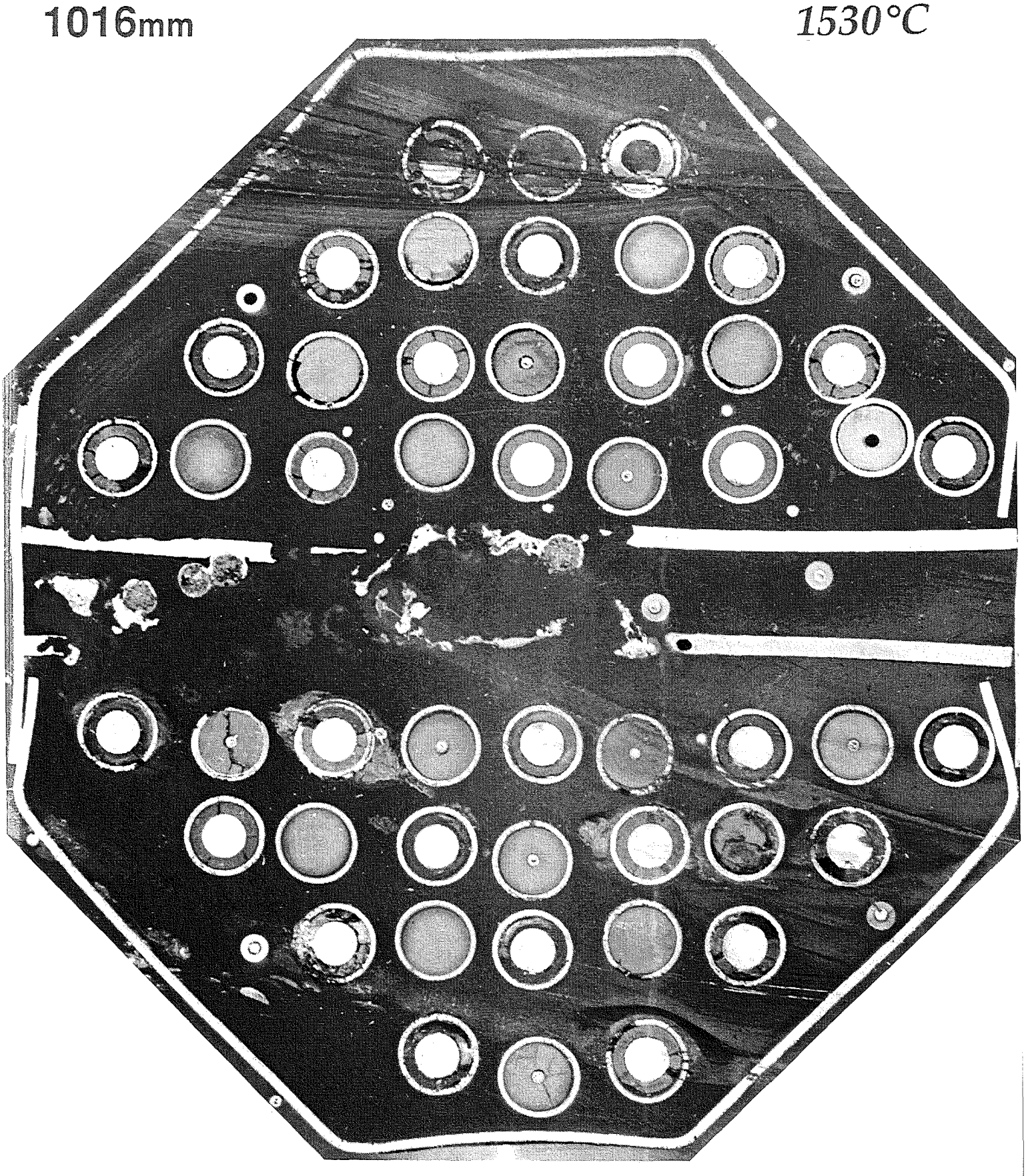

Fig. B2: CORA-18; horizontal cross-section at 1016 mm elevation.

874mm

1825°C

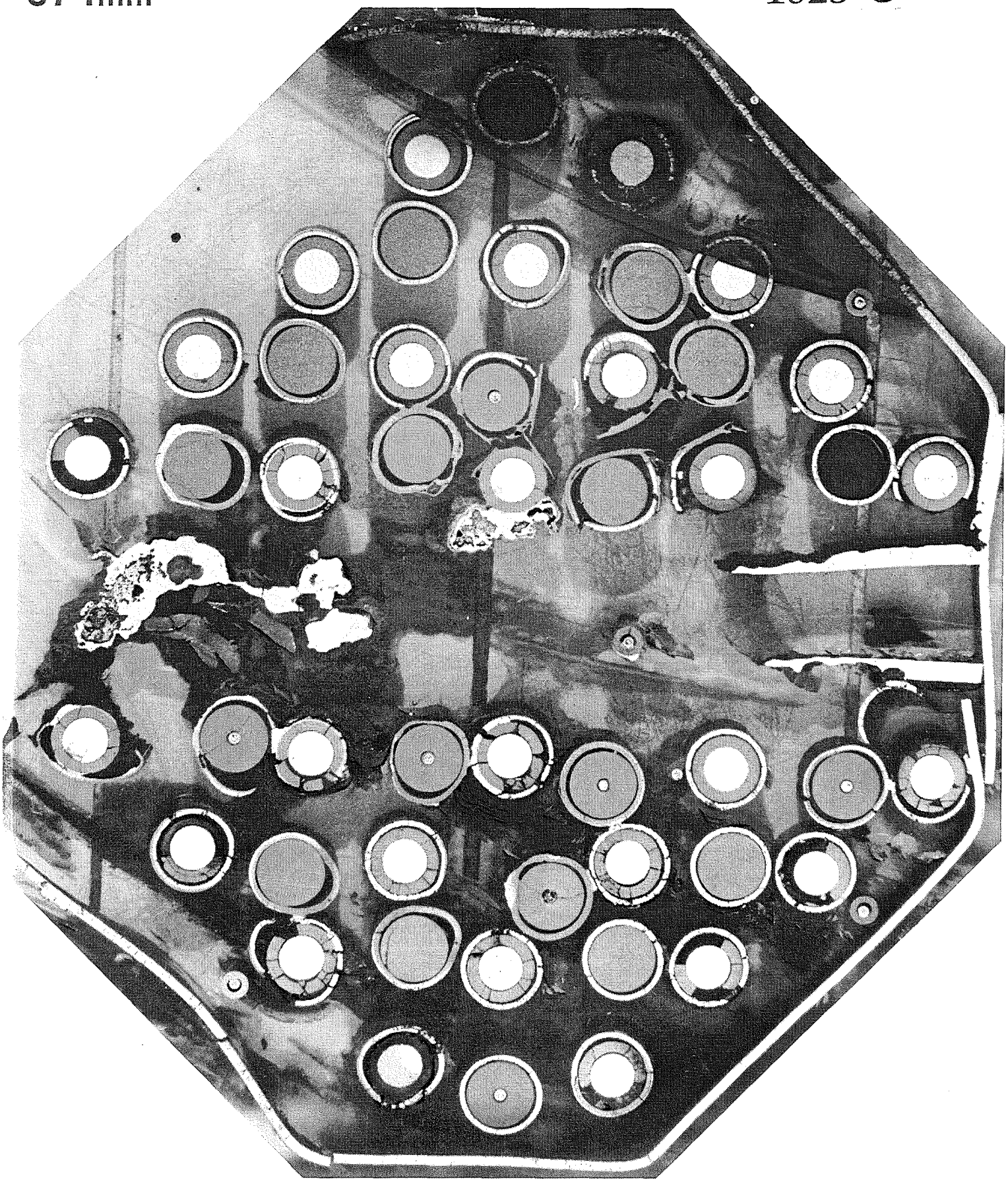

Fig. B3: CORA-18; horizontal cross-section at 874 mm elevation.

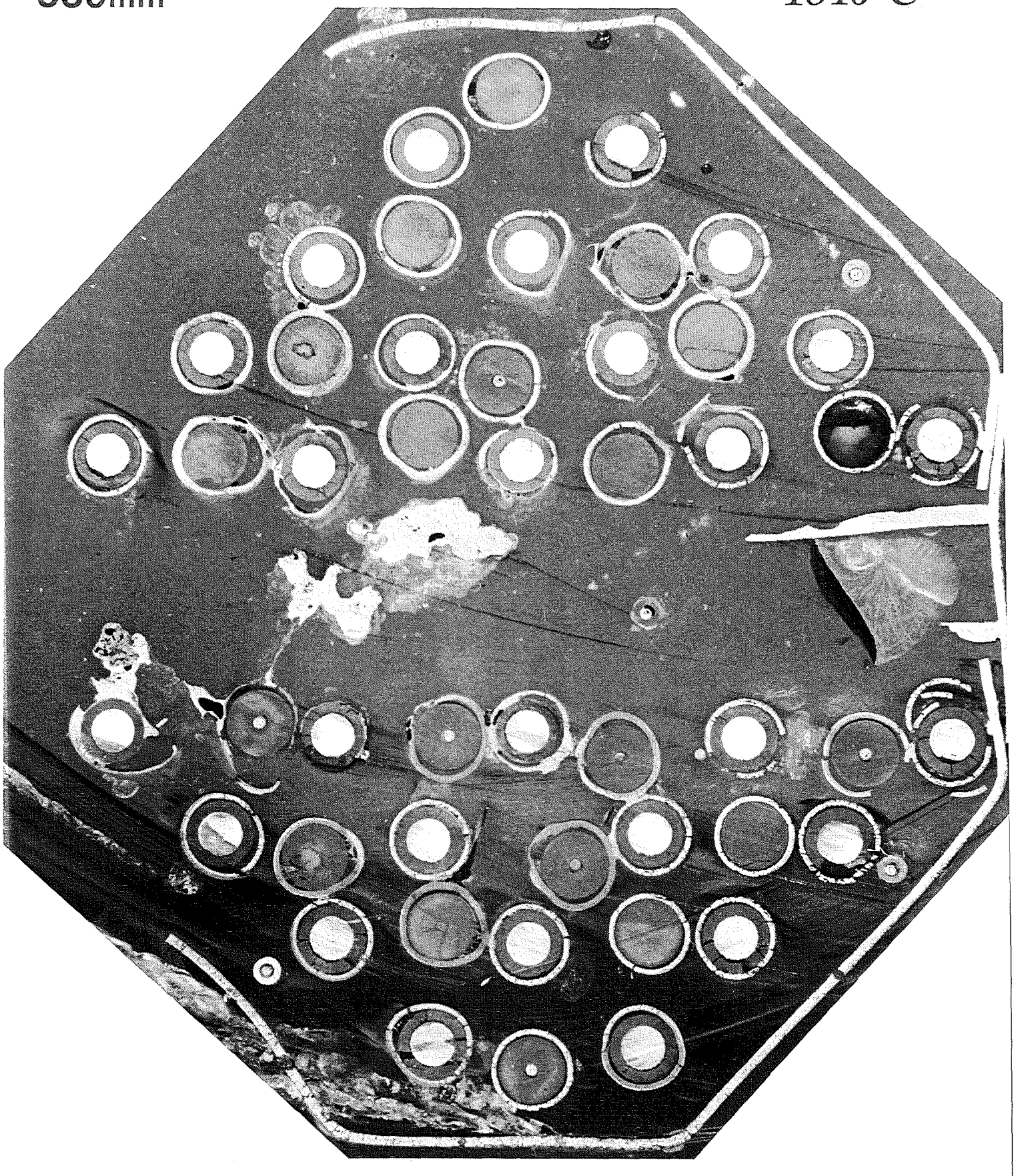

Fig. B4: CORA-18; horizontal cross-section at 859 mm elevation.

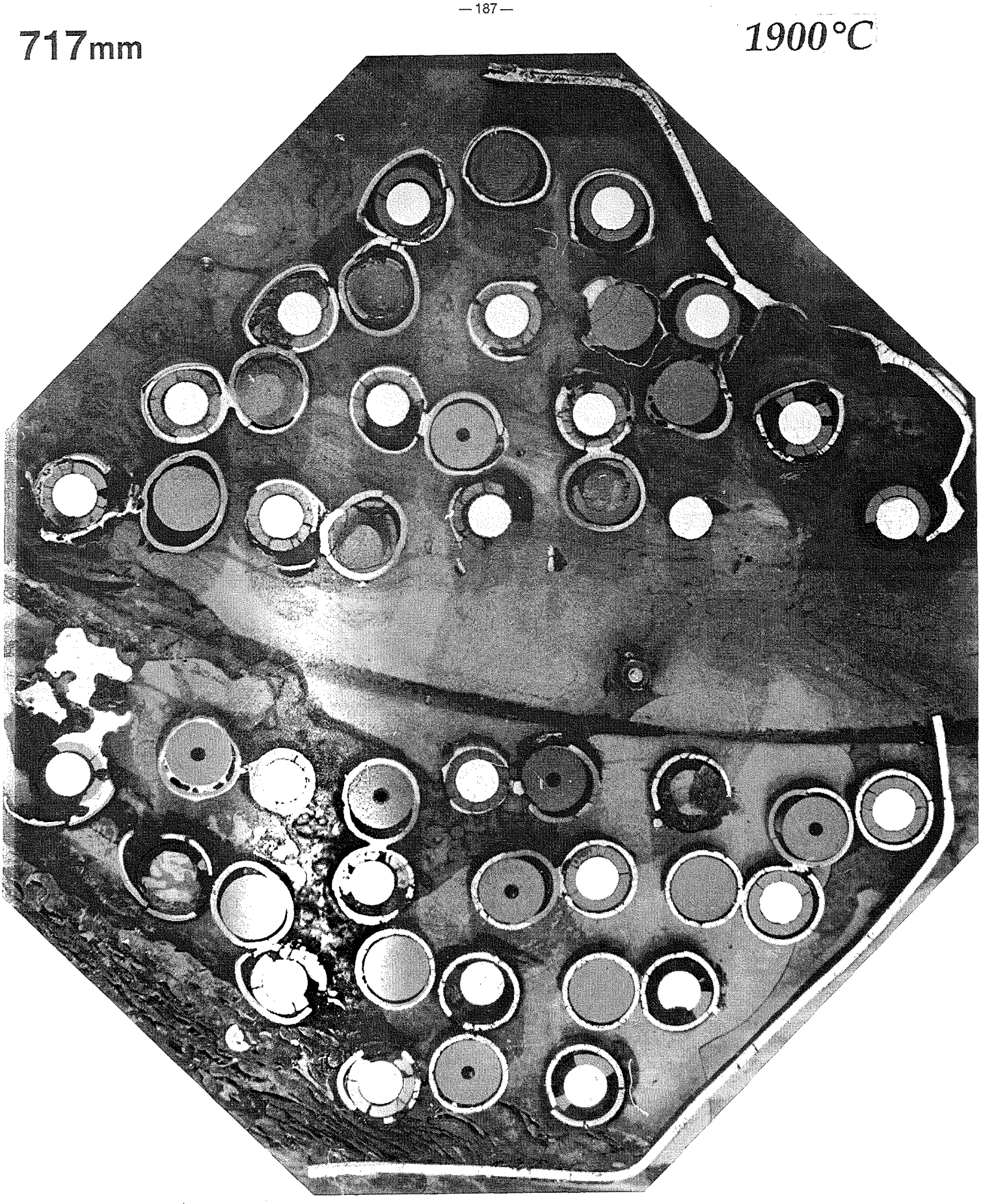

Fig. B5: CORA-18; horizontal cross-section at 717 mm elevation.

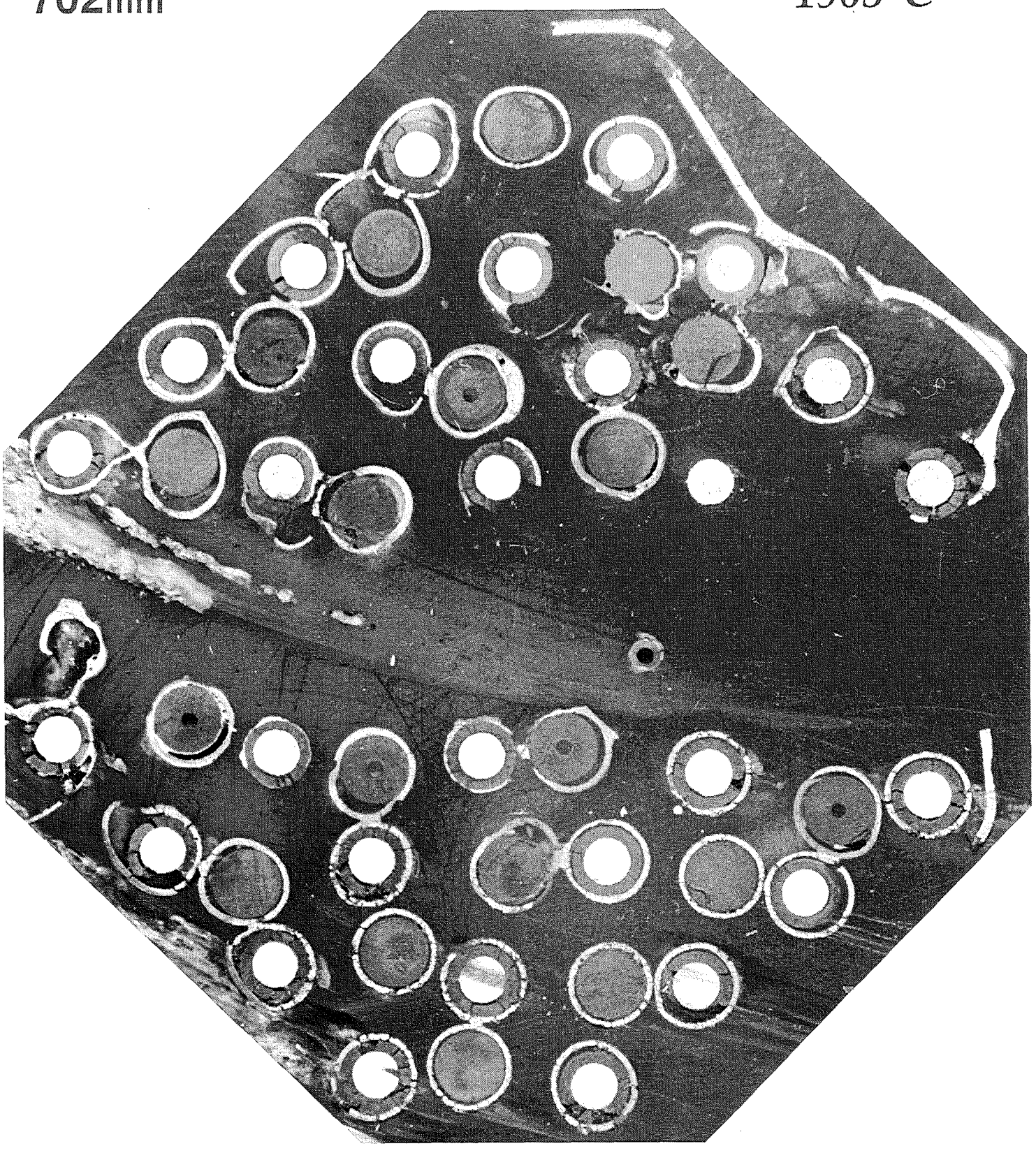

Fig. B6: CORA-18; horizontal cross-section at 702 mm elevation.

560mm

1895 °C

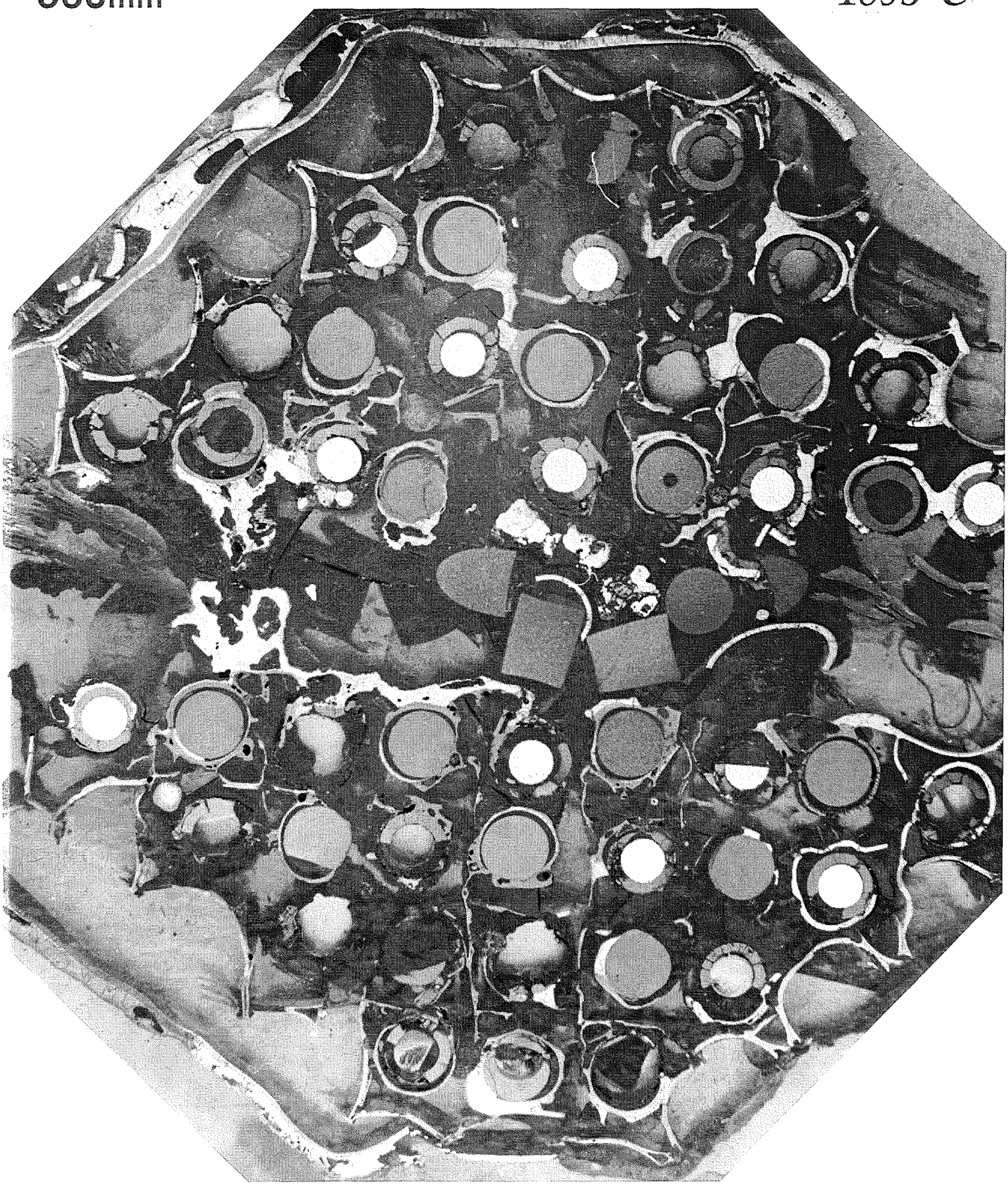

Fig. B7: CORA-18; horizontal cross-section at 560 mm elevation.

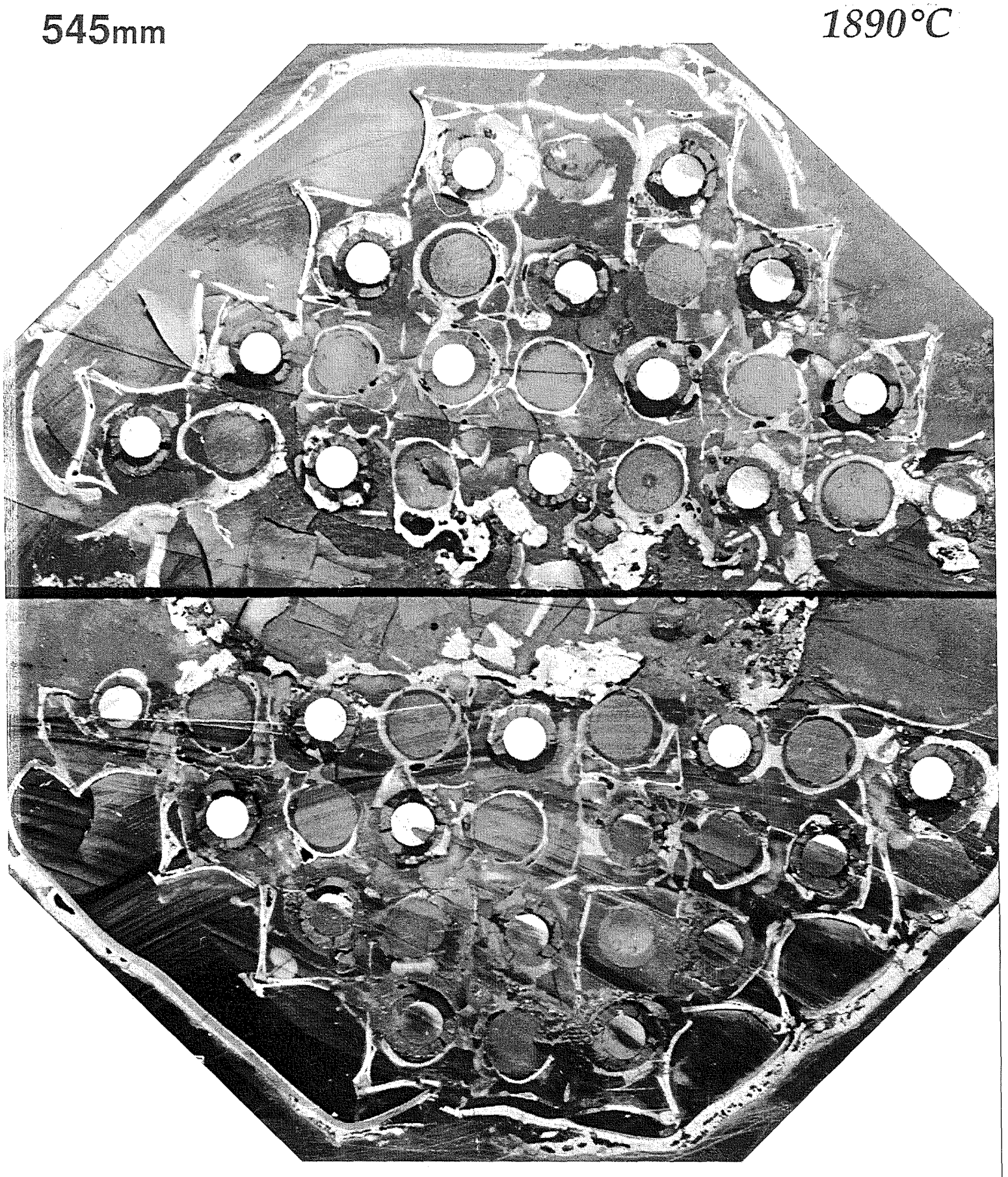

Fig. B8: CORA-18; horizontal cross-section at 545 mm elevation.

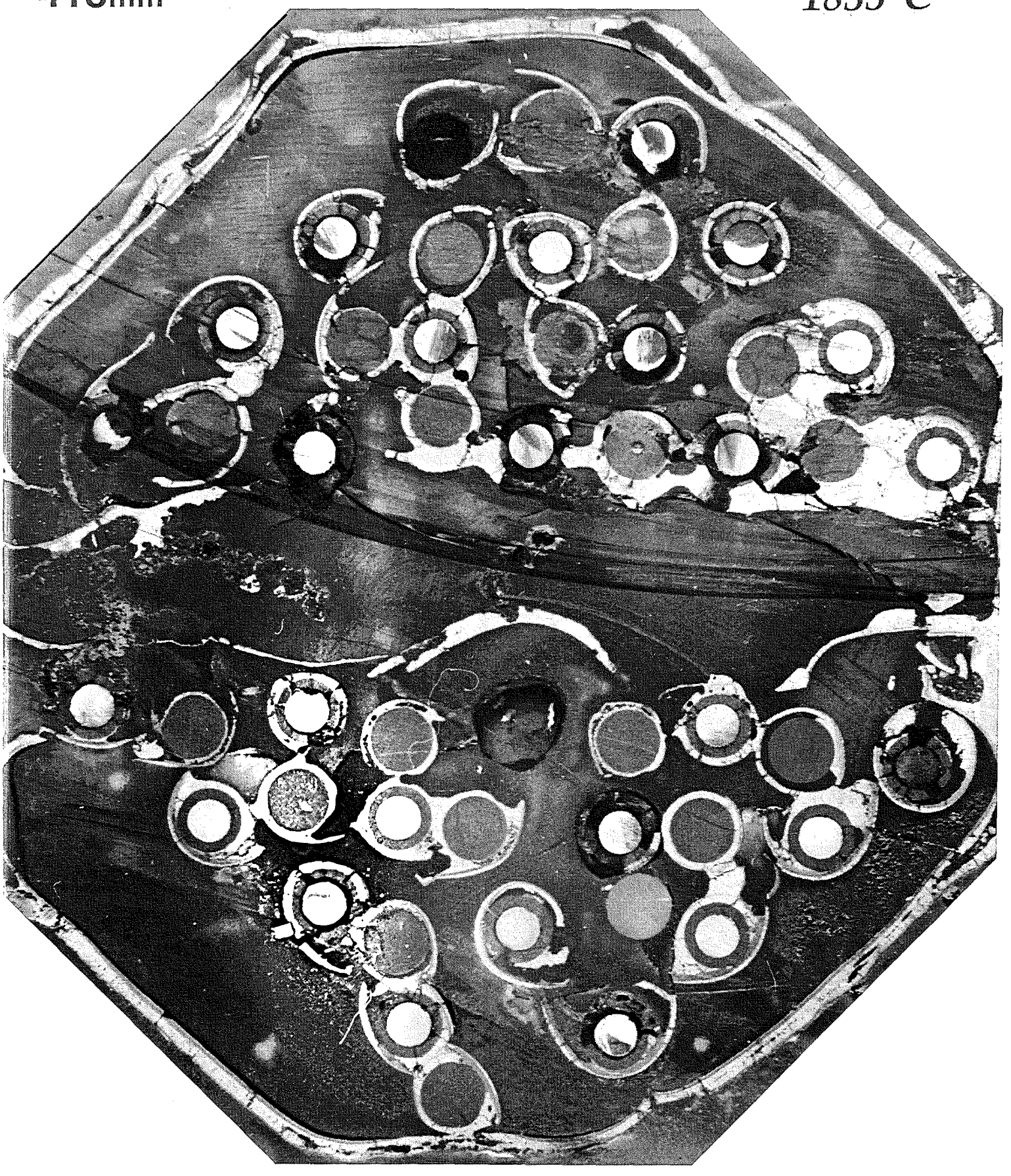

Fig. B9: CORA-18; horizontal cross-section at 413 mm elevation.

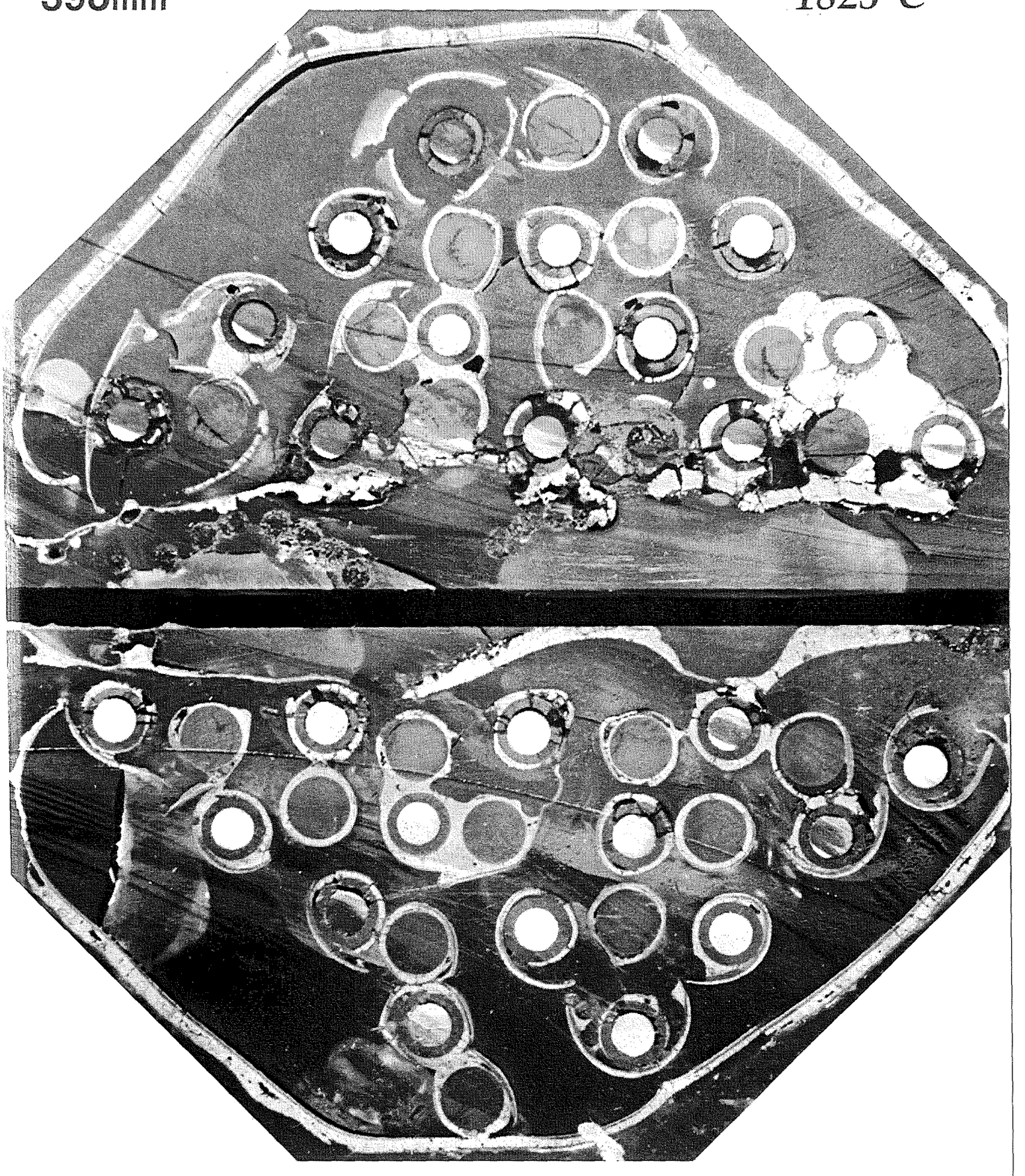

Fig. B10: CORA-18; horizontal cross-section at 398 mm elevation.

334mm

1745 °C

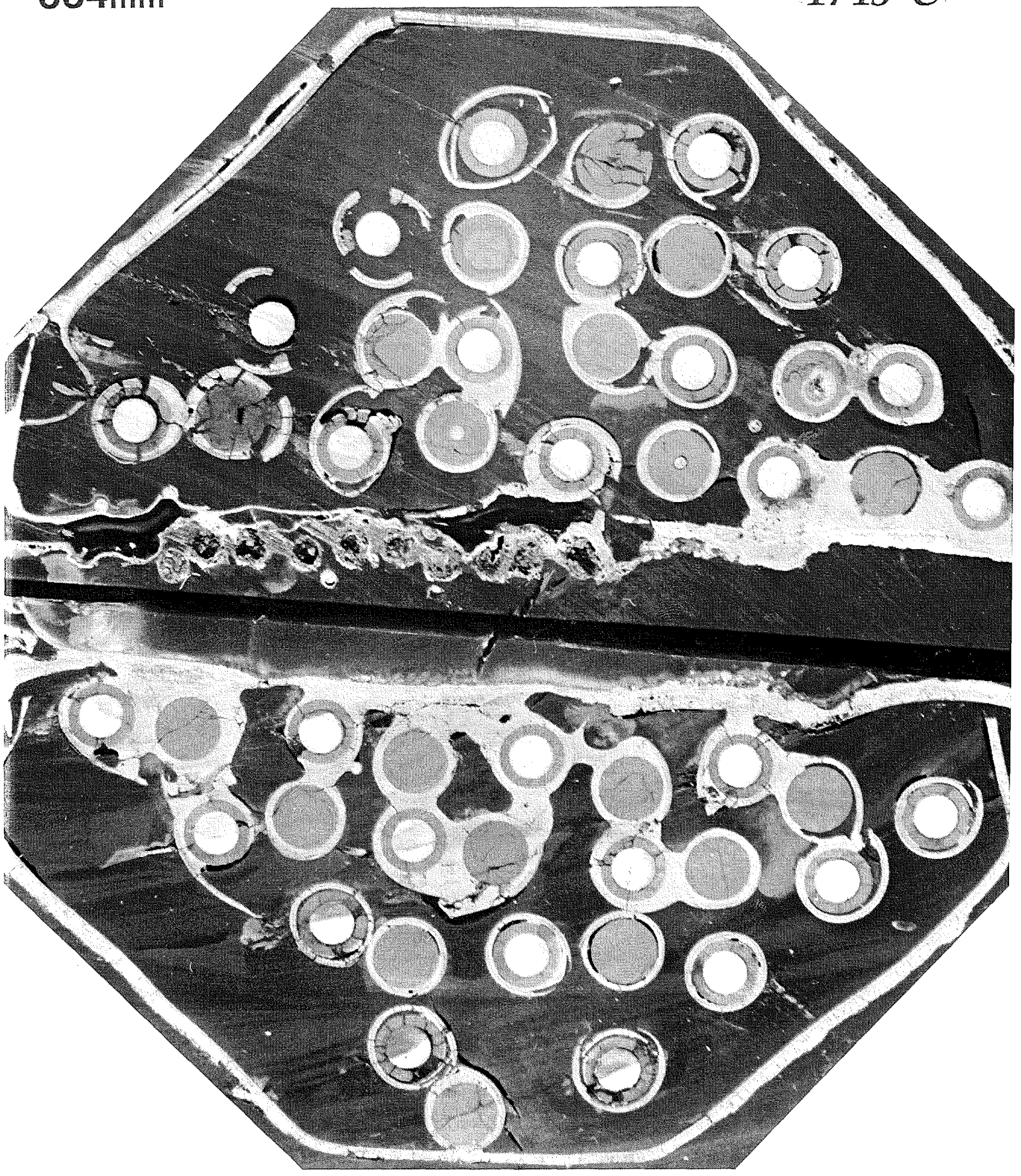

Fig. B11: CORA-18; horizontal cross-section at 334 mm elevation.

269mm

1585°C

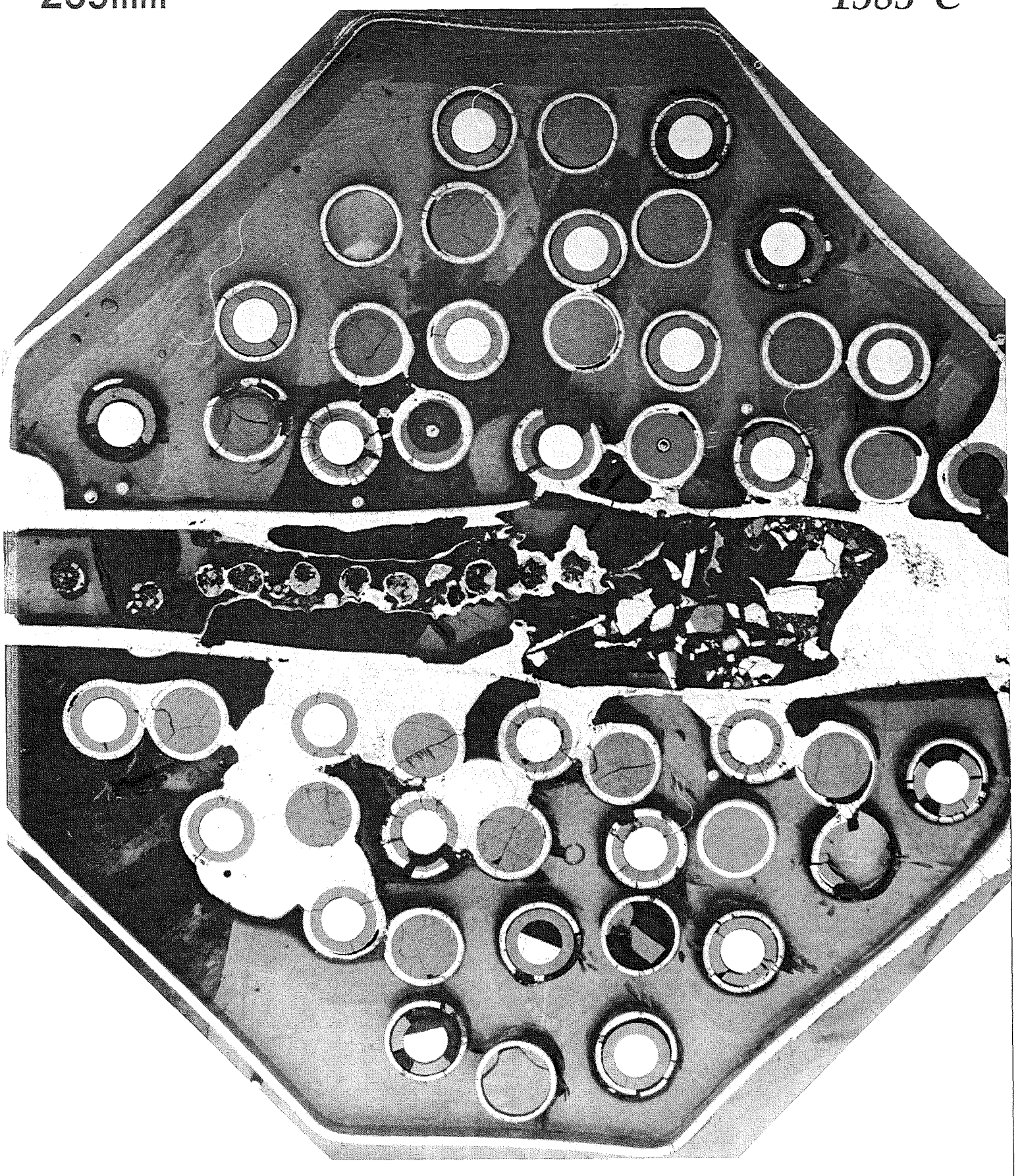

Fig. B12: CORA-18; horizontal cross-section at 269 mm elevation.

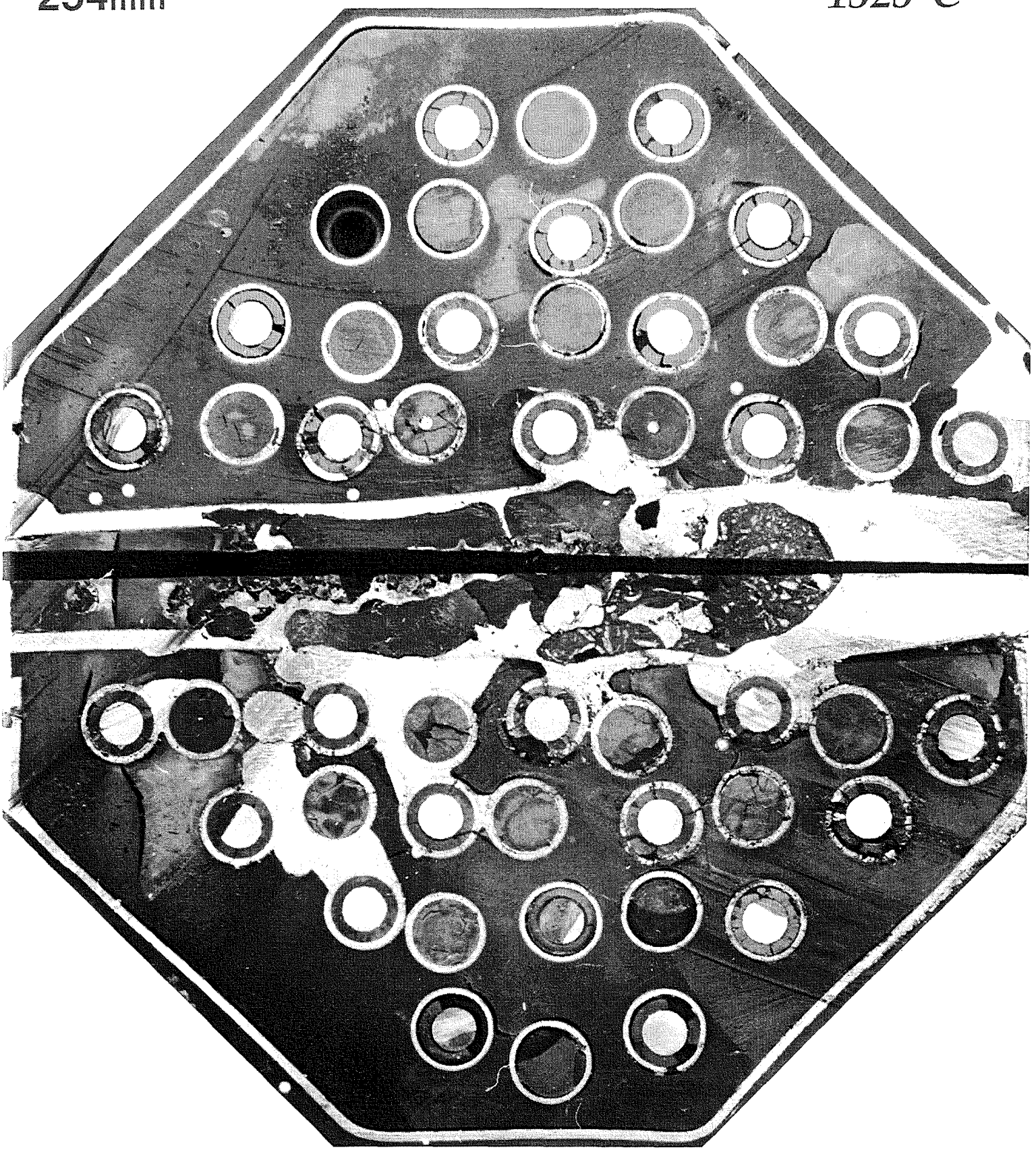

Fig. B13: CORA-18; horizontal cross-section at 254 mm elevation.

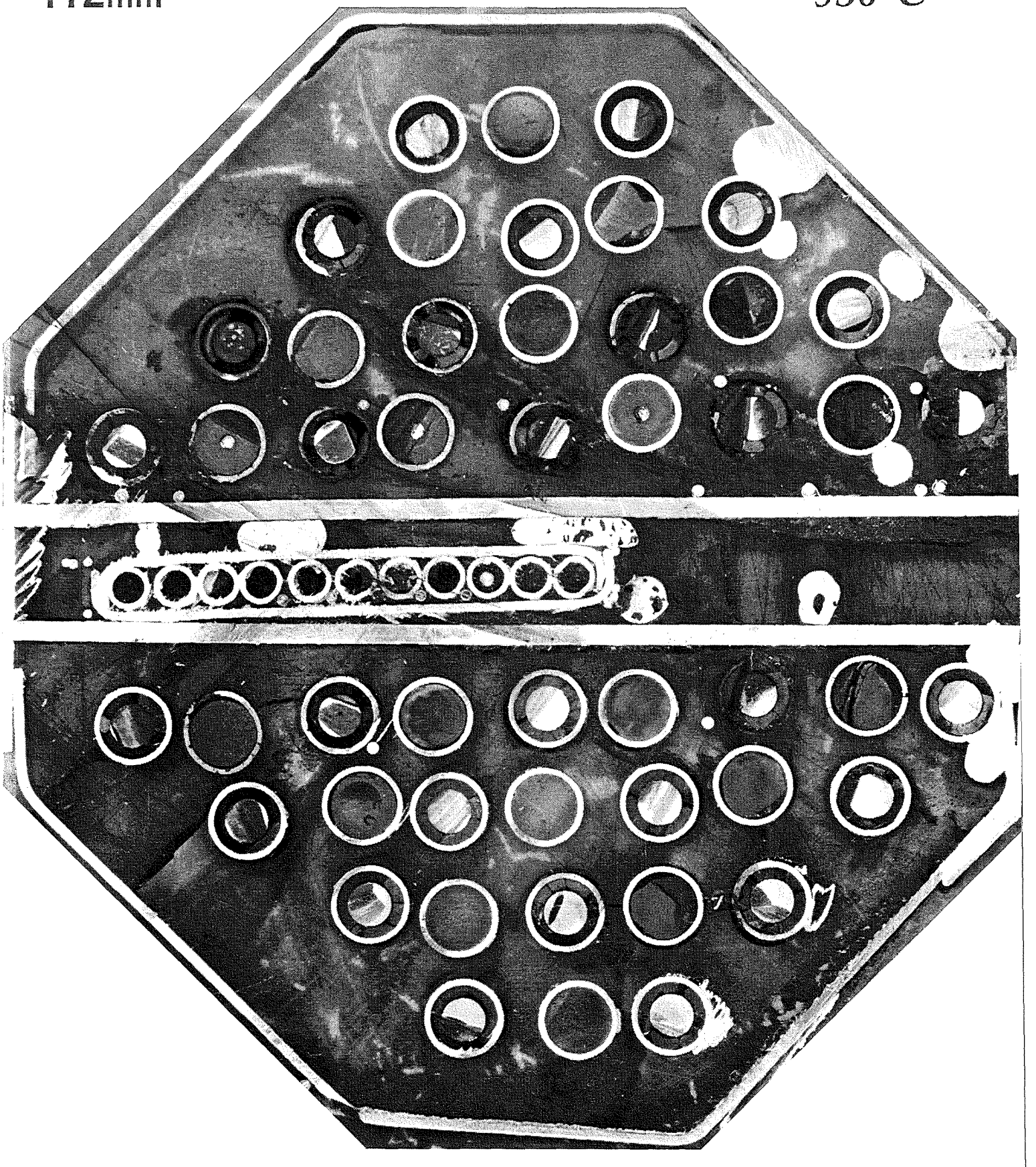

Fig. B14: CORA-18; horizontal cross-section at 112 mm elevation.

97mm

870°C

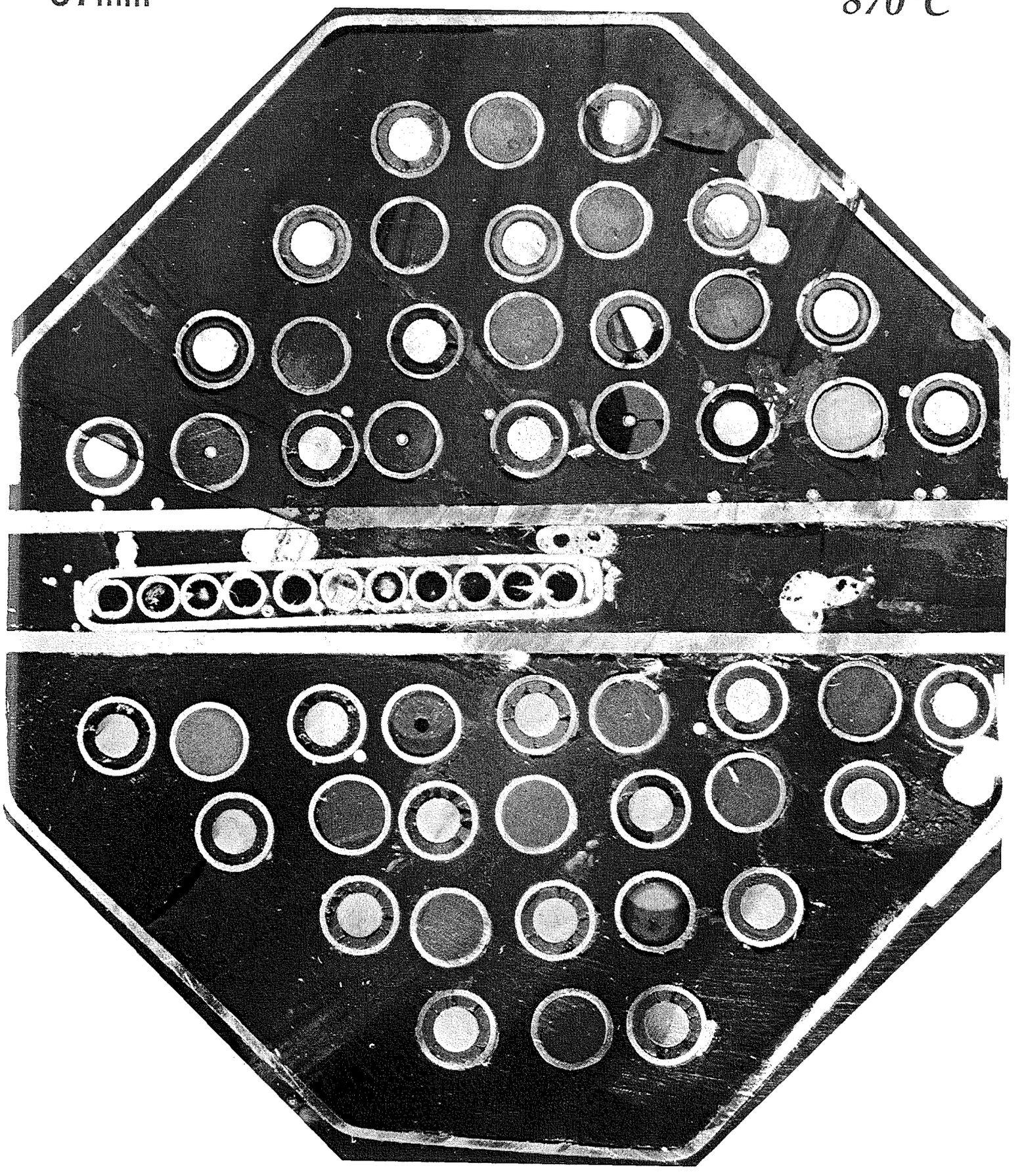

Fig. B15: CORA-18; horizontal cross-section at 97 mm elevation.